A Thesis Submitted for the Degree of PhD at the University of Warwick

Permanent WRAP URL:

http://wrap.warwick.ac.uk/184910
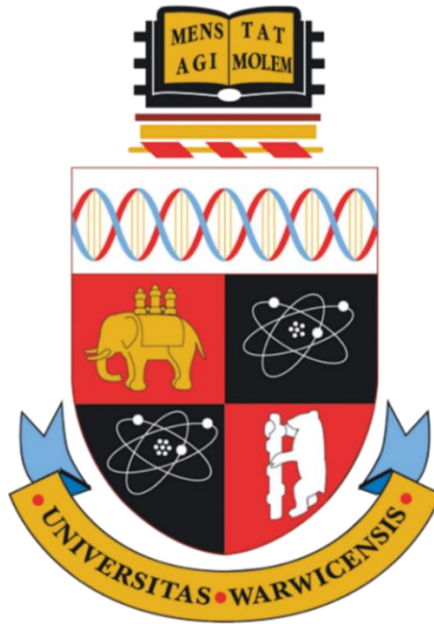
warwick.ac.uk/lib-publications

A Physics-Driven Model for the Remote Laser Welding and Development of Process Capability Space Framework for the Selection of Robust Process Parameters

by

Anand Mohan

A thesis submitted in partial fulfilment of the requirements for the
degree of Doctor of Philosophy in Engineering

Warwick Manufacturing Group, University of Warwick,
United Kingdom, CV4 7AL
December 2022

Dedicated to my parents and my beloved wife.

Table of Contents

List of Figures

List of Tables

List of Abbreviations

1D/2D/3D   1/2/3 - Dimensional

ANOVA   ANalysis Of VAriance

ARM   Adjustable Ring Mode

CP   Constant Power

CW   Continuous Wave

EBSD   Electron Back Scatter Diffraction

EDS   Energy Dispersive X-ray Spectroscopy

FE   Finite Element

FEM   Finite Element Method

FZ   Fusion Zone

HAZ   Heat Affected Zone

IMC   Intermetallic

ICE   Internal-combustion Engine

IPI   Intermediate Performance Indicator

KPI   Key Performance Indicator

LL	Lower Limit
MIMO	Multiple Input Multiple Output
OCT	Optical Coherence Tomography
PM	Pulsed Mode
POC	Percentage of Contribution
RLW	Remote Laser Welding
SEM	Scanning Electron Microscopy
SIMO	Single Input Multiple Output
SISO	Single Input Single Output
SPED	Specific Point Energy System
UL	Upper Limit
WPP	Welding Process Parameter

Declaration

This thesis is my original work and submitted to the University of Warwick to support my application for the degree of Doctor of Philosophy. I declare that this thesis has not been submitted in any previous application for any degree. The work presented was carried out by the author, except where explicitly stated. The author has published parts of this thesis which are listed in the list of publications.

Anand Mohan

05th December 2022

List of Publications

Publication related to this thesis:

Paper 1: **<u>Anand Mohan</u>**, Dariusz Ceglarek, Michael Auinger, Modelling of thermal quantities in laser welded joints for process assessment and parameters selection at the early design phase, Int J Adv Manuf Technol (2022). DOI: [10.1007/s00170-022-10182-7](#). Contributing to Chapter 3

Paper 2: **<u>Anand Mohan</u>**, Dariusz Ceglarek, Michael Auinger, Effect of beam oscillation on the fluid flow during laser welding, Mater. Today Proc. 59 (2022) 1846–1851. DOI: https://doi.org/10.1016/j.matpr.2022.04.435 Contributing to Chapter 4

Paper 3: **<u>Anand Mohan</u>**, Dariusz Ceglarek, Pasquale Franciosa, Michael Auinger, Numerical study of beam oscillation and its effect on the solidification parameters and grain morphology in remote laser welding of aluminium, Science and Technology of welding and joining. Accepted. Contributing to Chapter 4

Paper 4: **<u>Anand Mohan</u>**, Pasquale Franciosa, Dariusz Ceglarek, Michael Auinger, Numerical simulation of transport phenomena and its effect on the weld profile and solute distribution during laser welding of dissimilar aluminium alloys with and without beam oscillation. Int J Adv Manuf Technol. Accepted and under production. Contributing to Chapter 4 and chapter 5

Paper 5: Tianzhu Sun, **<u>Anand Mohan</u>**, Conghui Liu, Pasquale Franciosa, Dariusz Ceglarek, "Impact of energy distribution on the microstructure and mechanical performance in Adjustable Ring Mode (ARM) remote laser welding of high strength aluminium alloys", Journal of Materials Research and Technology. Accepted. Contributing to Chapter 6

Other peer-reviewed publications:

S.K. Dinda, D. Das, **<u>Anand Mohan</u>**, P. Srirangam, G.G. Roy, Effect of Beam Oscillation on Electron Beam Butt Welded Dual-Phase (DP600) Steel to 5754

Acknowledgements

Abstract

New environmental regulations and policies have transformed the manufacturing industry to develop capabilities for high uptake of structures which are lighter, stronger, and cost-effective. This transformation has expedited the development of new lightweight materials and joining technologies to support the high-volume manufacturing. The use of Aluminium alloys for lightweight manufacturing has increased in the past decades in the automotive industry from 35 kg to around 200 kg per vehicle. Welding of high-strength aluminium alloys is challenging due to high hot cracking susceptibility due to the rupture of the molten metal film at the grain boundaries during the solidification process. There are two possibilities to reduce the susceptibility to hot cracking: (*i*) Optimisation of process parameters to influence solidification conditions to promote generating equiaxed grain structure in the fusion zone; and (*ii*) Welding of dissimilar aluminium alloys and optimising the concentration of the weld.

It is crucial to have shortened lead time for the rapid development and deployment of new joining processes for the new lightweight materials. Current methodologies for the selection of robust process parameters provide limited performance due to (*i*) a limited understanding of the interaction of the material with the advancement in joining technologies; (*ii*) extensive dependence on manual expertise for the selection of process parameters based on a trial and error method; (*iii*) time intensive high fidelity models to survey the parameters space resulting in limited industrial applicability and scalability, hence constitute a significant barrier in quick selection of robust process parameters to decrease the lead time.

The proposed framework is based on three methodologies which explore Remote Laser Welding: (*i*) developing physics-based simulations to establish the relationship between material's behaviour with the varying process parameters; (*ii*) incorporating a sequential modelling approach to balance between high accuracy and computation time to survey the parameter space; and (*iii*) development of the process capability space for the quick selection of robust process parameters. Three physical phenomena are considered in the development of numerical modelling which are (*i*) heat transfer, (*ii*) fluid flow and (*iii*) diffusion to investigate the effect of process parameters on the weld thermal cycle, solidification parameters and solute intermixing layer during laser welding of high-strength aluminium alloys all of which provides a qualitative relationship to the grain morphology. The governing physical phenomena are decoupled sequentially, and process performance indicators are estimated based on the governing phenomena. At each step, the process capability space is defined over the parameters space based on the constraints specific to the current physical phenomena. The process capability space is defined by the constraints based on the process performance indicators. The process capability space is refined at each step (sequential modelling) based on the requirements of downstream processes.

The numerical model is developed using COMSOL Multiphysics software which is further verified experimentally with measurements specific to each physical phenomenon. The proposed modelling framework decreases the total computation time to survey parameter space by 55% and the developed model shows good accuracy with an error of 3.1%.

Chapter 1. Introduction

1.1 Motivation for the Thesis

The automotive industry is aiming towards lightweight manufacturing. The motivation behind the development of lightweight vehicles is to reduce CO_2 emissions and improve fuel efficiency. Ghassemieh *et al*. [1] reported that the fuel economy improved by 7% for every 10% reduction in weight. Swift changes in the requirements of the markets and the pressure of delivering high-quality products have accelerated the utilisation of new emerging technologies and breakthroughs in the automotive industry such as the use of new production technology (remote laser welding, RLW) for lightweight materials, collaborative automation with cobotic system for lightweight compliant structures and simulation solutions (advanced digital twins for production processes with lightweight compliant structures) to speed up the manufacturing process development phase and respond more rapidly to changing customer needs [2–5]. The automotive industry needs to ensure high productivity and cost efficiency in the increasing product variety needs with sustained or reduced time-to-market.

This has accelerated the development of joining processes such as RLW having capabilities such as non-contact, single-sided joining, the ability to create joints in different locations using robot repositioning and the ability to create a joint in seconds using a high-power laser beam for rapid development and deployment of new lightweight subassemblies such as used in battery electric vehicles (BEV). As a consequence, there is also a need for a paradigm shift towards right-first-time process development and ensuring near-zero defect manufacturing due to BEV engineering requirements. Therefore, the manufacturing industry requires a transformative

framework for the new product introduction (NPI) to reduce the design time and ensure product quality.

This framework can be built on efficient in-process monitoring, and weld quality assurance to accelerate the deployment of the welding processes for multiple product variants made of lightweight materials required by BEV. In the context, the selection of robust welding process parameters is the key challenge for high-volume manufacturing of multiple lightweight product variants. The selection of robust process parameters depends on the mechanical performance of the welded structure which depends upon the weld quality. The "Key Performance Indicators" (KPIs) evaluate the weld quality requirements such as weld width, throat thickness, penetration depth, and mechanical strength as defined by the industrial standards [6]. These KPIs depend on the weld thermal cycle, grain morphology, solidification parameters, weld profile and chemical composition of the weld. The weld formed must satisfy all the allowable ranges of each KPI and any violation from these ranges is considered as the formation of weld defects. Therefore, a considerable amount of research has been performed to develop a relationship between the process parameters and the KPIs [7,8]. Currently, the selection of robust process parameters and the process development is done through trials and errors and relies on time-consuming experiments [9,10]. Here, the robust process parameters refer to the specific combinations of parameter settings or variables within a manufacturing process that satisfies all the necessary requirements that are able to consistently deliver desired outcomes.

However, experiments alone are not sufficient to survey the parameters space, as it takes weeks or months to run and process them [11]. Numerical-based simulation models for laser welding are developed based on the Finite Element Method (FEM) to

provide insights into the process behaviour by providing Intermediate Performance Indicators (IPIs) such as peak temperature, heat affected zone (HAZ) volume, thermal gradient, cooling rate and solute concentration in the weld. These IPIs are either very difficult to measure or/and time extensive to be evaluated experimentally. The IPIs are the model outputs which may be determined directly from the experiments but provide critical insights to understand the process and have direct or indirect relation with the KPIs. KPIs are the final outputs which can be directly estimated from the experiments and are currently used for the comparison of a numerical model with the experiments. The KPIs are the key parameters which are defined to assess the quality of the weld which depends on processes and product variant. It also provides a direct analysis of the performance. These simulations of the laser welding process provide the direct estimation of KPIs to predict the weld quality saving time and resources. Efficient FEM laser welding models provide the option to be (*i*) run in the entire parameters space (high fidelity simulations which replace physical experimentations); or (*ii*) integrated with physical experiments in such a way that simulations are run in un-tested settings of parameters space decreasing the number of experiments required (lower fidelity simulations which reduce the number of necessary physical experiments). Low fidelity models in general predicts IPIs and develops correlation with KPIs either qualitatively or quantitatively. E.g., Thermal model can predict the depth of penetration based on the melting temperature of the alloy by applying the constraint. This is done by generating the correlation between the weld thermal cycle and KPIs. Whereas high fidelity model can directly predict some of the KPIs, e.g. Fluid flow model can predict the depth of penetration as defining the region where liquid molten pool is formed.

Laser welding is a multi-phase (solid, liquid and vapour) and multi-physics such as heat transfer, fluid flow, element transport, and driven process and thus, no current model has the potential to fully explain and co-relate all the governing physical phenomena, process parameters and KPIs. Furthermore, high computational runtime and resources (high-end processors, RAM, storage with solid-state drive) are required, depending upon the complexity of physical phenomena considered, which makes it impractical to utilise a high-fidelity FEM model for process parameter selection. So, there is a need for a framework such that the computation time can be reduced to survey the process parameters space for the selection of robust process parameters.

To sum up, RLW speeds up the welding process for lightweight manufacturing with improved weld quality and reduced time-to-market. Furthermore, it provides flexibility in design due to non-contact and single-side welding with large stand-off distance. However, the understanding of the effect of process parameters on the IPIs/KPIs is not fully understood and the selection of robust process parameters is time and resource intensive. Therefore, the motivation of this research is to develop a modelling framework for quick assessment and selection of robust process parameters during the early design phase.

1.2 Current challenges with Remote Laser Welding, Research Questions and Research Objectives

The automotive industry is aiming toward the reduction of body weight without hampering structural integrity. Davies *et al*. [12] suggested that the body-in-white (often referred to as the "white body") and internal combustion engine (ICE) were the major contributors to the weight of the vehicle therefore, body-in-white weight should be considered a critical design requirement for weight reduction. The

4

partial or complete replacement of traditional structural metals with lightweight metals such as high-strength steel, and aluminium alloys including new high-strength alloys, magnesium alloys or composites can significantly reduce the total body weight. The development of lighter structures enables not only a decrease in fuel consumption but also allows the ability to use equivalent weight for cargo and passenger transportation. Aluminium alloys are usually the material of choice due to their abundance, low cost, recyclability and corrosion resistance. The new design solutions focus on using a higher proportion of Aluminium alloys as a structural material or combining it with other automotive grades of aluminium alloys [13]. Welding techniques with high power density like laser welding (LW) are used for joining these lightweight materials with higher precision and speed as compared to conventional welding techniques. Sustainable manufacturing needs key enabling technologies that can help the welding industry to understand and answer the environmental and economic challenges. This means producing products with near-zero defects, cheaper, better and faster.

Remote Laser Welding (RLW) is one of the joining processes which can potentially meet the above-mentioned requirements as it offers a non-contact single-sided joining technology that allows high-speed welding for high-volume manufacturing [14]. It provides several advantages such as imposing heat in a very localised manner by modulating the power and location of the heat source which provides flexibility in terms of temperature field, flow field and concentration field developed to weld new generations of lightweight alloys. It provides a high depth-to-width ratio, less distortion due to less heat input to the workpiece, high welding speed with remarkable processing efficiency and can be easily automated by embedding the laser optics on the robot and scanning mirror as end-effector, for high productivity [15–17]. It creates a narrow fusion zone and heat-affected zone pertaining to less

metallurgical changes to the workpiece. The high-power density of the RLW leads to a high aspect ratio which makes it suitable to weld structures for dissimilar lightweight alloys in a hybrid joint configuration starting from thin sheets to thick plates having high throughput. The main advantages of high-power density (i.e., high power intensity but low overall heat input) such as high welding speed, more control over weld quality and low overall capital cost are shown in Figure 1.1. These advantages have accelerated the application of the RLW process for lightweight assembly in BEV manufacturing.
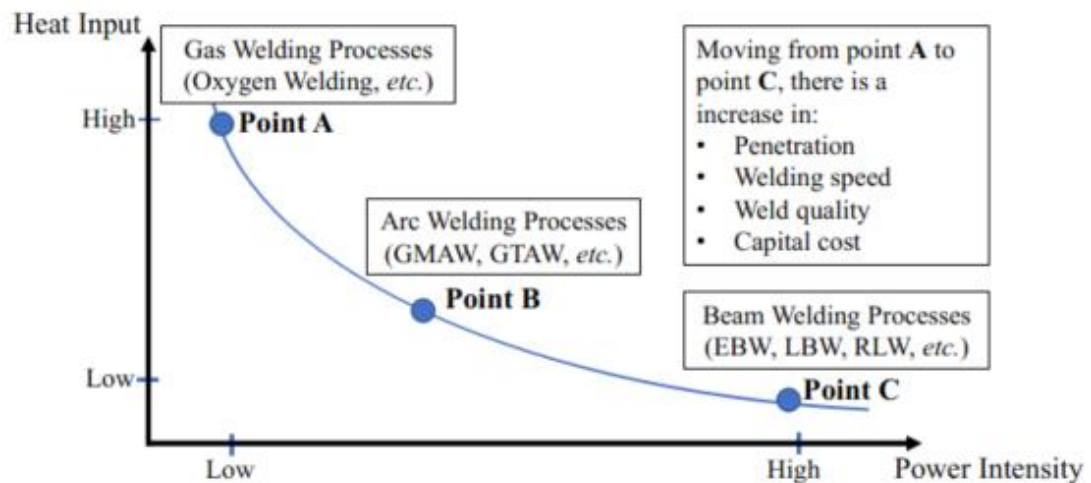
Figure 1.1 A variation of power density with the heat input to the workpiece for different welding techniques [18]

The selection of robust process parameters is important to avoid various unacceptable weld defects such as improper fusion, lack of penetration, and distortion. Currently, the quality of the weld is assured in four steps: (*i*) establishing optimum process parameters based on a trial and error approach; (*ii*) checking the variation (repeatability and reproducibility) and process capability of the selected process parameters for similar weld attributes and using the same parameters during the production phase; (*iii*) ensuring the required weld quality by performing various destructive and non-destructive weld characterization techniques to estimate the KPIs;

6

and (*iv*) conducting modification and refinement of the process parameters to satisfy all the KPIs.

A key challenge is the selection of robust weld process parameters (WPPs) to meet the weld quality, i.e., to satisfy all the KPIs. The effectiveness of the RLW process in enhancing weld quality relies on the intrinsic flexibility of RLW technology, which enables precise control over the application of heat to the welded materials. This includes the RLW capability for laser beam oscillation, beam shaping, and power modulation. This flexibility of RLW increases the number of initial weld process parameters whose effect needs to be understood and the selection of robust parameters is challenging especially based on the current method of trial and error. The selection of robust WPPs is critical to satisfying the weld quality requirements which depend on the requirements of the downstream processes such as surface finish, strength, weld dimensions and shape. With the increasing number of input process parameters, it is impractical to survey the parameters space by experiments alone as it is time and resource intensive. Therefore, the development of a numerical model is essential to establish the relationship between the weld quality and process parameters for the selection of robust process parameters during the design phase with a minimum number of experiments. High-fidelity numerical models require large computational time to solve which makes it impractical to survey the whole parameters space for the selection of robust process parameters whereas low-fidelity numerical models are able to describe the most prominent physics at a reduced computation time and resources. Therefore, a sequential modelling approach is proposed to balance between high accuracy and computation time (i.e., high-fidelity models) and low computation resource requirements models (i.e., low-fidelity models). The main steps to survey the parameters space using a sequential modelling approach are: (*i*) first step is the

7

development of a low-fidelity model based on one or two independent phenomena: (*ii*) defining IPIs/KPIs based on the physical phenomena with the allowable constraints to achieve the required weld quality; (*iii*) the WPPs within the allowable limits of IPIs/KPIs are selected and the region or space is defined as process capability space; (*iv*) in the low-fidelity model, next governing phenomena is added; (*v*) new IPIs and KPIs are defined based on the new physical phenomena and constraints are defined based on the required weld quality; (vi) the process capability space defined in the step (iii) is used instead of complete parameters space to define the new process capability space due to the addition of newly added phenomena. In this sequential modelling approach, a low-fidelity model based on a particular physical phenomenon such as heat transfer is developed to mirror the flow of heat but leave out all other physical phenomena such as mechanical deformation, fluid flow, and element transport. Relevant KPIs/IPIs are determined which is described by this low-fidelity model and the whole parameters space is surveyed. Based on the constraints on the KPIs/IPIs depending on the weld quality, the allowable WPPs are selected and these WPPs are feasible and can be selected for the welding such that they will maintain the weld quality which is assessed by the respective IPIs/KPIs. The combination of all possible WPPs within the allowable limits of the IPIs/KPIs is defined as the process capability space. In the next step, another governing physical phenomenon is added to the low-fidelity model which describes new KPIs/IPIs. However, in this step, only the determining process capability space of the previous step is surveyed. Just to note here that before the development of process capability space it must be tested if the newly added phenomena have an impact on the output under consideration. Again, new constraints are added to the new KPIs/IPIs and a more refined region on the parameters space is developed. This decreases the computational time as at each step fewer points

8

or smaller regions are required to be solved by the numerical model to survey the whole parameters space which is illustrated in Figure 1.2. It presents the schematic illustration of the sequential modelling approach.

In Figure 1.2 column one represents the parameters space (Figure 1.2 (a)) or process capability spaces (Figure 1.2 (b)-(e)), and the dotted points on these spaces represent the input parameter combinations for the numerical model to solve for, column two represents the number of simulations that need to be run to survey the parameter space and column three provides the computation time needed to solve to survey the respective space at each stage. It should be noted that the computation time mentioned is the average time taken to compute the numerical model to simulate the laser welding process based on the finite element method (described in detail in Chapters 3, 4, and 5) in this study. Three physics-driven phenomena are solved to survey the parameters space (Figure 1.2 (a)), which are heat transfer (detailed presented in Chapter 3), fluid flow (detailed presented in Chapter 4) and material mixing (mass transport) (detailed presented in Chapter 3). High fidelity model is a combination of all three physics which takes 36 hours (computation time as presented in this study) to compute a solution using a numerical model for each data point in the parameters space. Parameters space is defined as the area of the multidimensional combinations and interactions of process parameters (WPPs) and input variables that have been illustrated to assure quality [19]. It is a function or a relation between the critical WPPs and critical IPIs/KPIs. Figure 1.2 shows that there is a decrease in computational time by more than 55% to survey the parameters space using the sequential modelling approach. Just to note here that prior experiments are needed for the verification and validation of the numerical which includes the calibration of heat sources and absorptivity coefficient value which is discussed in detail in result chapter.
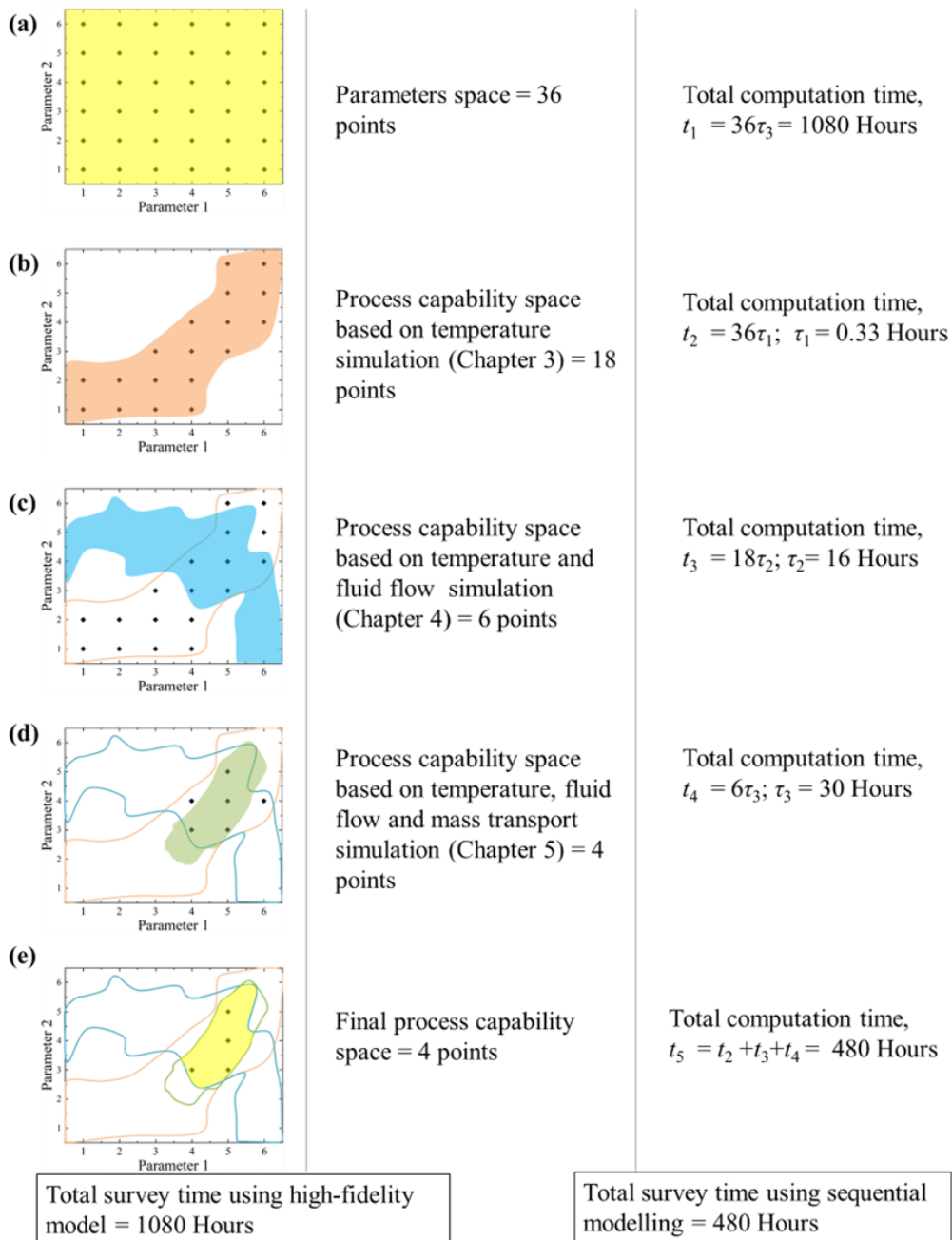
Figure 1.2 Schematic illustration of the sequential modelling approach to survey the complete parameters space. The points on the map are representative of the process parameter combinations and the computational time provided is the actual average time to solve the model solved in this study. (a) represents the parameters space for two process parameters, (b) process capability space based on the constraints on KPIs/IPIs based on temperature simulation, (c) process capability space based on the constraints on KPIs/IPIs based on temperature and fluid flow simulation, (d) process capability space based on the constraints on KPIs/IPIs based on temperature, fluid flow and mass transport simulation and (e) shows the final process capability space.

The scope of this thesis is to simulate the remote laser welding process for welding of high-strength aluminium alloy for lightweight manufacturing which is highly utilised in BEV as it combines the advantages of different grades of aluminium alloys such as low density, good formability, high strength-to-weight ratio, corrosion resistance, formability and weldability [20,21]. However, evidence indicates that high-strength aluminium alloys have high hot cracking susceptibility due to the rupture of the molten metal film at the grain boundaries during the solidification process [22–25]. Three distinct types of cracking referred to as "hot cracking." These types are as follows: (i) Solidification crack: These cracks appear at the fusion zone towards the end of the solidification phase, (ii) Liquation crack: These cracks occur in the heat-affected zone (HAZ) along the boundaries between grains, (iii) Weld metal liquation crack: observed in multi-pass welding, resulting from the remelting of grain boundaries [26]. Hot cracking typically occurs during the final stages of solidification and is influenced by a combination of mechanical, thermal, and metallurgical factors. The formation of such cracks is detrimental as they create stress concentrations that can lead to premature failure. Welding of 5xxx and 6xxx high-strength aluminium alloys together is considered beneficial as it results in more acceptable chemistry and the weld chemistry is moved from the peak of the crack sensitivity curve [26,27]. There are two possibilities to reduce susceptibility to hot cracking: (*i*) Optimisation of process parameters to influence solidification conditions to promote generating equiaxed grain structure in the fusion zone; and, (*ii*) Welding of dissimilar aluminium alloys and optimising the concentration of alloying elements by more mixing in the remote laser welding process. The formation of equiaxed grains and material mixing depends on the weld thermal cycle, convection due to fluid flow, solidification behaviour and mass transport due to diffusion and convection. These weld attributes

11

depend on the weld process parameters and proper selection of robust process parameters is critical and challenging to avoid weld defects. However, experiments are not sufficient to survey the parameters space as it is time and resource intensive. An alternative to the experimental investigation is a physics-driven model which solves numerically the governing physical phenomena to emulate the laser welding process. Even the survey of the whole parameters space by high fidelity numerical model is time intensive and not possible practically. The idea is to develop a process capability space framework based on a sequential modelling approach to reduce the computation time for the quick selection of robust process parameters. According to the reviewed literature in Chapter 2, the research gap identified as: (*i*) characterisation of the laser welding process in the current literature is mainly based on a single input, single output or multiple input single output scenario, (*ii*) time intensive high-fidelity numerical model to survey the parameters space, (*iii*) lack of understanding of the effect of welding process parameters on the IPIs/KPIs with consideration to beam oscillation and beam shaping, and (*iv*) lack of a framework for quick assessment and selection of robust process parameters during the early design phase.

Based on the aforementioned research requirements, the research questions (RQ) are outlined as articulated below:

RQ1: What is the effect of different laser welding process parameters on the weld thermal cycle, fluid flow, solidification behaviour, grain morphology and mass transport during the laser butt-welding of high-strength aluminium alloys with consideration to beam oscillation and beam shaping?

RQ2: How to quickly select the robust welding process parameters during the early design phase to achieve the weld quality requirements for the laser welding of high-strength aluminium alloys?

Therefore, the key objectives are mentioned below to pursue the above research questions:

- **Objective 1**: To investigate the effect of welding process parameters on the weld thermal cycle and development of process capability space during laser welding with consideration to beam oscillation.

- **Objective 2**: To investigate the effect of welding process parameters on the fluid flow, solidification behaviour and grain morphology and development of process capability space during laser welding of dissimilar high-strength aluminium alloys with consideration to beam oscillation.

- **Objective 3**: To investigate the effect of welding process parameters on the solute mixing development of process capability space during laser welding of dissimilar high-strength aluminium alloys with consideration to beam oscillation.

- **Objective 4**: To investigate the effect of an adjustable-ring mode laser beam (beam shaping) on the solidification behaviour and grain morphology during laser welding of high-strength aluminium alloys.

Table 1.1 provides a research roadmap of the problem, motivations, requirements, limitations, objectives, methodology and model validation.

Table 1.1 Research Roadmap

Problem	Motivations	Requirements	State of the art limitations	Objectives	Methodology	Contributions	Model validation
Estimation of weld attributes and reduction of physical experiments in Laser welding for NPI	Identifying joining process for lightweight manufacturing Improving the joining process to ensure *Near-Zero Defect Manufacturing* Understanding and proper selection of weld process parameters to ensure *Right First Time* Reduction of early design time for NPI Reduction of resource wastage and ensure increased productivity	Physics-based numerical model to simulate remote laser welding process	Time and resource expensive experimental estimation	Multi-physics model to estimate weld thermal cycle (Chapter 3, Paper 1)	Formulation of heat transfer model to estimate weld thermal cycle • Problem formulation, defining boundary conditions, heat source, optimise mesh for reducing computational time. • Identifying inputs and outputs of interest, formulation and defining IPIs and KPIs. • Developing surrogate model using data generated from FEM simulation for quick estimation	Estimation of influence of transport phenomena on weld attributes as function of process parameters to understand root cause of defects and improve performance of the welded structure Extending FEM models for variation in RLW like beam oscillation, beam shaping Process capability space framework for process assessment and reducing physical experiments Process capability space refinement based on the specific requirements of the downstream processes leading to reduction in cost and time	Validation of the model by comparing the obtained experimental results using case studies: 1. Joining of Al-6061 with Al-5754 in butt joint with and without oscillation configuration 2. Joining of Al-5083 in butt joint 3. Joining of Al-5754 with Al-6005 in butt joint 4. Joining of Al-6xxx in lap joint Scalability of the model to various process variations. Obtaining specific experimental results for the validating specific physics modelled. Interpretability of solidification behaviour and mechanical performance using numerical model and experiments
		Computationally less time-expensive numerical model to estimate weld thermal cycle	Computationally and time expensive high-fidelity FEM model	Computationally fast FEM model for weld thermal cycle estimation (t<= 2 hours) (Chapter 3, Paper 1)			
		Data generator for low fidelity surrogate model or data driven models	Statistical multivariate models with linear approximation	Development of regression model based on the data generated by the FEM model (Chapter 3, Paper 1)			
		Quantitative estimation of weld attributes as a function of WPPs	Capability restrictions to estimate weld attributes experimentally	Define IPIs and KPIs to determine weld quality (Chapter 3-6, Paper 1-5)	Sequential introduction of RLW process variation such as beam oscillation, beam shaping, power modulation • Sequential coupling of physics in the numerical model • Develop relation between WPPs, IPIs and KPIs based on MIMO • Scalability to different joint configuration and alloy combination • Develop relation between grain morphology, solidification behaviour and WPPs		
		Weld quality evaluation based on MIMO scenario	Weld quality is evaluated based on SISO or MISO	Evaluating weld quality as a function of WPPs to fulfil MIMO (Chapter 3-6, Paper 1-5)			
		Scalability to various alloy and joint configuration	Capability for fixed design	To investigate effect of WPPs on solidification behaviour and grain morphology with consideration to beam oscillation and beam shaping (Chapter 4 and 6, Paper 3 and 5)			
		Relation between WPPs, IPIs and KPIs	Capability for fixed alloy system	To investigate effect of WPPs on fluid flow and mass transport (Chapter 4, Paper 2 and 4)			
		Lack of datasets at initial design and production stages	Complex DOE matrix with an increase in input variables	Quick selection of process parameters to reduce development and design time for NPI (Chapter 3-5, Paper 1)	Process capability space framework for process assessment and process parameters selection for initial design phase Understand influence of WPPs on IPIs and KPIs for process improvement		
		Need of framework for quick selection of process parameters	Resource and time expensive parameter optimisation using experiments				
		Reduce number of experiments to save time and resources	Too many process parameters to be optimised				
		Optimum initial range of process parameters at early design phase to decrease development time for NPI	No data in NPI and process variation	Survey design space using high fidelity models in a less computational time and resources (Chapter 3-5, Paper 1)	Refinement of Process capability space based on the requirements of downstream processes by defining constraints over WPPs, IPIs and KPIs.		Demonstrate process capability framework for Al-5754 to Al-6005

14

1.3 Thesis Organization

Chapter 2, titled "*Literature Review*", reviews the related literature in the field of laser welding, operational characteristics of laser welding, and new developments in laser welding such as beam oscillation and beam shaping and highlights the research gap this thesis is focussing on. Further, it reviews the reported work in the field of numerical modelling of laser welding and process monitoring.

Chapter 3 proposes a methodology to estimate the weld thermal cycle with consideration to beam oscillation using a heat transfer model. It also proposes a surrogate model for the quick estimation of WPPs as a function of IPIs. (Paper-1 [28]).

Chapter 4 proposes a methodology to quantify the effects of fluid flow during laser welding. The fluid flow behaviour is estimated for circular and sinusoidal beam oscillation welding. It also provides a methodology to analyse the grain evolution by integrating the experiments and results from the numerical simulation and developing the process capability space based on the heat transfer and fluid flow model combined. (Paper-2 [29], Paper-3 [30] and Paper-4 [31]).

Chapter 5 proposes a methodology to estimate material mixing and provide the final process capability space. (Paper-4 [31]).

Chapter 6 discusses the advanced implementation of the numerical methodology to translate the developed model lap joint and Al-6xxx alloys with beam shaping and power modulation as add-on process variation to understand the effect of energy distribution on grain morphology. Also, it defines a process capability framework based on the solution of the numerical model for the selection of robust process parameters. (Paper-5 [32]).

Chapter 7 summarises the conclusions of the overall thesis and shows a direction for future work.

Chapter 2. Literature Review

The development of the research framework mentioned in the previous chapter requires a research review across the fields of welding and numerical modelling. This chapter provides a research review of the current state-of-the-art in RLW and presents fundamentals relevant to RLW including laser welding process parameters (WPPs), modes of laser welding, weld quality parameters, joint configurations and weldability of Aluminium alloys. This research review includes a deep analysis of previous work done in joining processes and a wide analysis and implementation of physics-based models to determine heat transfer, fluid flow and material mixing across variability of the RLW process to identify existing research gaps. This review includes an experimental and modelling approach for the development and assessment of the advances in the RLW process. The modelling and experimental approach to estimate the influence of the WPPs on the thermal cycle, fusion zone dimensions, melt pool behaviour, solidification behaviour and material mixing are discussed. The use of these relations for process monitoring is also reviewed. Hence, this chapter explores work done across RLW, including (*i*) the mechanism of the RLW process, modes of welding, laser welding process parameters, weld quality and joint configurations, (*ii*) laser welding of aluminium alloys, (*iii*) beam oscillation welding, (*iv*) beam shaping during using adjustable ring mode laser beam welding, (*v*) methods of process monitoring and process assessment, (*vi*) methods of developing and assessing new developments in the laser welding process assessment for the selection of robust process laser welding process parameters.

The overall goals of this thesis are: (*i*) to evaluate the influence of WPPs on the weld attributes such as weld thermal cycle, weld profile, solidification behaviour,

and material mixing; (*ii*) to develop a physics-based numerical model to emulate the recent developments in the RLW process such as beam oscillation and beam shaping to directly measure the weld attributes; and (*iii*) to develop a process capability space framework for process assessment and process parameters selection such that the number of experiments can be reduced for NPI. Furthermore, the developed physics-based numerical model is necessary to analyse the effect of the advancement in the RLW process such as beam oscillation, adjustable ring mode and associated additional process parameters. These additional parameters need to be studied, analysed and optimised for the required weld quality. To accomplish these goals, it is necessary to have a fast and accurate model which emulates the welding in a forward analysis manner (estimate weld attributes for given process parameters) and a framework which can be used as a backward synthesis model (relate weld attributes to the process parameters).

The remaining part of the chapter is organized as follows: Section 2.1 reviews the laser welding process parameters, modes of welding, weld quality indicators and joint configurations; Section 2.2 reviews the opportunities and challenges in the laser welding of aluminium alloys; Section 2.3 reviews influence of oscillating beam on the weld quality and weld performance; Section 2.4 reviews the beam shaping as an alternating approach for energy modulation in RLW; Section 2.5 reviews process monitoring and process assessment methods used in the laser welding process for the selection of robust process parameters; Section 2.6 reviews the numerical methods to model the temperature distribution, fluid flow and material mixing during laser welding, and finally Section 2.7 summarizes literature assimilation and knowledge gap identification.

2.1 Laser welding process

2.1.1 Physical principles of laser welding

Laser welding is a fusion welding process which produces joining between materials by partially melting the workpiece which creates a molten pool of metals followed by rapid solidification achieving a strong joint. The principle of the laser (light amplification by stimulated emission of radiation) is the use of a highly coherent monochromatic light beam having an energy density of 10^5-10^8 W/cm^2 [33], which is four times the magnitude of the conventional welding techniques [34]. The wavelength of the laser is in the visible or near infra-red region. Focussing the laser beam into a small spot can act as a heat source by generating sufficient energy for welding, cutting and piercing metals and other materials. The irradiation created by the laser is directed by the optics using mirrors and lenses to focus on the workpiece to achieve high power density [35]. A variety of lasers have been developed such as CO_2 laser, Nd: YAG laser, fibre laser, disk laser and high-power diode laser increasing the use of lasers in different industries. Lasers are categorised based on (*i*) the mode of operation or (*ii*) the type of gain medium. Depending upon the mode of operations, there are two types of lasers continuous wave (CW) mode laser and pulsed mode (PM) laser. In the continuous mode, the laser beam is composed of constant frequency and amplitude while in the pulse mode, a series of light is emitted at a certain amplitude and frequency. Therefore, the CW laser has a deeper depth of penetration as light is emitted continuously for the same average power [36]. Depending upon the power density and laser-material interactions, it can be classified into two modes: conduction mode and keyhole mode of laser welding.

2.1.2 Modes of laser welding

2.1.2.1 Keyhole mode of laser welding

This mode of laser welding is used to join thick material [37] having a very high power density laser of 10^6-10^8 W/cm^2. A very focused and high power density beam leads to localized vaporization of the workpiece and forms a blind hole/plasma cavity which is called a keyhole. This formed hole is surrounded by the molten metal pool. The stability of the keyhole formed is sustained by maintaining the equilibrium between vapour pressure and surface tension [38]. Vapour generated during the formation of the keyhole holds the molten materials from falling into the keyhole and keeps the hole open for the welding process. There is always a tug of war between recoil pressure, hydrodynamic pressure, radiation pressure and between surface tension, and hydrostatic pressure, where the former leads to opening and increasing the depth of the keyhole and the latter leads to closing of the keyhole [39]. Recoil pressure, surface tension, and hydrostatic pressure are predominant in terms of magnitude, influencing the opening and depth of the keyhole, while the others are of lesser significance and are primarily considered for numerical [38]. Figure 2.1 shows the keyhole mode of laser welding [40]. Keyhole mode of laser welding results in low distortion due to low heat input, and higher penetration enabling the welding of thick workpieces with a high aspect ratio and high productivity [41]. It also has some disadvantages as it leads to a high amount of porosity, high levels of spatter formation, and loss of alloying elements from the melt. From the modelling point of view to predicting keyhole formation, the temperature at the keyhole wall can be taken as the vaporization temperature [42]. It was also assumed by some researchers that when the peak temperature becomes larger than the vaporization temperature, it represents the

formation of a keyhole, and the mode of welding was treated as the keyhole mode of welding.
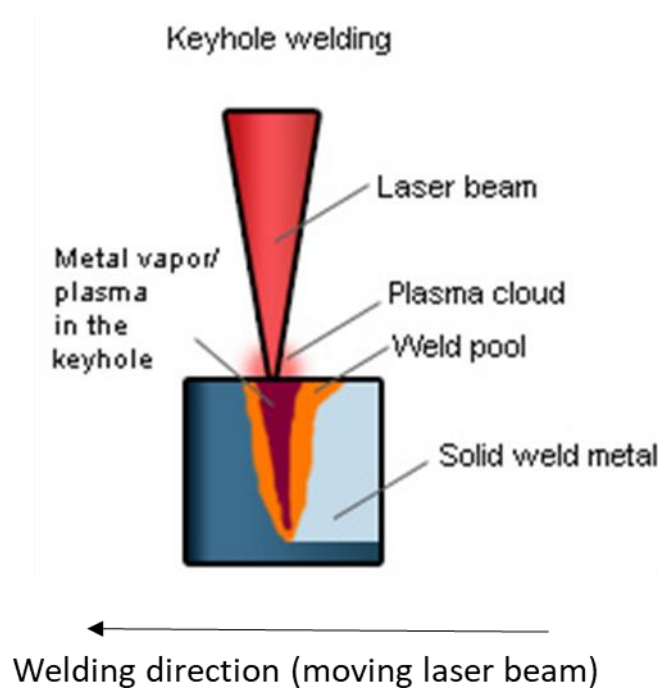
Figure 2.1 Schematics of the keyhole mode of laser welding [40]

2.1.2.2 Conduction mode of laser welding

In this mode, the laser power is just below the threshold beam power to start the formation of the keyhole i.e., just below the boiling point of the material. In this mode, there is only enough power to melt the surface of the workpiece without significant vaporization of the materials [37]. Often conduction welding is considered when the power density of the laser is less than 10^6 W/cm^2 [37,43,44]. Another definition of conduction welding states that it occurs when the vaporisation of the material is insignificant [43] or when the power density is not enough to cause boiling of the material [44] or when the aspect ratio (width-to-depth ratio) of the cross-sections is smaller than 0.5 [45]. The energy of the laser beam is partially absorbed on the surface and heat is distributed through conduction and convection of the molten pool

of materials throughout the materials resulting in the weld formation. This is used for joining thin sheets and has a bowl-shaped profile. It has a larger HAZ as compared to the keyhole mode and a smooth and gradual transition from the fusion zone to the base metal [46]. Figure 2.2 illustrates the schematics of the conduction mode of the laser welding process [40]. Conduction mode is more stable as compared to keyhole mode [47,48] as there is no vaporization of materials taking place leading to no porosity and spatter problems in welding. But this mode leads to high distortion of the workpiece due to high heat input. From the modelling point of view, predicting the conduction mode of welding the peak temperature should be below the vaporization temperature [49–51].
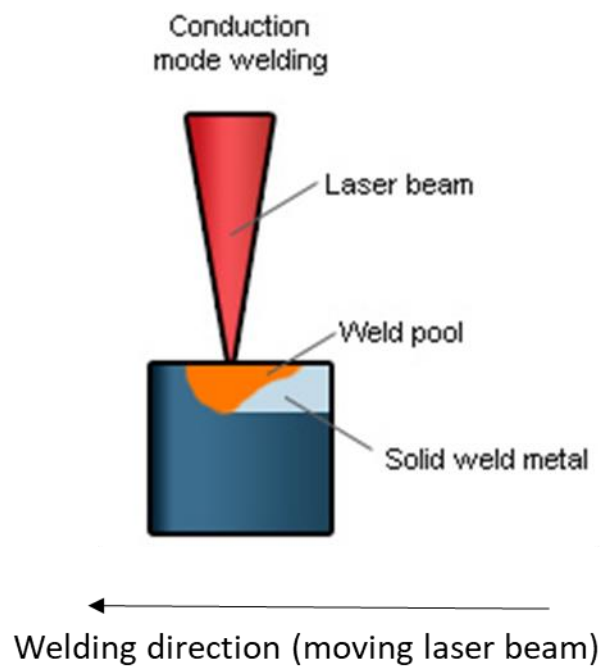
Figure 2.2 Schematics of conduction mode of laser welding [40]

2.1.3 Advantages and limitations of laser welding

With the development of new and powerful lasers, laser welding has revolutionised the whole field of welding. Remote laser welding (RLW) is an

emerging solution to material joining as it offers benefits such as a non-contact welding process, less distortion and remarkable processing efficiency [16,17]. Microstructural degradation is the minimum [34] and narrow heat-affected zone (HAZ) width and low distortion, as compared to conventional arc welding, due to the low heat input to the workpiece [52,53]. It has the ability to achieve a high depth-to-width ratio of welds which eliminates the need for multipass welds as done in arc welding. Laser welding is a high-precision welding technique with high speed and flexibility with the ability to weld difficult to weld materials such as titanium, copper etc. [33]. It does not require filler materials and can be done at room temperature by producing welds with little or no contamination at all. It can weld dissimilar materials and can be automated by using robotic arms.

The typical spot size of the laser beam is between 100 to 1000 µm which requires stringent positioning of the parts with allowable gaps around 0.1 times the thickness of the material. When welding at high speeds, the rapid solidification and cooling rates increased the chances of pore and crack formation within the weld [40]. The rapid cooling rate of the order of 4000 K/sec can lead to an increase in the hardness of HAZ and weld zone and deteriorate the toughness of the welds [54]. One of the major limitations of laser welding is against materials with high reflectivity such as aluminium, copper etc. where the loss of power is more than 70% of the power input [55]. Utilizing laser beams with high-power density gives rise to the creation of an exceedingly unstable molten pool, increasing the likelihood of spatter formation [56]. There is also the formation of metastable phases or intermetallics [57] which are brittle in nature and act as a crack initiation point for fracture. The thickness of the intermetallics layer depends upon the cooling rate, power and peak temperature acquired during the laser welding [58].

23

2.1.4 Laser welding process parameters

In the RLW process, a high-intensity laser beam is used as the source of heat energy which produces coalescence between the materials by melting the workpiece followed by rapid solidification. The delivery and distribution of the heat to the workpiece governs the weld thermal cycle, weld profile, solidification behaviour, grain morphology in the fusion zone (FZ) and HAZ, weld surface quality and weld strength [17,59]. This delivery and distribution of heat are regulated by the weld process parameters such as spot radius, welding speed, laser power, and focal offset. To achieve a high-quality defect-free weld, it is necessary to select appropriate process parameters and understand the influence of process parameters on the weld quality and strength [60]. These process parameters provide the flexibility to modify the joining processes such that the defects can be reduced and mechanical strength can be improved. This section represents the key process parameters which are divided into three broad sections namely; (*i*) design parameters which describe the geometric configurations of the parts to be joined; (*ii*) technological parameters which govern all the properties related to the heat delivery, (*iii*) material parameters related to the material properties of the part to be welded, and (iv) derived parameters which are derived from the combinations of other parameters but are utilised to analyse the process.

2.1.4.1 Design parameters

▪ **Joint Geometry** – This parameter has related to the configuration of how the parts

to be joint are connected for welding. Examples are butt welds, bead-on-plate, lap

joints, and T-joint. In this work butt and lap joints are produced. During butt

welding edges of the plates are put together in a close fit-up. In the case of lap

joints, the plates to be joined are placed on top of other as illustrated in the Figure

2.3 below.

(a)   (b)   (c)   (d)
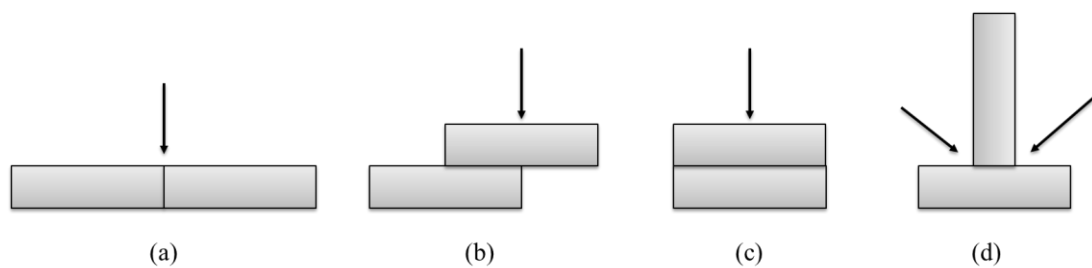
Figure 2.3 Schematic diagram of different joint configurations (a) Butt joint, (b) Lap joint, (c) Overlap joint and (d) T-joint. The arrows in the images indicate the position where the materials are welded together.

In general, butt welding is performed in the keyhole mode of welding such that deeper

penetration depth can be achieved to have an optimum mechanical performance of the

weld. Figure 2.4 shows the schematic illustration of the different stages of butt

welding. Butt welding is widely used in the manufacturing industry for the joining of

two dissimilar materials and materials with different thicknesses. The efficiency of

butt welding relies on the gap between the welding plates and the laser spot size. The

laser beam is defocussed to increase the spot size but in return, it decreases the power

density resulting in a lowering of the penetration depth. In practical cases, it is difficult

to maintain the gap below the threshold level due to the inconsistent trimmed edges of

the plates during machining. However, this can be improved by using beam oscillation

laser welding [61,62].
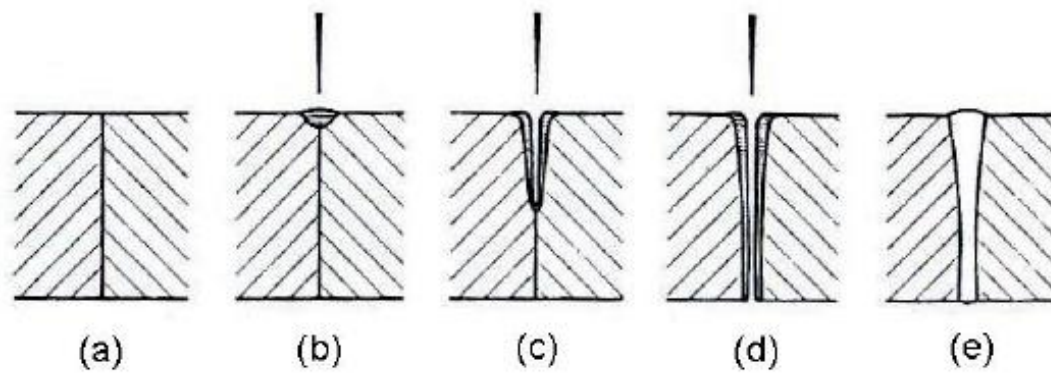
Figure 2.4 Schematic illustration of different stages in butt welding in keyhole mode (a) initial stage, (b) start of melting, (c) start of keyhole formation, (d) full penetrated keyhole and (e) solidified weld profile [63]

A lap joint is performed for thin plates extensively used in the automotive industry. Lap welding can be categorised into three types based on the state of the plates to be welded: (i) liquid/liquid, (ii) liquid/solid and (iii) solid/solid [64]. In the first case, both plates are melted followed by solidification to form a bond. In this case, there is no control over the mixing behaviour and if the metals are chemically incompatible leads to the formation of intermetallics, for example, welding steel with aluminium alloys. These intermetallics are brittle in nature and deteriorate the mechanical properties of the joint. In the second case, the material at the top is melted and the material at the bottom is in a solid state. A molten layer is formed in the interface between the plates leading to the formation of the bond after solidification. This is used for the materials having a significant difference in the boiling point. In the third case, both plates are in the solid-state and constant pressure is applied along with the heat such that the bond is formed based on the principles of diffusion welding. Figure 2.5 schematically shows the three categories for welding during lap joints.

26
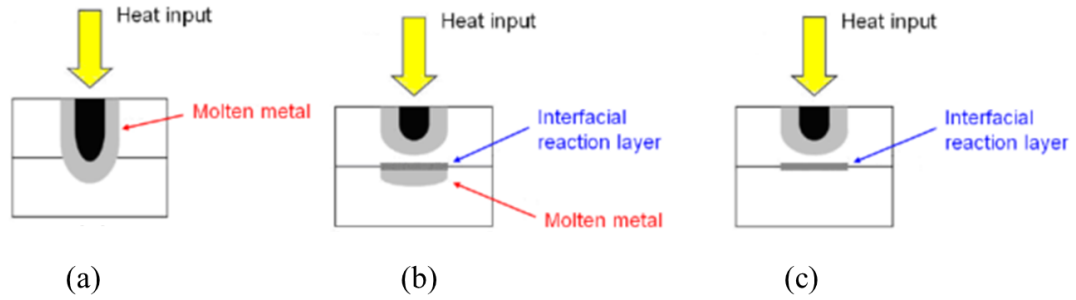
Figure 2.5 Schematic illustration of three categories of lap joint welding based on the state of the plates (a) liquid/liquid state, (b) liquid/solid state, and (c) solid/solid state [64].

- **Weld gap width** – The gap between the plates to be joined is a critical parameter as if the gap is large enough, the laser beam will pass through it. In general, the spot size of the laser beam is around 100-1000 µm which should have the correct positioning of the plates with allowable gaps. For keyhole welding for deep penetration, it is very crucial to have a close fit-up between the plates to achieve a good quality weld. This is a little bit relaxed for the defocussed beams due to the increase in the spot size.

- **Material thickness** – The thickness of the plates determines the process parameters which govern the amount of heat energy applied for efficient penetration and coalescence between the plates to be welded together. This parameter determines the efficient coupling between the welding speed and laser power to have proper coalescence and joint strength. Thicker plates require higher laser power and lower welding speed for full penetration welding.

- **Laser power** – Laser power is one of the most important process parameters that influence the [65] amount of heat flow from the laser source to the workpiece. Thus, it needs to be optimised to have a high-quality weld. If the laser power applied is too low, it will lead to a weak weld due to insufficient penetration and extremely high laser power leads to defects such as spatter, undercut, burning of alloy elements and drop through of the weld [65,66]. Laser power is selected based on the thickness of the material, material composition and absorptivity of the material. Khan *et al*. [67] suggested that the penetration depth could be controlled by laser power, and concluded that the penetration depth could be increased with increasing laser power if other parameters are kept constant. Li *et al*. [68] conducted an experimental investigation of laser power and found out that the welding speed for full penetration could be increased by increasing the laser power.

- **Welding speed** – The welding speed is the only process parameter which directly affects throughput, which means higher welding speed leads to higher throughput. It affects the weld shape and dimension, the flow of molten metal, the cooling rate, the solidification rate, and material mixing which determines the final grain morphology. At a higher welding speed, the solidification rate is higher which does not provide enough time for the molten liquid to flow from the periphery to the weld centre leading to the undercut [37,69]. Mai *et al*. [70] suggested that the higher welding speed improved the weld porosity as the weld became shallower thus leading to a favourable condition for the pores to move to the surface of the weld. Within the scope of the examined range of the welding speed, their findings indicated that augmenting the welding speed led to an elevated thermal gradient

along the solidification front. This escalation in thermal gradient enhanced the potential for crack formation and residual stress [71]. A higher welding speed could lead to a decrease in micro-segregation due to higher solidification restricting the formation of intermetallic phases [72]. DuPont *et al*. [73] found that at a lower welding speed, the molten pool was elliptical in shape and teardrop shape at the higher welding speed.

- **Focal Offset** – The focal offset controls the spot size on the workpiece and has a significant effect on the weld quality. Focal offset is selected to make the laser very finely focussed to increase the power density and defocussed to make a large spot size for performing gap bridging or conduction welding. Negative values of the focal offset mean that the laser beam focal plane is below the surface of the workpiece and positive values mean the position of the beam focal plane is above the workpiece [74] as shown in Figure 2.6. In their study, Sun *et al*. [75] discovered that defocusing the laser beam resulted in a reduction in peak temperature and porosity. However, they observed that increasing the defocusing beyond +3 mm caused a significant decrease in joint strength, reducing it by 40% according to their experimental setup.
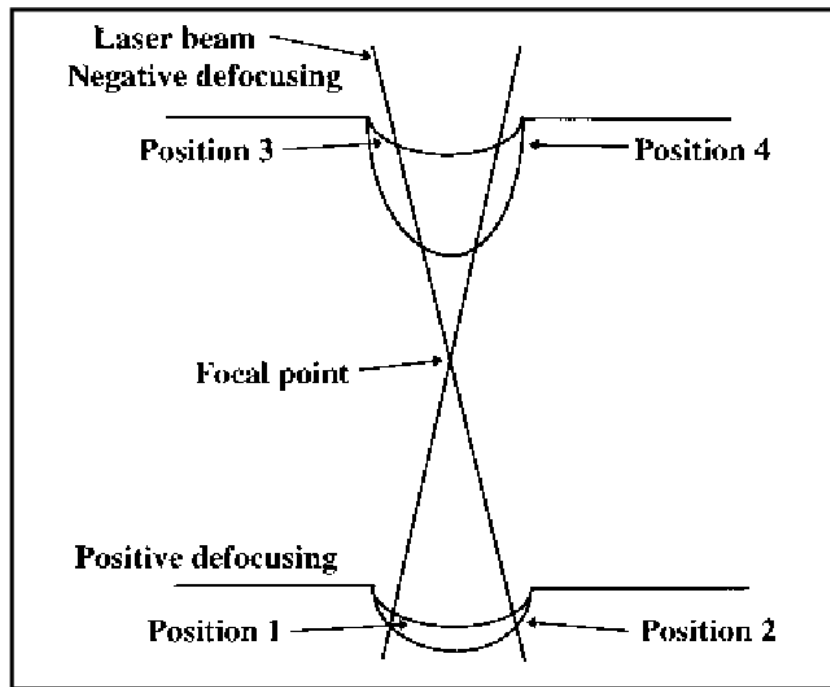
Figure 2.6 Difference between positive and negative focal point positioning [76].

▪ **Incidence Angle** – The angle between the laser beam axis and the vector normal to the workpiece is defined as the incidence angle. Due to the reflectivity of the laser beam from the metallic surfaces, the laser beam is not always perpendicular as it can damage the laser system and the objects right next to it by uncontrolled scattering. Incidence angle is a critical parameter for practical purposes as there are certain regions during the weld which can only be reached by the robot when it is inclined at a certain angle. When the beam is perpendicular to the surface of the workpiece the laser spot is circular and has the highest power density for a given power. When the laser beam is inclined at an angle, the laser spot becomes elliptical which leads to a decrease in power density. Liao and Yu [77] found that the depth of penetration and weld width at the top surface decreased as the angle of incidence was increased while maintaining the constant power which is shown in Figure 2.7. The power density drop had a cosine behaviour with the incidence angle.

30
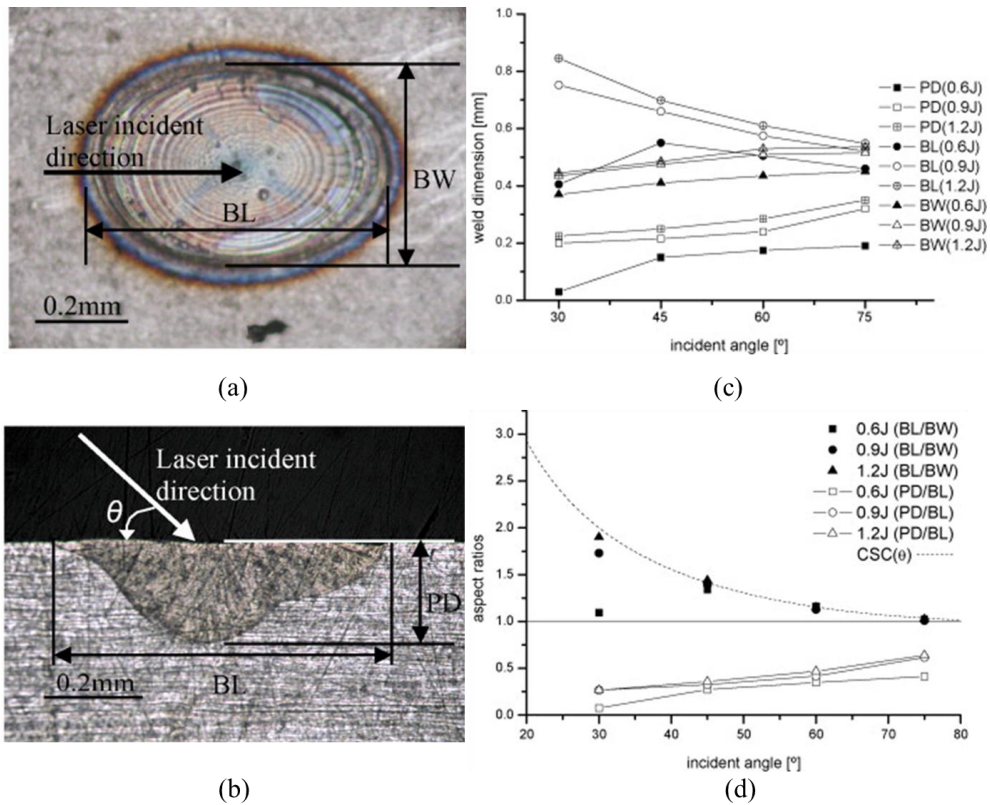
Figure 2.7 Experimental results obtained by Liao and Yu [77] depicting the influence of incidence angle on the weld shape (a) View of the top surface of the welded spot, (b) transverse cross-section of the weld formed, (c) characteristics length of the welds as a function of incident angle and (d) aspect ratio of the weld as a function of incidence angle.

2.1.4.3 Material parameters

The physical and chemical properties of the materials to be welded are dominant parameters deciding the weldability of the material by using the laser. Physical properties determine the degree of heat transfer and fluid flow [78]. It includes thermal conductivity, specific heat capacity, density, reflectivity, heat transfer coefficient, emissivity, latent heat, thermal expansion coefficient, thermal diffusivity, viscosity, surface tension gradient, melting point, boiling points etc. [79]. Chemical properties determine the phenomena such as the formation of cracking, oxidation, intermetallics formation, porosity, grain refinement, and segregation. These can be quantified based

31

on the chemical composition of the alloys, phases in the base metal, phases formed in the weld, grain orientation and morphology, and shape and density of pores.

2.1.4.4 Derived parameters

In laser welding, depth of penetration is one of the most important KPIs which needs to be adjusted depending on the joint geometry and application. To achieve a desired depth of penetration, a range of combinations of welding speed and laser power can be used for a constant laser spot size [80,81]. Also, for the given combination of welding speed and laser power, the depth of penetration can be different if the spot size is changed. Many researchers had tried to identify parameters to uniquely define penetration depth which enabled data transferability between different laser systems. Most of these parameters are power density, interaction time, energy density, heat input per unit length, heat input per unit area, Peclet number etc. [82,83]. The initial approach was to characterise the process based on the heat input to the workpiece [84]. However, the same heat input can be achieved for a different laser spot size. Many researchers used parameters such as energy required per unit thickness, normalised incident power and Peclet number to characterise penetration depth [82,85–87]. However, these parameters were used to roughly estimate general trends in laser welding such as melting efficiency, and threshold irradiance for melting rather than predicting the depth of penetration. Researchers had demonstrated that power density and interaction time could be used to distinguish laser welding processes [37,83]. An example of the processing map developed by Ion *et al.* [83] using dimensionless groups of process variables is shown in Figure 2.8.
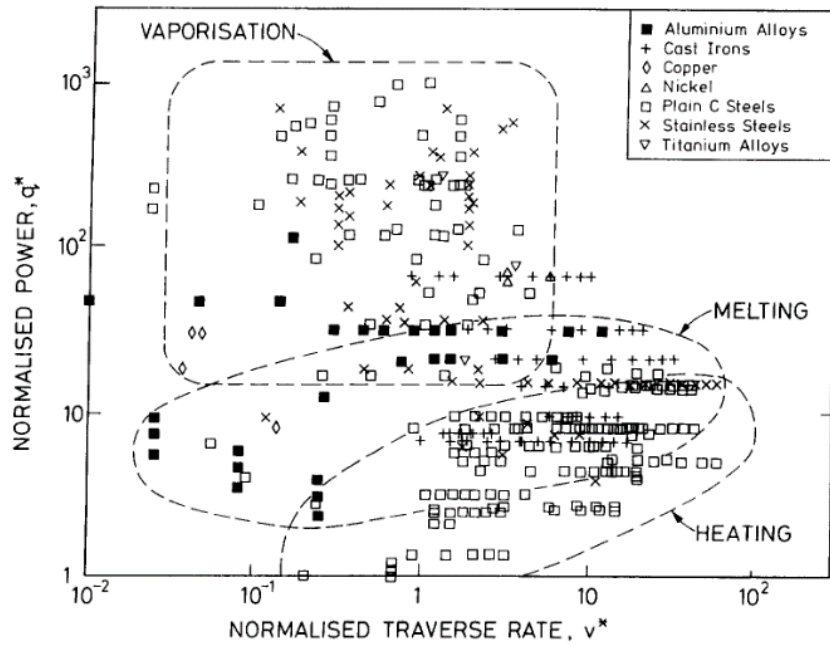
Figure 2.8 Laser processing map developed by Ion *et al*. [83] based on the dimensionless groups of process variables and identified by materials. The data were grouped together into three main classes of process.

- **Power density** – Power density is defined as the power of the laser beam applied

  to the area on the surface of the workpiece which is equivalent to spot size as

  given in Eq. 2.1

$$Power\ density = \frac{P}{\pi r^2} \qquad\qquad 2.1$$

 Where *P* is the power of the laser and *r* is the radius of the laser spot on the surface

of the workpiece. The shape of the beam spot will be elliptical with the change of

incidence angle. Power density determines the mode of welding i.e. conduction or

keyhole mode of laser welding and has a direct relation with the weld geometry and

fluid flow in the weld region [77,88,89]. In modelling, the power density is one of the

critical parameters to define the temperature distribution during laser welding [90–92].

Torkamany *et al*. [88] investigated the influence of power density on the welding mode

and grain morphology. He found that the power density influences the transition

between the conduction to keyhole mode. It had a significant impact on the grain morphology of the weld and fusion zone dimensions. Kawahito *et al*. [93] studied the effect of power density on the weld morphology using four different laser spot sizes ranging from 130 to 56 μm. The research revealed that the laser power density had a significant impact on enhancing weld penetration at higher welding speeds. Moreover, it was possible to produce sound partially penetrated welds without defects like porosity, underfilling, or humping within a wide range of process windows. Specifically, welding speeds range from 4.5 to 10 m/min, coupled with fibre laser beams measuring 360 μm or 560 μm in spot diameter. Tzeng *et al*. [94] and Cheng *et al*. [95] investigated the effect of power density and welding speed on various weld defects such as solidification cracking, centerline crack, holes and porosity.

- **Interaction time** – Suder and Williams [96] defined the interaction time as the time a particular point on the surface of the workpiece was exposed to the laser beam during the laser welding process which is given in Eq. 2.2 where t_i is the interaction time, r is the radius of the laser spot and S is the welding speed.

$$t_i = \frac{2r}{S} \qquad 2.2$$

 A series of experiments were conducted to examine the relationship between interaction time and the energy applied to the workpiece. It was discovered that the depth of penetration exhibits a logarithmic dependency on the interaction time as shown in Figure 2.9.
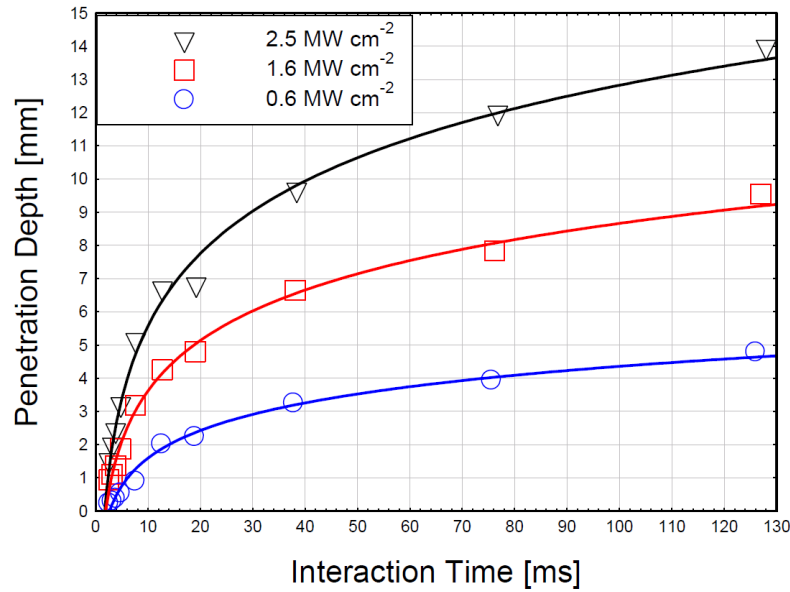
Figure 2.9 Experimental results obtained by Suder and Williams [96] showed the logarithmic dependencies of the penetration depth with the interaction time for three different laser intensities

2.1.5 Weld quality

In essence, welding is a process in which heat is applied using a very concentrated heat source such that two or more parts have coalesced together at their faying surfaces. These faying surfaces are where the heat is applied to melt and solidify to form a strong bond. The physical integrity of the welded structure depends upon the weld quality and is assessed based on the key performance indicators (KPIs). The critical weld quality requirements are as follows: (*i*) the weld formed must satisfy the tolerance of the design dimensions and should not have any distortion to the welded parts, (*ii*) there should be consistency on the weld bead formed with no cracks and holes, (*iii*) the weld should have required mechanical strength and fatigue life, and (*iv*) surface finish and appearance should be satisfied the required level depending upon the applications. The weld quality can be divided into three categories based on the

35

requirements: (*i*) aesthetic, (*ii*) metallurgical and (*iii*) mechanical. The discussion related to weld quality is in the context of laser welding in this dissertation.

2.1.5.1 Aesthetic weld quality

Aesthetic weld quality addresses the surface appearance and smoothness of the welded bead. Aesthetic weld requirements are generally assessed by visual inspection. Spatter deteriorates the aesthetic quality and is one of the prime reasons for the loss of mass. Spatter is the ejection of molten metal droplets and it is important to have less amount of spatters for Class-A surface finish [97]. Wu *et al*. [98] investigated the factors affecting spatter formation in laser welding of 5083 aluminium alloy and suggested that the surface tension around the keyhole and recoil pressure caused due to evaporation were two factors that affect the formation of spatter. He found that the spatter formation could be suppressed by increasing the stability of the keyhole. Schweier *et al*. [99] studied the effect of beam oscillation laser welding on the spatter formation and measured the spatter behaviour using a high-speed camera and object tracking algorithm. Their study's conclusion indicated that the suppression of spatter formation could be achieved by elevating welding speed, and conversely, it exhibited an increase with the rise in laser power for the range of power investigated. It was also noted that oscillation frequency exerted a minor influence on the phenomenon of spatter formation. Stritt *et al*. [100] proposed that the process monitoring system could be utilized to detect welding process features such as spatter formation. They discovered that increasing the welding speed from 1 m/min to 10 m/min caused spatters to transition from being generated in no predominant direction to being directed against the welding direction as shown in Figure 2.10. Also, corrosion, burn-through and cracks influence the aesthetic weld quality. A good quality weld must be leaking proof and have incurred sealing capabilities.
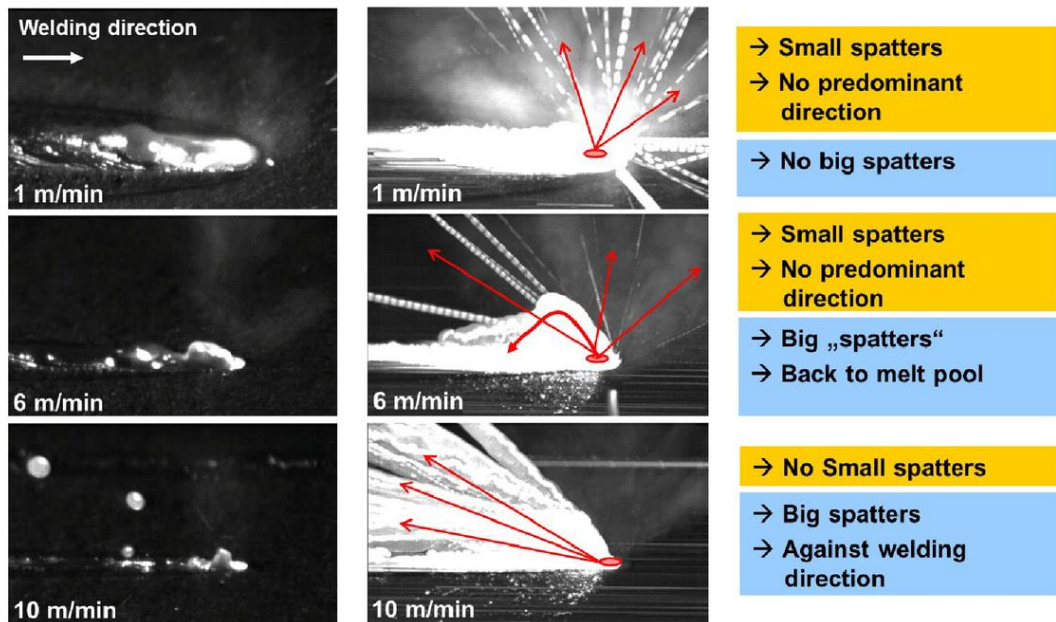
Figure 2.10 The experimental results obtained by Stritt *et al*. [100] depicted the spatter formation for different welding speeds.

2.1.5.2 Metallurgical weld quality

Metallurgical weld quality refers to the grain morphology (size, shape, distribution, structure, phases etc.) of the weld. The laser welding process is a combination of rapid heating and cooling cycles termed a weld thermal cycle. The grain morphology of the weld changes by the heat transfer and weld thermal cycle during welding as illustrated in Figure 2.11 [101,102]. It is critical to understand these changes in grain morphology as it affects the mechanical performance of the welded joints. Due to the very rapid rate of heating and cooling in laser welding, micro-segregation is least expected in laser welding as compared to other fusion welding processes while some brittle intermetallic phases are formed leading to the formation of cracks [103]. In general, the weld formed can be divided into three regions depending upon the temperature experienced: (*i*) the fusion zone (FZ) where the temperature experienced is above the liquidus temperature of the material, (*ii*) the heat-affected zone (HAZ) where the temperature is below the solidus temperature and

above the temperature which can modify the grain morphology due to significant recrystallisation and grain growth, and (*iii*) the base metal (BM) where no possible heat-treatment takes place.
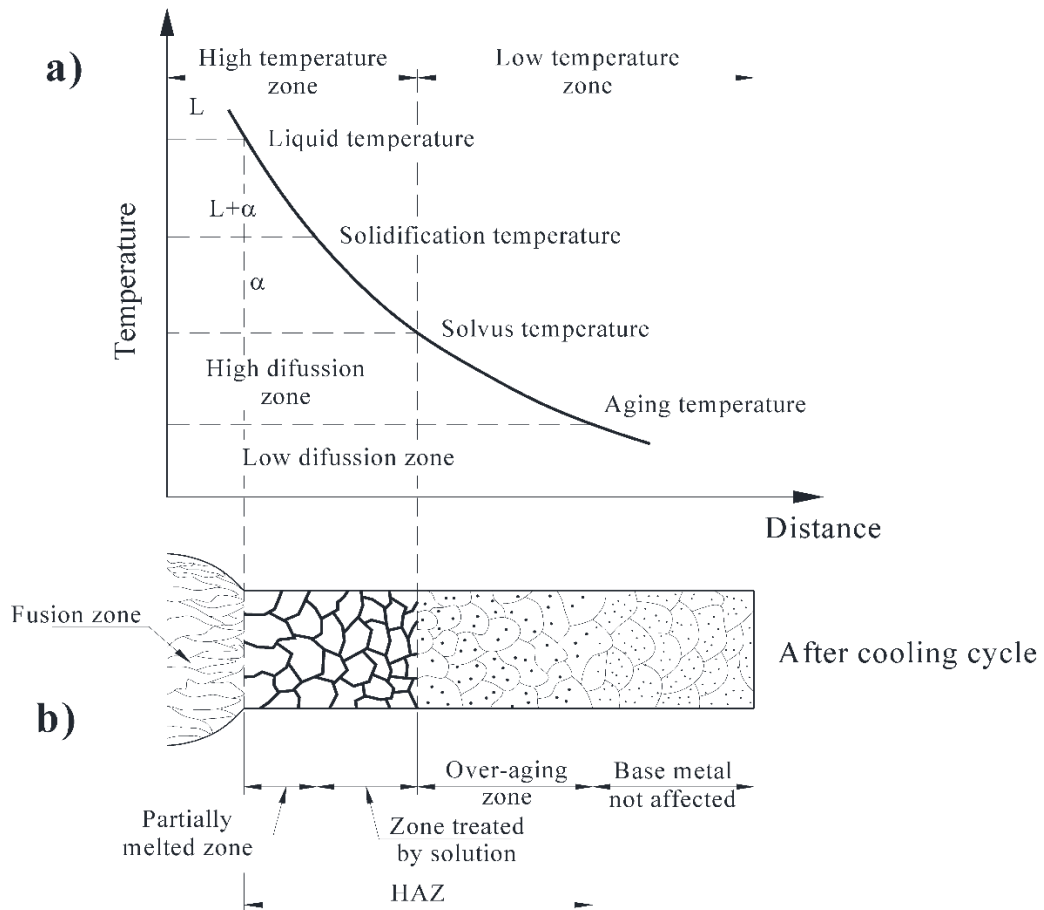
Figure 2.11 Relationship between the grain morphology of the weld and thermal cycle during laser welding of heat treatable aluminium alloys, (a) thermal cycle during the cooling cycle from peak temperature, and (b) grain morphology of the joint at ambient temperature [104].

- **The fusion zone** – The temperature of this region is above the melting point of the material for the melting and solidification process to occur. The solidification process is influenced by the process parameters which modify the weld grain morphology. During the solidification of molten metal, grains grow perpendicular to the direction of the maximum thermal gradient. The important parameters affecting the solidification process are thermal gradient (G), and solidification rate (R). Kou [35] suggested that the ratio of thermal gradient and solidification rate (G/R) determines the morphology of grains formed from the planer, cellular, dendritic or equiaxed grains. While the size of the solidified grains formed is determined by their product i.e., $G \times R$. The solidified grain morphology as a function of thermal gradient and solidification rate is shown in Figure 2.12.
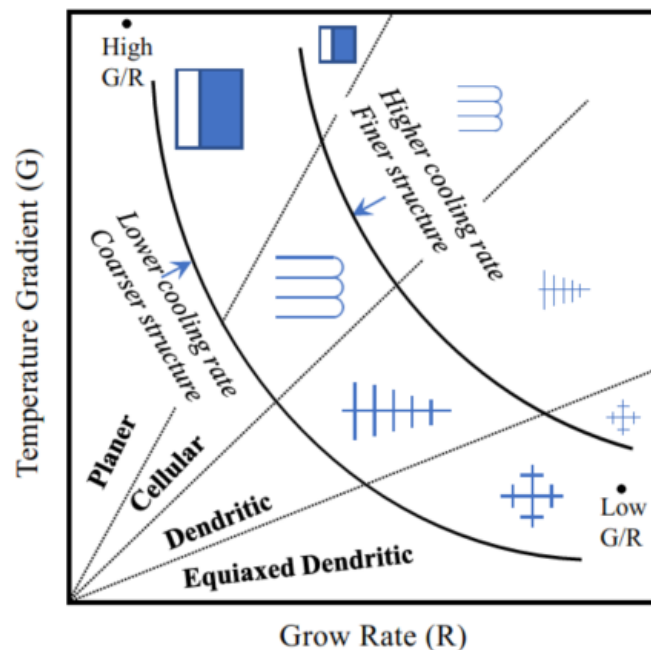
Figure 2.12 Relation between the temperature gradient (G) and solidification rate or grow rate (R) on the grain morphology and grain size [35]

The modes of solidification change continuously in the fusion zone as the ratio G/R varies from the fusion line to the centre line as shown in Figure 2.13. Hagenlocher *et*

al. [105] examined the effect of grain morphology on the susceptibility to hot cracking in AlMgSi alloys. They discovered that increasing the number of grain boundaries could decrease crack susceptibility. It was proposed by them that the grain boundaries could be increased by reducing the grain size or widening the equiaxed region. This could be attained through the optimization of welding process parameters or through the addition of alloying elements such as Titanium for grain refinement.
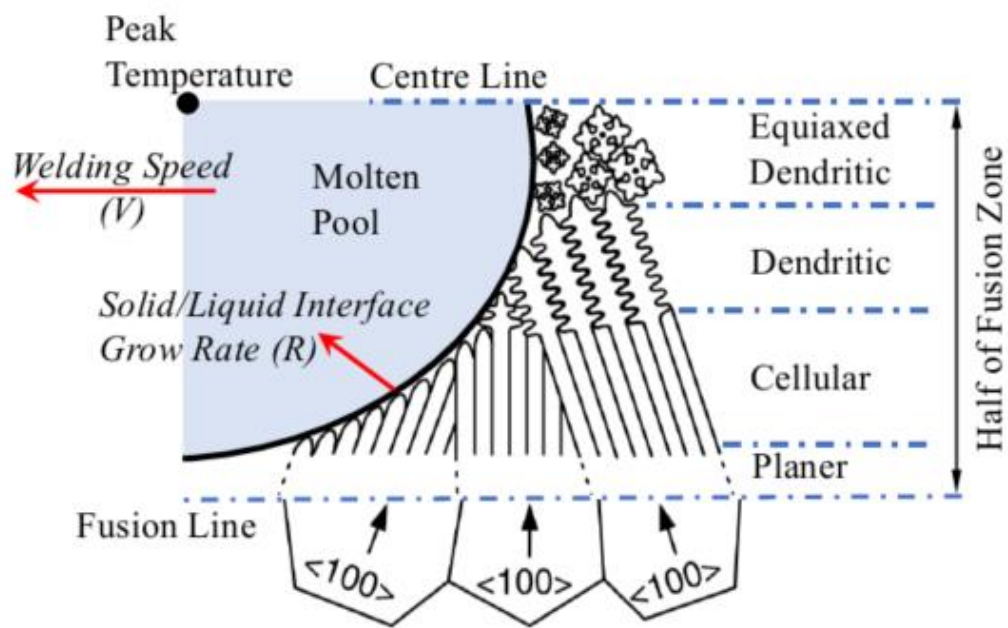
Figure 2.13 Changes in the solidification mode across the fusion zone [35].

- **The Heat-affected zone** – The temperature in HAZ is lower than the melting point but sufficient enough to cause modifications in the grain morphology. The thermal cycle applied during welding influences grain growth, phase transformation, and recrystallisation. Raouache *et al*. [106] reported the effect of the thermal cycle on the grain morphology of the weld and found that the rise in peak temperature of the weld thermal cycle had led to grain growth which is depicted in Figure 2.14.
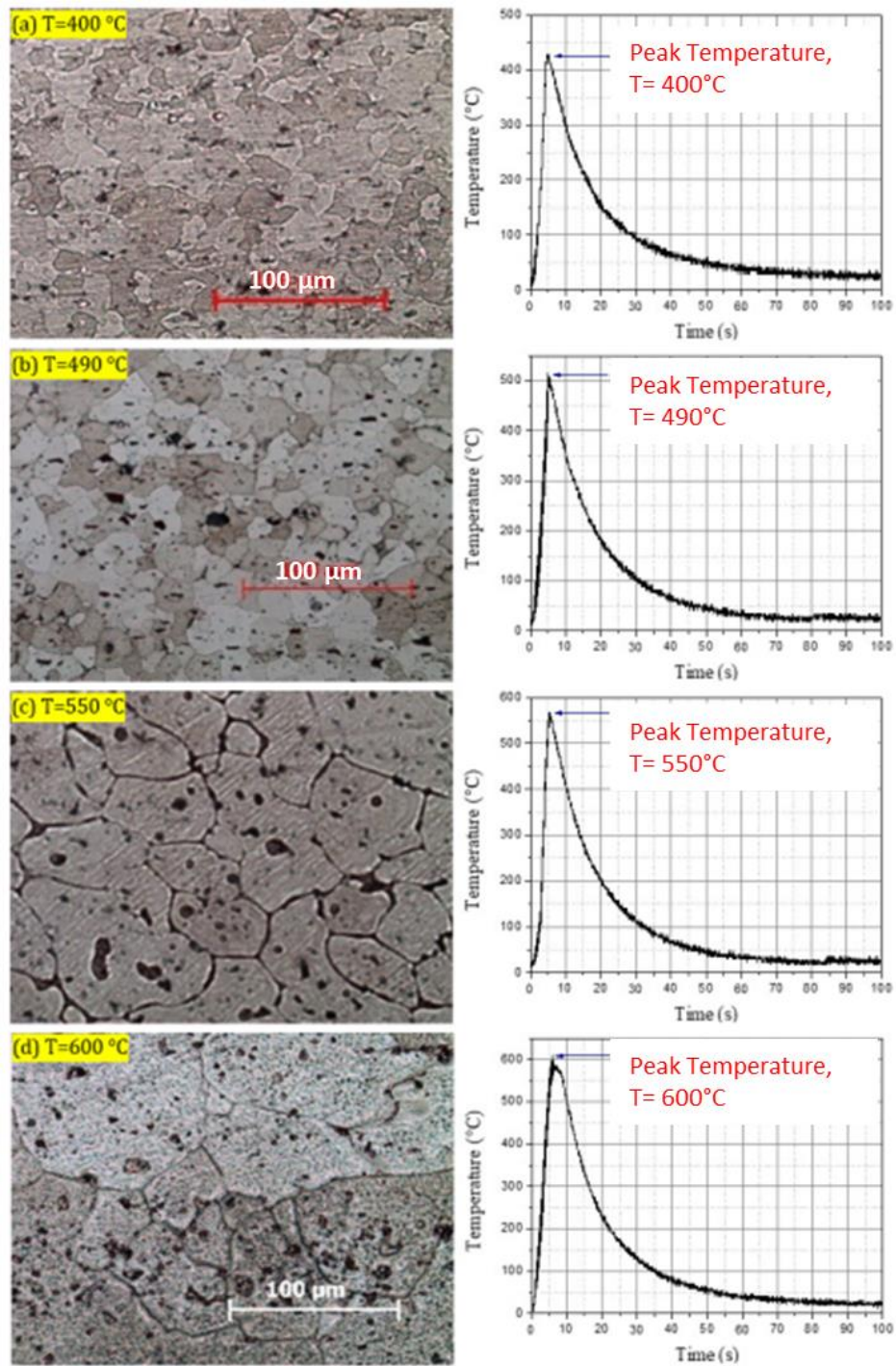
Figure 2.14 The experimental results obtained by Raouache *et al.* [106] for the grain morphology of the HAZ and their plotted weld thermal cycle (modified)

2.1.5.3 Mechanical weld quality

The mechanical weld quality determines the ability of the weld to maintain its structural integrity during its service life. The functional requirements of the welded

41

joints can be assessed by evaluating the strength in static loading or dynamic loading or both. Fatigue strength and tensile strength are mechanical properties commonly employed to assess the capacity of materials to endure diverse loading conditions. In general, tensile strength is measured using a tensile testing machine where a linearly increasing force is applied and calculating the maximum load the joint can withstand before failure. The elongation before failure and analysis of the fractured surface provides the dominant reason for failure. This analysis is important as it helps to improve the process for better strength. Inamke *et al*. [107] studied the effect of warm laser shock peening on the tensile strength of laser-welded AA6061-T6 and TZM alloys and found that the tensile strength increased by 20% and ductility by 30% as compared to as-welded samples. They found that this was due to the introduction of compressive stress introduced due to the shock peening. Douglas and Mazumder [108] performed the tensile test for Al 3003, 5754, 6111 and 6061-T6 alloys and found that all samples failed from the weld region and discovered that Al-6061 attains 60% of the base metal strength. The analysis of the fractured surface using scanning electron microscopy (SEM) revealed that all the failure was due to the formation of large spherical pores revealing that the pores were formed by gas entrapment rather than by shrinkage. In their study, Sun *et al*. [75] conducted a peel tensile test to assess the impact of focal offset on the mechanical properties of AA1050 during battery bus bar assembly through laser welding. They observed that the highest strength was achieved when the focal offset was positioned at a negative defocusing position of -1 mm as shown in Figure 2.15 and temperature measurement near the weld region had a linear relation with the tensile strength. This shows that the tensile strength had a direct relationship with the thermal cycle.
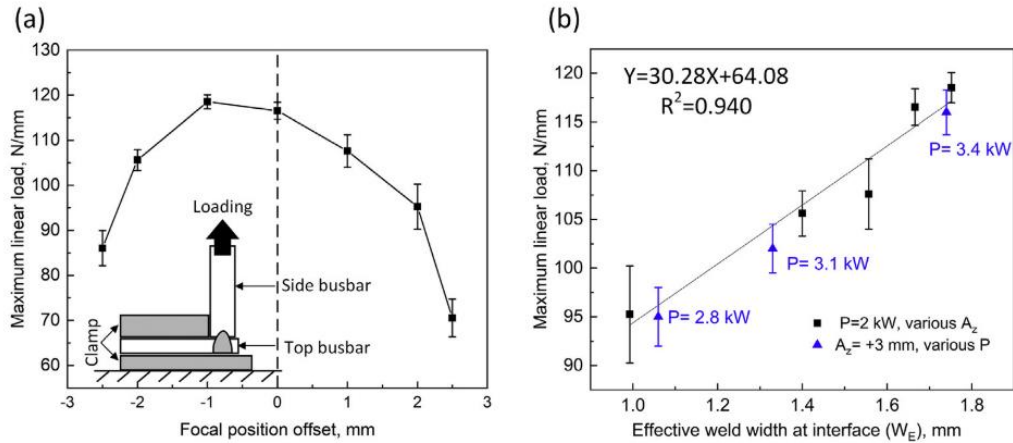
Figure 2.15 Experimental results obtained by Sun *et al*. [75] for the influence of focal offset on the load-bearing capacity of the welded joint (a) Maximum linear during tensile peel test (b) linear fitting between joint strength and weld width at the interface. Here, the linear load represented the force per unit length acting on the welded length and can be calculated by dividing the load by the length.

In contrast, fatigue strength refers to the maximum stress level that a material can endure under cyclic or repeated loading without experiencing fatigue failure. Typically expressed in units of force per unit area, the fatigue strength plays a pivotal role in engineering design, as it establishes the maximum load capacity of the material throughout its operational lifespan while avoiding fatigue-induced failure. Typically, the fatigue strength of a material is comparatively lower than its tensile strength. This disparity arises due to the increased susceptibility of materials to fatigue failure under cyclic or repeated loading conditions. The fatigue strength represents the material's capacity to endure such loading over a prolonged period. Chen *et al.* [109] conducted a study on the low-cycle fatigue properties of laser-welded joints made from Al-Zn-Mg-Cu 7075 aluminium alloy. In order to enhance the joint performance, a post-weld treatment technique known as double-sided ultrasonic impact treatment was applied. The double-sided ultrasonic impact treatment method introduced beneficial residual compressive stress on both the upper and lower surfaces of the joints. Notably, after

43

subjecting the joints to 2×10^6 cycles, the maximum fatigue strength reached 103.02 MPa following double-sided ultrasonic impact treatment. This represented a substantial increase of 111.8% compared to the untreated joints, which exhibited a maximum fatigue strength of 48.62 MPa. Sepe *et al.* [110] investigated the impact of residual stresses on the fatigue performance of laser-welded tube-tube joints. To assess the distribution of residual stresses within the specimens, a 3D numerical analysis was performed using a Finite Element model. The model simulated the welding process of tube-tube specimens made of AlMg3.5Mn alloy. The numerical findings revealed that the presence of residual stresses significantly influenced the area of crack initiation and subsequently affected the type of failure observed in the joints. Little *et al.* [111] conducted a study to analyse the influence of transient temperatures generated during the welding process of a steel plate. A finite element computer program was employed to examine the effects of thermal conductivity variations and weld efficiency on the resulting temperature distributions. Additionally, different approaches to modelling the heat exchange between the plate and its surroundings were investigated. The study's main finding emphasized the considerable impact of varying the conductivity within the typical range for steel. Furthermore, the researchers presented a set of parameters that could be utilized to express the results in a non-dimensional format.

Undergoing the extreme thermal cycle of welding, the microstructure of the weld joint and its internal stress experience notable changes distinct from the base metal [112,113]. These characteristics play a crucial role in determining the mechanical properties of the welded joint. Precisely analyzing the mechanical properties of different regions within weld joints is of great significance for the design and assessment of welded structures. The fusion zone, in particular, represents a vulnerable area in the weld joint where it undergoes complex thermal and mechanical

44

processes during laser welding. The resultant residual stress in the weld joint can surpass the yield stress, significantly impacting the hardness and tensile strength of the joints. Gao *et al.* [114] investigated the influence of resulting residual stress on hardness and tensile strength. They developed a thermomechanical finite element model to predict stresses and strains during welding and established an empirical relationship between residual stress, hardness, and yield stress. Their findings revealed a decrease of 16.5 MPa in yield stress for the Al 2024-T4 welded joint due to residual stress, highlighting the substantial impact of residual stress on the mechanical properties of laser-welded joints. Liu *et al.* [115] focused on fatigue life prediction for laser beam welded joints of 6xxx Al-alloy subjected to variable amplitude loading conditions. They introduced a residual stress relaxation coefficient, β, with a value of 0.5 to account for the relaxation of residual stress during the fatigue crack growth process in laser beam welded Al-alloy joints. Zain-ul-abdein *et al.* [116] investigated the impact of new phase formation on residual distortion and stress states. They observed that while the effect of phase transformations on in-plane and out-of-plane displacements was negligible, these metallurgical transformations significantly influenced the residual stress state. Consequently, addressing the metallurgical transformations of AA 6056-T4 was crucial for accurately predicting the residual stress state in laser-welded structures. The impact of thermal induced distortion and residual stress on mechanical properties is more pronounced in large components compared to the testing conducted on coupons. Since this dissertation focuses solely on testing conducted on coupons, the assumed effect of residual stresses on mechanical properties is negligible.

2.2 Laser welding of Aluminium alloys

In recent decades, there has been a significant surge in the demand for lightweight materials, including aluminium (Al), magnesium (Mg), and titanium (Ti), in the manufacturing industries such as automotive and aerospace. These industries prioritize technological advancements in energy efficiency to achieve the ambitious goal of achieving 'net-zero' emissions by 2050 [117]. Over the coming years, the rise of manufacturing of electric vehicles is expected to further drive the demand for cast Al alloys such as Al-Si, Al-Mg, Al-Mg-Si, Al-Mg-Mn, Al-Si-Cu, Al-Si-Ag, and Al-Si-Sn alloys in the market [118]. Notably, the automotive sector is experiencing increased investments, which is anticipated to boost the sales of high-strength Al-Si alloys, Al-Mg alloys, and Al-Si-Mg alloys. Extensive research has been conducted on casting technology, solidification fundamentals, and process control parameters for these alloys since the 1960s, as evident in various handbooks and articles [119–121]. These alloys possess desirable properties such as low density, high specific strength, high ductility, good castability, high thermal conductivity, high corrosion resistance, cosmetic surface quality, and resistance to hot tearing, making them well-suited for large-scale applications in the automotive and aerospace sectors [3]. Studies have shown that EVs that use aluminium emit approximately 1.5 tons less greenhouse gases throughout their lifecycle compared to those made of steel or cast iron [122].

Several welding techniques can be used for joining of aluminium alloy, including electron beam welding [123,124], laser-gas metal arc welding (laser-GMAW) hybrid welding [125], friction stir welding [126], and laser welding [127]. Laser welding utilizes the high energy of a laser beam to melt the welding materials and fuse them together [52,53]. Compared to other joining methods, laser welding

46

offers several advantages such as deep penetration, lower heat input, and a smaller heat-affected zone (HAZ), leading to increased efficiency and economic benefits. Consequently, laser welding is widely adopted in various industries [16,17]. The keyhole formed and maintained during laser welding enables deep penetration into metallic materials, facilitating high-intensity welding with a single-mode and small spot size [41]. Researchers often select 5xxx aluminium alloys i.e., Al-Mg alloys for their studies due to their inherent insensitivity to heat treatment. This characteristic makes them a suitable choice to produce cold and hot rolled sheets, particularly in Europe where they are extensively employed in automotive component fabrication. These alloys offer desirable properties, including excellent formability, high strength, and the capability of strain hardening[128,129]. Moreover, 5xxx Al alloys are commonly used in the manufacturing of marine vessels due to their excellent weldability, formability, and corrosion resistance [130]. The addition of magnesium to non-heat-treatable wrought alloys provides solid-solution strengthening, enhancing both strength and corrosion resistance, albeit slightly compromising workability. Applications requiring improved strength and the formation of complex shapes often necessitate higher magnesium content, particularly in structural components.

Huang *et al*. [131] had highlighted the difference in boiling points between Magnesium (1360 K) and Aluminium (2723 K), as well as the evaporation and escape of Magnesium from the weld pool during aluminium alloy laser welding. Bunaziv *et al*. [132] discovered that increased laser power led to substantial vaporization of Mg and Mn, resulting in reduced mechanical properties of the materials. Their research on pore formation factors revealed that pores were not only influenced by hydrogen and magnesium metal vapor but also associated with the segregation of magnesium within

the solute band. Additionally, Huang *et al.* [133] observed that the interaction between the vapor plume and the keyhole induced oscillations in both the keyhole and vapor plume. The 5xxx series alloys can exhibit different phases depending on the alloying elements present [134]. When the magnesium content in an aluminium alloy exceeds 3.5 wt.%, precipitates of the β-phase (Mg_2Al_3) can form [135]. Li *et al.* [136] determined that magnesium primarily existed in the form of the β(Mg_2Al_3) phase, which was uniformly distributed and contributed to material strengthening. If the magnesium content exceeded the solid solubility limit in aluminium, Al_8Mg_5 formed at the grain boundaries [137]. The equilibrium phase diagram of the Al–Mg system includes two intermediate phases: the β-phase Al_3Mg_2 and the γ-phase $Al_{12}Mg_{17}$ [138]. Njiokep *et al.* observed slower growth of the $Al_{12}Mg_{17}$ phase compared to the Al_3Mg_2 phase, with both phases exhibiting parabolic growth at all temperatures [139]. The Al-Mg phase diagram comprises a β-solid solution with a hexagonal crystal structure, a liquid phase region, a γ-solid solution with an α-Mn structure type, an R phase with a rhombohedral structure at 42% Mg, an aluminium solid solution with a maximum solubility of 18.9 at.% Mg at 723 K, and an Mg solid solution with a maximum solubility of 11.8 at.% Al at 710 K [140].

The initial microstructure of these materials demonstrates high solid solution supersaturation and can experience macro-segregation in the form of central eutectic segregates and micro-segregation, which scales with the arm spacing of dendrites [141]. Precipitation formation and structure are closely related to both hardness and microstructure[141]. Precipitates nucleate homogeneously as well as heterogeneously in specific locations such as grain boundaries, dislocations, and vacancies. Geng *et al.* [142] determined that the mechanical properties of laser weld joints were directly influenced by the solidification microstructures associated with grain and sub-grain

structures within the dendritic structures. The solidification process involves complex interactions between interface dynamics and heat and mass transfer processes, resulting in a diverse solid and liquid interface morphology. The morphology, size, and distribution of precipitates can significantly impact the mechanical properties. Vyskoc *et al*. [143] conducted a study on AW5083 aluminium alloy weld joints, using 5087 (AlMg4.5MnZr) filler wire with a diameter of 1.2 mm and protection from the ambient atmosphere by an argon and 30 vol.% helium mixture. TEM analysis revealed the presence of three intermetallic compounds: β-Al_3Mg_2, γ-$Al_{12}Mg_{17}$, and $Al_{49}Mg_{32}$, as shown in Figure 2.16. They also identified that the presence of Al_2O_3 particles caused a brittle fracture in the unshielded weld joint. The research findings indicated that optimal welding parameters were achieved as there were no cracks or pores observed in the shielded weld metal.
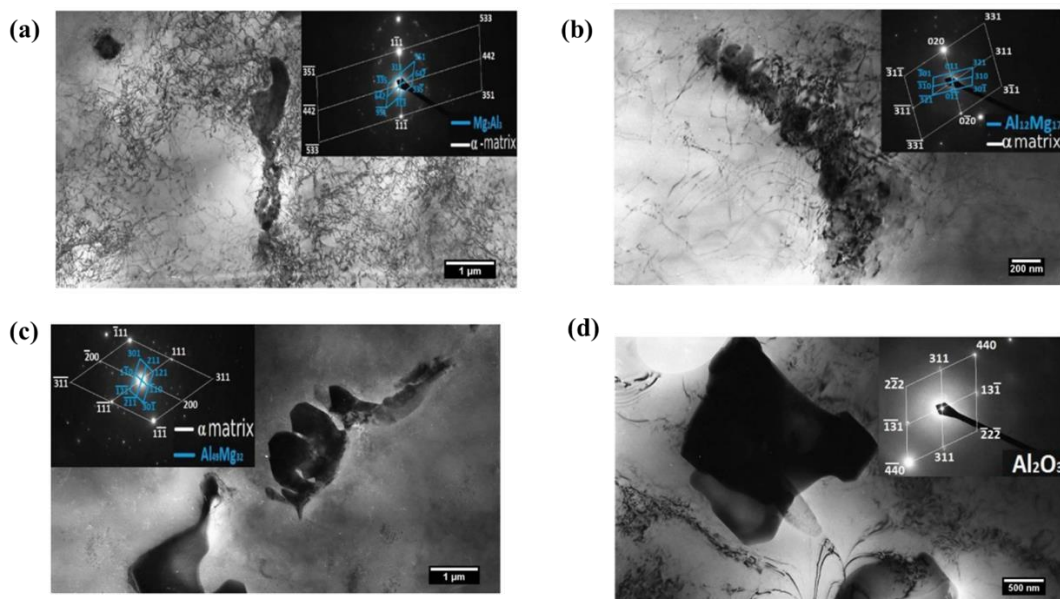
Figure 2.16 TEM image of the weld metal microstructure. The intermetallic phase (a) Mg_2Al_3, (b) $Al_{12}Mg_{17}$, (c) $Al_{49}Mg_{32}$ and (d) Al_2O_3 particles were identified by electron diffraction inside the inter-dendritic area.

Within the realm of commercial aluminium casting alloys, those that prominently feature silicon as the primary alloying element hold significance due to

their exceptional casting properties. The introduction of silicon into pure aluminium imparts noteworthy attributes such as high fluidity, favourable feeding characteristics, minimal shrinkage, and resistance to hot cracking. Particularly intriguing is their high strength-to-weight ratio. Remarkably, silicon, with a density of 2.3 g/cm^3, can be incorporated into aluminium (with a density of 2.7 g/cm^3) without compromising its weight advantage. Aluminium-silicon alloys, devoid of copper additions, are employed when there is a requirement for excellent castability and corrosion resistance. In this context, magnesium can serve as a viable alternative to copper [144].

The formation of intermetallic hardening phase Mg_2Si due to the combination of Magnesium and silicon, precipitates in the α-aluminium matrix and leads to an increases the yield strength [145]. Figure 2.17 depicts a pseudo-binary cross-section of the AlSiMg0.3 system. The solidification process occurs within a temperature range of approximately 60°C, and the temperature at which semi-solid forming occurs, known as T_{SS}, is observed at around 580°C when the liquid and solid fractions are both 50%.
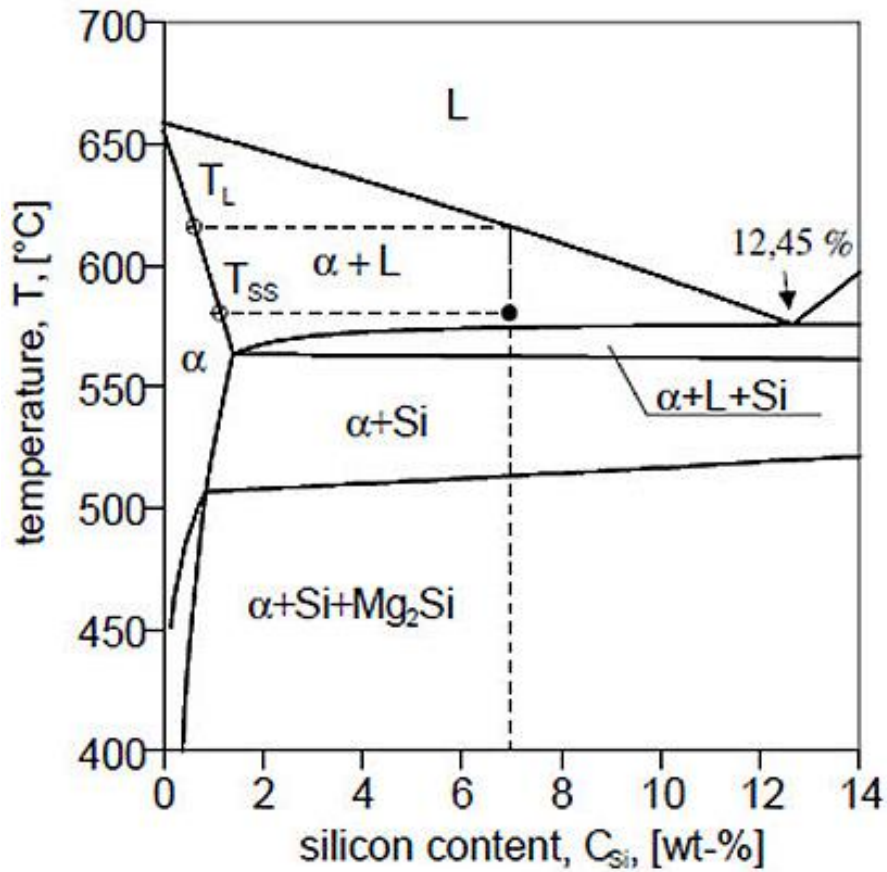
Figure 2.17 Pseudo-binary section of AlSiMg0.3 [144].

Increasing the amount of alloyed magnesium has been shown to effectively enhance

the yield strength. The solubility limit of magnesium in the α-aluminium phase, when

both silicon and Mg_2Si are present, lies between 0.45 wt% (Figure 2.18 (a)) and 0.75

wt% (Figure 2.18 (b)) at 555°C [144,146]. Magnesium that exceeds the solubility limit

within the matrix contributes to the formation of undesirable intermetallic compounds.

Notably, impurities such as iron, which is particularly detrimental to AlSiMg alloys,

form various intermetallic compounds with silicon and magnesium, including

$\alpha(Fe_2SiAl_8)$, $\beta(FeSiAl_5)$, and $\pi(FeMg_3Si_6Al_8)$ [147].
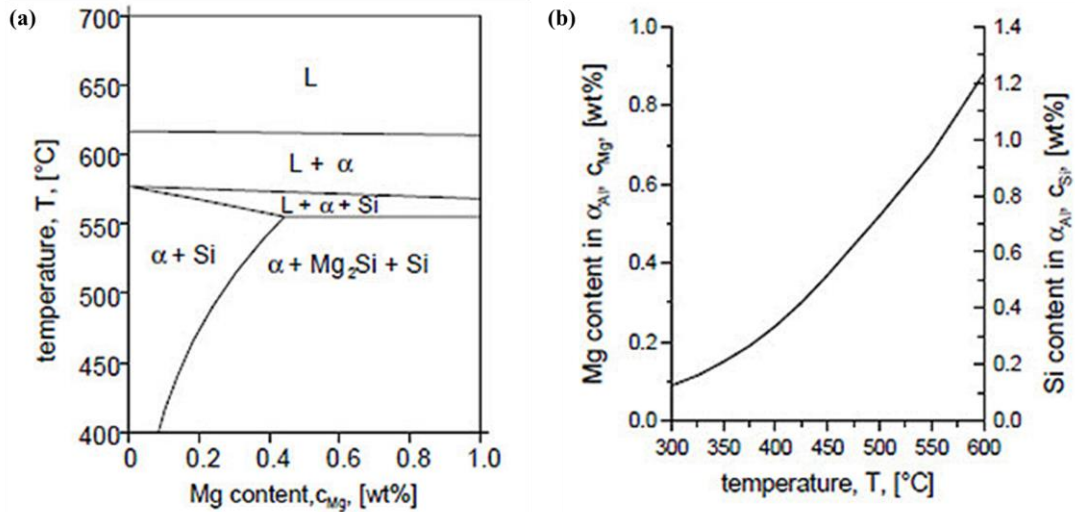
Figure 2.18 (a) Pseudo-binary section of the system AlSi₇Mg, and (b) solubility of Mg and Si in α-aluminium with concurrent presence of Mg₂Si and Si in equilibrium [144].

The enhanced strength observed in the 6xxx series alloy primarily stems from the presence of exceptionally fine precipitates embedded within a solid solution matrix, which consist of magnesium (Mg) and silicon (Si). Age hardening, a crucial process, significantly contributes to achieving the optimum properties of the alloy for specific applications. In recent years, extensive research efforts have been dedicated to thoroughly investigating various aspects related to precipitation formation, precipitation sequence [145], early stages of precipitate nucleation, and precipitate structure [148]. Additionally, there has been a focus on exploring the correlation between hardness and microstructure [145], conducting quantitative analyses of early-stage precipitates, clusters, and examining the evolution of precipitates following isothermal heat treatment have been investigated thoroughly during the past few years [145,149–151]. The generally accepted precipitation sequence in Al–Mg–Si alloys during heat treatment is [145,146]:

Super saturated solid solution → atomic clusters → GP zones → β'' → β' → β (Mg₂Si)

52

The demand for Aluminium alloys for lightweight manufacturing in the automotive industry has increased in the last four decades [152,153] and it was forecasted that the trend will rise in 2025 as shown in Figure 2.19 [154]. This is to decrease the weight of the body in white to cope with the stricter environmental regulations [153] and to improve fuel efficiency. Dissimilar aluminium alloy welding is now becoming popular as it combines the advantages of different grades of aluminium alloys such as low density, good formability, high strength-to-weight ratio, corrosion resistance, formability, and weldability [20,21]. The active response of 6xxx aluminium alloys to strengthening processes including thermal treatment and work hardening provides the opportunity for weight saving without compromising the strength. This is particularly crucial for battery electric vehicles (BEVs) as it allows for downsizing the battery system and reducing costs [155].
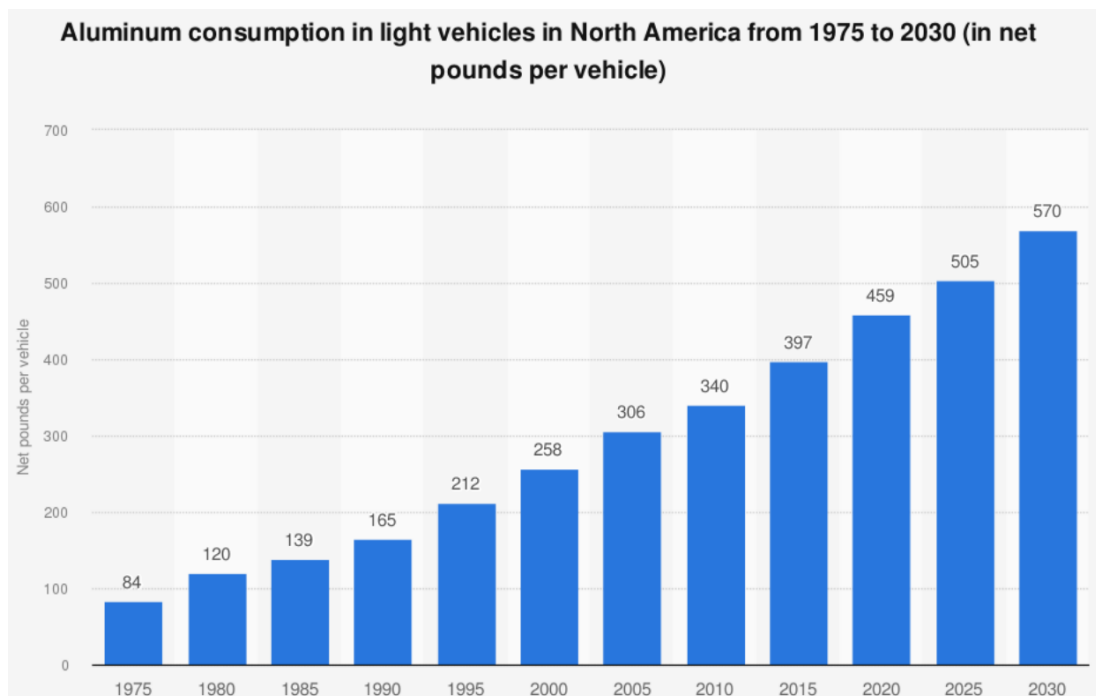
Figure 2.19 World average aluminium content per vehicle in Lbs [154].

5xxx and 6xxx aluminium alloys constitute the bulk of automotive production and they are the primary interest in this dissertation. 5xxx/6xxx dissimilar aluminium alloy welding is considered a good strategy to weld the side and back walls for the automotive industry, combining the advantages of both alloys such as low density, good formability, high strength-to-weight ratio, corrosion resistance, formability and weldability [2,3]. 5xxx and 6xxx aluminium alloys are widely used as structural components for the automotive industry due to their excellent formability, elongation and specific strength [128,129]. Concerning the nature of the RLW process in that no filler wire is used, the welding of 5xxx and 6xxx aluminium alloys are considered to be beneficial because it creates weld chemistry that has low crack sensitivity [27,156]. However, compared to steels, laser welding of Al alloys poses various challenges such as low energy efficiency due to the high reflectivity of the laser from the surface. The high thermal conductivity and low viscosity of Al alloys result in high susceptivity to weld porosity and solidification cracks [157,158].

Moon and Metzbower [159] investigated the laser welding of Al-5456 and observed a fine grain structure in the fusion zone. They also found that the dissolution of Mg_2Si and $(Fe, Mn)Al_6$ which led to the increased toughness of the welded joints. Ramasamy and Albright [160] performed a comparative study for the laser welding of 1.6 mm thick Al-5754-O with CO_2 and Nd-YAG lasers and found that weld grain morphology comprised of fine cellular dendritic grains and with a region of equiaxed grains at the centre. While Venkat $et\ al.$ [161] for the same alloy occasionally observed the equiaxed grains in the weld centreline at high welding speeds up to 0.17 m/s. For the range of process parameters investigated, no solidification cracking was observed in the continuous wave laser welding of 5xxx aluminium alloys [159–163]. Nevertheless, solidification cracking was apparent in pulsed laser welding based on

54

the studies done by some researchers, which indicated that the rapid cooling rate induced thermal strains that contributed to the formation of crack [163]. In prior studies focusing on the welding of 6xxx aluminium alloys, researchers observed the presence of fine cellular dendritic grains extending from the fusion line to the middle of the fusion zone. Additionally, a consistent occurrence of equiaxed grains was noted at the centre of the fusion zone [161,162,164,165]. Equiaxed grain formation was promoted, as it reduced the susceptibility to hot cracking by increasing the grain boundaries. Solidification cracking was identified and found to be more pronounced at higher welding speeds, attributed to the elevated cooling rate [160,161]. Softening occured in the HAZ of the 5xxx alloy, as it is a non-heat treatable aluminium alloy [159]. This softening was due to the loss of the strain-hardened structure and the growth of the grains in the HAZ region. On the other hand, in the case of the heat-treatable 6xxx aluminium alloy, the dissolution of the strengthening phase $\beta``(Mg_2Si)$ took place. The emergence of the needle-like $\beta`$ (Mg_2Si) phase resulted in a reduction of the strengthening mechanism, leading to softening in the HAZ. Sun *et al*. [166] discussed technological solutions for welding the 6xxx series aluminium alloy, utilizing capabilities such as beam oscillation, power modulation, beam shaping, filler wire, and beam shaping. They discovered that beam oscillation and power modulation could prevent weld centreline cracking. Their research suggested that modifying the thermal history through beam oscillation, power modulation, and beam shaping could reduce the occurrence of micro-cracks. Moreover, they observed that the use of filler wire was an effective approach to mitigating microcracks, resulting in a 40% increase in joint strength. Alternatively, achieving a similar strength level using only ring mode required a higher welding speed of 6.5 m/min, as opposed to the restricted 4 m/min with filler wire.

2.3 Beam oscillation welding

Recent progress in the development of high-power lasers led to an increase in efforts to weld materials like Aluminium which are hard to weld with conventional lasers due to the high reflectivity from the surface of Aluminium. In the effort to stabilise the molten weld pool, degassing the molten weld pool for reducing porosity formation and improving grain morphology during solidification spatial power modulation is applied by superimposing an oscillation movement to the laser head in the welding direction. During beam oscillation, a larger molten pool is generated, and the remelting of this molten pool provides additional time for pores (formed due to keyhole collapse) to rise to the top surface and escape from the molten pool. This process of degassing due to beam oscillation helps in reducing porosity. The methodology of beam oscillation presents multiple additional degrees of freedom, encompassing parameters like oscillation frequency, oscillation amplitude, and oscillation pattern. These aspects yield a heightened level of flexibility concerning the application and management of heat energy, thereby exerting influence over the temperature field, fluid flow field, and concentration field during the process of laser welding. Beam oscillation is characterized by the deviation of the laser beam from its linear trajectory, specifically a straight line, to follow a predetermined periodic motion, such as circular, elliptical, sinusoidal, square, triangular, and other defined patterns [167] as shown in Figure 2.20.
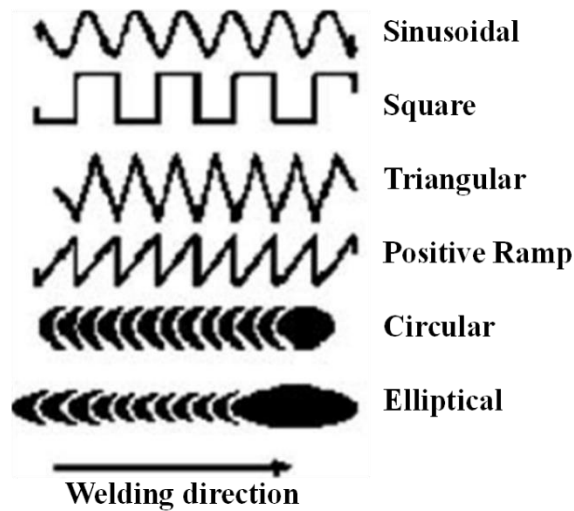
Figure 2.20 Depicting the schematics of different laser beam oscillation patterns [167]

The beam can be oscillated into various patterns by deflecting a two-axis coil. The setup consists of a set of amplifiers for deflecting *x*- and *y*-axes and a function generator to program the required oscillation pattern for the beam spot. A scan-head rapidly rotates the laser beam on its axis in the welding direction using a specified amplitude and frequency. Beam oscillation resulted in a broader weld seam, more consistent weld shapes, a stable molten pool and keyhole, and enhanced gap bridging [168–170]. The surface weld profile generated using different oscillation patterns is depicted in Figure 2.21 [171]. In this dissertation circular and sinusoidal oscillation patterns are studied. The trajectory of the oscillating laser beam as a function of weld parameters is described in Eq. 2.3 [172]:

$$x(t) = (x_0 + St + A_x(sin(2\pi f_x t + \varphi_x)))$$
$$y(t) = \left(y_0 + A_y(sin(2\pi f_y t + \varphi_y)) \right)$$

<div align="right">2.3</div>

Where *x(t)* and *y(t)* are the time-dependent positions of the beam spot, *x₀* and *y₀* are the initial positions, *S* is the welding speed, A_x and A_y are the oscillation amplitude

along the *x*-direction and *y*-direction respectively, f_x and f_y are the oscillation frequency in the x-direction and y-direction respectively, φ_x and φ_y are the initial phase angles.

Beam oscillation modified the temperature field, influencing the temperature distribution during welding and offering benefits for crack-sensitive materials [173]. Previous reports indicated that beam oscillation generated a churning effect in the liquid weld pool, enhancing mixing and reducing segregation, resulting in a more uniform dispersion of elements during welding [174]. In their study, Dinda *et al*. [175] reported that employing beam oscillation at optimal parameters reduced porosity and intermetallic formed during steel-aluminium welding. Murthy *et al*. [176] examined the impact of oscillated beams on Nb segregation. The experiment involved nine distinct heat inputs across three levels of welding speed and beam current. The weld quality was assessed and ranked based on factors such as weld geometry, microhardness, and mechanical properties. Interestingly, at low heat inputs under the conditions they studied, the welded samples exhibited exceptional weld strength, fracturing outside the weld zone. However, as the heat inputs increased for the range of process parameters investigated, the welded samples developed cracks and fractures within the weld. These findings established a benchmark for future research on electron beam welding (EBW) of selective laser melted IN718, enabling meaningful comparisons. Sivaprasad *et al*. [177] demonstrated that the use of beam oscillation improved the fatigue properties of Inconel 718 welds. Wang *et al*. [172] conducted a series of experiments with three beam oscillation patterns and found that beam oscillation improved weld surface morphologies by promoting the formation of equiaxed grains in the fusion zone. Fetzer *et al*. [178] experimentally investigated the effect of beam oscillation in the AlMgSi system and found that pore formation

decreased due to beam oscillation compared to linear welding. C. Hagenlocher *et al*. [179] worked on the solidification conditions using beam oscillation and suggested that the solidification conditions could be greatly influenced by the use of beam oscillation, potentially reducing the chances of hot cracking. Z. Wang *et al*. [180] analysed joint grain morphology, porosity, and mechanical properties with different beam oscillation patterns, suggesting that the use of beam oscillation reduced welding defects. They found that the average tensile strength of the samples produced with oscillation was higher than those without beam oscillation, resulting from refined weld grain sizes and lower porosity. Wang *et al*. [172] studied the effect of different oscillation patterns, i.e., transverse, longitudinal, and circular, on attributes of AA6061-T6 aluminium alloy joints. They concluded that beam oscillation effectively improved fusion morphologies and promoted the formation of equiaxed grains in the fusion region. They also found that beam oscillation with a circular pattern provided fewer defects, a smooth surface, fine equiaxed grains, and higher ductility compared to those produced by transverse and longitudinal patterns.
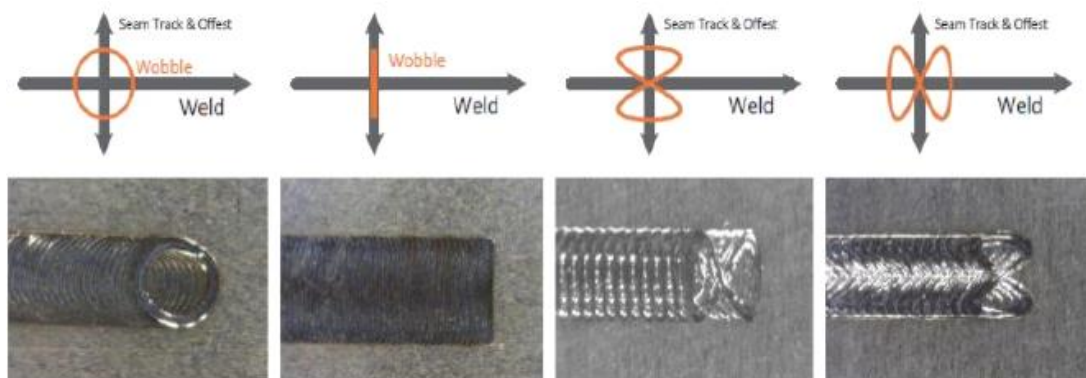
Figure 2.21 The surface weld profile for different beam oscillation patterns [171]

Beam oscillation is an effective and important process parameter in the laser welding process which can effectively modify fusion zone and HAZ grain morphology, surface smoothness, convection in the melt pool, spatter formation and

temperature field to get better properties. Research involving beam oscillation had indicated that the weldability of aluminium alloys can experience enhancements, resulting in fewer defects and improved mechanical properties [180–184], however, the impact on grain morphology is not fully understood. This is primarily due to the intricate and dynamic solidification behaviour within the molten pool, which is challenging to capture experimentally, compounded by the rapid solidification process [185]. The solidification process is affected by the critical interactions between heat transfer and fluid flow behaviour at the solid-liquid interface in the molten pool [186]. However, there has been limited investigation into the laser welding of two distinct grades of aluminium alloys utilizing beam oscillation. Furthermore, a majority of the studies conducted on aluminium alloys have concentrated on low-frequency oscillation, with a predominant focus on process stability. Another key challenge is shortening the new process development due to the increase in complexity due to the introduction and selection of key process parameters to meet welding outputs pertaining to weld quality.

2.4 Beam shaping – Adjustable Ring Mode (ARM) laser welding

Beam shaping has received increased attention in recent years as an alternative approach to the modulation of energy distribution that can be fully integrated into the RLW process. Rasch *et al*. [187] and Duocastella and Arnold [188] reported the benefits of ring shape laser beams for stabilising the molten pool and improving the weld surface quality. However, the application of ring beams had typically been observed within conduction mode laser welding setups, with the absence of substantial weld penetration limiting their feasibility for thicker materials. More recently, an adjustable ring mode (ARM) laser beam, consisting of the core Gaussian beam and

outer ring beam, was introduced by Coherent Inc, [189]. A schematic of the beam configuration in the fibre laser and five possible power patterns between the ring and core are shown in Figure 2.22. Under this beam configuration, pre-heating supplied by the leading edge of the ring beam increases the material's energy absorption rate and the post-heating enabled by the trailing edge of the ring beam enlarges the molten pool to promote the escape of gas bubbles, whilst the core beam guarantees a sufficient weld penetration. The benefits of ARM laser beam have been reported in a limited number of studies Mohammadpour *et al*. [190] performed a comparison study between the ARM and single beam laser experimentally for the laser welding of stainless steel. They studied the influence of beam sources and energy distribution in ARM laser on the weld profile while maintaining the welding speed and total laser power. The energy distribution for pure core, pure ring and dual modes performed by Mohammadpour *et al*. [190] is shown in Figure 2.23. The comparison of the weld profile for the different power distributions used is shown in Figure 2.24. They found that the depth of penetration increased as the power distribution changed from the pure ring to the pure core. They also reported a noticeable reduction in spatter formation on the weld bead at a power ratio of ring beam to core beam higher than one. Sokolov *et al*. [191] investigated the impact of ARM laser on the in-process weld penetration monitoring by optical coherence tomography (OCT) during RLW of Al-Cu dissimilar thin foil. Their study revealed decreased fluctuations in keyhole opening dynamics with the application of the ARM laser beam, leading them to assert that ARM laser had improved OCT accuracy by 50% in comparison to the Gaussian laser beam.

ARM fiber schematic

cladding
ring core
center core

Basic FL-ARM focused spot power patterns

| Equal power in center and ring | Higher power in ring than center | Higher power in center than ring | Power in center only | Power in ring only |
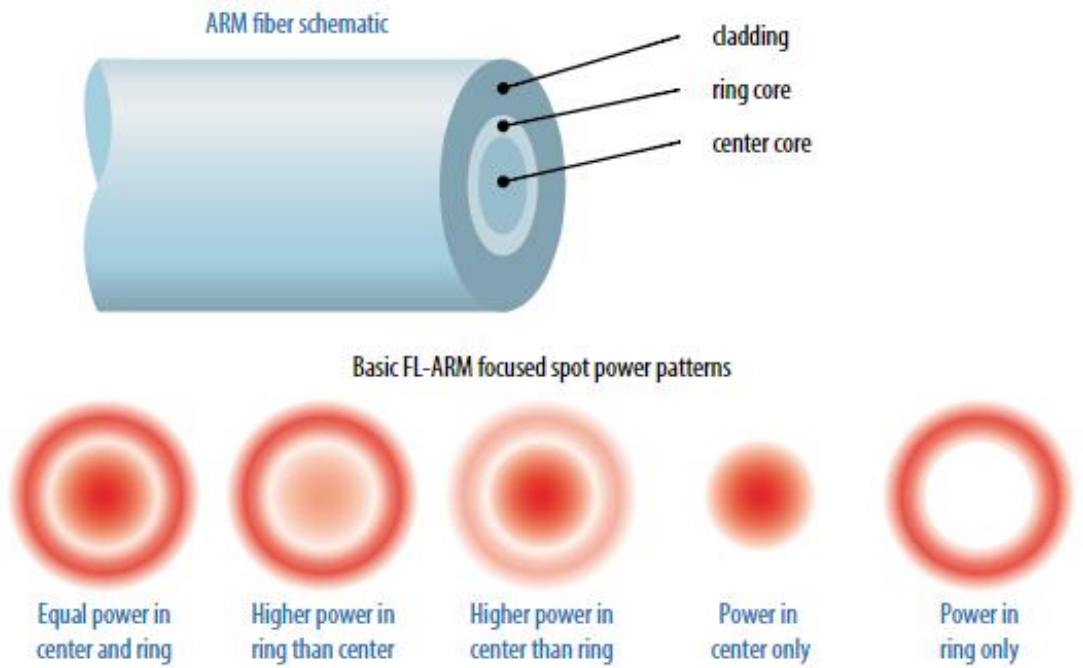
Figure 2.22 Simplified schematic of Adjustable Ring Mode (ARM) fibre laser and the possible five power patterns in the focussed laser spot

(a)   (b)   (c)   (d)
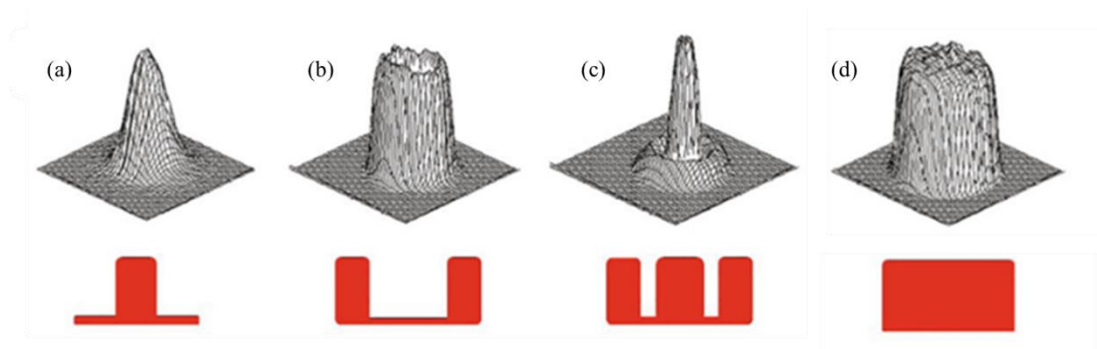
Figure 2.23 Energy distribution for the ARM laser in (a) pure core; (b) pure ring; (c) dual-mode and (d) and energy distribution of single beam laser [190]
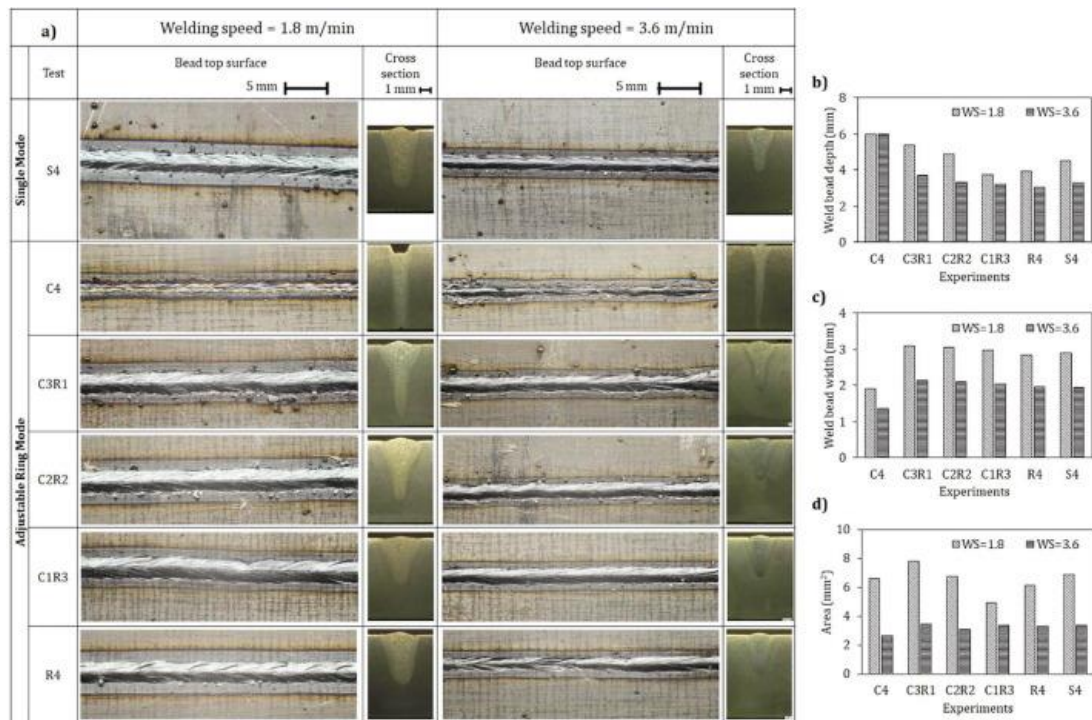
Figure 2.24 Experimental results obtained by Mohammadpour *et al*. [15] on the influence of changes in beam mode: (a) weld bead profile on the top surface and cross-section; (b) depth of penetration; (c) width; and (d) fusion zone area. In the test labels, C and R were represented as the centre and ring beams of the ARM laser, respectively. CxRy indicated the dual beam test mode with x-kW in the centre beam laser and y-kW in the ring laser beam. Sz is denoted as a test condition with z-kW in the IPG single laser beam arrangement.

The benefits of ARM laser beams have been reported in a limited number of studies. Maina *et al*. [189] demonstrated the improvements in both surface quality and keyhole stability in AA5022 laser welds using an ARM laser beam compared to the sole annular laser beam. Mohammadpour *et al*. [190] experimentally studied ARM laser welding of stainless steel and reported a noticeable spatter reduction on the weld bead at a power ratio of ring beam to core beam higher than one. Sokolov *et al*. [191] investigated the impact of ARM laser on the in-process weld penetration monitoring by optical coherence tomography (OCT) during RLW of Al-Cu dissimilar thin foil. The authors observed a clearly reduced fluctuation of keyhole opening using the ARM laser beam. Despite the aforementioned advantages of the ARM laser beam,

predominantly focusing on the process stability and seam surface finish, the impact of the ARM laser beam on the grain morphology of the weld and mechanical performance is still not clear. The impact of energy distribution on the grain morphology and mechanical performance using the ARM laser beam integrated with beam oscillation is missing in the literature. Furthermore, there is a need to investigate the effect of the ratio of the core/ring powers on the thermal history and solidification behaviour during ARM laser welding combined with beam oscillation. This will provide insight into the effect of the core/ring power ratio on the grain morphology and mechanical performance.

2.5 Process Monitoring

There is an increase in the number of input process parameters due to the recent advancement in the RLW process for the better capability to weld different materials and joint configurations. A critical requirement for the manufacturing process is to select robust process parameters which produce parts within the defined specification limits. These specified limits are determined by the weld quality and other requirements of the downstream process. In general, weld quality refers to using the technological methods and actions that can guarantee quality by gathering and understanding the physical phenomenon occurring based on the process information and developing a quality control methodology to reduce the weld defects. This information can be obtained by offline inspection or by in-process monitoring. The offline inspection includes different weld characterisation techniques such as metallurgical characterisation, chemical characterisation and mechanical characterisation [192,193]. The offline inspection is time and resource expensive reducing productivity and difficult to cope-up with the NPI requirements.

Furthermore, offline monitoring is used to develop a relationship between the process parameters and weld quality. In-line process monitoring is performed using sensors which convert surface radiation into electrical signals which are further converted to measurable variables. The data acquired by the sensors contain lots of noise, have a limited field of view and are unable to differentiate between various defects such as porosity, lack of penetration, microcracks etc [194,195].

Both the use of traditional offline and in-line process monitoring has their own limitations and boundaries. The relation between process parameters and weld quality is very critical and in general, it is developed by using statistical methods such as Response Surface Methodology (RSM). A large quantity of data is required to develop these relationships which are obtained from the experiments and using sensors during experiments [196–198]. Numerical simulation of laser welding can provide detailed information to obtain the relationship between the process parameters and the weld quality [199–202]. However, these models also provide details about the weld quality which are either difficult or impossible to be obtained by experiments such as thermal gradient, fluid flow, and weld thermal cycle [69,105,156]. These outputs are important as it provides valuable insight to understand the welding process such that the effects of process parameters on the weld quality can be understood.

The weld profile and solidification behaviour are critical to achieving the maximum strength as the weld must have the desired grain morphology and weld profile [11,69,105]. The weld profile and grain morphology are dependent on the transport phenomenon i.e., heat transfer, fluid flow and mass transfer during welding and their relationship with the process parameters. Therefore, a numerical model is proposed in this study which is suitable for developing relationships between process parameters and weld profiles. An integrated approach between experiments and

numerical simulation is utilised to analyse solidification behaviour. The corresponding assumptions and equations for the occurring physics needed to develop the numerical model are reviewed in Section 2.6.

Numerous researchers had utilized numerical models to generate processing maps, illustrating the relationship between weld quality and process parameters or derived parameters such as Peclet number (Pe_1), power density, and interaction time [82,83]. The Peclet number is defined in Eq. 2.4 where r is the keyhole radius, v is the welding speed, and κ is the thermal diffusivity [203].

$$Pe_1 = \frac{vr}{2\kappa} \tag{2.4}$$

$$Pe_2 = \frac{UL}{\alpha} \tag{2.5}$$

These plots can be used to estimate the initial process parameters window based on the required weld quality. Mukherjee *et al*. [204] explored the significance of heat transfer mechanisms, namely convection and conduction, in their study. The assessment of these mechanisms was achieved through the utilization of the Peclet number (Pe_2), as defined by Eq. 2.5, where U represents the characteristic velocity, α is the thermal diffusivity of the alloy, and L stands for the characteristic length. The authors specifically employed the Peclet number formulation in the context of molten material flow. In their analysis, the maximum velocity of the molten metal was chosen as the characteristic velocity for Peclet number calculation, while the length of the molten pool was considered as the characteristic length. It's noteworthy that a higher Peclet number indicated a more pronounced involvement of convective heat transfer in the overall heat transfer dynamics within the liquid metal pool. Ion *et al*. [83] developed a laser processing map between absorbed power density, interaction time and peak temperature and showed different regions of keyhole welding, cladding,

cutting, melting and hardening as shown in Figure 2.8. Lankalapalli *et al*. [82] developed the processing map between depth of penetration as a weld quality indicator and calculated the Peclet number for three different laser powers. In most of the literature depth of penetration was used as an indicator for the weld quality and derived parameters in place of actual welding process parameters for the development of laser processing map [82,85–87]. Beam oscillation was not considered a parameter in any of the laser processing maps. Most of the laser processing map was based on the single input and single output (SISO) or multiple input single output scenario (MISO) whereas the RLW process is characterised by multiple inputs and multiple outputs (MIMO) scenarios [11]. Therefore, a process capability space framework is proposed in this study to select robust process parameters based on the MIMO scenario.

2.6 Numerical methods of developing and assessing the laser welding process

The welding process parameters affect the quality and geometry of the weld. Challenges related to laser welding are controlled by optimising these parameters. The control of these parameters is critical for assessing and developing the laser welding process. However, a key challenge faced by the manufacturer is shortening the new process development and selection of key process parameters to meet the required weld quality. Characteristics of weld dimensions, the phases formed in the weld zone, grain morphology of the weld and mechanical strength govern the weld quality. Therefore, a significant amount of research has been conducted to develop the relationship between the process parameters and the weld quality attributes such that the selection of robust process parameters can be done. Consequently, process development at present has relied on experiments ("weld trials"). With the recent

advancement in the RLW process such as beam oscillation, power modulation and beam shaping, single-input or multiple inputs and single-output scenarios are not sufficient for laser welding, since this process is characterised by multiple inputs and multiple outputs (MIMO) scenarios [11]. Experiments alone are not sufficient to survey the entire parameters space, as it takes weeks to run them. Statistical models based on the experiment have been used to estimate weld attributes as a function of process parameters [196–198]. These models are based on the data gathered by performing destructive and non-destructive experiments and using statistical models like Response Surface Methodology (RSM), Taguchi method, and Artificial Neural Network (ANN) to predict the optimum process parameter to achieve required weld attributes.

Multi-physics-based numerical models [199,205,206] provide detailed knowledge concerning the physiology of the welding process such as weld thermal, fluid flow in the molten pool, material mixing, and laser-material interaction. Such models enable the researcher to understand and improve the laser welding process in detail. Finite element (FE) based models are used to simulate the laser welding process to (i) design sequences for the manufacturing process, (ii) select process parameters which will provide optimum weld quality [50,207] and (iii) evaluate KPIs for the weld in terms of weld profile, material mixing, distortion and residual stress [208–210]. Efficient simulation of the laser welding process cycle provides the option to (*i*) evaluate weld attributes such as depth of penetration, and weld width in the entire parameter space; or (*ii*) can be integrated with physical experiments to provide a reduced region in the parameter space which decreases the number of experiments required to identify robust process parameters.

The numerical simulation of laser welding is a complex process since it is a multi-physics and multi-phase process. This study focuses on the interactions of heat transfer, fluid flow and mass transport. Thus, this section reviews the physical phenomenon which determines the weld profile and solidification behaviour: (i) heat transfer to estimate the weld thermal cycle in FZ and HAZ, (ii) fluid flow in the molten pool and (iii) material mixing during welding.

2.6.1 Heat transfer

The time-dependent temperature field is a function of position (x, y, z) and time t is determined by the non-linear energy conservation equation as defined in Eq. 2.6 [211].

$$\rho C_p \left[\frac{\partial T}{\partial t} + \vec{\nabla} . (\vec{u} \, T) \right] = \vec{\nabla} \cdot \left(k \vec{\nabla} T \right) + S_{laser}(x, y, z, t) + h(T - T_0) + \varepsilon \sigma (T^4 - T_0^4) + Q_{vap} \qquad 2.6$$

Where ρ is the material density, C_p is the specific heat capacity of the material, T is the temperature of the workpiece, t is the time, k is the thermal conductivity of the material, $\vec{u}$ is the velocity of molten metal, S_{laser} is the energy of the laser, h is the surface heat transfer coefficient, ε is the emissivity of the material and σ is the Stefan-Boltzmann coefficient of radiation and Q_{vap} is the loss of energy due to vaporization. The Eq. 2.6 states that the change in temperature with respect to time is equal to the divergence of the heat flux, plus heat generated by the laser heat source and loss of heat due to convection, radiation and vaporisation of the material. The above-mentioned physical properties are different for the solid and the liquid phase. The phase changes from solid and liquid are considered to include temperature change due to latent heat by using the equivalent heat capacity enlarged between the liquidus and solidus temperatures which includes an additional term for latent heat as shown in Eq. 2.7 [199,212]

69

$$C_P = C_{P,solid} + L_f \frac{exp^{-\left(\frac{(T-T_{melting})^2}{(T_l-T_s)^2}\right)}}{\sqrt{\pi(T_l - T_s)^2}} \qquad 2.7$$

where, $C_{p,solid}$ is the heat capacity of the solid phase, $T_{melting}$ is melting temperature, T_l is the liquidus temperature, T_s is the solidus temperature, and L_f is the latent heat of fusion. The boundary conditions on the surface of the workpiece are heat energy deposition by the laser source and the loss of heat energy by convection, radiation and evaporation which are described in sections 2.6.1.1 and 2.6.1.2.

2.6.1.1 Heat influx or heat source

The heat flux to the workpiece depends on the laser-material interaction and the intensity distribution is assumed to have a Gaussian distribution as given in Eq. 2.8 [213]

$$I(x,y,z) = \eta \frac{\chi P_L}{\pi r_g^2} exp\left[-\chi\left(\frac{x^2 + y^2}{r_g^2}\right)\right] \qquad 2.8$$

Where P_L is the laser power, r_g is the radius of the laser spot size on the workpiece, χ is the distribution coefficient of the laser beam, (x,y,z) is the cartesian coordinate system, and η is the absorption coefficient of material and defined by Eq. 2.9 where α is the electrical resistivity of the workpiece and λ is the wavelength of the laser [214].

$$\eta(T) = 0.365\left(\frac{\alpha}{\lambda}\right)^{1/2} - 0.0667\left(\frac{\alpha}{\lambda}\right) + 0.06\left(\frac{\alpha}{\lambda}\right)^{3/2} \qquad 2.9$$

Laser welding is a highly coupled multi-physics process which makes it a computationally and time-expensive process. So, the idea is to decouple the possible physics depending on the requirement of the downstream processes. For example, numerical modelling of the keyhole is very computationally expensive for the prediction of the weld profile, so a volumetric heat source is defined as it quantifies

the heat input through complex keyhole interface geometry while still being computationally inexpensive and obtaining the fusion lines compared with the experiments [38]. The actual formation of the keyhole after the laser-material interaction can be replaced by the volumetric heat sources. This method saves a lot of computational resources and time to model complex keyhole phenomena which require modelling of the vapour phase, laser-material interaction, material properties in the gaseous phase, optics for the fall of laser on the material, reflection and absorption of the laser beam by the materials by assuming a volume generating heat as a keyhole having a Gaussian distribution while having the same degree of accuracy. These assumptions are useful depending upon the application and outputs required from the model required.

Goldak *et al*. [91] proposed a volumetric heat source model establishing a heat source term based on the experimental weld pool dimension to evaluate temperature distribution. This model was successfully implemented for arc welding. However, this model was less appropriate for keyhole mode laser welding. In this model, two three-dimensional ellipsoids were considered with a Gaussian distribution as given in Eqs. 2.10-2.11.

$$Q_f = \eta \frac{6\sqrt{3}f_f P_l}{a_f bc\pi\sqrt{\pi}} e^{-3\frac{(x-x_0)^2}{a_f^2}} e^{-3\frac{(y-y_0)^2}{b^2}} e^{-3\frac{(z-z_0)^2}{c^2}} \qquad 2.10$$

$$Q_r = \eta \frac{6\sqrt{3}f_r P_l}{a_r bc\pi\sqrt{\pi}} e^{-3\frac{(x-x_0)^2}{a_r^2}} e^{-3\frac{(y-y_0)^2}{b^2}} e^{-3\frac{(z-z_0)^2}{c^2}} \qquad 2.11$$

Here a_r, a_f, b, and c are the heat source distribution parameters depending upon the shape of the weld pool obtained by measuring the rear (a_r), front (a_f), width (b), and depth (c) of the half ellipsoids. f_f and f_r are the power distribution in the front and rear quadrants of an ellipsoid.

Cho *et al*. [215] proposed a Gaussian volumetric heat source to simulate laser welding of thin sheets leading to a cylindrical shape of the heat source, which was validated by Han *et al*. [216] and defined as:

$$Q = (1 - \eta)\frac{P_L}{\pi r^2}e^{-3\left(\frac{(x-x_{(t)})^2+(y-y_{(t)})^2}{r^2}\right)} \qquad 2.12$$

Where *r* is the radius of the laser spot on the surface of the workpiece and η is the energy attenuation, $x_{(t)}$ and $y_{(t)}$ are the coordinates of the moving track.

Wu *et al*. [217] proposed a three-dimensional conical volumetric heat source in the polar coordinate system, which was used to model keyhole formation. In this heat source, the power density was highest at the top surface and lowest at the root with a weld bead root that resembles a cone. The conical heat source was defined as:

$$Q_c = P_L e^{-3\left(\frac{(r)^2}{\left(r_e - \frac{(r_e-r_i)(z_e-z)}{z_e-z_i}\right)^2}\right)} \qquad 2.13$$

Where r_e and r_i are the radius at the top and bottom surface of the cone, the height of the conical heat source is defined as z_e - z_i.

A rotating Gauss body or rotating Gaussian model heat source model [182,218] was used as a volumetric heat source in which the attenuation of the laser intensity was modelled as a logarithmic function inside the keyhole along the thickness of the workpiece. The heat source is defined in Eq. 2.14 where *H* is the heat source height.

$$Q_{rg} = \alpha \frac{9P_l}{\pi r^2 H(1 - e^{-3})}e^{-9\left(\frac{(x-x_{(t)})^2+(y-y_{(t)})^2}{r^2 \log(H/z)}\right)} \qquad 2.14$$

Several other models have been proposed to predict the shape and size of the weld profile, which were termed as hybrid heat sources. These hybrid heat sources are the combinations of two or more volumetric heat sources [219]. For example, a

combination of conical and cylindrical heat sources [219,220], conical and double ellipsoid [221], and Gaussian damped and double ellipsoid heat source [222].

2.6.1.2 Heat outflux or heat loss during welding

The heat outflux or heat loss during laser welding is comprised of three mechanisms: radiation, convection, and evaporation of the materials. The heat loss due to the contact with the ambient atmosphere and by radiation during welding is governed by Newton's law of cooling and the Stefan-Boltzmann relation [223]. Convective and radiative heat loss is considered for the top and bottom surfaces which follows Eq. 2.15 [223]

$$-k\nabla T = h(T - T_0) + \varepsilon\sigma(T^4 - T_0^4) + Q_{vap} \qquad 2.15$$

Where h is the surface heat transfer coefficient, ε is the emissivity of the material and σ is the Stefan-Boltzmann coefficient of radiation. The heat loss due to vaporisation Q_{vap} is defined as given in Eq. 2.16 where W is the evaporation rate and L_v is the latent heat of vaporization.

$$Q_{vap} = WL_v \qquad 2.16$$

Some of the earlier models simulated heat transfer to compute the temperature distribution based on the user-defined heat source using finite element or finite volume methods. Rosenthal [213] proposed a point source moving in an infinite material and simulated surface melting which related to conduction welding. He also gave a mathematical model for moving heat sources assuming a quasi-stationary state [224] which is still the most popular analytical method for calculating the thermal history of the welds. Many researchers had shown that Rosenthal's analysis generates an error for estimating temperature in or near the HAZ [225]. Pavelec *et al.* [226] gave a circular disc-shaped heat source model with Gaussian distribution of heat on the surface of the welded workpiece which provided better prediction of the temperature

distribution as compared to the point heat source. Hook *et al.* [227] approximated the solution given by Rosenthal and suggested that the power needed to cause melting was proportional and function of incident power. They assumed the laser beam as moving line heat source and developed the relation between weld width, absorbed laser power and welding speed. They did not estimate the depth of penetration as all the welding conditions were assumed full penetration. Lax *et al.* [228] gave the numerical spatial distribution of temperature by converting it into a 1D model and provided a general solution of intensity distribution for a Gaussian beam. Dowden *et al.* [229] assumed two-dimensional models for heat transfer and fluid flow. He also considered that the keyhole was circular in nature and isothermal. They faithfully replicated the observed displacement of the boundary between the solid and liquid states using the model, with a more pronounced effect observed in models where the fluid motion was concentrated closer to the keyhole. Goldak *et al.* [91] developed a model to simulate welding processes with shallow and deep penetration using a double ellipsoid heat source. They performed a comparison of the temperature distribution around the weld revealed that the double ellipsoid model, which distributed the thermal load throughout the weld pool, provided more accurate results compared to the disc model, where the thermal load was only applied to the surface of the weld. Modest *et al.* [230] investigated analytically 1D unsteady state pulsed Gaussian laser and temperature distribution in a semi-infinite solid. They broadened the realm of exact analytical solutions for Gaussian laser irradiation to encompass pulsed lasers and laser beams that exhibit exponential decay as they penetrated the medium. To address applications involving complex geometries such as laser melting and evaporation, a straightforward integral method was introduced, utilizing one-dimensional diffusion, and its validity range was established. Little *et al.* [111] proposed a simplified model for the prediction of

residual stresses and distortions. Based on their findings, it was determined that the transient temperature distribution in a welded plate experiences notable variations depending on the selected thermal conductivity (k) value. Opting for a higher k value resulted in a lower peak temperature near the weld, but higher peak temperatures in regions distant from the weld. In close proximity to the weld, a higher k value led to a faster decline in temperatures after reaching the peak. Additionally, a higher k value facilitated a more rapid attainment of uniform temperature across the plate. Nguyen *et al*. [231] gave an analytical solution for the three-dimensional transient heat source and the temperature distribution derived from it was in good agreement with experimental results. They also studied the dependency of heat source parameters on temperature distribution and weld pool geometry. They demonstrated that the analytical solution obtained for a double ellipsoidal heat source was a general one that can be reduced to a semi-ellipsoidal, semi-sphere, 2-D Gaussian-distributed heat source and the classical instant point heat source. Hou *et al*. [232] provided a general solution for both stationary and moving heat sources and also co-related with different shapes and intensities of heat sources. Araya *et al*. [233] used a control volume approach to provide a numerical model for temperature distribution by a moving heat source. They found that the maximum temperatures were formed just behind the centre of the heating region and not at the centre. Bianco *et al*. [234,235] investigated numerically transient heat conductive fields for two-dimensional and three-dimensional infinite and semi-infinite solids due to a moving heat source. They also showed that a quasi-steady state was attained. They found that convective heat transfer played an important role in the temperature field inside the workpiece. They used COMSOL Multiphysics code for their numerical solution. They considered a Gaussian laser source with constant velocity moving along the welding direction. They also took

a loss by radiation to ambient temperature into consideration. Shanmugam *et al*. [236,237] used FE ANSYS code to numerically simulate thermal profiles and molten pool geometry during laser butt-joint welding of AISI304 stainless steel. They concluded that the distance between the laser beam spot and peak temperature increased minutely with an increase in source power and decreased with a decrease in welding speed. They concluded that peak temperature is always at the "heel" of the centre of the laser for all welding conditions. They found out the shape of the weld pool was elliptic in nature. Most of the existing studies are based on the examination of the grain morphology of post-welded and performance, but no studies have addressed the modelling of beam oscillation and its interactions on the welding thermal cycle during the welding of dissimilar Aluminium alloys, however, the interest is on the rise [184,238]. However, the current literature has focussed mainly on single or multiple inputs and single-output scenarios which are not sufficient for laser welding, and there is a requirement to assess the RLW process by MIMO scenarios [11]. There are not many conclusive studies reported in the literature so far which describe the interactions between the welding speed, heat source power and beam oscillation. In addition to the existing numerical models, it is a need to study the effect of beam oscillation on the weld thermal cycle.

2.6.2 Fluid flow in the molten pool

The velocity field in the molten weld pool is computed by solving the equations of conservation of mass and momentum whose general form is given below based on the assumption that the fluid is Newtonian, laminar and incompressible.

$$\nabla \cdot u = 0 \qquad\qquad 2.17$$

$$\rho \frac{\partial(u)}{\partial t} = -\rho(u \cdot \nabla)u - \nabla P + \eta(\nabla^2 u) + F \qquad 2.18$$

where u is the velocity vector, ρ is the fluid density P is the static pressure, η is the dynamic viscosity of the fluid and F is the force term. As fluid is considered incompressible, the density variation does not depend on pressure. The first term in Eq. 2.19 is according to the Carman-Kozeny equation for flow through a porous media [239] representing the frictional dissipation which ensures a smooth transition of velocity from zero to a large value in the mushy zone. The second term on the right-hand side of Eq. 2.19 accounts for the natural convection.

$$F \;=\; C\left(-\frac{(1-f_l)^2}{f_l^3 + B}\right)u \;+\; \rho g \beta (T - T_{melting}) \qquad 2.19$$

where B is a merely computational constant, a very small positive number to avoid division by zero is set at 0.001 and C is a mushy zone constant related to the morphology of the porous media which is a large number (a value of 1.6 x 10^4 was used in the present study) to force velocity of the solid zone to be zero and represents mushy zone morphology, β is the coefficient of volume expansion, g is the acceleration due to gravity, $T_{melting}$ is the melting temperature which is average of solidus and liquidus temperature and f_l is the fraction of liquid which is defined in Eq. 2.20, where, T_{liq} and T_{sol} are liquidus and solidus temperature of the materials respectively.

$$f_l = \begin{cases} 1 & T > T_{liq} \\ \dfrac{T - T_{sol}}{T_{liq} - T_{sol}} & T_{sol} \leq T \leq T_{liq} \\ 0 & T < T_{sol} \end{cases} \qquad 2.20$$

The flow of liquid in the molten weld pool is governed by buoyancy force, Lorentz force and surface tension. At the bottom and the top surface of the molten weld pool, Marangoni convection balances the surface tension and mainly drives the flow of the

fluid [240]. Marangoni convection is defined as the flow driven by the surface tension gradient produced by the difference in temperature. Flow condition for the free liquid surface due to the surface tension gradient is given by Eq. 2.21 which states that the temperature gradient is proportional to shear stress on the surface and $\partial\gamma/\partial T$ is the temperature coefficient of surface tension.

$$-\eta\frac{\partial u_x}{\partial z} = f_l\frac{\partial\gamma}{\partial T}\frac{\partial T}{\partial x}; \quad -\eta\frac{\partial u_y}{\partial z} = f_l\frac{\partial\gamma}{\partial T}\frac{\partial T}{\partial y} \ ; \quad u_z = 0 \qquad\qquad 2.21$$

For the negative value of $\frac{\partial\gamma}{\partial T}$ flow direction will be outwards from the weld leading to wider pools [241] and movement of solute particles away from the fusion zone leading to segregation (such as in the Cu-Steel system) [174] which can be countered by forced convection through beam oscillation. Also, due to forced convection mixing of solute particles will be more leading to better and uniform properties in the fusion zone.

All the studies had shown that beam oscillation improved the weld quality and stabilized the welding process, leading to a better surface finish and less spatter formation. However, most studies related to Aluminium alloys focus on process stability and were carried out at lower frequencies. However, to date, no study has investigated the effect of beam oscillation on the thermal cycle and flow behaviour for a constant heat input per unit length. The influence of beam oscillation, however, is important and can be understood when the heat input per unit length is kept constant for each oscillation frequency. A change in heat input would alter the thermal as well as flow behaviour, which makes it difficult to understand the effect of beam oscillation in its entirety.

2.6.3 Mass transport for material mixing

To evaluate the material mixing, the transport of species is evaluated by solving the conservation equation of species for laminar flow which is defined as given in Eq. 2.22 [242]

$$\frac{\partial C}{\partial t} + \overrightarrow{\nabla \cdot} (\vec{u}\, C) = \vec{\nabla} \cdot \left(D\vec{\nabla} C \right) + S_C \qquad \text{2.22}$$

Where C is the concentration of species, D is the diffusivity of the species and S_C is the source term which defines the buoyancy force due to mass transport as given in Eq. 2.23 where C_r is the reference composition of the species and β_C is the fraction difference in the densities of the two metals.

$$S_C = \rho g \beta_c (C - C_r) \qquad \text{2.23}$$

At the free surface, Marangoni-driven mass transport due to concentration gradient is given by Eq 2.24 [243].

$$\eta \frac{\partial u_x}{\partial z} = f_l \frac{\partial \gamma}{\partial C} \frac{\partial C}{\partial x}; \; \eta \frac{\partial u_y}{\partial z} = f_l \frac{\partial \gamma}{\partial C} \frac{\partial C}{\partial y}\; ; \qquad \text{2.24}$$

Sections 2.6.1-2.6.3 discuss the interaction between the physical phenomenon necessary to simulate the laser welding process. Furthermore, laser welding is a transient process where the heat source moves at a constant speed which makes an essential requirement to have a dense and fine mesh near the heat source and molten region and coarse mesh elsewhere. Numerical simulation of the laser welding allows a deeper understanding of the process to improve weld quality, efficiency and control over the process. Many realistic laser welding models have been developed but the challenge is the computation time to survey the whole parameters space.

Another challenge is an increase in the number of process parameters due to the recent developments in heat delivery by laser systems such as beam oscillation, beam shaping and power modulation which need to be analysed and optimised to select the robust process parameters combinations which satisfy the weld requirements. Various studies with beam oscillation have shown that the weldability of aluminium alloys has improved with fewer defects and improved mechanical properties [180–184], but none of them reports on an application in welding dissimilar aluminium alloys. In the current state of the art, the effect of beam oscillation on the solute distribution during laser welding of dissimilar aluminium alloys is missing in the literature. There is a need for a coupled three-dimensional heat transfer, fluid flow and mass transfer model to investigate the effect of process parameters on the weld thermal cycle, flow profile, fusion zone geometry, and solute distribution.

2.7 Conclusions

The majority of literature is concerned with the investigation of process parameters on the weld quality experimentally by performing characterisation techniques on the post-welded specimens. This method of analysing the process is a resource and time expensive. The use of numerical simulation to estimate the temperature field and fluid flow field to understand and improve the laser welding process is on the rise. In the literature, the estimated temperature field and fluid flow field were mainly used to predict the weld profile and fluid flow behaviour [244–248]. The main aim of this study is to develop the correlation between the process parameters and the KPIs to select robust process parameters, reducing the number of experiments required. The current limitations of the literature are: (*i*) the current literature has focussed mainly on single or multiple inputs and single-output scenarios

which are not sufficient as laser welding is characterised as MIMO [11], (*ii*) limited work on modelling of beam oscillation, beam shaping and laser welding process variation in terms of a varying range of process parameters, (*iii*) limited work on the effect of WPPs on the solidification behaviour during laser welding based on the weld thermal cycle and fluid field, (*iv*) limited work on developing the relationship between process parameter, IPIs and KPIs such as weld width, depth of penetration, thermal gradient, peak temperature, cooling rate to analyse the RLW process, and (*v*) limited availability of process maps or process monitoring methods to estimate the robust process parameters for early design phase based on MIMO scenario. In order to overcome these limitations, this study presents a simulation methodology that encompasses the following advancements:

(i) The development of a numerical model for the laser welding process that considers a system with multiple inputs and multiple outputs.

(ii) The incorporation of beam oscillation and beam shaping as input process parameters across the entire parameter space within the numerical model.

(iii) The implementation of a sequential numerical model that simulates the necessary physics to evaluate the temperature field, flow field, and concentration field.

(iv) The creation of a surrogate model that allows for rapid estimation of Important Process Indicators (IPIs) based on Welding Process Parameters (WPPs), utilizing solutions from the numerical model.

(v) The introduction of a multi-fidelity numerical model that provides refined process capability information throughout the complete range of the parameter space. To strike a balance between accuracy and computational time/resources, a sequential coupling of the governing physics within the numerical model was performed. The process capability space was defined at each stage based on constraints derived from

81

IPIs and Key Performance Indicators (KPIs) such as fusion zone dimensions, thermal gradient, peak temperature, and cooling rate. As new physics is incorporated into the model, the updated process capability space serves as the new parameter space, ensuring a balance between computation and accuracy in this study.

Chapter 3. Numerical modelling of thermal quantities for improving remote laser welding process capability space with consideration to beam oscillation[1]

3.1 Introduction

Newer environmental regulations and policies aimed at reducing greenhouse gas emissions have accelerated the development of industrial capabilities for a higher uptake of e-mobility technologies to fulfil the demands of lighter, stronger and cost-effective components [249,250]. In turn, these requirements have led to the development of joining processes with capabilities for (*i*) joining multi-material [251,252]; (*ii*) high welding speed for high-volume manufacturing of multiple product variants; and, (*iii*) rapid development and deployment of new joining processes as required by shortened lead time and increased product variants [2]. However, a key challenge is shortening the new process development and selection of key process parameters to meet welding outputs pertaining to weld quality. Currently, the development of the RLW process is time-consuming due to the interactions between those factors that provide flexibility.

Measuring the weld thermal cycle experimentally is a challenging, time-consuming, and expensive process, and it contains uncertainties with the measurements [253]. As a result, numerical welding simulations are used to predict the distribution and magnitude of the weld thermal cycle developed in different types

---

of materials and joint configurations during laser welding. Numerical welding simulations have advantages over conducting experiments as they are faster and cheaper. It can estimate quantities which are either difficult to measure experimentally or not possible to be measured with the required accuracy. It allows investigating systematically the effect of various conditions during welding such as different welding process parameters, various joint configurations, several types of alloy combinations, and different and complex geometries which can eliminate the practical limitations of conducting experiments for process optimisation. It can be utilised on two different levels (*i*) for predicting the weld outputs to optimise the welding process parameters which decreases the number of experiments required; and (*ii*) to improve the understanding of the complex physical phenomena which involve multi-field interactions such as laser welding.

The interactions between the metallurgical and thermal changes of the weldment during the welding determine the weld quality and mechanical performance of the welds. Therefore, understanding and selecting the welding thermal cycle is a crucial task in obtaining desired weld quality as described by the grain morphology and mechanical properties. To be able to do this, it is important to model the relations between the welding thermal cycle; welding process parameters (WPPs); and welding thermal outputs. It is worth noting that these relations are crucial not only to select WPPs but also to estimate welding process capability, to understand process variation and then being able to control the process during the production phase. In the case of laser welding, the key WPPs which govern the local temperature distribution during the weld thermal cycle are welding speed, heat source power modulation and beam oscillation [6].

Overall, there is a strong need for both welding process parameter selection and understanding their sensitivity to IPIs that need to be determined during the process design phase ideally via simulations or with a minimum number of physical experiments. Physical experiments alone are not efficient to survey the entire parameters space, as it takes weeks or months to run them. Efficient simulation of weld thermal cycle provides the option to be (*i*) run in the entire parameters space (high fidelity simulations which replace physical experimentations), or (*ii*) integrated with physical experiments in such a way that simulations are run in un-tested settings of parameters space decreasing the number of experiments required (lower fidelity simulations which reduce the number of physical experiments). Experimental measurements of peak temperature and cooling rate are difficult due to a very high peak temperature and small weld pool formed; however, they can be quantified by using simulation and modelling tools [9]. In welding simulation, inputs are understood as welding process parameters (WPPs) and the quality performance is evaluated by using multiple outputs which are called Intermediate Performance Indicators (IPIs) in this study. It was observed that these process parameters not only affect the weld thermal cycle IPIs, but also the Key Performance Indicators (KPIs) of other downstream processes.

This chapter introduces a numerical simulation methodology to develop (*i*) a numerical model for the estimation of weld thermal cycle considering multiple inputs (*i.e.* key WPPs) and multiple-outputs (*i.e.* IPIs) system by conducting computer simulations; (*ii*) the effect of WPPs is depicted by parametric contour maps based on the developed numerical model over the parameters space; and, (*iii*) process capability space (C_p-Space) which is depicted by parametric contour maps based on the developed numerical model that allows the estimation of a desired process fallout rate

in the case of violation of process tolerances. The proposed methodology provides a unique ability to: (*i*) simulate the effect of process variation as generated by the manufacturing process; (*ii*) generate the relationship between the WPPs and the IPIs and assess the sensitivity of process parameters on the IPIs; and (*iii*) understand the effect of beam oscillation on the weld thermal cycle. The rest of the chapter is organized as follows: Section 3.2 formulates the modelling strategy for the estimation of weld thermal cycle based on the finite element method and develops a surrogate model to generate regression relation between WPPs and IPIs; Section 3.3 provides experimental details; Section 3.4 discusses the effect of WPPs on the IPIs using parametric contour maps and finally, conclusions are summarized in Section 3.5.

3.2 Modelling strategy

3.2.1 Assumptions

The weld thermal cycle is estimated using a transient heat transfer model which enables the calculation of the spatial and temporal distribution of temperature ($T(x,y,z,t)$) during welding. To decrease the computation time within the required accuracy, the following assumptions were considered: (*i*) No gap between the two metal plates; (*ii*) Material properties such as thermal conductivity (k), heat capacity (c_p) and density (ρ) were assumed to be temperature-dependent; (*iii*) the latent heat of melting and solidification are included; (*iv*) No convection in the melt pool was considered in the model; (*v*) absorption coefficient is calculated using Eq. 2.9 and adjusted to calibrate the model based on the weld profile estimated from the experiments (*vi*) No vapour and plasma flow is simulated in the model. A Gaussian distributed volumetric heat source was considered which generates the heat inside the material such that fusion zone boundary lines are comparable to the experimental

results [221]; and (*vii*) additional contributions to the calculated temperature profile from exothermal reactions (e.g. oxidation) as originating from oxidation (i.e., exothermal reactions) and local effects of the shielding gas were not considered in this research work.
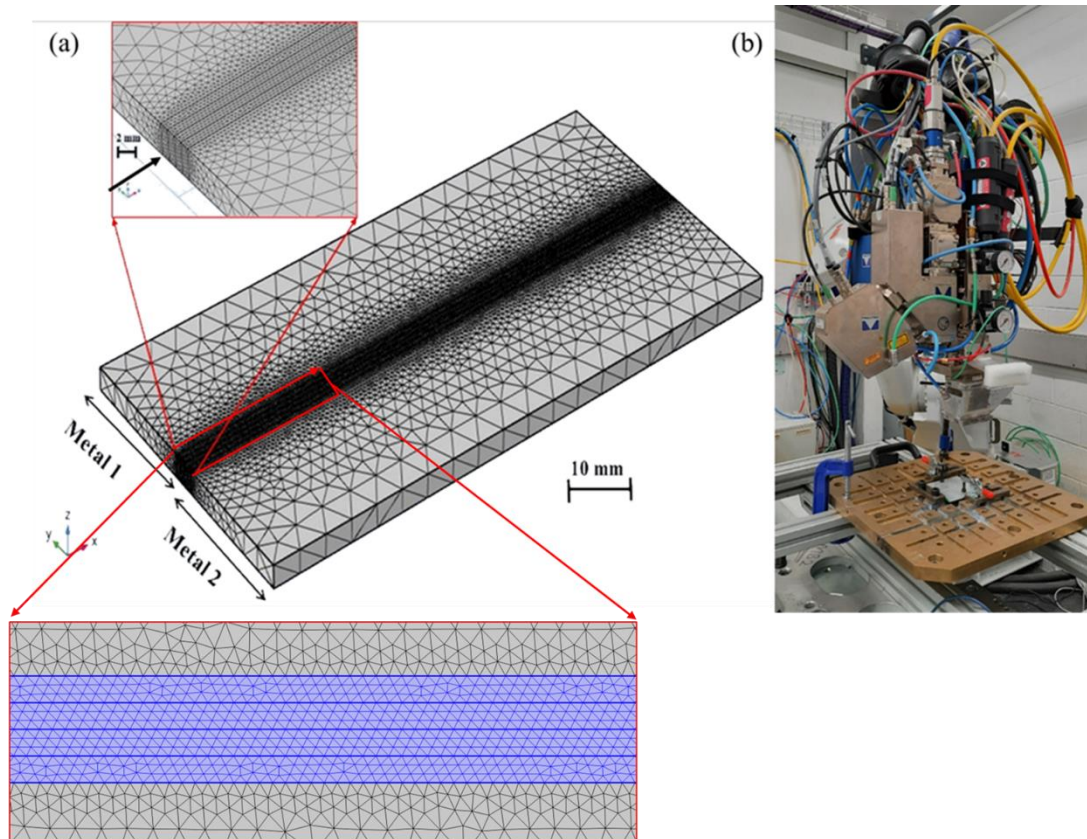
Figure 3.1 (a) Schematic illustrations of geometry and finite element mesh distribution across the three zones (base metal, fusion zone, and weld centerline), used for the simulations and (b) experimental setup for the welding.

3.2.2 Materials and Geometry

A 3D Cartesian coordinate system is used. The heat source is moving in the *x*-direction, and it is incident in the *z*-direction at $z = 0$. In the 3D model, the size of the plate was 100 mm × 50 mm with a thickness of 3 mm. Each plate was divided into three domains: 100 mm × 49 mm × 3 mm (base metal), 100 mm × 1 mm × 3 mm

(fusion region) and 100 mm × 1 mm × 3 mm (weld centerline) as shown in Figure 3.1. This improves the distribution of tetrahedral mesh elements for the simulation having a total mesh consisting of 1169117 domain elements as shown in Figure 3.1. The size of the mesh at fusion zone is taken as $r/4$ where r is the laser spot size, such each spot has at least 8 mesh elements. The validation of the model was done using the welding of Titanium to Aluminium alloys with material properties and coupon geometry as used in Sonia *et al.* [31] having a dimension of each plate as 100 mm × 50 mm with a thickness of 2 mm for the Titanium alloy and 3 mm for the Aluminium alloy. The material properties used for the model development are reported in Table 3.1 Thermo-physical properties of AA5754, Ti6Al4V and Al-6061 alloys used in this study [255,256]. and Table 3.2. In this study, the validation of the FEM heat transfer model for weld thermal cycle estimation was done by conducting welding of Aluminium 6061 and Aluminium 5754 alloys for no oscillation conditions and from the literature for beam oscillation conditions. In this study, the materials used for generating results are Aluminium 6061 alloy and Aluminium 5754 alloy. The thermal material properties of Aluminium 6061 and Aluminium 5754 used for the numerical simulation are obtained from the COMSOL material library [254]. Due to the unavailability of material properties beyond a certain temperature the values are kept constant for the value known at the last temperature value. All these properties are defined locally using a piecewise function as the temperature is a local quantity. The finite element mesh consisted of about 1169117 domain elements, 102412 boundary elements and 4528 edge elements having higher density near the fusion zone (FZ) and HAZ as compared to the rest of the structure.

Table 3.1 Thermo-physical properties of AA5754, Ti6Al4V and Al-6061 alloys used in this study [255,256].

Property	AA5754	Ti6Al4V	Al-6061
Density (g cm^{-3})	2.7	4.4	2.68
Liquidus Temperature (K)	870	1923	925
Solidus Temperature (K)	856	1880	855

Table 3.2 Temperature-dependent thermal conductivity value for alloys AA5754, Ti6Al4V and Al-6061used in this study [255,256].

Temperature (K)	Thermal Conductivity (W m^{-1} K^{-1})			Heat capacity (J kg^{-1} K^{-1})		
	AA5754	Ti6Al4V	Al-6061	AA5754	Ti6Al4V	Al-6061
293	138	6.01	162	900	525	917
373	147.2	7.1	177	950	550	978
473	152.7	8.5	192	998	579	1028
573	162.7	9.4	207	1055	610	1078
673	152.7	11.3	216	1096	628	1098

773	158.75	14.78	223	1140	660	1133
873	138	17.20	253	1400	698	1230
1773	138	34.3	253	1240	680	1230

3.2.3 Governing Equations

The heat source is considered perpendicular to the workpiece surface along the z-axis and moving with constant welding speed along the x-axis. The calculated temperature field is a function of space (x, y, z) and time (t) which is determined by the non-linear energy conservation Eq. 3.1 [211].

3.1

$$\rho c_p \left[\frac{\partial T}{\partial t}\right] = \vec{\nabla} \cdot \left(k\vec{\nabla}T\right) + Q_{laser}$$

Where ρ is the material density, c_p is the specific heat capacity of the material, T is the temperature of the workpiece, t is the time, k is the thermal conductivity of the material, and Q_{laser} is the energy input of the laser heat source. The phase changes are considered to include temperature change due to latent heat by using the apparent heat capacity method which includes an additional term for latent heat as shown in Eq. 3.2

$$C_P = C_{P,solid} \cdot (1 - f_l) + C_{P,liquid} \cdot f_l + L_{s\rightarrow l} \frac{\Delta f_l}{\Delta T} H_m$$

3.2

Where, $C_{p,solid}$ is the heat capacity of the solid phase, $C_{p,liquid}$ is the heat capacity of the liquid phase, $L_{s\rightarrow l}$ is the latent heat and f_l is the phase transition function. For pure solid $f_l = 0$, and pure liquid $f_l = 1$.

3.2.4 Heat source design and boundary conditions

Here, a hybrid heat source is adopted to simulate the heat input to the workpiece. Multiple combinations of volumetric heat sources are simulated and compared with the experimental results to predict the shape and dimensions of the weld profile. The general trajectory of the moving heat source is given in Eq. 3.3 where $x_{(t)}$, $y_{(t)}$ and $z_{(t)}$ are time-dependent heat source spot coordinates, x_0, y_0 and z_0 mark the initial position of the heat source, S is the welding speed, A is the oscillation amplitude (for sinusoidal oscillation), R is the radius of oscillation (for circular oscillation), t is the time and f is the oscillation frequency. The term St gives the displacement in the welding direction, *(1-Rcos(2πft))* and *Rsin(2πft)* produce the circular rotation for the oscillation of the beam and *Asin(2πft)* produces sinusoidal movement of the beam.

$$(x_{(t)}, y_{(t)}, z_{(t)}) = \begin{cases} (x_0 - St, y_0 , z_0) & \text{No oscillation} \\ (x_0 - St, y_0 + Asin(2\pi ft), z_0) & \text{Sinusoidal} \\ (x_0 + St - R(1 - cos(2\pi ft)), y_0 + Rsin(2\pi ft), z_0) & \text{circular} \end{cases} \quad 3.3$$

The power density distribution of the five different hybrid heat sources with origin (x_0, y_0, z_0) is described as follows:

- Case-1: 3D volumetric Gaussian heat source which is defined in Eq. 3.4. They have a volumetric Gaussian-shaped energy distribution, with the nominal power of the heat source at the centre (x_0, y_0, z_0) is defined as shown in Eq. 3.4. Note that this relationship represents the 3σ range (99.7% of total heat input) of a heat source [239].

$$Q_g(x, y, z, t) = \eta \frac{3P_l}{\pi r^2 d} e^{-3\left(\frac{(x-x_{(t)})^2 + (y-y_{(t)})^2}{r^2} + \frac{(z-z_{(t)})^2}{d^2}\right)} \quad 3.4$$

Where P_l is the power of the heat source beam, r is the heat source spot radius, and d is the maximum depth of penetration. In the conical design of the heat source,

the temperature is maximum at the surface and minimum at the bottom which is a simplified representation of the keyhole formation during laser welding. η is the absorption coefficient of material and is defined by Eq. 2.9 [257].

- Case-2: Hybrid 3D volumetric Gaussian and double ellipsoid heat source - According to previous research [37, 40], laser absorption is described as Fresnel absorption inside a keyhole. The hybrid volumetric heat source is a combination of a double ellipsoid heat source and a 3D volumetric Gaussian damped heat source. The Bremsstrahlung absorption is modelled by the double ellipsoid heat source [258] and is described as follows:

$$Q_f(x,y,z,t) = \eta \frac{6\sqrt{3}f_f P_l}{a_f bc\pi\sqrt{\pi}} e^{-3\frac{\left(x-x_{(t)}\right)^2}{a_f^2}} e^{-3\frac{\left(y-y_{(t)}\right)^2}{b^2}} e^{-3\frac{\left(z-z_{(t)}\right)^2}{c^2}} \qquad 3.5$$

$$Q_r(x,y,z,t) = \eta \frac{6\sqrt{3}f_r P_l}{a_r bc\pi\sqrt{\pi}} e^{-3\frac{\left(x-x_{(t)}\right)^2}{a_r^2}} e^{-3\frac{\left(y-y_{(t)}\right)^2}{b^2}} e^{-3\frac{\left(z-z_{(t)}\right)^2}{c^2}} \qquad 3.6$$

$$Q_{laser}(x,y,z,t) = f_1 Q_g(x,y,z,t) + f_2(Q_r(x,y,z,t) + Q_f(x,y,z,t)) \qquad 3.7$$

Where a_r, a_f, b, and c are the heat source distribution parameters depending upon the shape of the weld pool obtained by measuring the rear (a_r), front (a_f), width (b), depth (c) of the half ellipsoids, $Q_f(x,y,z,t)$ and $Q_r(x,y,z,t)$ are the power densities in the front and rear quadrant of the double ellipsoid heat source (Eqs. 3.5-3.6). The effective heat absorbed by the hybrid heat source i.e., double ellipsoid and 3D Gaussian conical heat source is given by Eq. 3.7. f_1 and f_2 are the power distribution coefficient between the 3D Gaussian and double ellipsoid heat source which follows $f_1 + f_2 = 1$ and in this study, it is set as 0.6 and 0.4 respectively. f_f and f_r are the power distribution in the front and rear quadrant of an ellipsoid which follows $f_f + f_r = 2$ [222], and in this study, it is set as 0.4 and 1.6 respectively. Just to note that the value of the f_1, f_2 f_f and f_r are calibrated from the experimental results based on the weld profile obtained using

optical microscopy. This calibration is performed via a trial-and-error method and the value best showing the correlation is selected and kept constant throughout the study. The shape of the weld pool depends upon heat source distribution parameters obtained by measuring the rear (a_r), front (a_f), width (b), and depth (c) of the half ellipses.

- Case-3: Hybrid Gaussian damped heat source and double ellipsoid heat source combined - The Gaussian damped heat source model suggested by Yuewei *et al.* [222] was adopted to describe the heat distribution, which is given in Eq. 3.8 as follows:

$$Q_{gd}(x,y,z,t) = \eta \frac{6P_l}{\pi r^2 D(1-e^{-3})} \frac{mz+r}{md+2r} e^{-3\left(\frac{\left(x-x_{(t)}\right)^2 + \left(y-y_{(t)}\right)^2}{r^2}\right)} \qquad 3.8$$

$$Q_{laser}(x,y,z,t) = f_2(Q_r(x,y,z,t) + Q_f(x,y,z,t)) + f_3 Q_{gd}(x,y,z,t) \qquad 3.9$$

The effective heat absorbed by the hybrid Gaussian damped heat source and double ellipsoid combined is given by Eq. 3.9. f_3 and f_2 are the power distribution coefficient between the Gaussian damped and double ellipsoid heat source respectively which follows $f_3 + f_2 = 1$ and in this study, it is set as $f_3 = 0.6$. D is the depth of penetration, and the damping coefficient m is selected to minimise the simulated errors which are taken as 0.1 in this study.

- Case-4: Rotary Gauss body heat source - A rotating Gauss body heat source model [182,218] was used as a volumetric heat source is given in Eq. 3.10 where H is the heat source height.

$$Q_{rg}(x,y,z,t) = \eta \frac{9P_l}{\pi r^2 H(1-e^{-3})} e^{-9\left(\frac{\left(x-x_{(t)}\right)^2 + \left(y-y_{(t)}\right)^2}{r^2 \log(H/z)}\right)} \qquad 3.10$$

- Case-5: Hybrid modified Gaussian damped heat source and double ellipsoid heat source combined - The Gaussian damped heat source is modified to account for the decay of the heat distribution through the thickness of the workpiece in place of specifying it to the depth of penetration. In general, the depth of penetration is provided as input in the model which is calculated experimentally or by interpolation using a surrogate model based on a few experiments. The experimental calculation will not serve the advantages of performing numerical simulations to predict the fusion zone dimensions. The modified Gaussian damped hybrid heat source eliminates the requirement of providing depth of penetration as an input and is defined as:

$$Q_{mgd}(x,y,z,t) = \eta \frac{6f_4 P_l}{\pi r^2 d(1-e^{-3})} \frac{mz+r}{md+2r} e^{-3\frac{(x-x_{(t)})^2+(y-y_{(t)})^2}{r^2}} e^{-3\frac{(z-z_{(t)})^2}{d^2}} \qquad 3.11$$

$$Q_{laser}(x,y,z,t) = f_2(Q_r(x,y,z,t) + Q_f(x,y,z,t)) + f_4 Q_{mgd}(x,y,z,t) \qquad 3.12$$

The effective heat absorbed by the hybrid heat source i.e., double ellipsoid and modified Gaussian damped heat source is given by Eq. 3.12. f_4 and f_2 are the power distribution coefficient between the modified Gaussian damped and double ellipsoid heat source ($f_4 + f_2 = 1$), respectively, and the value of f_4 is set as 0.6.

The initial temperature of the workpiece is assumed to be maintained at room temperature (T_0). The energy absorbed by the workpiece is transferred by conduction, which further is partially lost due to contact with the ambient atmosphere and by radiation leading to cooling. The heat loss due to the contact with the ambient atmosphere and by radiation during welding is governed by Newton's law of cooling and the Stefan-Boltzmann relation [223]. Convective and radiative heat loss is considered for the top and bottom surfaces which follows Eq. 2.15 [223].

The governing energy conservation equation is discretized using the finite element method. The input process parameters are welding speed, heat source power, radius of oscillation, frequency of oscillation and heat source spot size as depicted in Eqs. 3.3-3.12. The output of the model is the temperature distribution which represents a function of position and time taken to complete the welding. Three outputs of interest have been derived from the transient temperature distribution which are (*i*) peak temperature (T_{peak}), (*ii*) heat-affected zone volume (V_{HAZ}) and (*iii*) cooling rate (C_{rate}). The T_{peak} is defined as the maximum temperature recorded during welding. The V_{HAZ} is defined as a region bounded between the temperature to cause metallurgical transformation and grain growth but less than the melting point of the material as defined in Eq. 3.13.

$$V_{HAZ} = \frac{\int_{t_1}^{t_2} \iiint T(x,y,z,t)dx\,dy\,dz\,dt}{t_2 - t_1}, \qquad T \in [470\,K, 933\,K] \qquad \text{3.13}$$

The temperature range lies between solidus and where grain growth is not possible and is taken as 933 K-470 K temperature range. The cooling rate C_{rate} is defined as the change in temperature from the melting point to the 470 K divided by the time taken.

3.2.5 Numerical implementation

The commercial COMSOL Multiphysics 5.6 software is used for the numerical simulation. COMSOL Multiphysics solver is based on the Finite Element Method (FEM). The calculation domain is discretised into a finite number of elements and general conservation equations are solved on this set of elements. Time is discretised using the backwards differential formula (BDF). The system is solved fully coupled, and the system of non-linear equations is solved using the damped Newton method.

The heat transfer interface is employed to solve the elliptical partial differential equation in temperature.

A three-dimensional model and grid are set inside the COMSOL Multiphysics using a graphical user interface provided in the software. A Parallel Direct solver (PARDISO) is used as it is robust and fast. The convergence criteria for the residuals of the energy equation are 10^{-6}. The domain size, time step and mesh size are investigated to attain high accuracy of the numerical model. The domain size of the numerical model is selected large enough to eliminate the boundary effect for fluctuation of the temperature field. The time step is selected based on the frequency of oscillation such that it can map the effect of frequency on the temperature field. The time step is taken as $1/(4f)$ where f is the frequency of oscillation. The FEM model solves problems at a series of discrete points called as elements. These elements or nodes add degrees of freedom (DOF) to the simulation. So, the more the DOFs, the better the model captures the physical behaviour. But each DOF increases the complexity of the model and thus increases the computation time and too few DOFs lead to inaccurate outputs from the model. So, to have an accurate result from the model, the solution should be independent of the mesh size. A mesh convergence study was performed which represents the number of mesh elements required in the numerical model to ensure that the results are not affected by changing the mesh size and additional mesh refinement does not affect the results. Mesh analysis was performed at a constant material property, welding process parameters and time step. The example for the calculation of time step and mesh size if given in appendix. The minimum mesh size at the fusion zone region is a function of spot size of the laser beam. If the r is the radius of laser beam, then the minimum spot size is r/4. The plot between the number of mesh, computation time and deviation are calculated as shown

in Figure 3.2. Deviation of temperature is calculated for the maximum temperature over the global domain. Figure 3.2 also represents the region of efficient and inefficient FEM mesh. Mesh size is selected which can be solved in reasonable computation time and has less deviation in the global peak temperature. Compiled user-defined functions are introduced for the calculation of the position of the laser heat source at a given time as a function of welding speed, beam oscillation parameters (amplitude and frequency) and the volumetric Gaussian heat source in terms of spatial distribution.
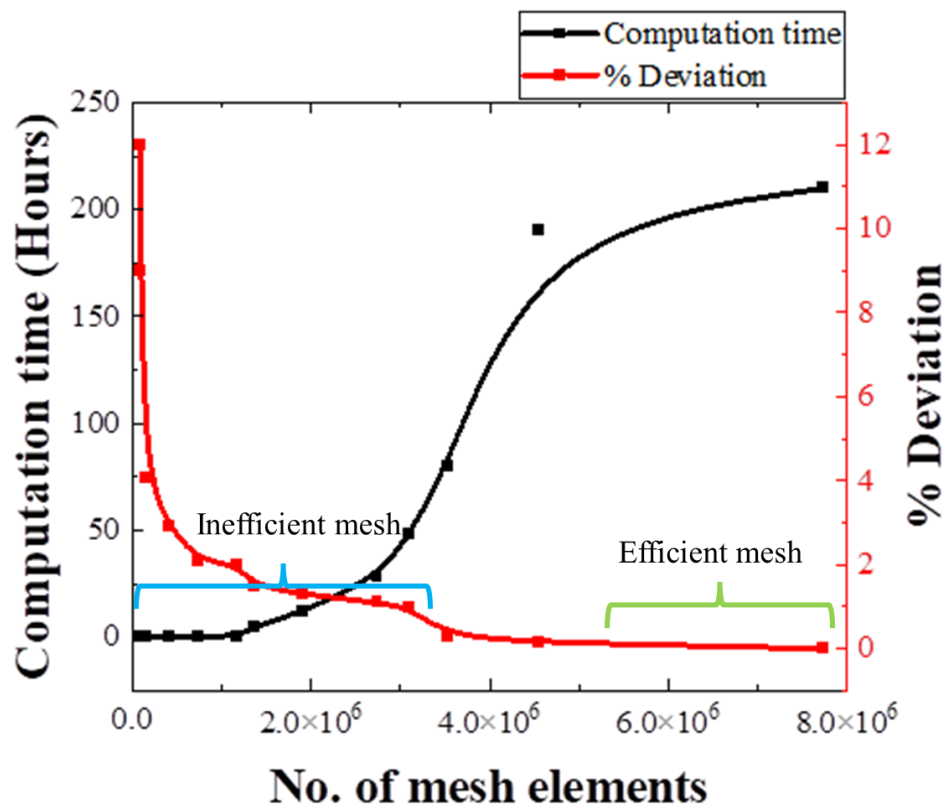
Figure 3.2 Relation between computation time, number of mesh and % deviation performed for mesh analysis.

The model outputs have been calculated after the solution attains a quasi-steady state such that all output values attain a quasi-steady state and can be calculated to be compared with the experimental results. Similarly, the experimental calculations

are made after 20 mm from the start and end of the weld seam. In the present numerical model, three different outputs are calculated which need to attain a quasi-steady state. These are the peak temperature as well as the width and length of the weld. The evolution of the temperature field for no oscillation conditions at different times is shown in Figure 3.3. The peak temperature attains a quasi-steady state at time $t = 0.025$ seconds, width attains at time $t = 0.05$ seconds and length attains at time $t = 0.08$ seconds which is depicted in Figure 3.3 below. It is worth noting that the output from the numerical model must be checked and calculated after it attains the quasi-steady state such that the values are constant to be compared with the experimental results.
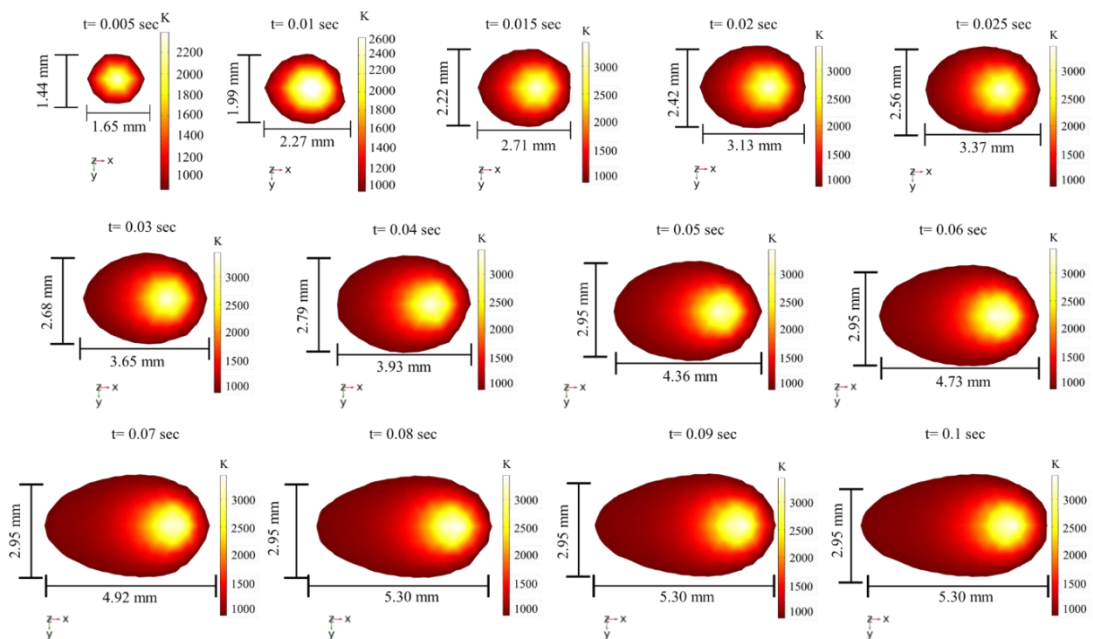
Figure 3.3 The evolution of temperature field, width and length of the weld at different times for no oscillation condition with a welding speed of 4000 mm/min and laser power of 4500 W.

The evolution of the temperature field depicting the top surface weld morphology for beam oscillation conditions is shown in Figure 3.4. In beam oscillation conditions, the peak temperature attains the quasi-steady state at time $t = 0.05$ seconds, width attains the quasi-steady state at time $t = 0.10$ seconds and the length of the weld pool attains quasi-steady state at time $t = 0.17$ seconds. It is evident from the

temperature field that beam oscillation requires more time to attain a quasi-steady state. In fact, beam oscillation takes almost twice as long to attain a quasi-steady state for all the outputs. This is due to the modification of the temperature field due to beam oscillation.
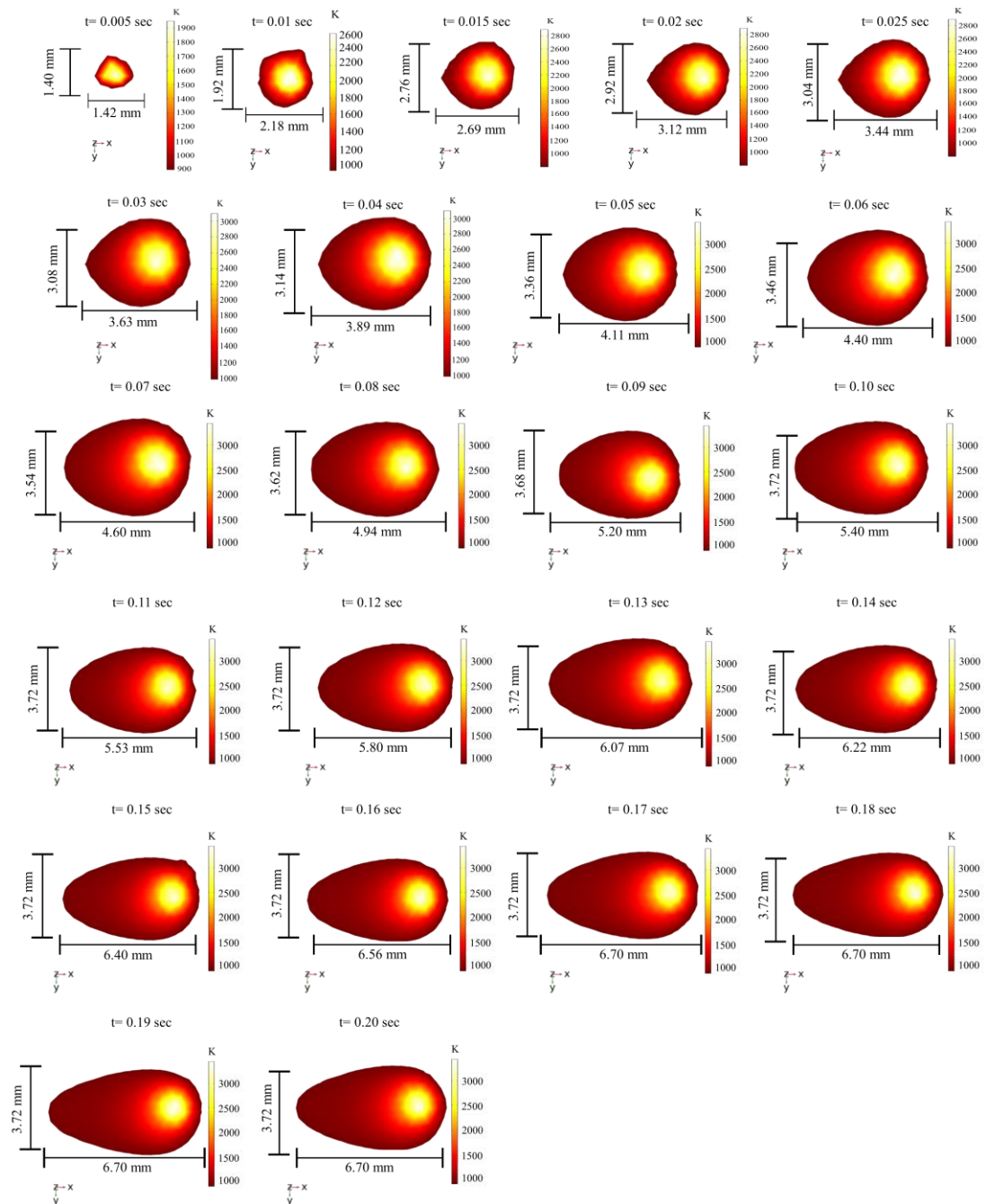
Figure 3.4 The evolution of temperature field, width and length of the weld at different times for beam oscillation conditions with a welding speed of 2500 mm/min, laser power of 4500 W, oscillation radius of 0.6 mm and oscillation frequency of 200 Hz.

3.3 Experimental details

Dissimilar welding of Al-5xxx with Al-6xxx is performed in this study. The welded coupons are machined into the size of 100 mm (length) × 45 mm (width) × 3 mm (thickness) and cleaned with acetone to remove surface contaminations before welding. A butt joint configuration was employed. No shielding gas or filler wire was used during the experiments. A 10 KW Coherent ARM FL10000 laser system as shown in Figure 3.1 (b), with a beam parameter product of 16 mm mrad with a core optical fibre of 100 μm diameter was used. The laser system coupled with the WeldMaster remote welding head (Precitec GmbH, Germany), has a 150 mm collimating length, a focal length of 300 mm and a resulting Rayleigh length of 5.3 mm. Beam oscillation is generated by the motorized mirror and collimator integrated with the WeldMaster Scan&Track remote welding head (YW52 Precitec GmbH, Germany). Only a core beam was used to carry out the experiments. To ensure precise alignment of the laser beam, a pilot laser, integrated into the laser head, is employed to position the laser spot accurately. The laser spot is aligned in such a way that half of its size falls on one plate, while the other half falls on the adjacent plate. The setup is securely clamped to maintain a tight configuration and prevent any gaps between the plates. Additionally, the edges of the plates are trimmed to create a straight cup shape, minimizing the occurrence of gaps. To ensure repeatability, two samples are created from each weld seam, while for reproducibility, three to five separate weld seams are generated depending upon the variation and output. The experimental results include the calculation of standard deviation to demonstrate the variation observed in the outcomes. The weld dimensions were measured using a Keyence VHX7000 optical microscope at five different points on the weld seam which is 20

mm away from the start and end of the welding position. The welding head is tilted at 4° from the vertical direction. Constant laser power of 4500 W is adopted throughout the welding experiments. The welding speed is increased from 4000 mm/min to 6000 mm/min in a step size of 500 mm/min such that to generate enough data points to compare the experimental results with the numerical model and also to analyse the effect of welding speed in no oscillation condition.

3.4 Results and Discussions

The transient heat transfer model is validated by the experimental results from the literature [255,259]. A total number of around 800 numerical simulations were carried out which serve as a base for the discussed results. Each simulation took 25 minutes to solve for no oscillation conditions and 105 minutes for oscillation conditions. This is due to the increased complexity introduced with the heat source oscillation and an increase in the number of mesh elements as the heat source traversing area has been increased. All outputs from the model have been calculated after it attains the quasi-steady state. The evolution of the temperature field at different times and time required to attain a quasi-steady state for different outputs have been added in supplementary materials for both no oscillation and beam oscillation conditions.

3.4.1 Model validation

The model is validated in three steps: (*i*) validation of 3D temperature distribution based on the data from the literature [255]; (*ii*) validation of the model for welding of Al-5xxx to Al-6xxx in butt joint configuration with no beam oscillation based on the weld profile at the top surface; (*iii*) validation for the cases of welding

with beam oscillation and, finally, (*iv*) the validation is based on the weld profile by comparing the shape and dimensions of the fusion zone with the optical micrographs.
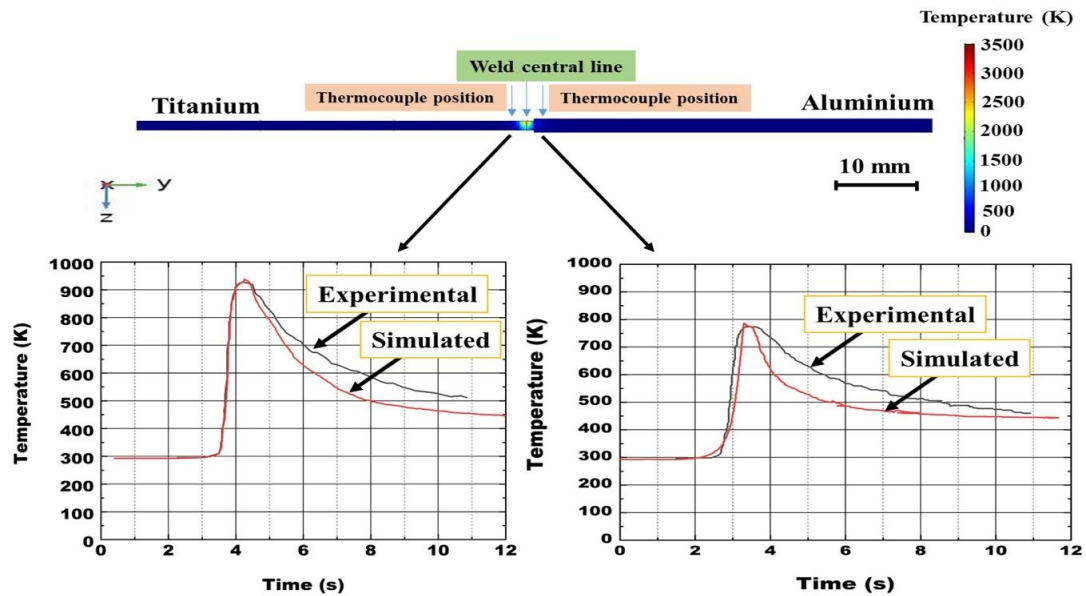
Figure 3.5 Calculated temperature distribution of Al-Ti welded joint, investigated in this study (top). The position of the weld central line and the thermocouple (top) is indicated by the arrow (top). Comparison between experimental and simulated thermal cycle at the Titanium (bottom left) and Aluminium side (bottom right). Experimental data has been reproduced from [255].

The initial step involves the validation of the 3D temperature distribution in Al-5754 and Ti_6Al_4V welded joints by comparing it to a single-point temperature profile obtained from literature using thermocouples [255]. The objective is to assess the accuracy of the 3D temperature measurements. Figure 3.5. illustrates the thermal cycle obtained from both simulation and experimental data using thermocouples. The simulated thermal cycle closely matches the experimental results, indicating the reliability of the numerical model. The peak temperature values obtained exhibit a difference of less than 0.1%, which remains consistent throughout the model and falls

within an acceptable range. Comparing the calculated heating cycle with the experimental results reveals a difference of less than 0.5%, while the cooling cycle shows a deviation of 8% for Titanium alloy and 2% for Aluminium alloy, which is within an acceptable range. This variation can be attributed to the higher thermal conductivity of Aluminium (158.7 W m^{-1} K^{-1}) as compared to Titanium (14.7 W m^{-1} K^{-1}). It should be noted that the thermocouples might underread transient condition while capturing the weld thermal cycle which could be a reason for the variation with the simulated results. Consequently, heat transfer through conduction is more dominant in Aluminium due to its higher thermal conductivity. Additionally, the difference in peak temperature between the two alloys can be attributed to their respective heat capacities and thermal conductivities. The higher heat capacity of Aluminium requires more energy to raise its temperature, while the higher thermal conductivity results in faster heat dissipation, leading to a decrease in temperature. In the second step, the model is validated for the welding of Al-5xxx and Al-6xxx in butt joint configuration with no beam oscillation. The intention is to estimate the accuracy of the model for the change of material used for welding and the geometry of the joint configuration. The goodness of the model is compared based on the weld width at the top surface obtained experimentally for varying welding speeds as shown in Figure 3.6. The maximum error seems to be 6%. Results show that an increase in welding speed at constant laser power can effectively decrease the weld width. This is due to a decrease in heat input to the workpiece. Due to the reduced heat input, less melting of the material occurs. Due to the smaller volume of the molten pool, weld beads with reduced widths are formed. In the third step, the model is translated from no oscillation to beam oscillation condition for a varying radius of oscillation using experimental data from the literature [259] which is shown in Figure 3.6 (f). The model shows good

accuracy with an error of 4.5% thus, demonstrating that the model can be used for laser welding with and without oscillation. To analyse the effect of WPPs on the IPIs and the process capability space, the validated numerical model is solved for the butt welding of Al-5xxx with Al-6xxx as the results are based on steps 2 and 3 of the model validation. Variations of IPIs due to the variation in process parameters are studied for both no-oscillation and beam oscillation conditions.
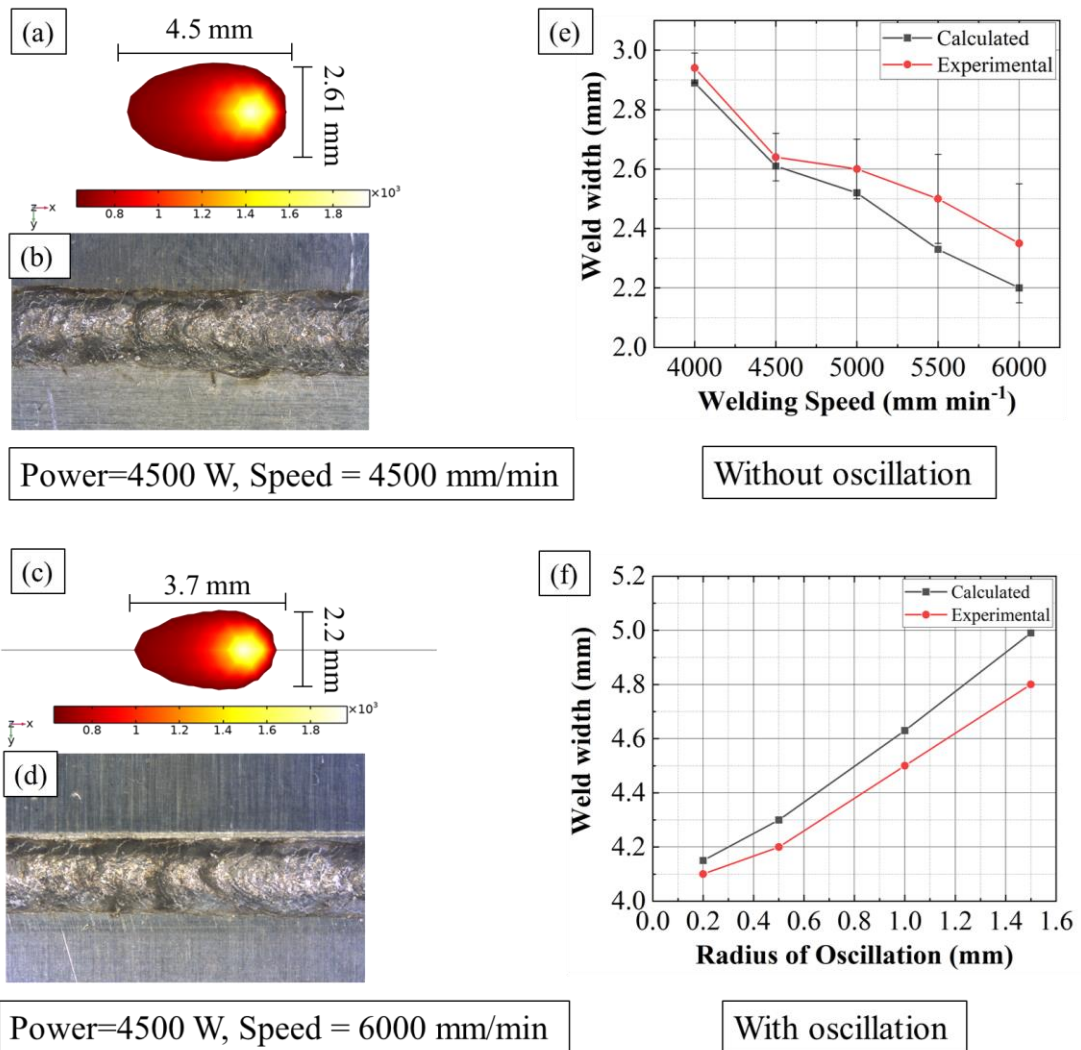
Figure 3.6 Comparison between the calculated weld morphology from the model and the experimented weld optical micrographs for Al-5xxx and Al-6xxx laser welded joint. Figure (a) shows the calculated weld width, and Figure (b) an optical micrograph at a heat source power of 4500 W and welding speed of 4500 mm/min. Figure (c) shows the calculated weld width, and Figure (d) an optical micrograph at a heat source power of 4500 W and welding speed of 6000 mm/min. Figure (e) shows the comparison between the calculated and experimented value of weld widths for varying welding speeds at a constant power of 4500 W for welding of Al-5754-6061. Figure (f) shows the comparison between the calculated and experimented value of weld widths for a varying radius of oscillation at a constant power of 3500 W, 1500 mm/min and frequency of oscillation of 100 Hz for the welding of Al-6xxx (experimental data taken from [259]). The error bar represents standard deviation, and 3 weld seams are generated for repeatability of the process.

In the final step, the numerical model is validated by comparing the shape of the fusion zone, weld width and depth of penetration with the corresponding experimental results. The process parameters combinations used for welding trials and corresponding experimental values for the weld width and weld depth calculated experimentally are given in Table 3.3. The setup number is used to refer to the process parameter combination in the rest of the thesis.

Table 3.3 Detailed welding process parameters of the setups and experimental results

Set-up	Power (kW)	Welding speed (m/min)	Amplitude (mm)	Frequency (Hz)	Weld depth (mm)	Weld width (mm)
#1	4.5	4	-	-	3.00 ± 0.00	2.85 ± 0.38
#2	5	4	0.6	200	3.00 ± 0.00	3.72 ± 0.20
#3	4.5	4	0.6	100	2.6 ± 0.64	2.91 ± 0.41
#4	4.5	4	0.6	200	2.44 ± 0.79	2.95 ± 0.22
#5	4.5	4	0.6	300	2.32 ± 0.59	3.02 ± 0.6
#6	4.5	4	0.6	400	2.16 ± 0.51	3.12 ± 0.8
#7	4.5	4	0.6	500	2.04 ± 0.50	3.17 ± 0.10
#8	4.5	5	-	-	2.16 ± 0.82	2.60 ± 0.41
#9	4.5	6	-	-	1.95 ± 1.10	2.20 ± 0.44
#10	5	5	-	-	2.05 ± 0.94	2.65 ± 0.34
#11	4	4	-	-	2.25 ± 0.84	2.65 ± 0.39
#12	4.5	4	1.2	200	1.88 ± 0.70	3.10 ± 0.29
#13	4.5	4	1.8	200	1.33 ± 0.39	3.28 ± 0.5

| #14 | 4.5 | 4 | 2.4 | 200 | 0.87 ± 0.22 | 3.65 ± 0.58 |

It is required to estimate the similarities between the different heat sources based on the heat distribution such that the most appropriate heat sources can be identified. Also, this will showcase the position of the new heat source based on different distribution functions. The volumetric heat source model is the simplified approach to model keyhole as it quantifies the heat input and distribution through the complex keyhole formation. The shape of the weld profile depends on the heat distribution along the surface and the volume of the workpiece. This heat distribution is governed by the power densities at the surface and inside the volume of the workpiece. Figure 3.7 (a) shows the variation of surface power density with volume power density for all 5 volumetric heat sources for setup #1. It also represents the shape of the weld cross-section predicted from the numerical model for all heat sources based on the temperature distribution. It was found that the heat sources for cases 2, 3 and 5 can be combined based on the similarity of the surface and volume power densities. Case 1 has the highest surface power density of all the cases which suggests that it has the highest peak temperature in all cases. Case 4 has the highest volume power density which suggests that it has the highest heated volume which can be seen from the temperature distribution for the weld profile. The heat distribution developed by case 4 is different from the rest. Figure 3.7 (b) shows the optical micrograph of the weld cross-section obtained. It is evident from Figure 3.7 (a-b) that the shape of the weld cross-section predicted in case 5 has the best agreement with the experimental observation. Figure 3.7 (c-d) summarises the weld width and depth of penetration obtained from the experiments and the numerical models for all the experimental setups performed in this work for all volumetric heat sources. The average percentage

error of different volumetric heat source models based on the weld width and depth of penetration are 6.7% (case-1), 9.2% (case-2), 9.5% (case-3), 10.1% (case-4) and 3.1% (case-5). The weld width and depth of penetration predicted in case 5 have the lowest error of 3.1% of all as shown in Figure 3.7 (c-d) for all the experimental setups performed in this work.
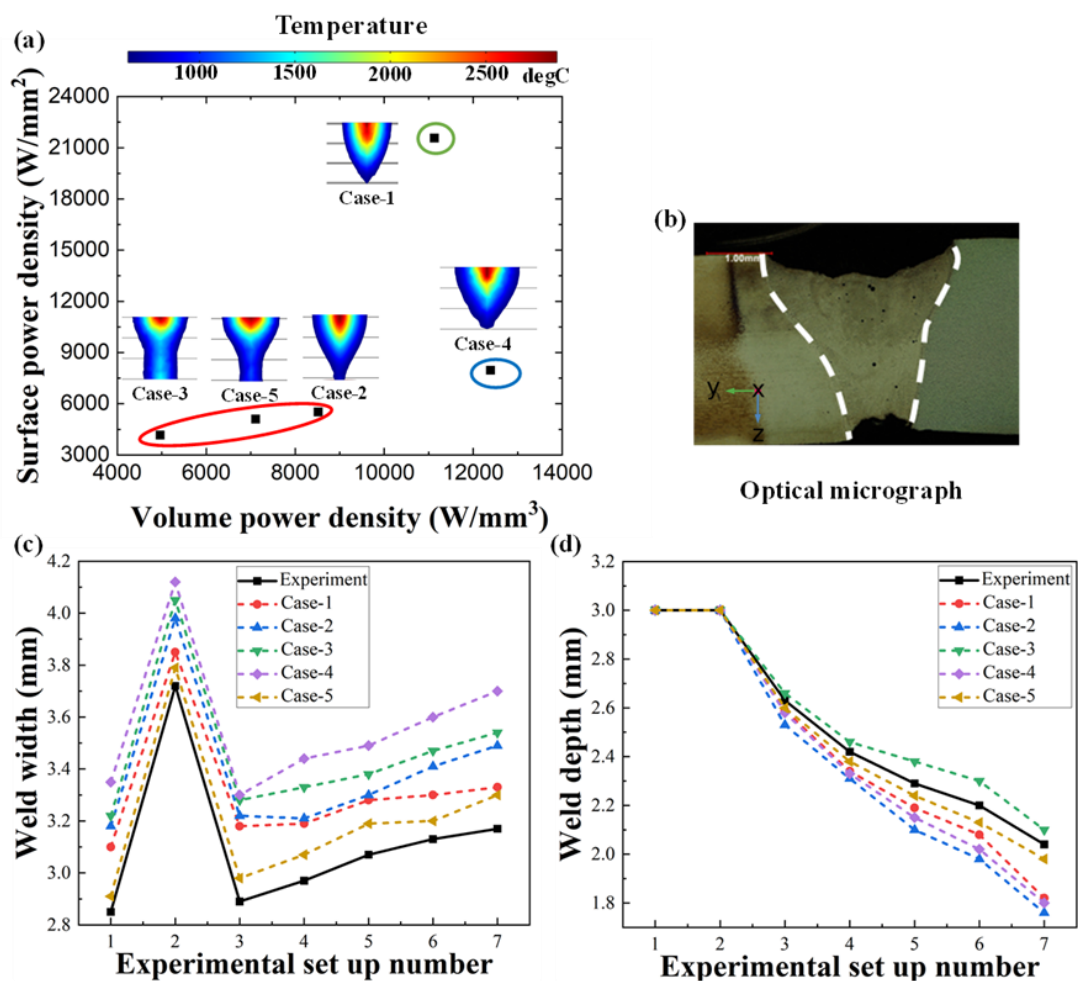
Figure 3.7 (a) Variation of surface power density with the volume power density and simulated weld cross-sections for all 5 volumetric heat sources. (b) optical micrograph of the welded region from experimental weld trails, (c) comparison between experimental and simulated weld width at the top surface and (d) depth of penetration for the different heat source models. The experimental setup is given in Table 3.3. Here, Case-1: 3D volumetric Gaussian heat source; Case-2: Hybrid 3D volumetric

Gaussian and double ellipsoid heat source; Hybrid Gaussian damped heat source and double ellipsoid heat source combined; Case-4: Rotary Gauss body heat source and Case-5: Hybrid modified Gaussian damped heat source and double ellipsoid heat source combined.

3.4.2 Characterization of peak temperature, HAZ volume and cooling rate for no oscillation condition

For the no-oscillation condition, Figure 3.8 (a) shows the simulated peak temperature contours for different combinations of laser power and welding speed. For laser welding in conduction mode, the peak temperature must remain between the melting and the boiling point of the metal. For the keyhole mode, the peak temperature must be above the boiling point of the metal being welded. In laser keyhole welding, the laser intensity is high enough to evaporate the metal which leads to the formation of a "keyhole". So, it is a reasonable assumption to make that if the temperature reaches above the boiling point, it is likely that a keyhole will form. In this study, for full penetration welding, the peak temperature at which the temperature at the bottom surface is just below the melting point leading to full penetration during welding is found to be 3500 K. The upper limit of peak temperature is 3500 K, and the lower limit is the melting point. The space above the upper peak temperature limit will lead to the cutting of the workpiece and the space below the lower limit will lead to only the heating of the workpiece without any melting.
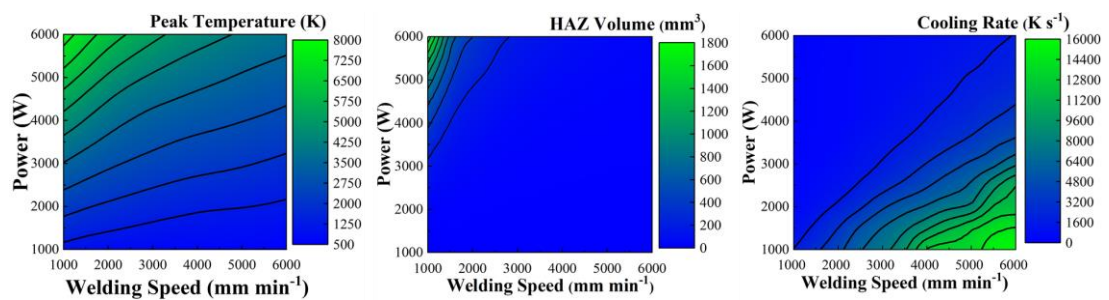
Figure 3.8 Parametric contour maps for laser power vs welding speed for no oscillation welding. Figure (a) contour maps for peak temperature, (b) contour maps for HAZ

109

volume, and (c) contour maps for cooling rate. The parametric contour maps are developed for the joining of Al-5xxx with Al-6xxx alloy system for butt welding configuration.

It was observed that with the increase in power at constant speed the peak temperature increases due to the local increase in net heat input per unit length to the workpiece defined as $(\eta P)/S$. Whereas when the welding speed is increased at constant power, the net heat input to the workpiece decreases, leading to a decrease in peak temperature. The simulated cooling rate and heat-affected zone volume profiles are shown in Figure 3.8 (b) and (c), respectively, for different combinations of heat source power and welding speed. It was observed that at constant welding speed with the increase in power HAZ volume increases due to the higher heat input to the workpiece while the cooling rate decreases. Whereas when the welding speed is increased at constant power, the HAZ volume decreases as net heat input to the workpiece decreases, causing a decrease in peak temperature which leads to an increase in cooling rate.

An important characteristic of the results in Figure 3.8 is that a particular weld attribute, such as the peak temperature or cooling rate or HAZ volume can be achieved by multiple combinations of welding process parameters. The weld thermal cycle depends on heat input and heat distribution during welding as described by Eq. 3.1. The heat input due to a laser heat source is described by Eqs. 3.4 - 3.12 which is a function of WPPs. If the quotient of process parameters is the same, then the same peak temperature can be attained. For example, from Eq. 3.4 heat input is a function of laser power and welding speed, the same peak temperature can be attained if the laser power is high at a very high welding speed and low laser power at a low welding speed. Thus, the same quotient of process parameters in both cases results in similar

heat input resulting in a similar peak temperature. The heat distribution can be described by the heat capacity and thermal conductivity of the material as described by Eq. 3.1. For the similar quotient of thermal conductivity and heat capacity, heat transport is expected to be similar. Also, for an alloy system, the same heat transport can be generated due to the similar heat capacity and thermal conductivity. This existence of multiple paths to achieve the desired weld requirements exhibits the flexibility of the laser welding process.

3.4.3 Characterization of peak temperature, HAZ volume and cooling rate for beam oscillation condition

In no oscillation welding, it was identified that laser power and welding speed are relevant, and this section focuses on the effect of radius of oscillation and frequency of oscillation because it has been established laser power and welding speed are important factors affecting the weld thermal cycle. Process variables that correspond to the shape and overlapping of the heat source are the radii of oscillation, frequency of oscillation, and welding speed. Heat input per unit length in the case of oscillating heat source is defined as $[(\eta P)/ (\sqrt{(S^2 + (2\pi Rf)^2 + (4\pi srf\sin(2\pi ft))))}]$. There are two possibilities during circular beam oscillation: (i) no overlapping of the path traversed by the oscillating heat source and, (ii) overlapping of the path traversed by the oscillating heat source as shown in Figure 3.9 . For the onset of overlapping the position of the heat source in the y-axis should be R (using the negative sign for negative y-direction) as shown in Figure 3.9 (a) and the time taken is t_1,

$$y(t_1) = -R \qquad\qquad 3.14$$

Putting Eq. 3.14 in Eq. 3.3 gives,

$$y_0 + Rsin(2\pi f t_1) = -R \qquad\qquad 3.15$$

Considering the initial position of the heat source at the origin ($y_0 = 0$) gives

$$t_1 = \frac{3}{4f} \qquad\qquad 3.16$$

Now, at the onset of overlapping the position of the heat source in the x-direction at time t_1 should be $2R$ as given in Eq. 3.17

$$x(t_1) = 2R \qquad\qquad 3.17$$

$$x_0 + St_1 - R(1 - cos(2\pi f t_1)) = 2R \qquad\qquad 3.18$$

Putting $t_1 = \frac{3}{4f}$ in Eq. 3.18

Which gives, $\qquad\qquad S = 4Rf \qquad\qquad 3.19$

Eq. 3.19 gives the condition for the onset of the overlapping. Welding speed greater than this value will have no overlapping points. The term $2\pi Rf$ denotes the circular motion of the oscillating heat source and S denotes the welding speed of the heat source in the welding direction. A higher value of ($2\pi Rf/S$) implies that the circular motion is more dominant compared to the linear forward motion of non-oscillation welding, leading to more overlapping as shown in Figure 3.9 (b) and (c). A lower value implies forward motion is dominantly leading to either no overlapping or few overlaps. The number of overlapping points is estimated graphically in terms of welding speed, the radius of oscillation and frequency of oscillation due to the complexity of equations. The graphical solution comprises plotting and counting the number of overlapping points in terms of process variables and finding the general series as given in Table 3.4 . Using the general method of induction of $S = (4/(2n+1))$

Rf and adding two more overlapping points for each cross-over. Graphical solutions yield the number of overlapping points as a function of welding speed, radius of oscillation and frequency of oscillation which is given in Table 3.4 .
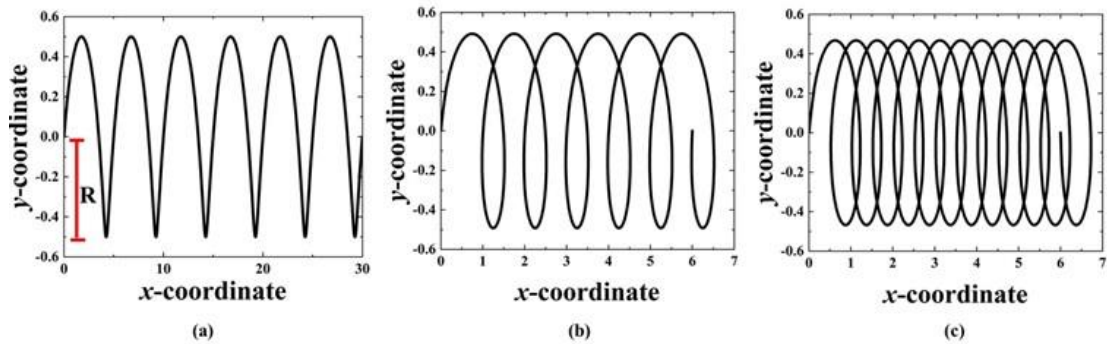
Figure 3.9 Trajectory of the oscillating laser beam for no overlap $S \geq 4Rf$ (left), overlapping at a lower frequency of oscillation when $S \leq 4Rf$ (middle); and overlapping at a high frequency of oscillation when $S \ll 4Rf$ (right).

Table 3.4 Number of overlapping points with the corresponding mathematical condition for the radius of oscillation (R), frequency of oscillation (f) and welding speed (S).

Number of overlapping points	Condition
0	$S \geq 4Rf$
2	$4Rf > S > \dfrac{4}{3}Rf$
4	$S = \dfrac{4}{3}Rf$
6	$\dfrac{4}{3}Rf > S > \dfrac{4}{5}Rf$
$4n$	$S = \dfrac{4}{2n+1}Rf$

$4n + 2$	$\dfrac{4}{2n + 1}Rf > S > \dfrac{4}{2n + 3}Rf$

3.4.3.1 Effect of frequency of oscillation

There are two opposing factors governing heat uptake during oscillating heat source: (i) decrease in heat input per unit length due to increase in effective speed $(S + 2\pi Rf)$ i.e., linear plus circumferential speed and, (ii) increase in heat input due to increase in the number of overlapping points. Figure 3.10 (a) shows the contour plot between the frequency of oscillation f, the ratio of circumferential to linear forward speed $(2\pi Rf/S)$ and the heat input per unit length considering overlapping points. The heat input per unit length (in one revolution) is given as:

$$E = \eta(T)\frac{Pn}{lf}$$

3.20

Where P is the power of the heat source, n is the number of overlapping points, l is the distance travelled by the heat source in one revolution defined in Eq. 3.21, η is the absorption coefficient of material and f is the frequency which is also equal to the time taken for one revolution to take place. This is to note that the Eq.3.20 is a representative that with the increase in the number intersection the heat input increases which is equivalent to the number of intersections. As there is not possible to have relationship mathematically due to the complexity of problem, this is used to represent as a approximation to show the hypothesis that this intersection leads to an increase in the heat input which balances the decrease in heat input as the interaction time decreases leading to a decrease in heat input due to increase in oscillation frequency.

$$l = \int_0^{1/f} \sqrt[2]{v^2 + (2\pi R f)^2 + \left(4\pi R f v \sin(2\pi f t)\right)} dt \qquad \text{3.21}$$

For a constant ($2\pi Rf/S$), heat input remains constant with the increase in f. It can be inferred from the plot that at a constant value of the ($2\pi Rf/S$), heat input remains constant with the increase in the frequency of oscillation. This illustrates that the range of frequency, welding speed and radius of oscillation investigated in this study shows that the frequency has a negligible effect on the heat uptake during welding. At a constant frequency, with an increase in the value of ($2\pi Rf/S$) heat input increases. In this case, the increase in heat input is due to the increase in overlapping points as R increases or decreases in S which leads to an increase in heat input per unit length. This explicit solution is supported by the transient heat transfer simulations as shown in Figure 3.10. Figure 3.10 (b) and (c) present the simulated peak temperature for various combinations of frequency, welding speed, and heat source power. It is apparent that the frequency of oscillation has a negligible effect on the peak temperature in both cases. This is indicated by the contour lines running parallel to the y-axis, suggesting that changes in frequency do not significantly impact the peak temperature. Similar trends are found for the cooling rate and HAZ volume. With an increase in oscillation frequency, the number of overlapping points for every rotation will increase which leads to re-heating and also the effective speed of the heat source increases as it has to rotate more times in the same amount of time. This re-heating should lead to a rise in temperature, but it is compensated by a decrease in heat energy absorbed per unit length due to the increase in the actual speed of the heat source. The increase in the actual distance travelled by the heat source with an increase in f is demonstrated in Figure 3.9.
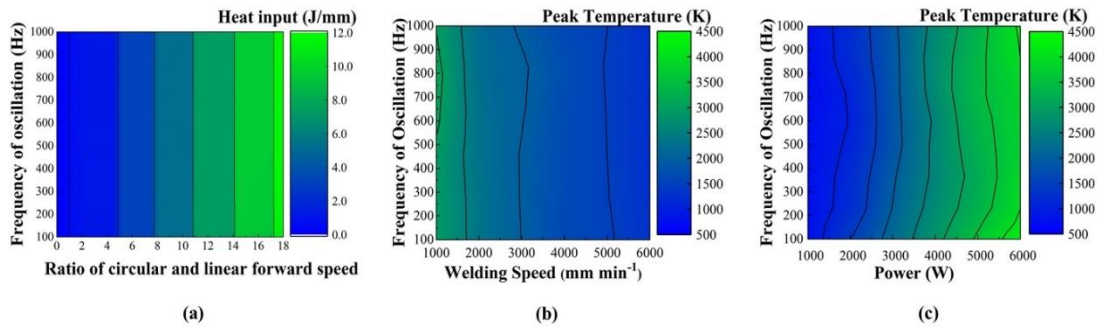
Figure 3.10 Heat input per unit length with varying frequency and ratio of circular speed and linear forward speed (welding speed) (a). Figure (b) shows the parametric contour maps for peak temperature depending on the frequency of oscillation and welding speed at a constant power of 3500 W and figure (c) shows the parametric contour maps for peak temperature depending on the frequency of oscillation and heat source power at a constant welding speed of 2500 mm/min. The oscillation radius R was kept constant at 0.3 mm. The parametric contour maps are developed for the joining of Al-5xxx with the Al-6xxx alloy system for butt welding configuration.

3.4.3.2 Effect of the radius of oscillation

To examine the effect of the radius of oscillation during laser welding, two types of parametric contour maps are generated: (i) contour maps of IPIs between the radius of oscillation and heat source power at a constant welding speed and frequency of oscillation; and (ii) contour maps of IPIs between the radius of oscillation and the welding speed at a constant heat source power and frequency of oscillation.
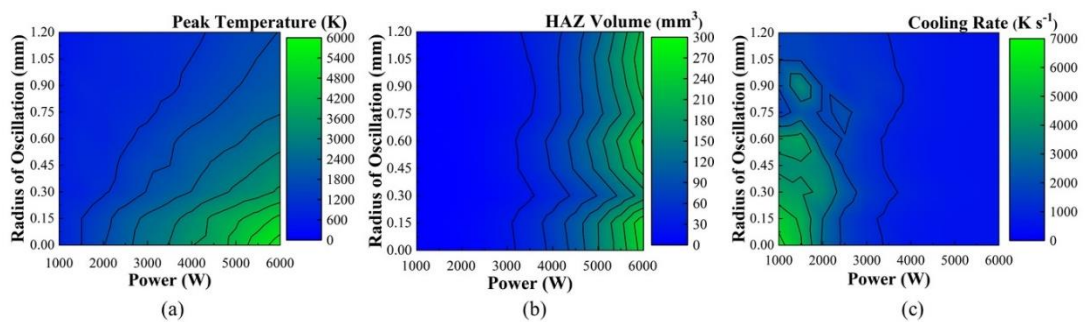
Figure 3.11 Parametric contour maps for heat source power vs radius of oscillation at a constant welding speed of 2500 mm/min, frequency of oscillation of 200 Hz, and spot radius of 0.2 mm. Figure (a) contour maps for peak temperature, (b) contour maps for HAZ volume, and (c) contour maps for cooling rate. The parametric contour maps are developed for the joining of Al-5xxx with Al-6xxx alloy system for butt welding configuration.

116

Figure 3.11 shows the simulated parametric contour maps of the peak temperature, HAZ volume and the cooling rate for different combinations of the radius of oscillation and heat source power at a constant welding speed of 2500 mm/min and frequency of 200 Hz. As shown in Figure 3.11 (a), at a constant power with an increase in the radius of oscillation, the peak temperature decreases as the effective heat source speed increases which results in a decrease in the heat input per unit length. However, for the HAZ volume, it depends on the relative length of the heat source spot radius (r), which is 0.2 mm in this study and the radius of oscillation. When $R \leq r$, the HAZ volume remains constant with the increase in R as it is equivalent to the situation with a heat source having a larger spot radius. So, an increase in the width of HAZ is compensated by the decrease in depth leading to constant HAZ volume. When $R > r$, there is a sharp decrease in HAZ volume when R is just above r which is depicted in Figure 3.11 (b) at $R = 0.3$ mm. With an increase in R, HAZ volume increases until it reaches $R = 3r$. This is due to the delay in the cooling process due to repeated heating. Though the maximum value of HAZ volume is still smaller than for $R \leq r$. When $R > 3r$, the heat input rate decreases leading to quick removal of heat which decreases the HAZ volume. So, it can be concluded that HAZ volume decreases with the application of heat source oscillation as in practical cases $R > 2r$. Similarly, the cooling rate remains constant when $R \leq r$, there is a sharp increment when $R > r$ which is shown in Figure 3.11 (c) at $R = 0.3$ mm. It again decreases with an increase in R till $R = 3r$. When R is further increased it decreases due to the decrease in heat input rate as the velocity of the heat source increases. At constant power, the lowest cooling rate is found when $R \leq r$. So, the cooling rate increases when beam oscillation is applied (as for practical cases $R > 2r$). This is due to the decrease in the peak temperature due to the application of beam oscillation which reduces the net heat content and thus requires

less time to cool the material which increases the cooling rate. In this study, the cooling rate is calculated as the difference of temperature from melting point to 470 K upon the time taken to the drop of temperature. At a constant welding speed and laser power, the heat accumulation decreases due to a decrease in heat input per unit length. This leads to a decrease in the cooling time required and hence increases the cooling rate. In some of the cases at a very large radius of oscillation, the peak temperature decreases below the melting point which leads to a decrease in temperature difference and also the cooling time which leads to a very high cooling rate. A resonance effect is found for the HAZ volume and cooling rate which is a function of oscillation radius and heat source spot size.

Figure 3.12 shows the simulated parametric contour maps of the peak temperature, HAZ volume and cooling rate for different combinations of the radius of oscillation and welding speed at a constant heat source power of 4000 W and frequency of 200 Hz. The generated parametric contour maps (Figure 3.12) show similar trends as in Figure 3.11, but the maxima and minima are exchanged from right to left as both welding speed and heat source power are related to heat uptake. An increase in heat source power is like a decrease in welding speed leading to an increase in heat input per unit length. This effect is also depicted in Figure 3.10 (b) and (c).
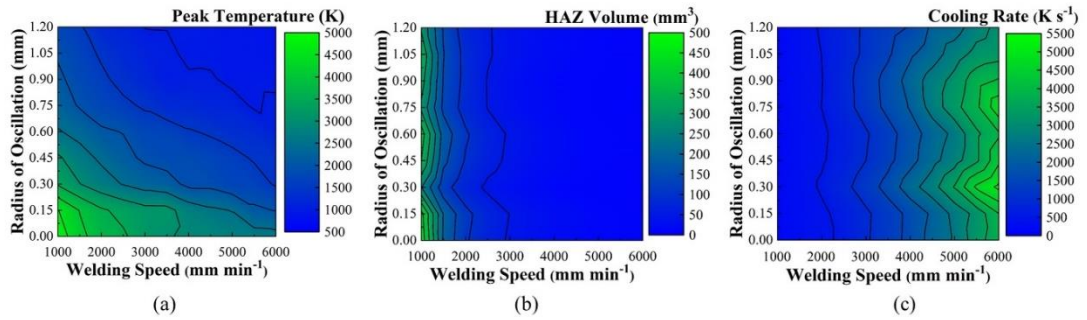
Figure 3.12 Parametric contour map for the radius of oscillation vs welding speed at a constant power of 4000 W and frequency of oscillation of 200 Hz. Figure (a) shows a contour map for peak temperature, (b) shows HAZ volume, and (c) shows for cooling rate. The parametric contour maps are developed for the joining of Al-5xxx with the Al-6xxx alloy system for butt welding configuration.

The parametric contour maps are discussed above depicts the influence of two Welding Process Parameters (WPPs) on Intermediate Performance Indicators (IPIs). However, it is challenging to visualise how the change in one parameter influence the IPIs. To facilitate a clearer visualization of how each parameter individually impacts the IPIs, a response profiler was constructed based on the data derived from FEM heat transfer simulations. Figure 3.13 presents the response profiler for IPIs under oscillation and no oscillation conditions, with central values set at Power = 3500 W, welding speed = 2000 mm/min, and R = 0 mm for no oscillation and R = 0.3 mm for beam oscillation conditions. The response profiler is developed for welding speed, laser power and radius of oscillation as frequency of oscillation have no effect on the IPIs studied as discussed in section 3.4.3.1.

As shown in Figure 3.13 (a), (b), (d), and (f), it is evident that peak temperature and Heat-Affected Zone (HAZ) volume are consistently lower when beam oscillation is applied to the same WPPs. The peak temperature diminishes nonlinearly with increasing welding speed, as indicated in Figure 3.13 (a), due to the reduced interaction time between the heat source and the workpiece. Figure 3.13 (b) reveals a linear increment in peak temperature with an increase in laser power. This is essentially due to delivering more energy per unit time to the workpiece. This increase in energy input raises the temperature of the materials being welded, causing them to reach a higher peak temperature. Figure 3.13 (c) shows the influence of radius of oscillation on the peak temperature, the peak temperature decreases with an increase

in radius of oscillation. This occurs because during oscillation welding, laser beam traverses over a larger area, reducing the heat input per unit length.

An increase in welding speed leads to a decrease in HAZ volume, as depicted in Figure 3.13 (d). When the welding speed is increased, the laser beam spends less time in contact with any spot on the workpiece. This means that the total heat input into the material is reduced because the energy from the laser beam is distributed over a smaller region. Lower heat input results in less heat being conducted into the surrounding material, leading to a smaller HAZ volume. Conversely, increasing power results in a larger HAZ volume, as demonstrated in Figure 3.13 (e), as more energy is available to melt the materials. Laser power represents the amount of energy delivered to the workpiece per unit time. An increase in the laser power leads to providing more energy to the material. This higher energy input causes a greater amount of material to be heated to elevated temperatures, contributing to a larger HAZ volume. HAZ volume, as seen in Figure 3.13 (f), displays a cyclic effect in response to changes in oscillation radius, as two opposing phenomena come into play. A larger oscillation radius distributes heat over a broader area, decreasing heat input and leading to shallower penetration, hence a decrease in HAZ volume. However, it also widens the melt pool, increasing HAZ volume.

The cooling rate is consistently higher for beam oscillation condition for varying welding speeds at a constant power, as illustrated in Figure 3.13 (g). Beam oscillation involves moving the laser beam laterally during welding, which effectively interrupts the continuous heat input to the material. The intermittent exposure to the laser beam allows the material to cool more rapidly between heating cycles. In contrast, in a no oscillation condition, the material is continuously subjected to the laser beam's energy, resulting in a more prolonged period of heating and slower cooling. Conversely, for varying power at a constant welding speed, the cooling rate under beam oscillation conditions may exhibit fluctuations, as demonstrated in Figure 3.13 (h).

Figure 3.13 (i) shows that beam oscillation induces a cyclic effect on the cooling rate with an increase in oscillation radius, with the outcome depending on various factors. Beam oscillation involves moving the laser beam laterally or in a specific pattern, which results in an intermittent or cyclical application of heat to the material. During

each oscillation, the material is heated as the laser beam is in contact, and when the beam moves away, the heat input ceases. This intermittent nature of heat input leads to variations in temperature, creating a cyclical pattern in the material's thermal history. This phenomenon is attributed to the distribution of heat over a larger area, which affects heat input and consequently influences the welding process. The intermittent nature of beam oscillation allows the material to be periodically exposed to cooling mechanisms, such as air, during the brief intervals when the laser beam is not in contact. These cooling mechanisms operate more effectively during these periods, which contributes to rapid cooling. The cyclical heating and cooling pattern can result in cyclic temperature fluctuations within the material. During the "off" phase of the oscillation, the material cools down, and during the "on" phase, it is reheated. This cyclic temperature variation is responsible for the observed cyclic effect on the cooling rate. These factors lead to a cyclic behaviour of HAZ volume and cooling rate with an increase in the radius of oscillation.
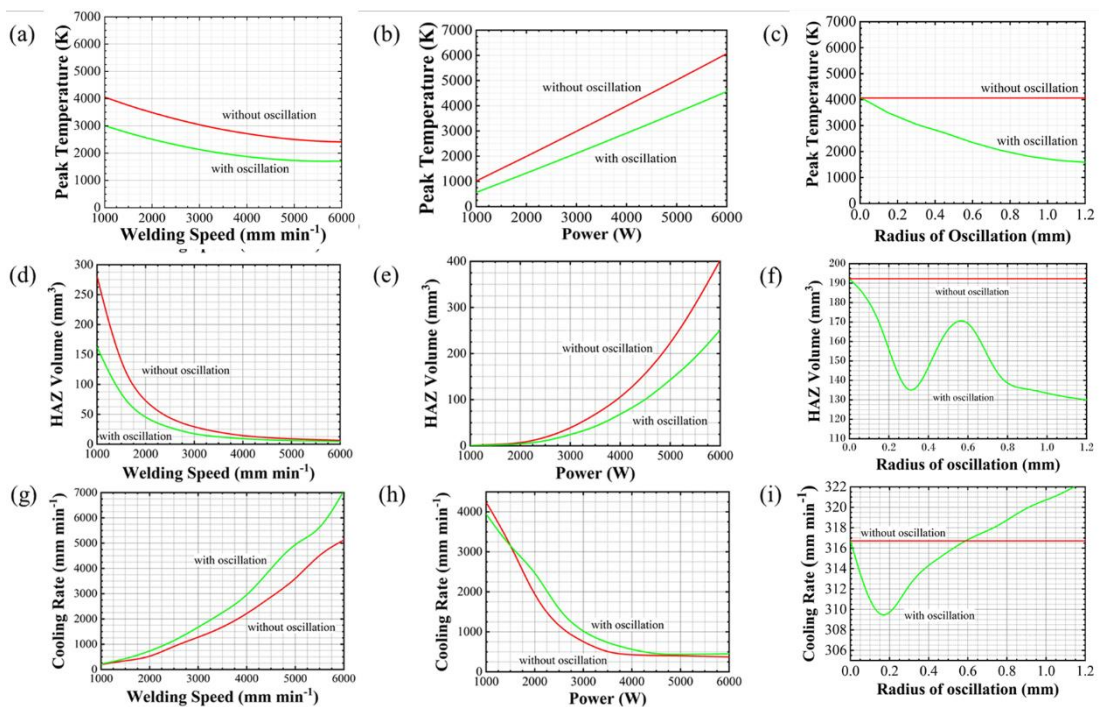
Figure 3.13 Response profiler for the peak temperature (a-c), HAZ Volume (d-f) and cooling rate (g-i) for both the no oscillation and beam oscillation conditions to depict the relationship between the welding process parameters and the thermal responses, and to depict the linear/non-linear dependency between them. The centre values are

Power = 3500W, Speed = 2000 mm/min and R = 0 for no oscillation and R=0.3 for beam oscillation condition

3.4.4 Process parameters selection using process capability space framework

3.4.4.1 Process capability space framework

The input welding process parameters (WPPs) considered in this study are welding speed (*S*), heat source power (*P*), the radius of oscillation (*R*) and frequency of oscillation (*f*). The four WPPs (*S*, *P*, *R*, *f*) are defined in Eq. 3.22, where *i* represents the index of WPP, and *n* represents the total number of WPPs.

$$WPPs = \{WPP_1, WPP_2, \dots, WPP_n\} \tag{3.22}$$

The quality performance of laser welding is governed by the IPIs and KPIs and are formulated in Eq. 3.23-3.26, where *j* represents the index of IPI and KPI, *m* represents the total number of IPIs, *l* represents the total number of KPIs and *g* represents the MIMO-model.

$$IPI = \{IPI_1, IPI_2, \dots, IPI_m\} \tag{3.23}$$

$$KPI = \{KPI_1, KPI_2, \dots, KPI_l\} \tag{3.24}$$

$$IPI_j = g(WPP_1, WPP_2, WPP_3, \dots, WPP_n) \tag{3.25}$$

$$KPI_j = g(WPP_1, WPP_2, WPP_3, \dots, WPP_n) \tag{3.26}$$

The upper limits (*UL*) and lower limits (*LL*) of WPPs have been determined by considering technological constraints based on the physical experimental studies present in the literature. The combination of all possible WPPs within the permitted limits defines the parameters space (ω_0). The parameters space is represented in the form of parametric contour maps where the *x* and *y*-axis show the variation of two different WPPs and the coloured contour surface shows the derived values of IPIs and KPIs. If the estimated IPI or KPI violates the allowance limits, WPPs are considered

unfeasible. For the jth IPI and KPI, process capability space is defined as expressed in Eq. 3.27-3.28, where k is the index of the individual C_p-Space and m is the total number of IPIs and l is the total number of KPIs

$$\alpha_j = \{\ IPI_j \qquad if\ IPI_j^{LL} \leq\ f(WPP_1,\ldots.,WPP_n)\ \leq\ IPI_j^{UL} \qquad\qquad 3.27$$

$$\beta_j = \{\ KPI_j \qquad if\ KPI_j^{LL} \leq\ f(WPP_1,\ldots.,WPP_n)\ \leq\ KPI_j^{UL} \qquad\qquad 3.28$$

The definition of process capability space from the parameters space is demonstrated for no oscillation welding based on the weld thermal cycle calculated in Section 3.2-3.4. Three IPIs derived from the 3D transient temperature distribution calculated using the heat transfer model are (*i*) peak temperature (T_{peak}), (*ii*) heat-affected zone volume (V_{HAZ}) and (*iii*) cooling rate (C_{rate}). The upper and lower limits of the WPPs and IPIs are given in Table 3.5 and Table 3.6 respectively. The upper limit of the T_{peak} (T_{peak}^{UL}) is 3500 K as at this temperature, the temperature at the bottom surface is at the melting point of the material which shows that it is full penetration welding. The lower limit of the T_{peak} (T_{peak}^{LL}) is the melting point of the material. As different combinations of process parameters yield the same T_{peak} but have different C_{rate} and V_{HAZ}. To select the lower and upper limits of the C_{rate}, the C_{rate} is maximised for those combinations which yield the T_{peak}^{LL} and T_{peak}^{UL} respectively. So, the maximum value of C_{rate} at the T_{peak}^{LL} is the lower limit of cooling rate (C_{rate}^{LL}). Similarly, for the upper limit of cooling rate (C_{rate}^{UL}) maximum value of C_{rate} is selected at T_{peak}^{UL} This is because a higher cooling rate promotes fine grain formation. In the case of selecting lower and upper limits of V_{HAZ}, the minimum value of V_{HAZ} is selected for the combinations which provide T_{peak}^{LL} and T_{peak}^{UL} respectively. So, the minimum value of V_{HAZ} at the T_{peak}^{LL} is the lower limit of cooling rate (V_{HAZ}^{LL}) and similarly for the upper limit of V_{HAZ} (V_{HAZ}^{UL}). This is because V_{HAZ} should be minimum for better welded joint performance.

Table 3.5 Welding process parameters and their allowance limits for defining parameter space.

Welding Process Parameters (WPPs)	WPP^{LL}	WPP^{UL}
Speed S (mm min^{-1})	1000	6000
Power P (W)	1000	6000
Radius of oscillation R (mm)	0	1.2
Frequency f (Hz)	0	1000

Table 3.6 IPIs and their allowance limits for defining C$_p$-Space.

Intermediate Performance Indicators (IPIs)	IPI^{LL}	IPI^{UL}
Peak temperature T_{peak} (K)	933	3500
Cooling rate C_{rate} (K min^{-1})	Maximum C_{rate} at LL of T_{peak}	Maximum C_{rate} at UL of T_{peak}
Heat-affected zone volume V_{HAZ} (mm^3)	Minimum V_{HAZ} at LL of T_{peak}	Minimum V_{HAZ} at UL of T_{peak}
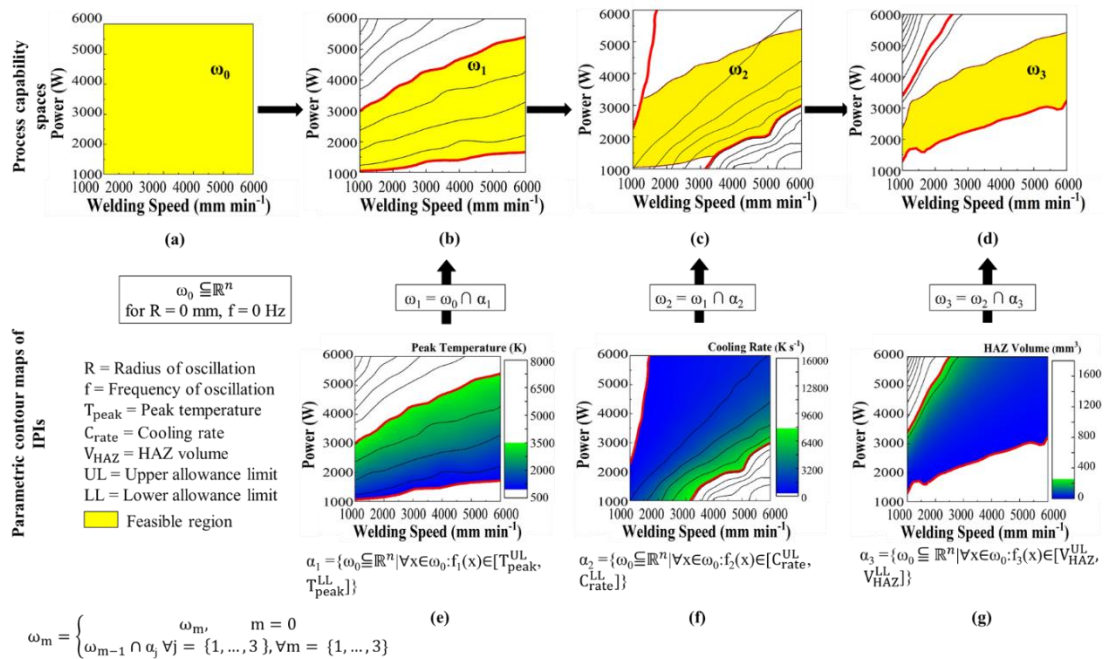
Figure 3.14 Process capability space (C$_p$-Space) for no oscillation condition (where R = 0 mm and f = 0 Hz). The top row shows the process capability spaces (at each step with an intersection with IPIs) and the bottom row shows the parametric contour maps of each IPIs with the allowance limit.

Figure 3.14 demonstrates the definition of the final process capability space from the parameters space (Figure 3.14 (a)) based on the intersection of the individual process capability space of each IPIs. The shaded area in yellow represents the feasible region and any process parameters inside this region satisfy all the requirements. The final process capability space (ω_m) is the intersection of process capability space of individual IPI (α_j) and (ω_{j-1}) as defined in Eq. 3.29-3.30 and illustrated in Figure 3.14, where the final image in the upper row (Figure 3.14 (d)) is the intersection of all individual process capability spaces (ω_j) based on the allowable limits of all the IPIs.

$$\omega_j \ = \ \omega_{j-1} \bigcap \alpha_j \tag{3.29}$$

$$\omega_m \ = \ \omega_{m-1} \bigcap_{j=1}^{m} \alpha_j \tag{3.30}$$

The final process capability space ω_m envelops all the feasible WPPs values inside the parameters space ω_0. The parameters space is limited by the technical feasibility of the process and therefore by the upper and lower limits of the WPPs. Similarly, if the requirements have multiple IPIs and KPIs, the final process capability space (ω_{m+l}) will be the intersection of the process capability space of individual IPI (α_j), KPI (β_j) and (ω_{j-1}) and the modified equation is given below:

$$\omega_{m+l} \ = \ \omega_{m-1} \bigcap_{j=1}^{m} \alpha_j \bigcap_{k=1}^{l} \beta_k \tag{3.31}$$

The process capability space shows the feasible space for the two WPPs at a time for any number of IPIs and KPIs. If the third WPP is added to the system giving a 3D process capability space, where x, y, and z axes are the three WPPs. The visualisation

of 3D process capability space is limited by the visibility of the plot. This can be improved by stacking up 2D contour plots in the *xy* plane with a constant value for the third process parameter. This represents the influence of the third process parameter on the process capability space. An increase in process capability space suggests that the process parameter provides more flexibility to the whole process and a decrease in the process capability space suggests that the process parameter makes the whole process more constrained. For example, three WPPs considered in this illustration are welding speed, laser power and radius of oscillation for laser butt welding based on the heat transfer model. The generated stack-up of contour maps to represent 3D process capability space is shown in Figure 3.16. From Figure 3.15 shows the process capability space for three process parameters to show the 3D response surface as a stacked-up 2D contour map. The *z-axis* for the 3D response surface is the radius of oscillation which is varied at (a) $R = 0$ mm, (b) $R = 0.15$ mm, (c) $R = 0.30$ mm, (d) $R = 0.45$ mm, (e) $R = 0.60$ mm and (f) $R = 0.75$ mm in the 2D contour maps at a constant frequency of 300 Hz., the size of the process capability space increases and is applicable for broader process parameter ranges with an increasing radius of oscillation. This demonstrates the increase in flexibility of the laser welding process due to the application of beam oscillation. The upper limit of the allowed peak temperature ceases to exist at the highest radius of oscillation as shown in Figure 10(f). For the same combination of welding speed and heat source power, the peak temperature decreases though the net heat input to the workpiece is the same when compared to the non-oscillating heat source. To attain the same peak temperature, an oscillating heat source requires more heat input as compared to a non-oscillating condition which is shown in Figure 3.16 (a) and (b).
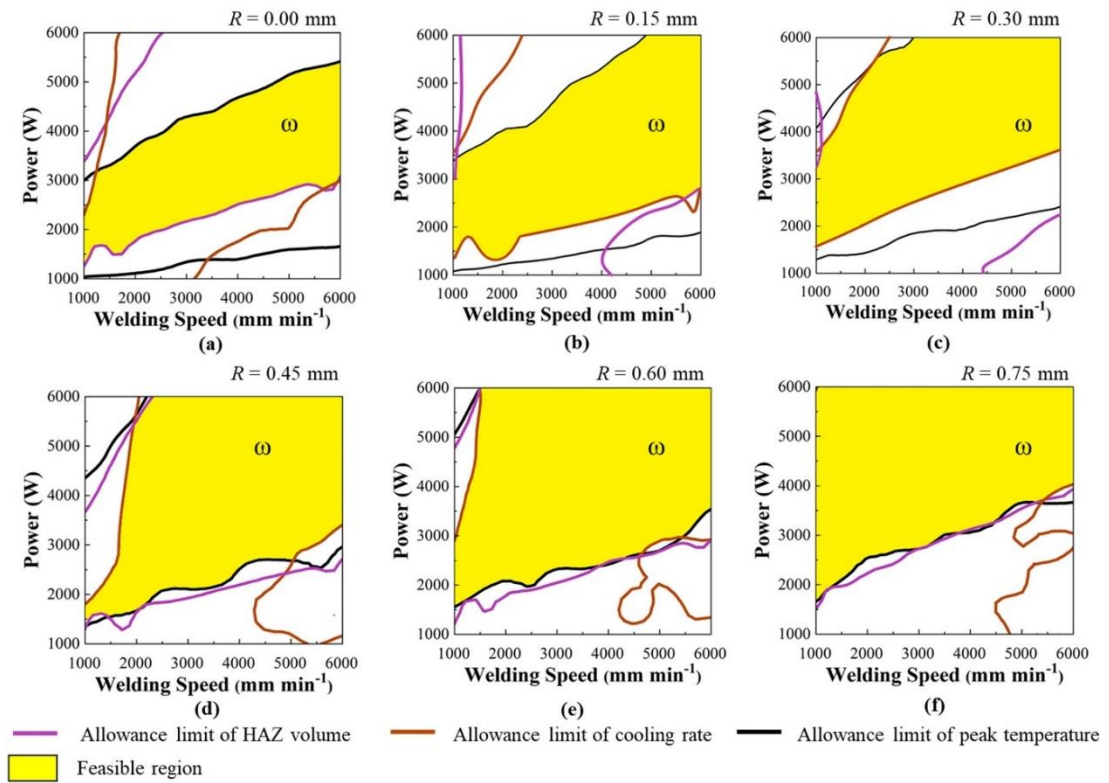
Figure 3.15 shows the process capability space for three process parameters to show the 3D response surface as a stacked-up 2D contour map. The *z*-axis for the 3D response surface is the radius of oscillation which is varied at (a) $R = 0$ mm, (b) $R = 0.15$ mm, (c) $R = 0.30$ mm, (d) $R = 0.45$ mm, (e) $R = 0.60$ mm and (f) $R = 0.75$ mm in the 2D contour maps at a constant frequency of 300 Hz.

3.4.4.2 Process capability space refinement strategies

The next objective of this study is the refinement of Process capability space (C_p-Space) depending on the requirements of the downstream processes to further reduce the number of welding trials during the early design phase. It is important to note down that the methodology for process parameters refinement provided in this study is for the early design phase and process assessment. The process parameters refinement is performed on the ω_m. In this work, sequential refinement strategies are developed based on three requirements of welding manufacturers which are defined as boundary constraints. The first constraint set is related to the IPIs and KPIs constraints which address the proper coalescence of metals produced by heating to a suitable temperature

127

such that enough molten metal is formed to have proper fusion. This is assessed by the IPIs and KPIs such as temperature profile, fusion zone dimension, fusion zone shape and mode of welding. The second requirements set is related to the overall design objective function which addresses the functional and strength requirements to control weld defects and strength of the weld. This is depending upon HAZ volume and cooling rate. The third constraint set is related to being able to address the key application requirements such as high production rate, low cost, and/or additional welding requirements, i.e., aesthetic requirements of welded joints. This includes the weld process parameters like higher welding speed (ensure high productivity), lower laser power (low operational cost), and single or multi-pass weld (operational cost and productivity). Sequential refinement strategies for a few of the downstream processes based on the heat transfer model are given in Table 3.7 in order of their hierarchy. This table is to illustrate the process capability space refinement strategies. Welding can be considered as a combination of two processes: the first one is the melting and evaporation of the workpiece to have a fusion and the other is the heat treatment of the workpiece. Both processes are governed by the transport phenomena during welding. Proper control over them can improve weld properties and reduce weld defects.

Table 3.7 Proposed multiple strategies for process capability space (C_P-Space) refinement for various downstream processes and requirements.

Target downstream processes requirements	IPIs constraints	Objective function	Welding Process parameters (WPPs) constraints	Remarks
Improving mechanical properties	$T_{peak}^{UL} \geq T_{peak} \geq T_{peak}^{LL}$	min (V_{HAZ}), max (C_{rate})	$WPP_i^{LL} \leq WPP_i \leq WPP_i^{UL}$ $\forall i = \{1,\dots,N_i\}$ max(S), min(P), R > 0	Fine grains formation, uniformly dispersed dendrites (when $R>0$)
Reducing segregation and intermetallics formation	$T_{peak}^{UL} \geq T_{peak} \geq T_{peak}^{LL}$	max (C_{rate}), min (V_{HAZ}) Stirring using beam oscillation	$WPP_i^{LL} \leq WPP_i \leq WPP_i^{UL}$ $\forall i = \{1,\dots,N_i\}$ max(S), min(P) $R > 0$	Reduces diffusion and improves mixing
Reducing Porosity	$T_{peak}^{UL} \geq T_{peak} \geq T_{peak}^{LL}$	Stirring using beam oscillation max (C_{rate}), min (V_{HAZ})	$R > 0$ $WPP_i^{LL} \leq WPP_i \leq WPP_i^{UL}$ $\forall i = \{1,\dots,N_i\}$ max(S), min(P)	Mechanical stirring by beam oscillation helps in escaping trapped gasses reducing porosity
Partial penetration	$T_{peak}^{UL} \geq T_{peak} \geq T_{bp}$	min (V_{HAZ}), max (C_{rate})	$WPP_i^{LL} \leq WPP_i \leq WPP_i^{UL}$ $\forall i = \{1,\dots,N_i\}$ max(S), min(P)	Partial penetration requires peak temperature above the melting point and lower than full penetration welding

Process capability space refinement is illustrated by using the example of improving mechanical properties for full penetration welding in keyhole mode. In this example, the final process capability space is chosen for no oscillation condition which is illustrated in Figure 3.16 (a). The region above the feasible region (marked in

yellow) corresponds to the cutting or over-weld region. The region below the yellow-coloured region depicts the under-weld region where due to insufficient penetration leads to a poor coalition of the materials. The region at the bottom is no welding region/ preheating as the peak temperature is below the melting point of the material. The first step for process capability space refinement is to select the proper peak temperature thus satisfying IPIs constraints as given in Table 3.7. The peak temperature should be between the boiling point of the metal and 3500 K for the keyhole mode of welding as shown by the yellow-coloured region in Figure 3.16 (b). The region just below the yellow-coloured region (in between the red and black lines) represents the region of the conduction mode of welding. In the second step, the WPPs combinations are narrowed down based on the objective functions (Table 3.7) which are minimising HAZ volume and maximising cooling rate. The narrowed down process capability space based on the objective function is shown in Figure 3.16 (c). In the final step, those WPPs combinations are selected from the refined space which has faster welding speed and lower heat source power (WPPs constraints as given in Table 3.7). For a special case of full penetration keyhole welding, the peak temperature should be 3500 K, so the refined process capability space will be just a line as shown in Figure 3.16 (d). Therefore, the final refined process capability space has full penetration welding with the lowest HAZ volume, highest cooling rate, highest welding speed, and lowest power. The robust process parameters can be selected from the refined process capability space having estimates about the quality of the weld from the IPIs without prior experimental characterization and mechanical testing. This approach reduces the number of experiments required.

Final process capability space for welding

Process capability space refinement based on IPIs constraints

Process capability space refinement based on objective function

Final refined process capability space for full penetration welding

$\omega_4 = \omega_3 \cap \alpha_4$

$\omega_6 = \omega_5 \cap \alpha_6$ where, $\omega_5 = \omega_4 \cap \alpha_5$

$\omega_7 = \omega_6 \cap \alpha_7$

T_{peak} = Peak temperature
T_{bp} = Temperature at boiling point
T_{3500} = Peak temperature of 3500 K
C_{rate} = Cooling rate
V_{HAZ} = HAZ volume
UL = Upper allowance limit
LL = Lower allowance limit
ω_m = Process capability spaces

$\alpha_4 = \{\omega_0 \subseteq \mathbb{R}^n | \forall x \in \omega_0 : f_1(x) \in [T_{peak}^{UL}, T_{bp}]\}$

$\alpha_5 = \{\omega_0 \subseteq \mathbb{R}^n | \forall x \in \omega_0 : f_2(x) \in [C_{rate}^{UL}, C_{rate}^{LL}]\}$

$\alpha_6 = \{\omega_0 \subseteq \mathbb{R}^n | \forall x \in \omega_0 : f_3(x) \in [V_{HAZ}^{UL}, V_{HAZ}^{LL}]\}$

$\alpha_7 = \{\omega_0 \subseteq \mathbb{R}^n | \forall x \in \omega_0 : f_2(x) = T_{3500}\}$

— Allowance limit of previous step

— Allowance limit of minimum HAZ volume

— Allowance limit of maximum cooling rate

Feasible region

$\omega_m = \omega_{m-1} \cap \alpha_j \forall j = \{4, \dots, 7\}, \forall m = \{4, \dots, 7\}$

Figure 3.16 (a) Final process capability space for welding having cutting/over-welding region, welding region, under-welding region and no-welding/pre-heating region (b) Process capability space refinement based on IPIs constraints i.e. 3500 K ≥ *Tpeak* > *T_bp* having cutting/over-welding region, keyhole mode welding region, conduction mode welding region and under-welding region; (c) Process capability space refinement based on the objective functions i.e. minimising HAZ volume and maximising cooling rate and (d) Final refined process capability space for full penetration welding. The temperature of 3500 K shows the estimated peak temperature for full penetration welding.

3.5 Conclusions

This chapter presents a novel methodology for the process capability space refinement for the laser welding process with and without beam oscillation. During this research, a FEM-based heat transfer model has been developed to simulate the intermediate performance indicators (IPIs) peak temperature, heat affected zone volume and cooling rate. The process capability space has been depicted by using parametric contour maps. The main conclusions are as follows:

− There is a good agreement between the FEM model and the experiments both in terms of the transient temperature profile and the weld width calculated on the top

surface (a key performance indicator). The model is validated for both no oscillation conditions (having a highest error of -6% which means underestimating the experimental value) and for beam oscillation (having a maximum error of 4.5% which means overestimating the experimental value). The effect of convection should be more dominant in the case of beam oscillation; therefore, it overestimates the experimental results as compared to the no oscillation condition.

− At a radius of oscillation greater than 0.65 mm, the peak temperature drops below the threshold for full penetration welding. This shows that the radius of oscillation can be increased up to a critical limit, depending upon the peak temperature to achieve full penetration welding.

− The application of beam oscillation leads to a decrease in the peak temperature and HAZ volume for the same net heat input to the workpiece due to the decrease in heat input per unit length.

− The cooling rate and HAZ volume vary cyclically with the change in the radius of oscillation and depend upon the ratio of the radius of oscillation (R) and heat source spot radius (r). For the practical range of use of beam oscillation (where $R/r > 2$) HAZ volume decreases and cooling rate increases.

− The area of the final process capability space increases with the application of beam oscillation. This increase in area exhibits the increase in flexibilities due to the application of beam oscillation as the process will be more robust due to larger acceptable regions and smaller fall out areas.

Chapter 4. Numerical simulation of fluid flow behaviour and effect of beam oscillation on the solidification parameters and grain morphology in remote laser welding of high strength aluminium alloys[2]

4.1 Introduction

This chapter proposes the effect of process parameters on the fluid flow which affects the weld pool morphology and solidification characteristics. The previous studies have suggested that the fusion zone geometry (i.e., weld depth, weld width, overall weld shape) in conjunction with microstructural weld attributes (i.e., cooling rate, thermal gradient) governs the weld quality and properties [128,158,261]. Fusion zone geometry and solidification behaviour are determined by the history of temperature distribution and the history of melt pool development. These characteristics have an important causal relationship with transport phenomena (heat transfer and fluid flow) during welding [239,262,263]. Numerical simulations of transport phenomena during laser welding can be used to calculate the weld thermal cycle, flow profile, weld pool geometry and solidification behaviour [264,265]. These numerical calculations have enabled us to gain detailed insights into the physical processes that occur in a weld

---

pool to assess and improve the laser welding process. A thorough understanding of the geometrical weld parameters and molten pool behaviour is critical to use beam oscillation for improving the performance of the welded joints with fewer defects. Several models have been proposed to develop the relationship between heat transfer, fluid flow and the weld profile [264–266]. AlMg-Si are well known for their susceptibility to hot cracking and solidification behaviour and grain morphology has a major influence on the hot cracking susceptibility [22–25]. Equiaxed grains have less susceptibility to hot cracking as compared to the oriented grain like columnar grains due to an increase in grain boundaries as it leads to the distribution of thermomechanical loads across the increased grain boundaries. So, understanding the effect of process parameters on the solidification behaviour and grain morphology of the weld is important. The effect of various process parameters on the weld thermal cycle via parametric contour maps has been discussed in chapter 3 where the relationships are solely based on the effect of temperature as no convection is considered.

In this chapter, circular and sinusoidal beam oscillation pattern has been investigated. A base model has been developed to analyse the effect of circular beam oscillation on the fluid flow during the RLW process. The influence of beam oscillation, however, is important and can be understood when the heat input per unit length is kept constant for each oscillation frequency. A change in heat input would alter the thermal as well as flow behaviour, which makes it difficult to understand the effect of beam oscillation in its entirety. A three-dimensional heat transfer and fluid flow model is developed for Al-5xxx to investigate temperature distributions and fluid flow behaviour during laser butt welding with and without beam oscillation. This study will investigate the effect

of beam oscillation on the thermal and fluid flow regimes considering the effects of natural convection, gravity, surface tension and forced convection. The developed model is validated using experimental results, reported in the literature based on the weld pool morphologies [267]. The reliability of the developed model is analysed, based on the dimensionless numbers for flow and heat transport. These numbers also provide information to analyse the effect of driving forces such as surface tension and buoyancy force during laser welding.

In the next step, the developed model is translated to investigate the sinusoidal beam oscillation pattern. The different combinations of the hybrid heat source models have been simulated and modified to best predict the fusion zone shape and dimensions. The effect of process parameters on the weld profile, fluid flow profile, vorticity profile, solidification behaviour, grain morphology and mechanical strength is developed. The developed model is validated with the corresponding experimental measurements using weld profile from the optical micrographs, and weld pool top surface morphology from the high-speed camera. All the studies related to investigating the effect of process parameters on the weld profile, solidification behaviour, grain morphology and mechanical strength are performed for sinusoidal and no oscillation conditions due to the constraints of the available experimental setup of RLW to carry out the study. New KPIs/IPIs are defined based on the heat transfer and fluid flow model based on the sequential modelling approach to refine the process capability space defined in this chapter to survey the parameters space for the selection of robust process parameters.

4.2 Effect of circular beam oscillation on fluid flow

4.2.1 Modelling strategy

4.2.1.1 Assumptions

A three-dimensional heat transfer and fluid flow model has been developed using a hybrid volumetric heat source. A three-dimensional Cartesian coordinate system is used where the positive x-axis direction is the welding direction, the y-axis is the weld cross-section direction and the z-axis is the weld penetration direction. The motion of the heat source during beam oscillation is composed of two parts in the x-y plane, one is a circular motion and the other is a linear forward motion in the welding direction. The overall trajectory of the heat source is typically a spiral. The following assumptions were made during the development of the numerical model: (a) the fluid is considered incompressible and the flow is laminar (as the typical range of Reynolds Number is 300-400 in this study); (b) to decrease the computational time, the model was simplified and keyhole dynamics are not considered but instead a volumetric heat source model is used to replicate the keyhole which is a common practice as described in [268]; (c) no vapour and plasma flow is simulated in the model; (d) the effect of shielding gas on the heat transfer and fluid flow is ignored, and (e) the laser beam is assumed perpendicular to the surface of the workpiece.

4.2.1.2 Governing Equations for fluid flow and boundary conditions

A three-dimensional model based on the finite element method (FEM), was developed using COMSOL Multiphysics. To determine velocity fields, a transient fluid flow

model was developed based on the solution of the equations of conservation of mass and momentum as given in Eq. (4.1-4.2) [267].

$$\nabla.(u) = 0 \qquad\qquad 4.1$$

$$\rho\frac{\partial(u)}{\partial t} = -\rho\nabla.(uu) - \nabla P + \nabla.\eta(\nabla u) + F \qquad\qquad 4.2$$

where u is the velocity vector, ρ is the fluid density P is the static pressure, η is the dynamic viscosity of the fluid and F is the force term which is defined in Eq. 4.3. The first term in Eq. 4.3 is according to the Carman-Kozeny equation for flow through a porous media [239] representing the frictional dissipation which ensures a smooth transition of velocity from zero to a large value in the mushy zone. The second term on the right-hand side of Eq. 4.3 accounts for natural convection.

$$F = C\left(-\frac{(1-f_l)^2}{f_l^3 + B}\right)u + \rho g\beta(T - T_{melting}) \qquad\qquad 4.3$$

where B is a merely computational constant, a very small positive number to avoid division by zero is set at 0.001 and C is a mushy zone constant related to the morphology of the porous media which is a large number (a value of 1.6×10^4 was used in the present study) to force velocity of the solid zone to be zero and represents mushy zone morphology, β is the coefficient of volume expansion, g is the acceleration due to gravity, $T_{melting}$ is the melting temperature which is average of solidus and liquidus temperature and f_l is the fraction of liquid which is defined in Eq. 2.20. Flow condition for the free liquid surface due to the surface tension gradient is given by Eq. 2.21 which states that the temperature gradient is proportional to shear stress on the surface.

4.2.1.3 Governing equations for heat transfer and boundary conditions

To determine temperature fields, a transient heat transfer model was developed based on the solution of the equation of conservation of energy formulated as [267].

$$\rho C_P \frac{\partial T}{\partial t} + \underbrace{\rho C_P u . \nabla T}_{\text{heat transfer by convection}} = \nabla . (\lambda \nabla T) + Q_{laser} + Q_{vap} \qquad 4.4$$

where C_P is the specific heat capacity of the material, T is the temperature of the workpiece, t is the time, λ is the thermal conductivity of the material, Q_{laser} is the energy input of the laser heat source per unit volume and Q_{vap} is the energy loss by evaporation. The second term on the left-hand side (underlined) of Eq. 4.4 is the convection term which represents the energy change due to the flow of fluid which is added as a term compared to energy conservation Eq. 3.1 defined in Chapter 3 section 3.2.3. The phase changes are considered to include temperature change due to latent heat by using the apparent heat capacity method as shown in Eq. 3.2 in section 3.2.3. A three-dimensional volumetric heat source with origin (x_0, y_0, z_0) is defined by a Gaussian distribution as given in section 3.2.4. The initial temperature of the workpiece is assumed to be maintained at room temperature (T_0). At the top surface, the heat loss due to convection, radiation and evaporation is governed by Newton's law of cooling and Stefan-Boltzman as follows in Eq. 2.15-2.16

4.2.1.4 The relative importance of driving forces from dimensionless numbers

The relative importance of heat transfer by conduction and convection in the weld pool is estimated using the Peclet number, *Pe*, which is defined as [267].

$$Pe = \frac{u \rho C_p L_R}{\lambda} \qquad 4.5$$

Where u is the characteristic fluid velocity, L_R is the characteristic length taken as the pool radius at the top surface. When $Pe < 1$, the heat transfer in the molten weld pool is primarily by conduction and $Pe > 1$, the primary mechanism of heat transfer is convection. The relative importance of driving forces for fluid flow in the liquid melt pool formed is estimated using the Marangoni number, Ma, and the Grashof number, Gr. Gr is the ratio of buoyancy force to viscous force while Ma is the ratio of surface tension gradient force to viscous force. The relative significance of the primary driving forces during fluid flow can be determined by the ratio of these dimensionless numbers as given in Eq. 4.6 [269]

$$R_{s/b} = \frac{Ma}{Gr} = \frac{L_R \left|\frac{d\gamma}{dT}\right|}{g\rho\beta L_b^3} \qquad 4.6$$

where L_b is the characteristic length taken as one-eighth of the weld pool radius for buoyancy. The numerical implementation of the numerical model in COMSOL Multiphysics 5.6 is discussed in section 3.2.5.

4.2.2 Results and discussions

4.2.2.1 Materials and Geometry

A 3D cartesian coordinate system was adopted for the welding Al-5xxx alloy in the butt-welding configuration. The thermo-physical of the Aluminium alloy is reported in Table 4.1. The size of the entire simulation domain for a single plate is 50 mm × 25 mm × 2 mm and was divided into three sections with dimensions 50 mm × 22 mm × 2 mm, 50 mm × 2 mm × 2 mm and 50 mm × 1 mm × 2 mm for better mesh distribution near the weld centreline as shown in Figure 4.1 (a) Schematic illustrations of finite element mesh size and mesh distribution were used for the simulations of a laser

welding process The mesh size and distribution are modified from the previous chapter to have better resolution of fluid flow as fluid flow requires a finer mesh size as compared to the heat transfer model. The modified mesh distribution is shown in Figure 4.1 (a) Schematic illustrations of finite element mesh size and mesh distribution were used for the simulations of a laser welding process Tetragonal mesh is used with a minimum mesh size of 0.1 mm, having a total number of 350639 mesh elements. The mesh sensitivity analysis was performed for both the temperature and fluid flow field over the global domain. The time step is selected based on the frequency of oscillation such that it can map the effect of frequency on both temperature and fluid flow field. The time step used in this study $1/(4f)$ to have at least 4-time instants in each revolution of the oscillation. Compiled user-defined functions were introduced for the calculation of the position of the heat source at a given time as a function of welding speed, beam oscillation parameters (amplitude and frequency) and the volumetric Gaussian heat source.

Table 4.1 Thermo-physical properties of Aluminium 5xxx alloy used.

Physical properties	Value
Density of liquid	2380 kg/m^3
Density of solid	2660 kg/m^3
Viscosity	1.2×10^{-3} kg/m s
Heat capacity of solid phase	1150 J/kg K
Heat capacity of liquid phase	1198 J/kg K
Thermal conductivity of solid phase	120 W/m K
Thermal conductivity of liquid phase	90 W/m K
Solidus temperature	864 K
Liquidus temperature	911 K
Heat transfer coefficient	20 W/ m^2 K
Emissivity of the metal	0.3
Surface tension	0.871 N/m
Surface tension gradient	-0.155×10^{-3} N/m K
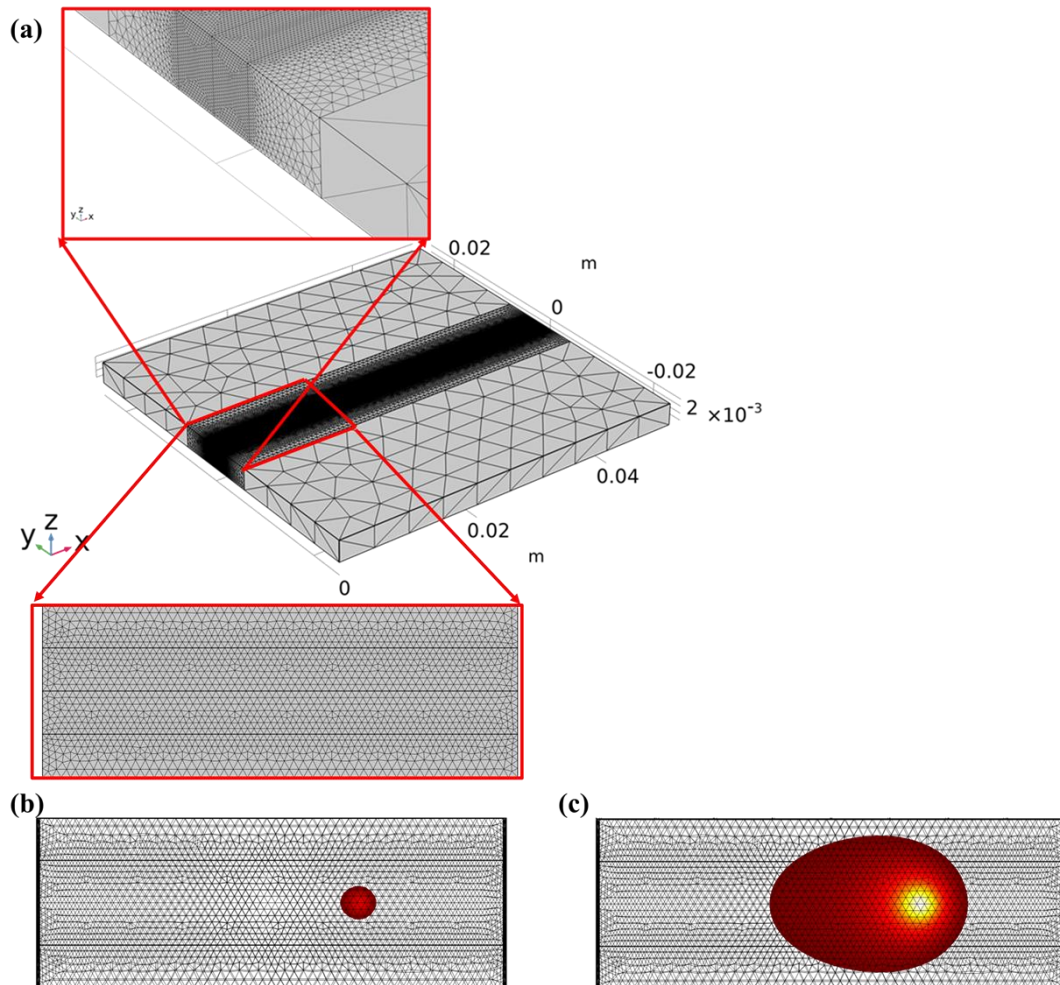
Figure 4.1 (a) Schematic illustrations of finite element mesh size and mesh distribution were used for the simulations of a laser welding process, (b) smallest weld pool with a mesh distribution and (c) largest weld pool with a mesh distribution

4.2.2.2 Model Validation

The model is validated using the experimental results from the literature [267]. The top surface morphologies of the weld pool and the temperature distribution along the weld centreline have been validated. The length of the melt pool formed is 4.6 mm as shown in Figure 4.2 which is comparable to the experimental value of 4.2 mm as measured by using a high-speed camera [267]. The temperature distribution manifests the validity of the heat transfer numerical model and the weld pool morphology

manifests the validity of the fluid flow numerical model. Both the weld pool morphology and the temperature profile are in good agreement with the literature.
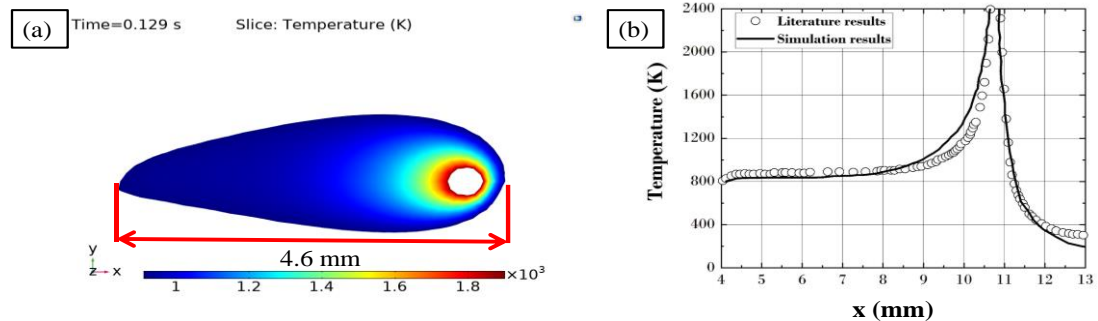
Figure 4.2 (a) Weld pool morphologies, simulated from the numerical model. The length of the simulated molten pool is 4.6 mm and 4.2 mm in the experiments [267], (b) Comparison between the calculated and simulated temperature distribution along the weld centreline. Welding parameters are Power (P_l) = 2500 W and welding speed (S) = 80 mm/s.

4.2.2.3 No Oscillation Condition

Table 4.2 shows the welding process parameters, peak temperature, maximum flow rate, weld dimensions, and the values of dimensionless numbers for both no oscillation and beam oscillation welding. The laser power is kept constant at 4 kW for all cases. For no oscillation welding, peak temperature, width and length of the weld pool and maximum flow rate decrease with an increase in welding speed. This is due to the decrease in the heat input per unit length, described as (ηP_l)/V, which decreases as given in Table 1. With an increase in welding speed, the net heat input to the workpiece decreases and hence peak temperature decreases. But it was found that there is a sharp decrease in the length and width of the weld pool as compared to the peak temperature. This shows that the welding speed has more effect on the top surface weld morphologies as compared to the peak temperature. This may be due to the high thermal conductivity of Aluminium where heat is lost quicker at the boundary as compared to the centre. *Pe* is calculated at the rear end of the keyhole in the liquid

melt pool and on the weld centreline. It should be noted that Pe is a function of position as it depends on u and L_R. It was found that Pe decreases with an increase in welding speed which indicates that at lower welding speeds convection is more dominant. As welding speed increases, the Pe number decreases to a lower value where conduction becomes dominant. This can be attributed to the decrease in the size of the melt pool region formed and the high thermal conductivity of Aluminium. The ratio of Marangoni number to Grashof number $R_{(s/b)}$ increases with the increase in welding speed and is of the order of 10^3-10^4 suggesting that the liquid flow is mainly driven by Marangoni convection due to surface tension force. It was observed that $R_{(s/b)}$ is maximum at the highest welding speed. This signifies that the effect of buoyancy force decreases with an increase in welding speed. The thermal gradient along the fusion zone boundary from the weld centreline increases with an increase in welding speed. This is due to the decrease in the heat input per unit length and the weld width.

Table 4.2 Welding simulation values of peak temperature (T_{peak}), weld width, length of the weld, maximum flow rate (U_{max}), Peclet number (Pe), the ratio of Marangoni number to Grashof number ($R_{s/b}$), thermal gradient (G) and heat input per unit length.

	S	R	f	T_{peak}	Weld width	Length of weld	U_{max}	Pe	$R_{s/b}$ (x10³)	G	Heat input
	(m/min)	(mm)	(Hz)	(K)	(mm)	(mm)	(mm/min)			(K/mm)	(J/mm)
No Oscillation	1	-	-	4677	9.9	31.3	1350	3.5	6.4	694	144
	2	-	-	4194	4.8	14.4	760	0.9	25	869	72
	3	-	-	3639	3.5	10.1	380	0.3	48	1235	48
Beam Oscillation	1	0.3	600	3882	9.8	27.7	1710	4.3	6.5	506	3.5
	1	0.6	300	3174	9.7	25.9	1450	3.7	6.2	577	3.5
	1	0.9	200	2329	9.1	23.3	1110	2.6	7.5	410	3.5

4.2.2.4 Beam Oscillation Condition

In beam oscillation welding, the heat source has two kinds of motions, circular motion and linear forward motion in the welding direction. This naturally results in an elliptical motion. The circular part of the motion is governed by the circumferential velocity defined as *2πRf* and linear forward motion by welding speed *S*. The net heat input to the workpiece depends on the laser power (P_l) and the welding speed (*S*) but the heat input per unit length for the beam oscillation welding is defined as (*ηP$_l$)/(S+2πRf)*. Because the actual speed of the oscillating laser beam is much higher than in no oscillation laser welding, the laser beam traverses a longer distance in the same amount of time due to additional oscillation. Hence, in the case of beam oscillation, the heat input per unit length and total heat input are important to understand while in the case of no oscillation, the total heat input is sufficient to investigate the process. So, the process parameters chosen for beam oscillation welding have an identical heat input per unit length. While comparing beam oscillation with no oscillation welding total heat input is kept constant. Figure 4.3 shows the calculated weld thermal cycle, weld morphology and velocity fields (along *x-y*, *y-z*, and *z-x* planes) for three different cases of beam oscillation whose welding process parameters are given in Table 4.2. Note that these parameters are selected to have a constant circumferential velocity and constant heat input per unit length. As can be seen from Figure 4.3 (e-h), the weld pool is elongated opposite to the welding direction. A typical V-shaped melt contour is formed due to the latent heat of the solid-liquid phase transition. The direction and magnitude of the fluid velocity are shown by the length and colour of the arrows. Figure 4.3 (e-h) depicts the flow on the surface points from the centre of the molten pool towards the outward periphery of the molten pool. This is due to the negative temperature coefficient of surface tension *dγ/dt*. The

force of buoyancy acts in the upward direction. This makes the flow of fluid circulate which can be seen in Figure 4.3 (i-l). Also, the flow speed is higher at the top surface of the weld and reduces along the *z*-direction which is shown in Figure 4.3 (m-p). The beam oscillation cases are compared with the no oscillation condition, having the same laser power and welding speed such that the total heat input is constant, which is also shown in Figure 4.3. The *Pe* number decreases from 4.3 to 3.7 to 2.6 with an increase in *R* while *Pe* for no oscillation condition is 3.5, which shows that convection is again the dominant mode of heat transfer in the weld pool. It is justifiable to use heat transfer and fluid flow models for the analysis of beam oscillation in place of only heat transfer as *Pe* is greater than one. It should be noted that *Pe* changes with the heat input. It increases with the increase in heat input since the maximum velocity increases with an increase in temperature [269]. It is evident from no oscillation conditions, that an increase in welding speed leads to a decrease in the *Pe* number. An increase in welding speed is associated with a decrease in heat input. *Pe* is higher for beam oscillation welding as compared to no oscillation welding for the same welding speed and laser power. This can be attributed to the incorporation of forced convection due to beam oscillation. The ratio of the Marangoni number to Grashof number $R_{(s/b)}$ is of the order of 10^3 confirming that the flow is mainly driven by the surface tension force and to a much lower extent by the buoyancy force. The peak temperature and weld dimensions decrease from no oscillation welding to beam oscillation welding as shown in Figure 4.3 (a-d). This is due to the decrease in heat input per unit length. The weld thermal cycle shows a different trend at a higher radius of oscillation. The two peaks in the weld thermal cycle are because the same point gets heated up twice due to a larger oscillation radius for a distance travelled by the heat source in the time between the two peaks in Figure 4.3 is equivalent to *2R*. At the longest radius of oscillation, the

peak temperature is below the boiling point which suggests that there is no formation of a keyhole. During beam oscillation welding, the peak flow rate decreases with the increase in radius of oscillation (values given in Table 4.2). This can be attributed to the decrease in the frequency of oscillation which leads to a decrease in the forced convection due to beam oscillation. With the increase in radius of oscillation, the high-speed flow area gradually increases as shown in Figure 4.3. The thermal gradient along the fusion zone from the weld centreline decreases from no oscillation welding to beam oscillation welding due to repeated heating and melting.
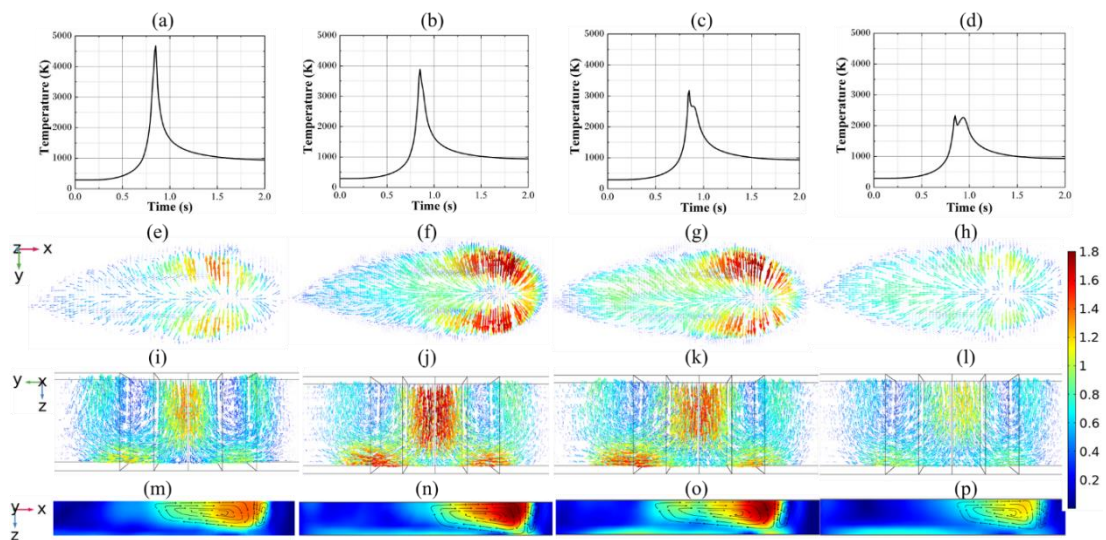
Figure 4.3 Calculated temperature (K) variation with time (top row Fig. (a-d)), velocity fields (mm s^{-1}) along x-y (top view Fig. (e-h)), y-z (front view Fig. (i-l)) and z-x (side view Fig. (m-p)) planes for no oscillation welding having (a) $P = 4$ kW, $S = 1$ m/min, and for oscillation welding having constant $P = 4$ kW, $S = 1$ m/min, and varying other parameters as (b) $R = 0.3$ mm, $f = 600$ Hz (c) $R = 0.6$ mm, $f = 300$ Hz, (d) $R = 0.9$ mm, $f = 200$ Hz. For the x-z plane, magnitude is shown using contour plots and the direction of fluid motion using arrows. The flow rate is the absolute velocity magnitude shown in the m min^{-1} scale.

4.3 Weld morphology prediction based on fluid flow model for two Aluminium alloys with consideration to sinusoidal beam oscillation

4.3.1 Modelling Strategy

The assumptions for the numerical model have been explained in Section 4.2.1.1. The governing equation to determine temperature distribution and velocity field, a numerical model was developed based on the solution of the equations of conservation of energy (Eq. 4.4), mass (Eq. 4.1) and momentum (Eq. 4.2) and corresponding force terms as discussed in Section 4.2.1.2 and 4.2.1.3. The initial and boundary conditions are given in Eq. 2.15-2.16 in Section 4.2.1.3. Flow condition for the free liquid surface due to the surface tension gradient due to variations in temperature is given in the Section 4.2.1.2. The numerical implementation of the model is similar as explained in Section 3.2.5.

4.3.1.1 Materials, geometry and calculation domain

In this case study, Al-6005 and Al-5754 are joined together in a butt joint configuration. A sinusoidal beam oscillation pattern is utilised with no nominal gaps between the workpieces. The numerical model is performed using COMSOL Multiphysics software where space is discretised using the finite element method and time is discretised using BDF. The size of the simulation domain for a single plate is 100 mm $\times$ 50 mm $\times$ 3 mm with each plate is divided into three plates to improve the mesh distribution having fine mesh at the centre of the fusion zone to coarser mesh towards the base metal as shown in Figure 4.4 (a). Mesh sensitivity analysis was performed over the global domain of temperature and fluid velocity and model outputs are calculated after the model attained the quasi-steady state with respect to temperature and fluid flow fields. Tetragonal mesh is used with a minimum mesh size of $r/8$ mm having a total number of mesh elements of 750639 elements over the whole domain. To map the effect of oscillation of frequency, the time step is selected as

0.0001 seconds. The thermophysical properties of AA-5754 and AA-6005 alloys are taken from [270,271].
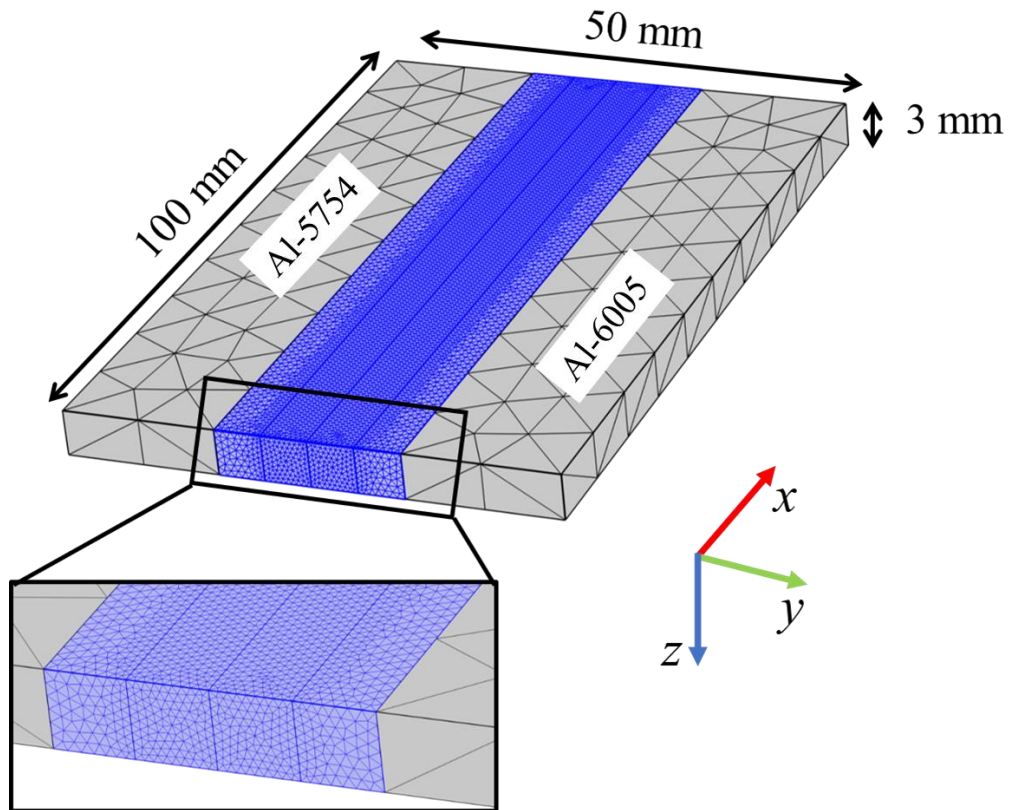
Figure 4.4 Schematic illustration of geometry and finite element mesh distribution used for the simulations.

4.3.2 Experimental Strategy

A 10 KW Coherent ARM FL10000 laser system, with a beam parameter product of 16 mm mrad with a core optical fibre of 100 μm diameter was used. The laser system coupled with the WeldMaster remote welding head (Precitec GmbH, Germany) and beam oscillation is generated by the motorized mirror and collimator integrated with the WeldMaster Scan&Track remote welding head. Only a core beam was used to carry out the experiments. The Guillotine cutter was used to machine the sheets into a coupon having dimensions 100 mm × 50 mm × 3 mm. Neither filler wire nor shielding

gas was used throughout the experiments. Welding experiments are carried out in butt joint configurations and the incident beam is inclined at an angle of 4 degrees with a focal offset of 13 mm. The matrix of studied process parameters is summarised in Table 3.3. The experimental set-up #1-7 is used for the selection of the heat source model based on the shape of the weld profile, weld width and depth of penetration. Set-ups #1 and #2 are selected to study the effect of beam oscillation during full penetration welding and set-ups #3 to #7 are selected to investigate the effect of oscillation frequency on grain morphology, solidification parameters and tensile strength. A high-speed camera (FASTCAM Nova S6) was used to monitor the dynamic behaviour of the weld pool at a photographing speed of 30000 frames per second having a recording time of 2.2 seconds. A laser illuminator was used to illuminate the weld zone. The experimental setup with the high-speed camera is shown in Figure 4.5.
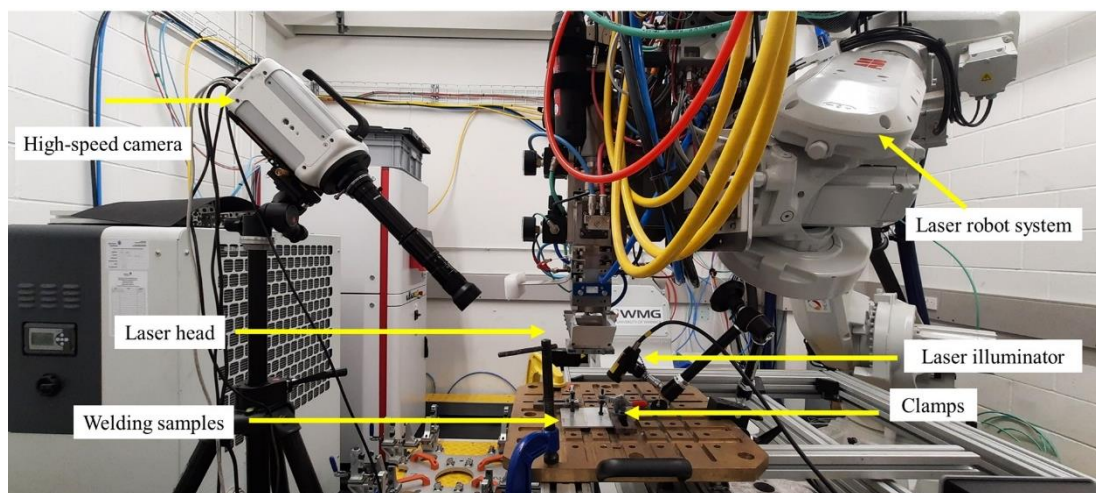
Figure 4.5 Weld experiment setup for welding AA-6005 with AA-5754 in butt welding configuration using remote laser welding. The setup shows the position of clamps, welding samples, high-speed camera, laser illuminator and laser head.

After welding, the welded samples were sectioned normal to the welding direction and polished to a surface finish of 0.05 μm, and the respective steps are given in Table 4.3, followed by etching in caustic sodium fluoride reagent (2%NaOH + 5%NaF + 93% water) [105]. The weld dimensions were measured in a Keyence VHX7000 optical microscope. Weld zone grain morphology was characterised by EBSD mapping conducted on a JEOL 7800F scanning electron microscope, equipped with an Oxford Instruments' Symmetry II EBSD detector and AZtec acquisition software with an accelerating voltage of 20 kV and step size of 2 μm. Grain size is determined by the equivalent diameter of the circle for equiaxed grain and fitted ellipse major diameter for columnar grain using AztecCrystal software. The different methods used for the calculation of average grain size are based on the shape of the equiaxed grains which is mostly circular and columnar grain which is closer to elliptical in shape. An area-weighted mean value, $\overline{D} = \frac{\sum W_i D_i}{\sum W_i}$ was used to express the averaged grain size. The average area of the equiaxed and columnar regions is calculated by adding the area of individual grains. The total area of the equiaxed and columnar grain will provide an area of the fusion zone. The mechanical properties of the joints formed are assessed using a uniaxial tensile test performed using a 30 KN static Instron Universal tensile machine according to ASTM-E8 using a sub-sized tensile specimen whose dimensions are shown in Figure 4.6 [272]. The dog bone shaped tensile specimens are prepared with the welded region at the centre using high precision Datron M7HP CNC milling machine. The tensile tests are carried out with a constant crosshead velocity of 2 mm/min. During the test, the applied load is recorded by an integrating load cell. Extensometer is used to measure the precise strain along the gauge length of 32 mm. Bluehill 3 software is used to analyse and acquired tensile

test data associated with Instron tensile testing machine. To check the repeatability of each welding condition, three weld seams are prepared for each weld setup and five tensile test samples were prepared from each weld seam.

Table 4.3 5-step polishing method for Aluminium alloys

Step number	Surface	Size/Abrasive	Load (N)	Speed (rpm)	Time (sec)
1	CarbiMet	P400 SiC water cooled	22	300	Until Plane
2	TexMet C	9 µm MetaDi Supreme Diamond	22	150	300
3	TexMet C	3 µm MetaDi Paste	22	150	240
4	TexMet C	1 µm MetaDi Paste	22	150	120
5	ChemoMet	0.06 µm MasterMet Colloidal Silica	22	1450	90
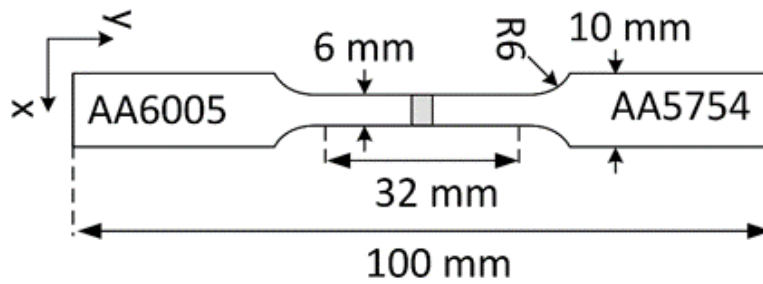
Figure 4.6 The schematic diagram for the sub-sized tensile specimen used in the study.

Weld zone grain morphology was characterised by EBSD mapping conducted on a JEOL 7800F scanning electron microscope. Grain size is determined by the equivalent diameter of the circle for equiaxed grain and fitted ellipse major diameter for columnar grains using AztecCrystal software. The different methods used for the calculation of average grain size are based on the shape of the equiaxed grains which is mostly circular and columnar grain which is closer to elliptical. The average area of the equiaxed and columnar regions is calculated by adding the area of individual grains. The total area of the equiaxed and columnar grain will provide an area of the fusion zone. The mechanical properties of the joints are assessed using a uniaxial tensile test performed using a 30 KN static Instron Universal tensile machine according to ASTM-E8 using a sub-sized tensile specimen [272]. To check the repeatability of each welding condition, three weld seams are prepared for each weld setup and five tensile test samples were prepared from each weld seam.

4.3.3 Results and Discussions

4.3.3.1 Model Validation

In this chapter, the model is validated for the fluid flow part of the model based on the weld pool morphologies of the top surface. Case-5 is used for the development

of weld pool morphology at the top surface as it generates the best results based on the shape and dimensions of the weld cross-section as discussed in section 3.4.1. (The experimental setup is given in Table 3.3). The experimental high-speed camera images of the top surface of the weld pool for no oscillation and beam oscillation welding for different setups are shown in Figure 4.7 (a-d) respectively. Figure 4.7 (e-h) shows the simulated weld pool morphologies which are indicated by isothermal contours from liquidus temperature to boiling point. The keyhole profile is roughly circular (Figure 4.7 (a-d)) which matches the simulated contour map (Figure 4.7 (e-h)). The comparison of the length of the weld pool and width of the weld pool between the experiment and simulation are in good agreement with an overall 5% difference, demonstrating the validity of the employed model. To ensure consistent and replicable measurements of the top surface weld pool morphologies, the dimensions are assessed at distances of 30 mm, 50 mm, and 70 mm from the initial weld point. The total length of the weld is 100 mm, with the initial 20 mm and final 20 mm disregarded. For reproducibility purposes, two weld seams are generated for each combination of process parameters. The average value of these measurements is then utilized for comparison with the simulated results.
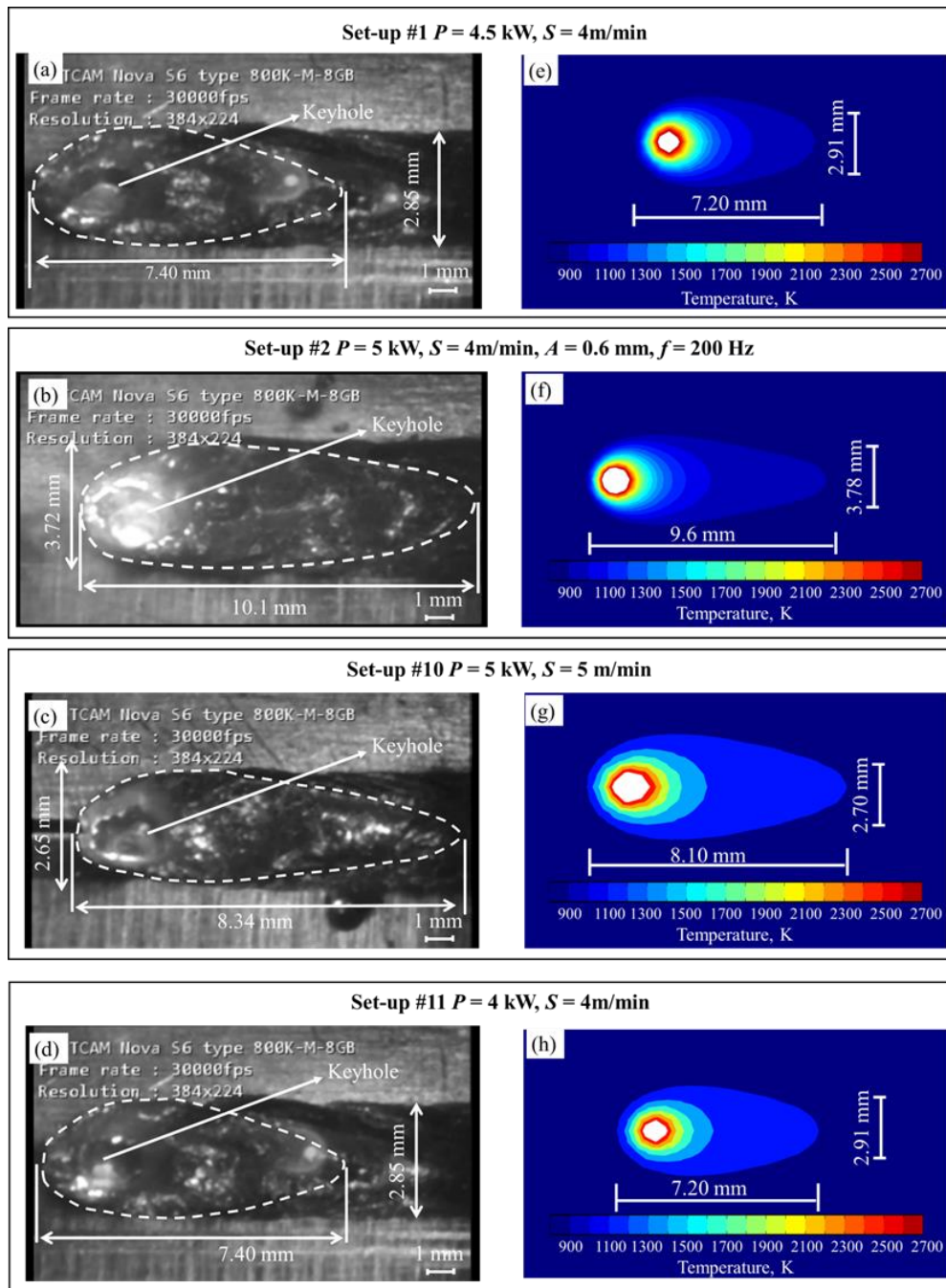
Figure 4.7 Comparison of the weld pool top surface morphologies between the experimental high-speed camera (a-d) and numerical simulation (e-h) for a different setup. The temperature above the boiling point where the keyhole is formed is shown in white colour in the simulated contour map. The experimental setup is given in Table 3.3

4.3.3.2 Effect of welding speed on weld zone dimensions and flow profile

Figure 4.8 provides the main numerical results at the three different welding speeds (setup #1,#8 and #9) at a constant laser power and the two different welding

155

speeds at a constant specific point energy density (SPED) [273] (setup #10 and #11).

Figure 4.8 (a-e) shows the shape and dimension of the weld on the transverse section,

Figure 4.8 (f-j) demonstrates the fluid flow fields in the *x-z* plane and Figure 4.8 (k-o)

depicts the vorticity formed at the top surface of the weld pool formed. As expected,

the higher the welding speed, the narrower and shallower the weld pool whose

dimensional values are given in Table 4.4. The length of the weld pool decreases with

an increase in welding speed (setup #1, #8 and #9), this is due to a decrease in net heat

input to the workpiece which leads to less formation of liquid metal. But at constant

SPED (setup #10 and #11), the length of the weld pool increases with an increase in

welding speed while width and depth almost remain constant. The velocity field of the

weld pool is indicated by the arrows whose magnitude can be estimated by the colour

of the arrows. The peak velocity increases with an increase in welding speed even at

a constant SPED due to the flow caused by the increase in movement of the laser beam.

The velocity profile in Figure 4.8 (f-j) shows a distinct vortex formed along the vertical

mainly moving up and down [274]. The liquid metal tends to flow first through the

length section as compared to the depth and this flow tendency is a result of a change

in the temperature gradient. Figure 4.8 (k-o) shows the obvious vortexes formed near

the keyhole opening position on the horizontal plane. The higher the fluid flow rate

magnitude indicates the higher vorticity. The vorticity profile confirms that the liquid

metal is flowing from the centre to the outward periphery. This outward flow of the

liquid metal is due to the Marangoni convection where flow is from a higher

temperature area to a lower temperature area [182]. The values of peak flow rate is

given in Table 4.4. In the core region of the weld pool, especially during the cooling

cycle, the temperature gradient increases as welding speed increases. When welding

speed increases from 4 m/min to 6 m/min, the thermal gradient increases from 2367

K/mm to 2607 K/mm. The thermal gradient during the cooling cycle is important as it governs the grain morphology during solidification [35]. The cooling rate calculated in the core region shows an increasing trend with an increase in welding speed. This is due to the decline in heat input and the values of the thermal gradient and cooling rate is given in Table 4.4. The cooling rate governs the scale of the grains formed, the higher the cooling rate finer will be the structure will be.

Table 4.4 Simulated weld characteristics for different welding speeds while other parameters are kept constant for the butt welding of AA-5754 with AA-6005. The experimental setup is given in Table 3.3

Setup	Weld length (mm)	Weld width (mm)	Weld depth (mm)	Peak flow rate (mm/s)	Thermal gradient (K/mm)	Cooling rate (K/s)
#1	7.2	2.91	3.00	5.31	2367	5515
#8	6.74	2.54	2.20	5.96	2545	8768
#9	6.1	2.2	1.93	6.04	2607	13385
#10	8.1	2.7	2.20	6.67	2652	6909
#11	6.2	2.71	2.24	5.26	2330	6630
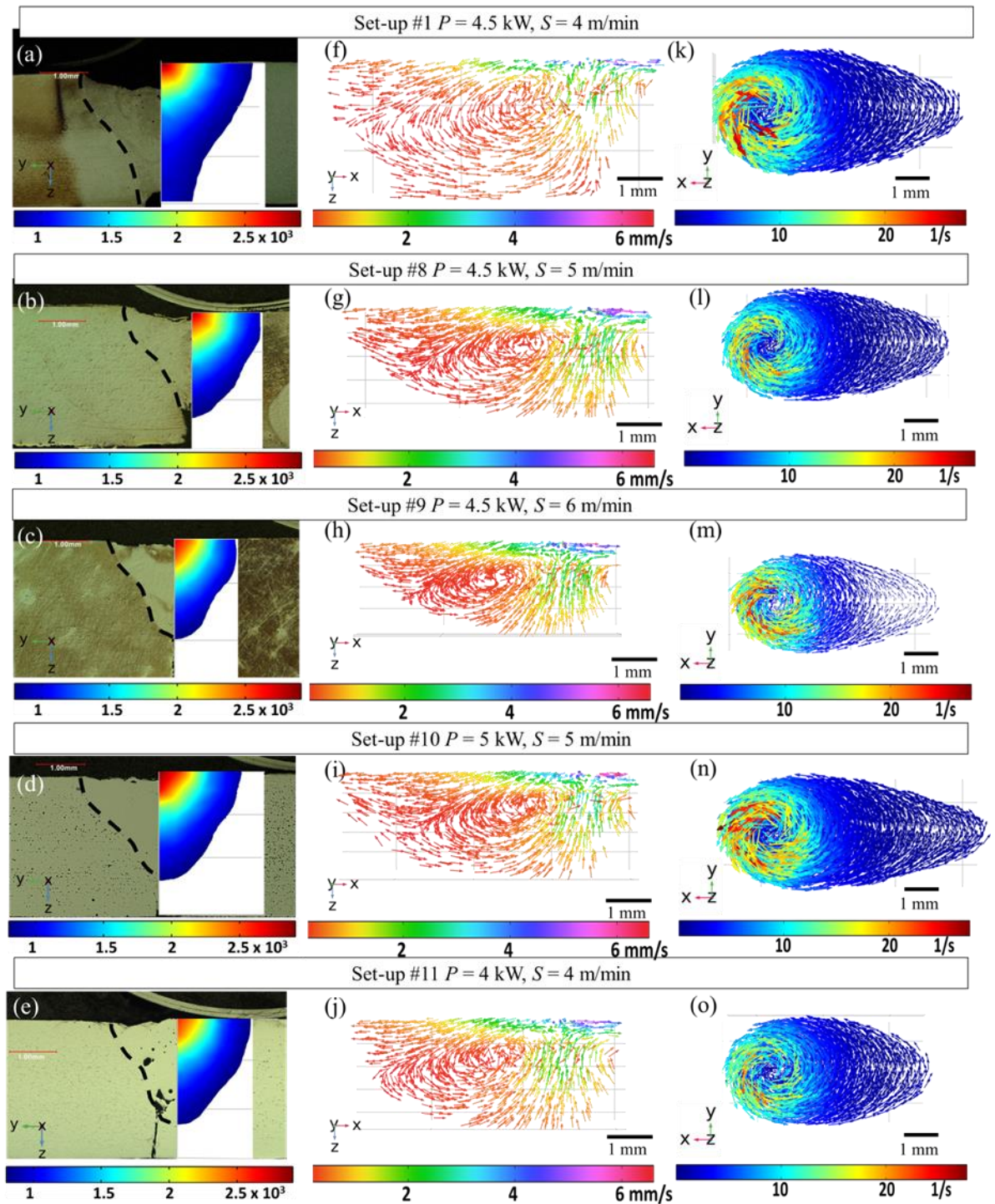
Figure 4.8 Showing weld shape comparison between experiment and simulation (a-e), velocity profile in the *x-z* plane (f-j) and vorticity profile in the *x-y* plane (k-o). The experimental setup is given in Table 3.3

4.3.3.3 Effect of oscillation amplitude on weld zone dimensions and weld flow profile

Figure 4.9 (a-d) shows the experimental and simulated fusion zone, Figure 4.9 (e-h) shows the fluid flow profile in the *x-z* plane and Figure 4.9 (i-l) depicts the vorticity profile in the *x-y* plane. The oscillation amplitude is increased from 0.6 mm to 2.4 mm while all other parameters are kept constant to understand the effect of oscillation amplitude on the fusion zone dimension and flow profile. With an increase in oscillation amplitude, the penetration depth and length of the weld pool decrease while the weld width increases. This is because the laser beam covers a larger distance in the same amount of time so the energy input per unit length decreases though the net heat input to the workpiece remains constant. It was found that with the increase in oscillation amplitude the mode of welding changes from the keyhole to the conduction mode of welding which can also be confirmed from the peak temperature calculated from the model as the temperature drops down below the boiling point of the material. As compared to no oscillation condition, beam oscillation leads to the formation of three distinct vortices. One vortex along the vertical plane as shown in Figure 4.9 (e-h) and two vortices on the horizontal lane as shown in Figure 4.9 (i-l). The two vortices formed in the horizontal plane are distinguishable for the higher oscillation amplitude Figure 4.9 (k-l). The two vortices formed on the horizontal plane are because of the stirring action due to the application of beam oscillation. The peak flow rate (values given in Table 4.5) decreases with the increase in oscillation amplitude due to the decrease in the Marangoni-driven convection because of the decrease in the temperature. The thermal gradient at the core calculated during the cooling cycle decreases with an increase in oscillation radius while the cooling rate increases. This is due to the less retention of heat with increasing oscillation amplitude. The values of the thermal gradient and cooling rate are given in Table 4.5.
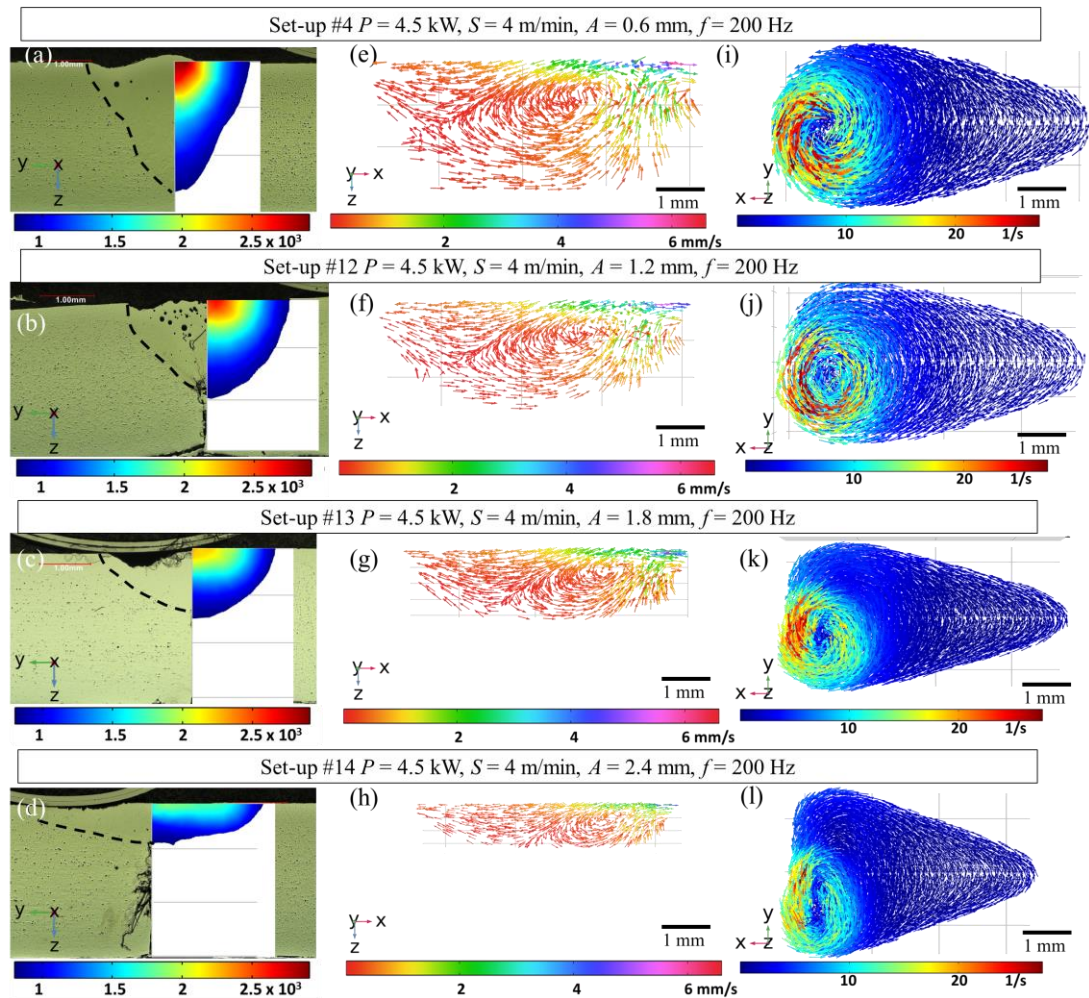
Figure 4.9 Showing weld shape comparison between experiment and simulation (a-d), velocity profile in the *x-z* plane (e-h) and vorticity profile in the *x-y* plane (i-l). The experimental setup is given in Table 3.3

When compared with no oscillation and beam oscillation conditions at the same welding speed and laser power, penetration depth decreases due to a decrease in the energy input per unit length. Whereas there is an increase in weld width and length of the weld pool which suggests that a larger area is in molten form. The thermal gradient of beam oscillation is lower than the no oscillation due to the churning action of the oscillating beam in the weld pool. This is evident from the formation of one more vortex on the horizontal plane. The implementation of beam oscillation in

welding results in a higher cooling rate, indicating reduced heat retention at each point compared to non-oscillating welding. Furthermore, beam oscillation leads to a higher peak flow rate due to the stirring effect induced by the oscillating beam. However, at higher oscillation amplitudes, there is a decrease in the peak flow rate compared to the non-oscillation condition. This decrease is attributed to the reduction in peak temperature, which in turn diminishes the Marangoni driven flow.

Table 4.5 Simulated weld characteristics for different oscillation amplitude while other parameters are kept constant for the butt welding of AA-5754 with AA-6005. The experimental setup is given in Table 3.3

Setup	Weld length (mm)	Weld width (mm)	Weld depth (mm)	Peak flow rate (mm/s)	Thermal gradient (K/mm)	Cooling rate (K/s)
#4	8.40	3.01	2.45	5.81	2130	7304
#12	8.15	3.1	1.98	5.31	1980	8265
#13	7.83	3.35	1.42	4.80	1845	12017
#14	7.20	3.7	0.92	4.05	1492	14783

4.3.3.4 Effect of oscillation frequency on weld zone dimensions and weld flow profile

Figure 4.10 shows the weld shape in the transverse direction, fluid flow profile and vorticity profile formed with different oscillation frequencies while other process parameters are kept constant. There are not many differences is found in terms of weld width and length of the weld pool with increasing frequency. The peak flow rate

increases with increased oscillation frequency due to the stirring produced at a higher frequency [275]. The re-heating and re-melting due to sinusoidal beam oscillation are less as compared to circular or infinity beam oscillation as the movement of the beam in case of sinusoidal oscillation is always in the forward direction. The thermal gradient decreases with increasing frequency and at higher oscillation frequency it almost becomes constant. This is due to the decrease in peak energy accumulation which leads to a decrease in the thermal gradient of the weld pool. The increasing oscillation frequency accelerates the flow and promotes the heat transfer which leads to an increase in the cooling rate. The values of the cooling rate and the thermal gradient are given in Table 4.6. There is a gradual increase in high-speed flow area with the increase in the frequency of oscillation which is depicted in the flow profile and vorticity profile in Figure 4.10.

Table 4.6 Simulated weld characteristics for different oscillation frequencies while other parameters are kept constant for the butt welding of AA-5754 with AA-6005. The experimental setup is given in Table 3.3

Setup	Weld length (mm)	Weld width (mm)	Weld depth (mm)	Peak flow rate (mm/s)	Thermal gradient (K/mm)	Cooling rate (K/s)
#3	8.41	3.01	2.46	5.30	2250	7021
#4	8.40	3.01	2.45	5.81	2130	7304
#5	8.38	3.00	2.32	5.95	2030	7540
#6	8.36	2.99	2.26	6.20	2000	7920
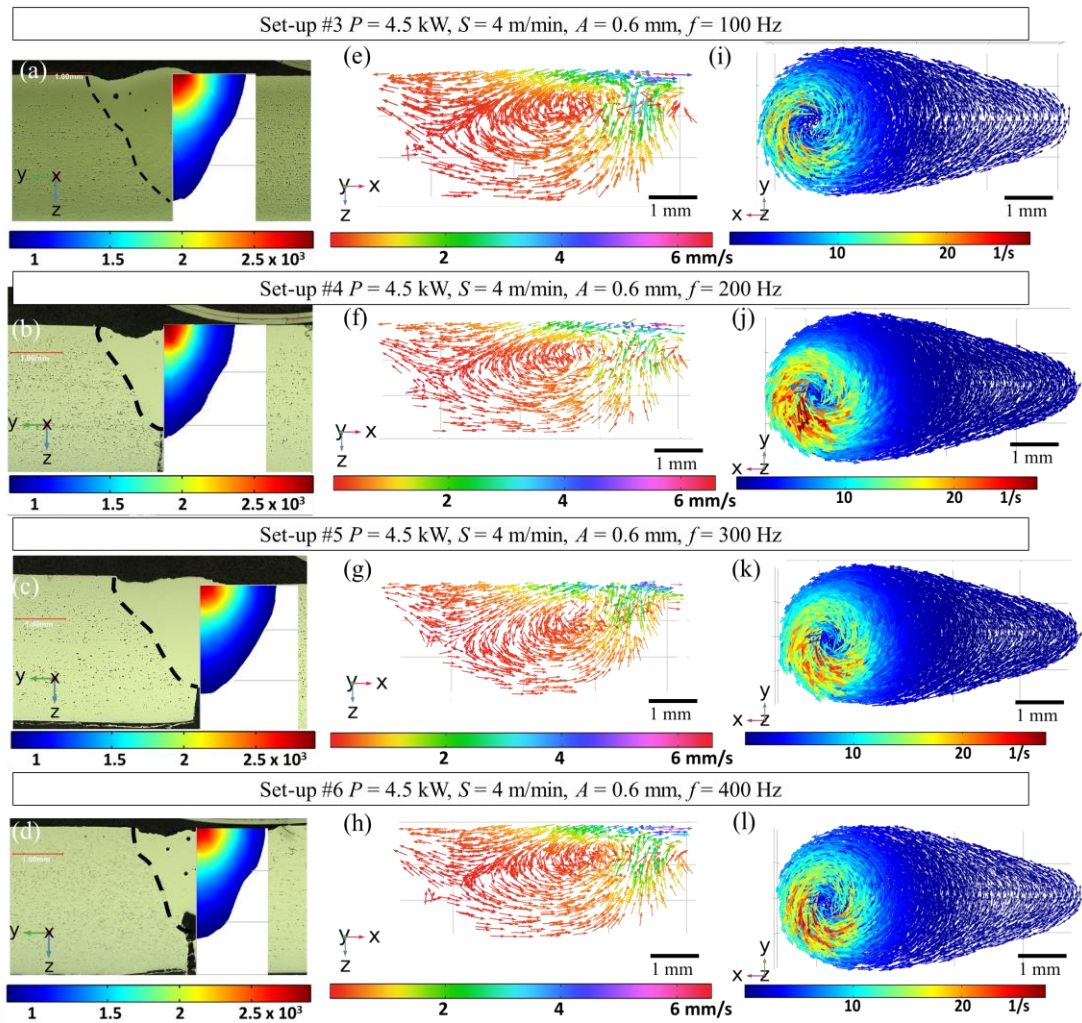
Figure 4.10 Showing weld shape comparison between experiment and simulation (a-d), velocity profile in the *x-z* plane (e-h) and vorticity profile in the *x-y* plane (i-l). The experimental setup is given in Table 3.3

4.3.3.5 Influence of beam oscillation on Grain morphology during full penetration

A steep thermal gradient, high cooling rate and rapid solidification behaviour of the molten weld pool are expected in the laser welding process. The simulated temperature, flow fields and solidification process are combined to investigate the effect of beam oscillation on grain morphology. The evolution of the solidification behaviour of the top surface at the solid-liquid interface is demonstrated by studying the solidification parameters. It has been proposed that the grain structure of a weld

depends on the solidification rate (R) and temperature gradient (G) during solidification [18,267]. The ratio G/R is proportional to the morphology of solidification and $G{\times}R$ is proportional to the size of the grains formed [69]. The threshold value for G/R is $7{\times}10^3$ Ks/mm for the dendritic structure of the aluminium alloys and a lower value of G/R promotes equiaxed dendritic structure [105,267]. Figure 4.11 compares the variation of solidification parameters (G, R, $G{\times}R$ and G/R) along the representative isotherm (898 K) on the top surface of the molten pool boundary. In both no oscillation and beam oscillation cases, G exhibits uniform distribution at the weld centre and increases rapidly along the fusion boundary and beam oscillation conditions have a lower temperature gradient as shown in Figure 4.11 (a). The solidification rate decreases from the weld centre to the fusion boundary and a relatively high peak is found for the no oscillation condition as shown in Figure 4.11 (b). The $G{\times}R$ follows a peak shape with a peak value at the weld centre suggesting that the refined grains are formed at the weld centre and grain growth occurs towards the fusion boundary. The no oscillation condition has higher $G{\times}R$, which suggests that the grain size will be smaller as compared to the beam oscillation condition. The G/R value for both cases is below the critical value for the formation of cellular or dendritic grains, therefore, a dendritic grain is expected in the fusion zone. The G/R follows a 'U' shaped distribution with a minimum value located at the weld centre suggesting that the equiaxed grains form at the weld centre [69]. The lower value of G/R for beam oscillation conditions demonstrates the formation of more equiaxed grains. The shape of $G{\times}R$ is similar to R and the shape of G/R is similar to G. The solidification parameters also suggest that there is the formation of a larger fusion zone for beam oscillation condition as compared to no oscillation condition. This can be attributed to the larger width of the solidified region at the top surface as shown in Figure 4.11.
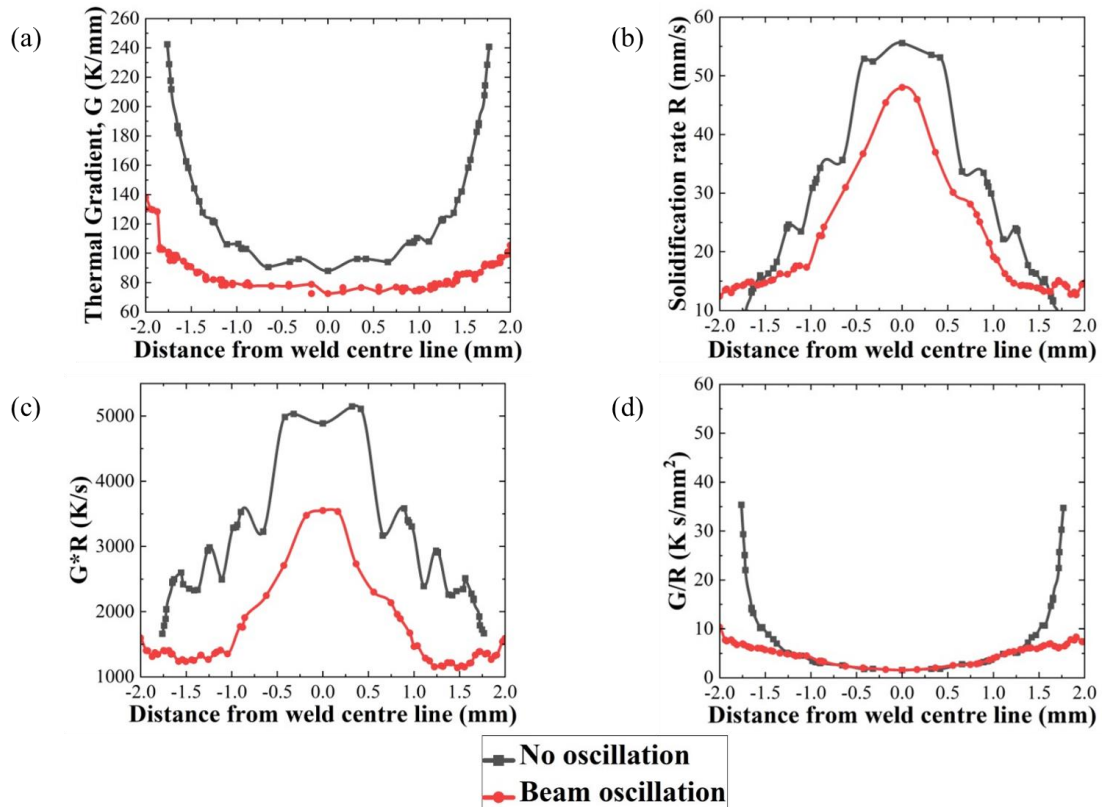
Figure 4.11 Comparison of the solidification parameters for welds produced with no oscillation and beam oscillation during full penetration, extracted from the solidification isotherm in the mushy zone on the top surface: (a) thermal gradient G, (b) solidification rate R, (c) $G \times R$ and (d) G/R. The experimental setup is given in Table 3.3

EBSD analysis was performed across the transverse cross-section of the weld zone to investigate the impact of beam oscillation on the grain morphology of the weld and to compare the findings obtained from the numerical model. The grain structure maps for both oscillation and no oscillation conditions are shown in Figure 4.12. The weld cross-sections are comprised of equiaxed grains marked as fusion zone 1 (FZ1) at the centre and columnar grains marked as fusion zone 3 (FZ3) at the boundary of the fusion line. The columnar grain morphology is typical for dendritic growth, which is in the direction of the thermal gradient. The average grain size and area of the equiaxed and columnar region is given in Figure 4.12 (c). It is evident that the fusion zone region and the region of equiaxed grains both increase with beam oscillation. An

increase in the equiaxed region in the fusion zone, which is evident from the ratio of equiaxed area to total fusion zone area, increases the isotropy of the weld preventing crack propagation during the tensile test [181] and reducing crack susceptibility [105]. Consequently, an increase in tensile strength by 21.4% is determined with the application of beam oscillation (Figure 4.12 (c)). The average grain size of the equiaxed and columnar region is smaller for no oscillation conditions which are well correlated to the region with the highest cooling rate ($G \times R$) values, which follows the same trend as in the numerical model. The beam oscillation condition has a larger region of equiaxed grains which is correlated to the lower G/R value, which again is consistent with results from the numerical model. In both the cases, the fractures occurred in the fusion zone. Figure 4.13 shows the fractography of welds produced with and without oscillation after the tensile test. Uniform distribution of dimples was observed in the case of beam oscillation condition with few pores and micro-cracks. In comparison, a much more frequent and larger pores and micro-cracks was captured in the weld produced without beam oscillation which facilitates the rapid failure subjected to external tensile loading.

(a) Set up #1 *P* = 4.5 kW, *S* = 4 m/min

(b) Set up #2 *P* = 5, kW, *S* = 4 m/min, A = 0.6 mm, *f* = 200 Hz

0.5 mm

Aluminium
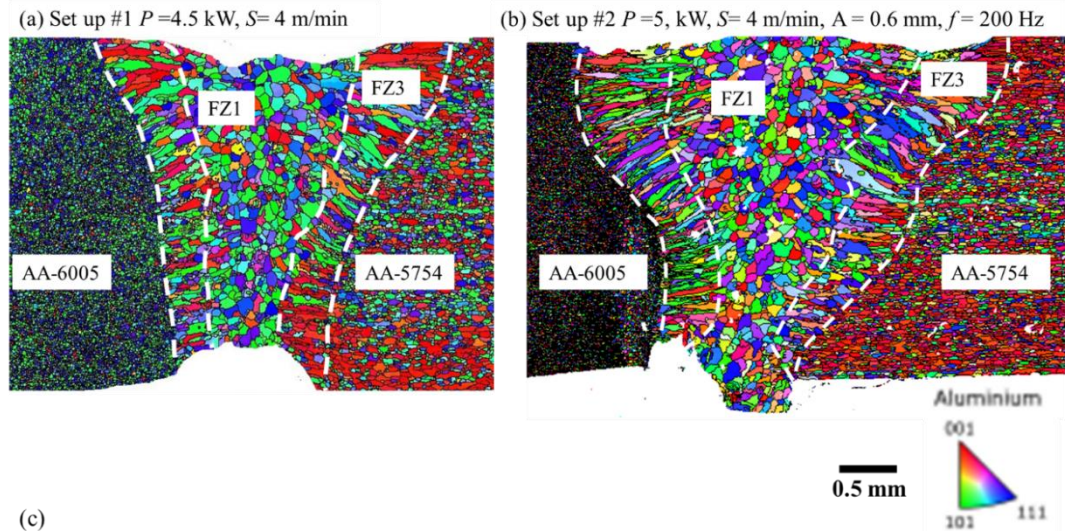
(c)

Set-up	Equiaxed grain size (μm)	Equiaxed grain area (mm²)	Columnar grain size (μm)	Columnar grain area (mm²)	Total area (mm²)	Ratio of equiaxed area to fusion zone area	Tensile strength (MPa)
#1	79.58	1.32	177.82	1.97	3.29	0.40	163 ± 4.9
#2	82	2.74	189	2.83	5.57	0.49	198 ± 2.9

Figure 4.12 EBSD IPF maps showing the grain structures in welds produced with (a) no oscillation having power *P* = 4.5 kW, welding speed *S* = 4 m/min, (b) beam oscillation having power *P* = 5 kW, welding speed *S* = 4 m/min, oscillation amplitude *A* = 0.6 mm and oscillation frequency *f* = 200 Hz and (c) provides the grain size and area of a different region and ultimate tensile strength for full penetration welding. The experimental setup is given in Table 3.3. Error for the tensile strength is standard deviation.
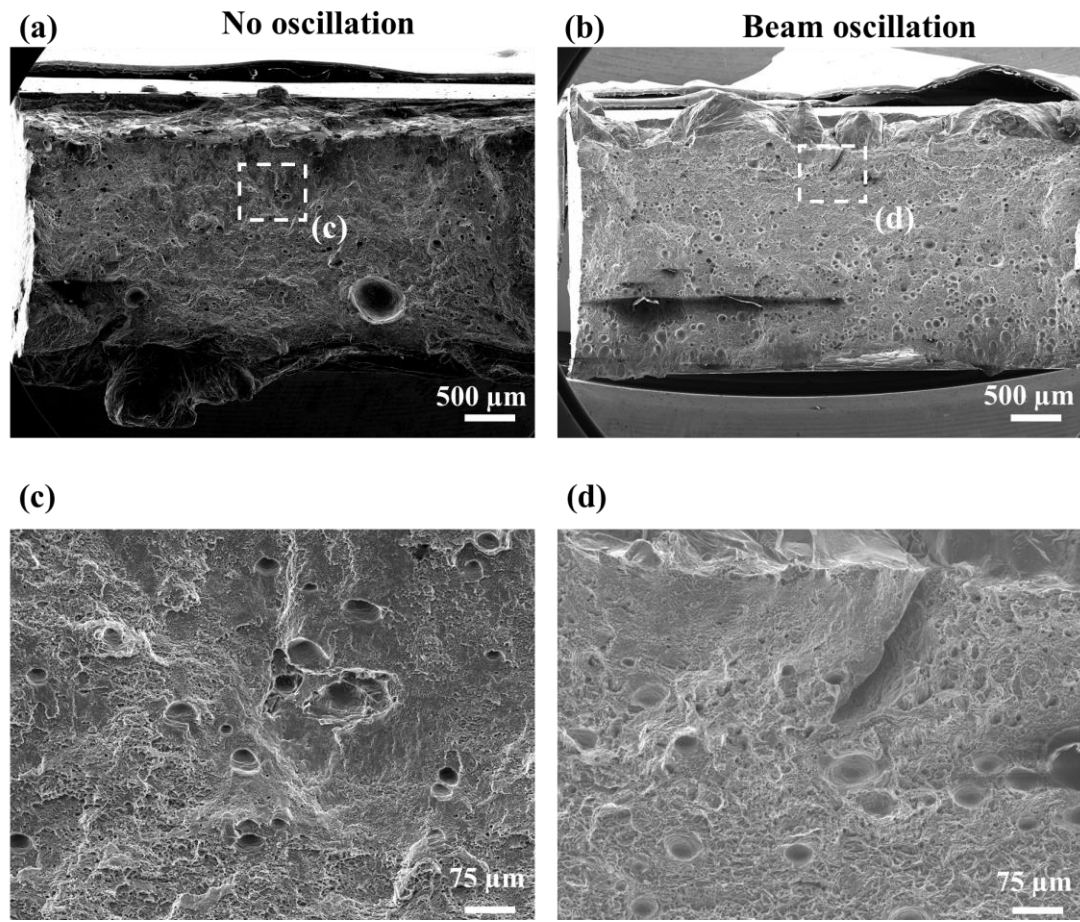
Figure 4.13 SEM fractography of welds produced (a) without oscillation and (b) beam oscillation, after the tensile test. (c) and (d) are high-magnification views of the area highlighted in (a) and (b), respectively.

4.3.3.6 Influence of frequency of oscillation on Grain morphology

To investigate the influence of the frequency of oscillation on the evolution of solidification behaviour, solidification parameters are studied along the top surface of the molten weld pool boundary. Figure 4.14 shows the solidification parameters for different oscillation frequencies while the rest of the welding parameters were kept constant. The thermal gradient G demonstrates uniform distribution at the centre and increases along the fusion boundary as shown in Figure 4.14 (a). The G value remains constant with an increase in oscillation frequency. The solidification rate, R increases with an increase in oscillation frequency. This is due to an increase in the travel speed

of the laser beam with increasing oscillation frequency which increases the R. The cooling rate, $G{\times}R$ has a peak shape which shows that the fine grains will form at the centre and coarse grain growth around the boundary of the fusion zone. The peak of $G{\times}R$ increases with an increase in oscillation frequency suggesting that the smallest grains will be formed at the highest oscillation frequency. It is also worth noting that the peak broadens with the increase in oscillation frequency, suggesting that grain growth is hindered and more regions of finer grains will be formed. The G/R is below the threshold value of $7{\times}10^3$ Ks/mm for the dendritic structure [105,267] and a lower G/R value at the centre suggests the formation of equiaxed grains as shown in Figure 4.14 (d). Slight differences in the value of G/R were observed among the welds with varying frequencies. Overall, the solidification parameters suggest that an increase in oscillation frequency leads to the formation of finer grains and hinders grain growth at a higher frequency.
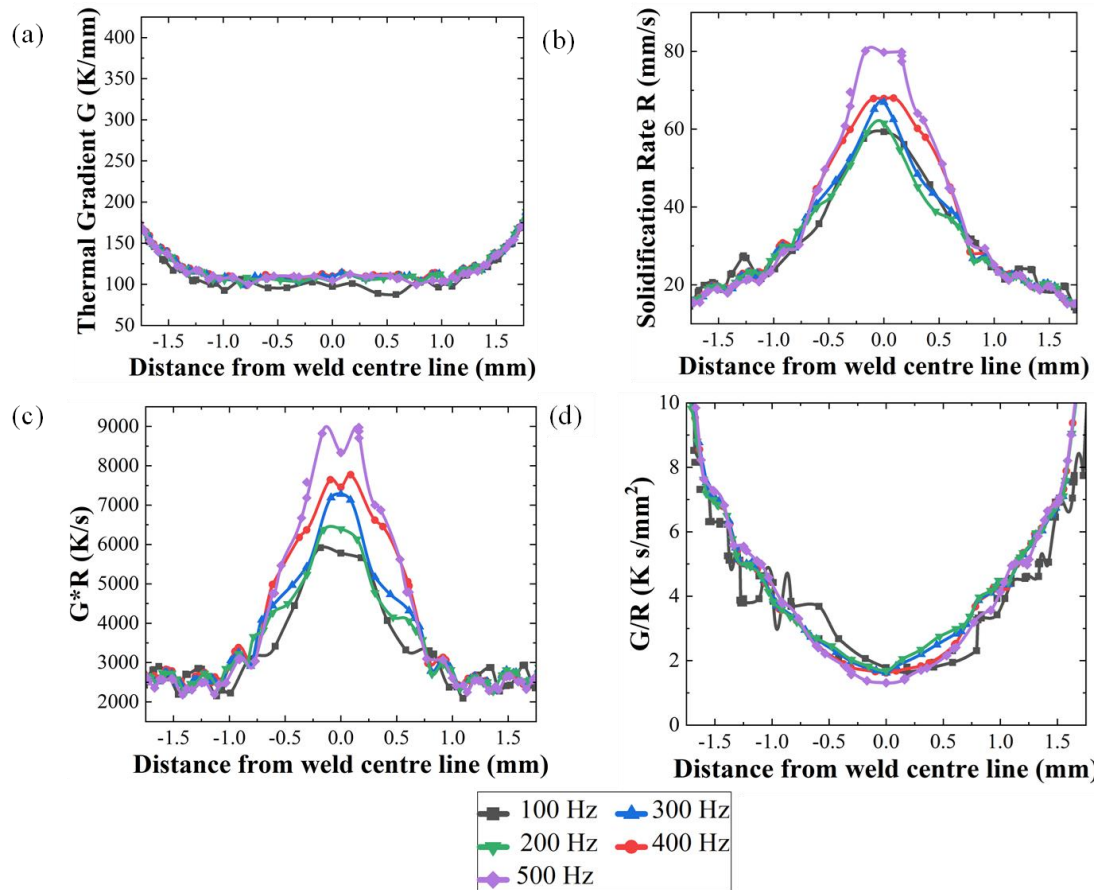
Figure 4.14 Comparison of the solidification parameters for welds produced with varying oscillation frequency from 100 Hz to 500 Hz, extracted from the solidification isotherm in the mushy zone on the top surface: (a) thermal gradient G, (b) solidification rate R, (c) $G \times R$ and (d) G/R. The experimental setup is given in Table 3.3

EBSD analysis across the transverse cross-section was performed to investigate the influence of oscillation frequency on the grain morphology of the weld and to validate the findings observed from the numerical model. The grain structure maps for different oscillation frequencies are shown in Figure 4.15 (a-e). The weld cross-sections are comprised of two distinguishable zones: equiaxed grains (FZ1), and long columnar grains (FZ3). The presence of broken columnar grains can also be seen and this is due to stirring action in the weld pool which disturbs the growth of the columnar grains in the mushy zone and promotes finer grains [181]. This disturbance

breaks the growth of the columnar dendrites in the mushy region and promotes the formation of fine columnar grains [181] which is consistent with the findings obtained from the numerical model. With an increase in oscillation frequency, the fusion zone dimensions decrease, which is evident from Figure 4.15 (f). This is due to the decrease in line energy with the increase in oscillation frequency. With the increase in oscillation frequency, it was found that the grain size gradually decreases [156], and the grains size, area of the equiaxed grains and columnar grains are given in Figure 4.15 (f). It should be noted that the ratio of areas is estimated in place of absolute value as the fusion zone area is not constant for all the cases and ratio is a more critical parameter for the comparison. The tensile strength (given in Figure 4.15 (f)) increases with the increase in oscillation frequency to 300 Hz and then again decreases with increasing frequency. The increase in tensile strength is due to the decrease in grain size of both the equiaxed and columnar regions but the decrease in the tensile strength with an increasing frequency above 300 Hz is due to the decrease in the percentage of equiaxed grains formed which is demonstrated as the ratio of equiaxed area to fusion zone area reported in Figure 4.15 (e). The decrease in the percentage of equiaxed grains leads to a decrease in grain boundaries which acts as a barrier for crack propagation and thus makes the weld susceptible to cracking [105,181]. In all cases, the fracture occurs close to the Al-6005 boundary.
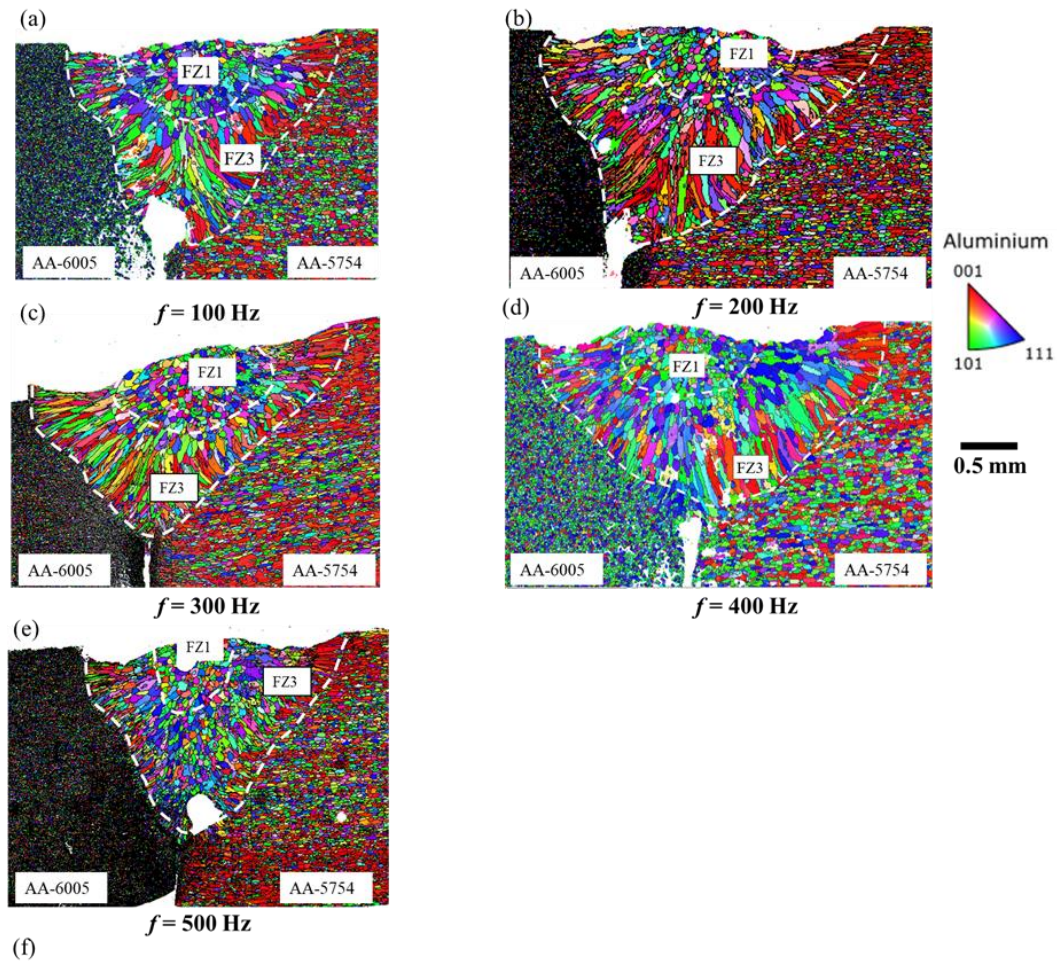
f (Hz)	Equiaxed grain size (μm)	Equiaxed grain area (FZ1) (mm²)	Columnar grain size (μm)	Columnar grain area (FZ3) (mm²)	Total area (mm²)	Ratio of equiaxed area to fusion zone area	Tensile strength (MPa)	Ratio of FZ1 area to columnar grain area
100	78	1.122	280	2.17	3.29	0.34	130 ± 3.8	0.10
200	77	1.120	230	2.08	3.20	0.35	152 ± 5.2	0.15
300	72	1.000	204	2.17	3.17	0.46	165 ± 4.7	0.21
400	68	0.800	199	2.51	3.10	0.26	132 ± 7.4	0.37
500	59	0.550	136	1.73	2.33	0.23	102±13.4	0.44

Figure 4.15 EBSD IPF maps showing the grain structures in welds produced having power $P = 4$ kW, welding speed $S = 4$ m/min, oscillation amplitude $A = 0.6$ mm and only vary oscillation frequency f systematically from (a) 100 Hz, (b) 200 Hz, (c) 300 Hz, (d) 400 Hz (e) 500 Hz and (f) provides the grain size and area of a different region and ultimate tensile strength for all the cases. The experimental setup is given in Table 3.3

4.4 Process capability space based on sequential modelling approach for the heat transfer and fluid flow model.

Section 1.2 illustrates the sequential modelling approach and Section 3.4.4 explains the process capability space framework. Chapter 3 establishes the process capability space based on the weld thermal cycle model where the constraints are applied to the IPIs peak temperature, HAZ volume and cooling rate. The parameters space for this chapter would be the final process capability space (ω_3) established in the previous chapter. This approach decreases the total computation time to survey the whole parameters space. The two IPIs defined in this section are penetration depth (D_p) and the ratio of the width of an equiaxed zone (FZ1) and fusion zone (FZ) (W_{eqx}) at the top surface of the workpiece. The ratio of the width of the equiaxed and fusion zone is representative of the percentage of the equiaxed grains formed in the fusion zone. In laser welding, G/R values suggest the formation of columnar and equiaxed grain (see Section 4.3.3.5) in the fusion zone. The behaviour or criteria of transition of columnar grains into equiaxed grains have been well investigated in the literature [276–278], so only the final mathematical expression is discussed here, which describes the relationship between volume fraction of the equiaxed grains Φ, material-dependent and primary solidification parameters [267,277]:

$$\frac{G^n}{R} = a\left[\frac{1}{n+1}\left(\frac{-4}{3}\frac{\pi N_0}{ln(1-\Phi)}\right)^{\frac{1}{3}}\right]^n \qquad 4.7$$

$$\Delta T = (aV)^{1/n} \qquad 4.8$$

Where a and n are material-dependent properties for the constitutional tip undercooling for the growth of columnar and equiaxed dendritic growth as defined in Eq. 4.8. ΔT is the undercooling and V is the dendrite growth rate which is approximated

as the solidification rate, R. Hunt [276] found that $\Phi > 0.49$ should be considered for the fully equiaxed growth. Greer [279] proposed the value for the material dependent parameters as $n = 3$ and $a = 6.19$ K^3 m/s and N_0 is fitted to the value of 2.77×10^{13} m^{-3} for Al5xxx alloys. Geng *et al.* [267] provided the critical condition for fully equiaxed grain formation as $G^3/R < 1.66 \times 10^5$ K^3 s/mm^4. Based on this critical value for the equiaxed grain formation the width of the equiaxed grains was calculated from the numerical model. The parametric contour map for the penetration depth and width of the ratio of FZ1 and FZ is shown in Figure 4.16 for no oscillation and beam oscillation conditions with R = 0.3 mm and R = 0.6 mm.
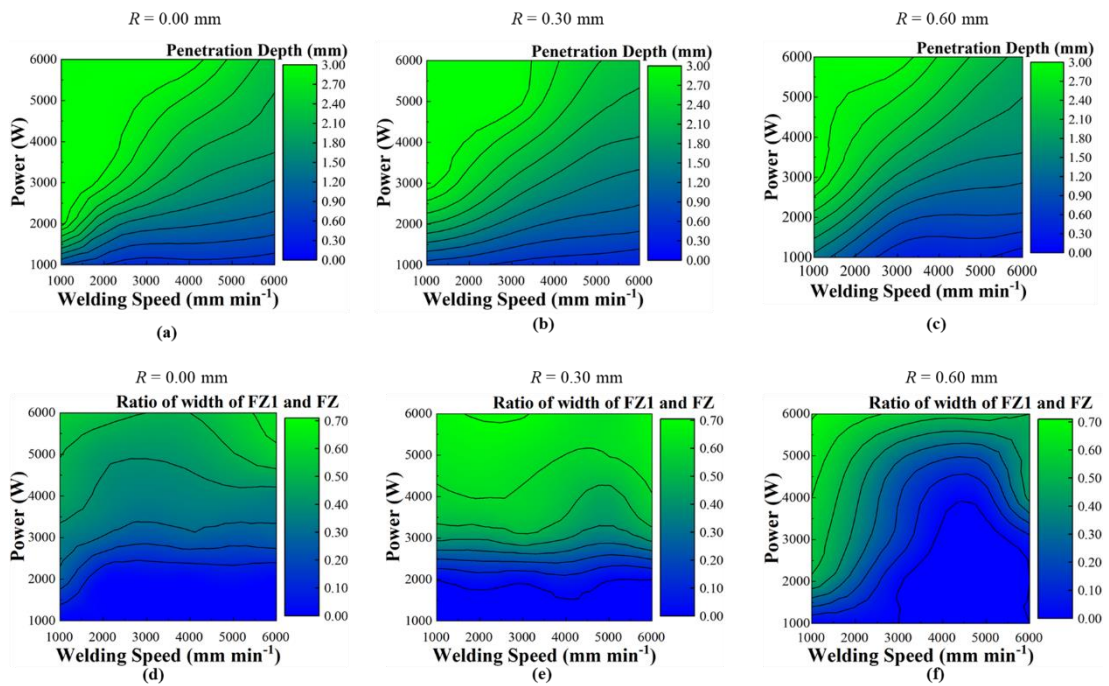
Figure 4.16 Parametric contour maps for laser power vs welding speed with and without oscillation conditions at a constant frequency of oscillation of 200 Hz. (a-c) shows a contour map for penetration depth and (d-f) shows contour maps for the ratio of the width of the equiaxed zone (FZ1) and fusion zone (FZ).

As expected, the penetration depth increases with an increase in power or decrease in welding speed for both with and without beam oscillation as shown in Figure 4.16 (a-

c). Also, for the same combinations of welding speed and power, the depth of the penetration decreases with beam oscillation due to the decrease in heat input per unit length. The ratio of the width of the equiaxed region and fusion zone increases with an increase in laser power due to a decrease in thermal gradient due to an increase in the temperature of the weld pool. As the thermal gradient decreases more regions of the fusion zone have equiaxed grain formation due to a decrease in G^3/R. At the constant depth of penetration, the W_{eqx} increases with the beam oscillation and even increases with an increase in the oscillation radius. This result is consistent with the experimental findings for the sinusoidal oscillation pattern (see Section 4.3.3.5). This is due to an increase in solidification rate R with the beam oscillation and also a decrease in thermal gradient G which decreases the total value of G^3/R, so more regions of equiaxed grains will form.
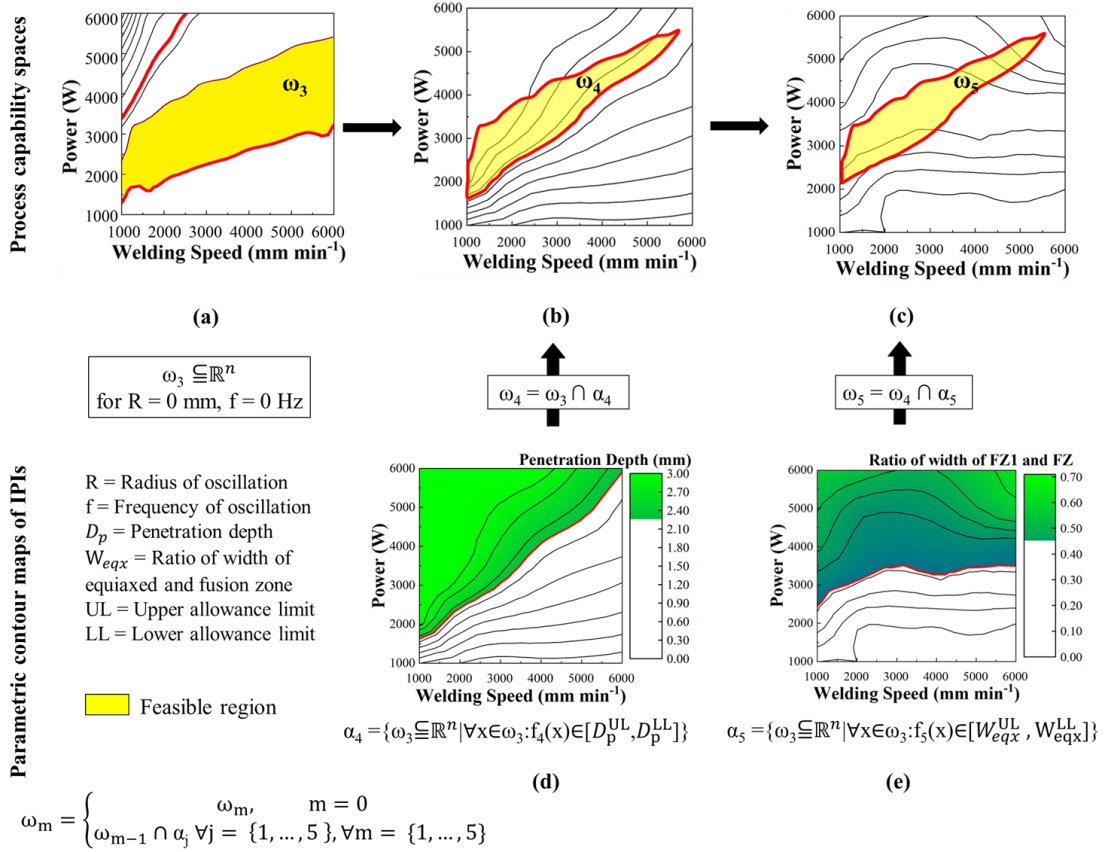
Figure 4.17 Process capability space (C_p-Space) for no oscillation condition (where $R = 0$ mm and $f = 0$ Hz). The top row shows the process capability spaces (at each step with an intersection with IPIs) and the bottom row shows the parametric contour maps of each IPIs with the allowance limit.

Figure 4.17 shows the process capability space for no oscillation welding based on the penetration depth and ratio of the width of the equiaxed zone and fusion zone. The upper limit for the D_p is through the thickness of the workpiece as in principle higher the penetration higher will be the strength in the case of butt-welding joint configuration. The lower limit of D_p is selected as 75% of the thickness of the plate because below this range the interface at the bottom region of the fusion zone act as a stress raiser which hampers the mechanical strength of the joint. Based on the experimental results in the previous section the lower limit of W_{eqx} is selected as 0.45 and the upper limit is the highest possible value. A larger region of equiaxed grains, it

generates more grain boundaries which hinder the crack propagation and improves the mechanical performance of the joints [69,105]. ω_3 is the process capability space based on the weld thermal cycle model, ω_4 is the process capability space based on the penetration depth and ω_5 is the final process capability space based on the combined weld thermal cycle and fluid flow model. It should be noted that the ω_3 will have the same region even if the order of IPIs is changed. Also, for butt welding, the penetration depth is considered an important KPI but for simplicity, it is termed IPI in this study. The final process capability space (ω_5) from the combined weld thermal cycle and fluid flow model will be the initial region or in other words parameters space when the material mixing is included.

Figure 4.18 shows the effect of beam oscillation on the process capability space. It can be also visualised as the stack up of 2D contour maps in the *xy* plane at a constant third process parameter. The process capability space will represent a plane in the 3D space which has been sectioned at a constant value of the third process parameter for better visualisation. The process capability space increases with the application of beam oscillation which suggests that the beam oscillation provides an extra degree of freedom to modify the weld thermal cycle, fluid flow and solidification behaviour of the weld.
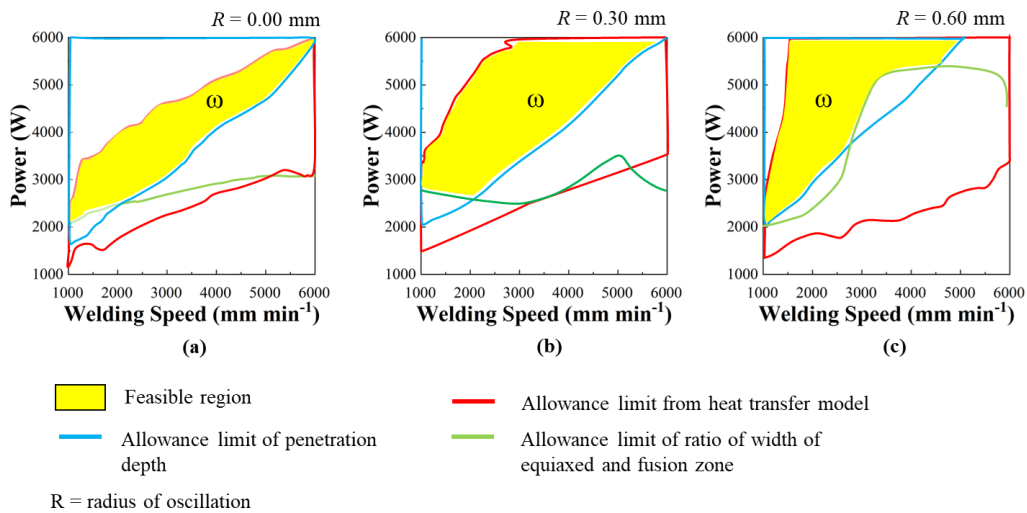
Figure 4.18 shows the process capability space for three process parameters to show the 3D response surface as a stacked-up 2D contour map. The z-axis for the 3D response surface is the radius of oscillation (R) which is varied at (a) $R = 0$ mm, (b) $R = 0.30$ mm and (c) $R = 0.60$ mm.

4.5 Conclusions

A numerical model was developed based on the finite element method to simulate heat transfer and fluid flow for laser welding for circular and sinusoidal beam oscillation patterns. The Peclet number was used to describe the ratio between heat transport by convection and conduction. Comparing no oscillation welding with beam oscillation welding shows that the Peclet number for no oscillation is greater than the value for the largest radius of oscillation. In combination with the flow profiles for larger radii, which become similar to no oscillation welding conditions, it can be inferred that the change in Peclet number is attributed to differences in thermal conduction of the oscillating heat source. This could potentially serve as a critical limit for the oscillation radius where both welding conditions are indeed similar in terms of heat transport.

The peak flow rate decreases with an increase in oscillation amplitude due to a decrease in Marangoni-driven convection due to a decrease in peak temperature. While the peak flow rate increases with an increase in oscillation frequency when the rest of the parameters are kept constant.

During full penetration welding, tensile strength increases by 21.4% with the application of beam oscillation as compared to no oscillation conditions. This is due to an increase in the percentage of equiaxed grains formed along the tensile direction which hinders crack propagation.

The solidification rate and the peak of $G{\times}R$ increase with an increase in oscillation frequency suggesting that the smallest grain will be formed at the highest oscillation frequency.

There is an intersection of the process capability spaces based on heat transfer and fluid flow models which reduces the region demonstrating the decrease in the number of experiments required to select the robust parameters.

Chapter 5. Numerical simulation of material mixing and effect of beam oscillation on the solute intermixing layer during laser welding of dissimilar high strength aluminium alloys[3]

5.1 Introduction

AlMg-Si alloys have high hot cracking susceptibility due to the rupture of the molten metal film at the grain boundaries during the solidification process [22–25]. The addition of alloying elements such as silicon, Magnesium, and copper are added to increase the strength of the alloy utilizing precipitate strengthening. But, due to the thermal treatment during the welding increases the crack susceptibility in the fusion zone of the weld. The high content of the alloying elements results in a wide solidification temperature range whereas a low concentration of alloying elements leads to a small solidification range. This results in the separation of low melting liquid film at the grain boundary leading to a crack due to the high thermal stress and thermal conductivity of Aluminium [280]. The crack sensitivity curve shows that the crack sensitivity of Aluminium is highest for the 1 wt% of Si and Mg [280]. Therefore, in conventional laser welding, a filler wire with a high concentration of Si or Mg is used to weld to decrease the susceptibility of cracking. With the use of filler wire, it serves two purposes, the first one it increases the concentration of alloying elements and moves the concentration of the fusion zone away from the peak of the crack sensitivity

---

[3] The details in this chapter have been published as:

A Mohan, Pasquale Franciosa, Dariusz Ceglarek, Michael Auinger, Numerical simulation of transport phenomena and its effect on the weld profile and solute distribution during laser welding of dissimilar aluminium alloys with and without beam oscillation. Int J Adv Manuf Technol (Under review)

curve. The second one is that it increases the solidification temperature range and reduces the cracking tendency of the welds. Modifying and optimising the chemical composition in the fusion zone is a well-studied metallurgical approach to improve the performance of the laser welds but it has a limitation in the welding speed it can go [281]. Concerning the nature of the RLW process where no filler wire is used such that it can offer high welding speed, the addition of alloying elements to the base material [105] and utilisation of dissimilar base material [282] is a logical alternative. The welding of 5xxx and 6xxx aluminium alloys is considered to be beneficial because it creates weld chemistry that has low crack sensitivity [26,27]. There are two possibilities to reduce the crack susceptibility to hot cracking: (*i*) Optimisation of process parameters to influence solidification conditions to promote the generation of equiaxed grain structure in the fusion zone and (*ii*) Welding of dissimilar aluminium alloys and optimising the concentration of alloying elements by more mixing in the RLW. The beam oscillation technique is a thermal approach to improving the weld performance by improving the mixing, which is enabled by the scanning welding head and can be fully integrated into the RLW process. This chapter focuses on the effect of process parameters on the intermixing of alloying elements and the formation of an intermixing layer with consideration to beam oscillation such that the chemical composition of the fusion zone is far away from the peak of crack susceptibility. This chapter develops a numerical simulation methodology to develop a numerical model to simulate the solute mixing during laser welding of dissimilar Aluminium alloys. The thickness of intermixing layer is estimated during laser welding with and without beam oscillation using a hybrid volumetric heat source. The dominant mechanism of solute mixing at various positions of the weld regions due to diffusion and convection is determined. The developed model is validated with the corresponding experimental

measurements. The effect of process parameters on solute mixing is determined by estimating the thickness of intermixing layer for a more direct quantitative comparison. Chapter 4 discusses the effect of process parameters on the solidification behaviour and grain morphology of the fusion zone and provides the process capability space based on the width of the equiaxed zone.

5.2 Modelling strategy

5.2.1 Assumptions

In this chapter, a 3D transient FEM model is developed to simulate the heat transfer, fluid flow and solute mixing due to diffusion and convection with a Cartesian coordinate system. The sinusoidal beam oscillation pattern is used, moving in the *xy*-plane and *x*-direction as welding direction. The following assumptions are made with the aim of reducing the computation time without significantly affecting the accuracy of the numerical solution: (a) The fluid is considered Newtonian and incompressible, and the Boussinesq's approximation is utilised to account for the change in density due to variation in the temperature and concentration; (b) No resistance to the transfer of heat, fluid and mass due to the contact between the two workpieces are considered; (c) the mass diffusion coefficient and thermal diffusion coefficient of species are considered for the species in pure Aluminium; (d) in the simulation only Aluminium, Silicon and Magnesium components are considered, and other alloy elements are ignored due to very low concentration. Please note that the other assumptions related to heat transfer and fluid flow are mentioned in Sections 3.2.1 and 4.2.1.1.

5.2.2 Governing Equations, Heat source design and Boundary Conditions

To determine the temperature distribution, velocity field and solute distribution, a coupled transient FEM model was developed based on the solution of the equations of conservation of energy (Eq. 4.4), mass (Eq. 4.1), momentum (Eq. 4.2) and solute transport (Eq. 5.1) [283]

$$\frac{\partial(\rho C_i)}{\partial t} + u.(\nabla C) = \nabla.\left(D_i \nabla C_i + D_{Ti}\frac{\nabla T}{T}\right) + \rho g \beta_c (C - C_{ref}) \qquad 5.1$$

where ρ is the density, t is the time, u is the fluid velocity, T is the temperature, C_i is the concentration of species i, D_i is the mass diffusion coefficient for species i and D_{Ti} is the thermal diffusion for species i. The first term on the left-hand side of the Eq. 5.1 represents the rate of change of the mass concentration of species i (C_i) with respect to time (t). It accounts for the temporal variation of the concentration. The second term on the left-hand side of the Eq. 5.1 represents the convective flux of species i. "u" is the velocity vector of the fluid flow, and (∇C) represents the gradient of the concentration. The dot product of these two quantities represents the flux of the species due to fluid convection. The first term on the right-hand side of the Eq. 5.1 represents diffusive flux of species i. This term accounts for the diffusive transport of the species driven by concentration and temperature gradients. The second term on the right-hand side of the Eq. 5.1 represents the buoyancy effect, often referred to as "buoyancy-driven convection" or "buoyancy-driven diffusion". This term accounts for the movement of the species caused by density variations induced by temperature differences. The Eq. 5.1 combines the effects of temporal changes in concentration, convective transport, diffusive transport driven by concentration and temperature gradients, and buoyancy-driven convection to describe the overall movement and transport of species i in a fluid.

The corresponding force terms as discussed in sections 4.2.1.2 and 4.2.1.3. Here, a combination of modified Gaussian damped, and the double ellipsoid volumetric heat source is used as discussed in Section 3.2.4. The initial temperature of the workpiece is taken as room temperature (T_0). The boundary condition for the loss of heat due to convection, radiation and evaporation are described in section 4.2.1.3. The effect of surface tension gradient due to the variation in temperature and concentration on the top surface of the workpiece is given in Eq. 5.2-5.3 [283] and the velocity along the z-direction is zero

$$-\eta \frac{\partial u_x}{\partial z} = \frac{\partial \gamma}{\partial T}\frac{\partial T}{\partial x} + \frac{\partial \gamma}{\partial C}\frac{\partial C}{\partial x} \qquad 5.2$$

$$-\eta \frac{\partial u_y}{\partial z} = \frac{\partial \gamma}{\partial T}\frac{\partial T}{\partial y} + \frac{\partial \gamma}{\partial C}\frac{\partial C}{\partial y} \qquad 5.3$$

Hybrid modified Gaussian damped heat source and double ellipsoid heat source are adopted to simulate the heat input to the workpiece.
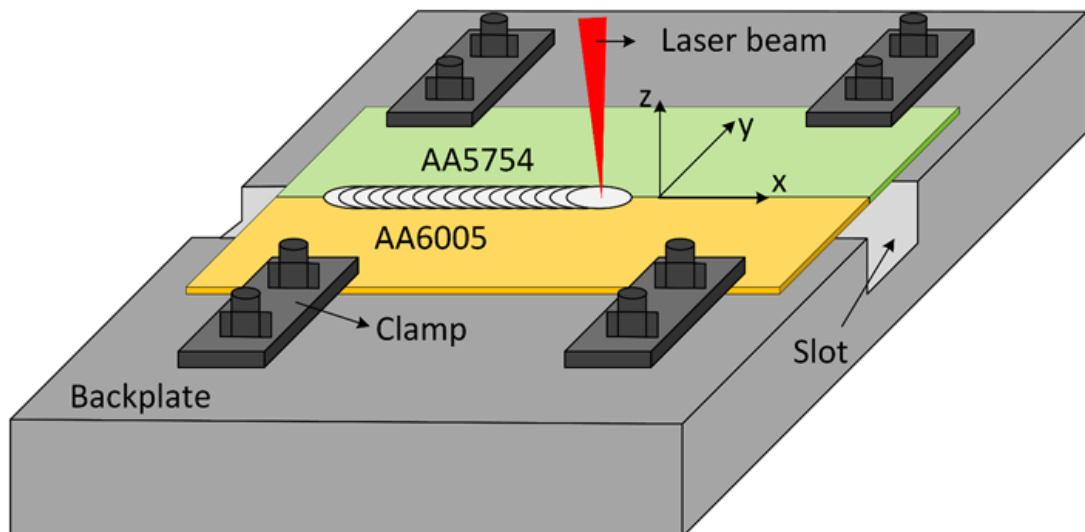
Figure 5.1 Schematic representation of the joint configuration and clamps for butt laser welding.

5.3 Experimental Strategy

Laser welding was performed in butt welding configuration with and without oscillation, the schematics of the joint configuration, and position of the clamps are shown in Figure 5.1. A 10 KW Coherent ARM FL10000 laser system was used to weld Al-5754 and Al-6005 whose chemical composition is listed in Table 5.1. The Guillotine cutter was used to machine the sheets into a coupon having dimensions 100 mm × 50 mm × 3 mm. Neither filler wire nor shielding gas was used throughout the experiments. Before welding, these coupons are cleaned with acetone to remove surface contaminations. Welding experiments are carried out with a 0 mm nominal gap between the coupons and incident beam is inclined at an angle of 4 degrees. After welding the welded samples were sectioned normal to welding direction and polished to a surface finish of 0.06 μm and the respective steps are given in Table 4.3. The samples were characterised using Zeiss Sigma scanning electron microscopy. The energy dispersive spectroscopy (EDS) data were acquired using the Aztec software platform. To ensure both repeatability and reproducibility, two samples are prepared for each weld seam, and two weld seams are generated for each combination of process parameters. A line scan is performed at a consistent position for each sample, revealing that the variation is less than 2% once noise has been eliminated from the data.

Table 5.1 Chemical composition of Aluminium alloys in weight %.

Composition	Mg	Si	Mn	Cr	Cu	Fe	Al
AA-5754	2.6-3.6	0.6-0.9	≤ 0.5	≤ 0.3	≤ 0.1	-	Bal.
AA-6005	0.4-0.8	0.9-1.4	≤ 0.1	≤ 0.1	≤ 0.1	≤ 0.35	Bal.

5.4 Results and Discussions

5.4.1 Model validation

Transport of solute during laser welding is governed by two mechanisms, namely convection due to fluid flow and diffusion due to temperature gradient. Figure 5.2 shows the comparison between the experimental and simulated solute distribution. The line scan length and position are shown in Figure 5.2 (a) and (c). Figure 5.2 (b) and (d) show the variation of the composition of Mg and Si with the distance. The fluctuation in the experimental data of the element concentration is due to the presence of pores, voids, and cracks. There is no observed fluctuation in the numerical model as these attributes have not been simulated in the numerical model. Other possible reasons for the fluctuation of the experimental data can be types of the detector, dead time of the detector, oxygen content and software settings [50]. Line scans L4, L5, and L6 are vertical scans and line scans L2 and L3 are horizontal line scans. The vertical lines are scanned from top to bottom and the horizontal lines are scanned from left to right as shown in Figure 5.2. The position of the vertical line scans is selected in such a way as to provide granular details of the element concentration in Al-6005, Al-5754 and through fusion zones. Similarly, the position of the horizontal line scans is selected to provide the transition between the alloys and the transition between the alloys through the fusion zone. The combinations are selected such that proper validation is possible. Line scan L4 is in the complete region of Al-6005 which is a Si-rich alloy, so the element distribution on line L4 shows a horizontal line for Si and Mg throughout the scan length which shows no change in the element concentration. The simulated line is also straight. In line scan L5, the scanning starts from the fusion zone to the AL-6005 crossing the fusion zone boundary. The Mg concentration increases inside the fusion zone centre to the boundary of the fusion zone and again decreases from the fusion boundary to the Al-6005 alloy. This is due to the movement of the Mg from a

higher concentration to a lower concentration. The concentration of the Mg is higher at the boundary of the fusion zone as compared to the middle of the fusion zone. The concentration of the Si decreases from the middle of the fusion zone to the boundary and increases from the fusion boundary to the Al-6005 alloy as it is rich in Si concentration. The same trend is found in the simulated results. The line scan L6 is in the complete region of Al-5754 which is an Mg-rich alloy. The concentration profile for both alloys is constant throughout the length of the scan which matches the simulated results. The horizontal line scan L3 start from the Al-6005 to Al-5754 alloy. So, the concentration of Mg and Si remains constant till the boundary of one alloy changes suddenly according to the other alloy. Similar values are estimated from the simulation. The line scan L2 which originates from Al-6005 passes through the fusion zone to Al-5754 alloy. Due to the convection and diffusion solute concentration changes. The Mg concentration remains constant till the fusion zone boundary and then increases in the fusion zone and becomes maximum at the Al-5754 alloy. Similarly, the Si concentration is constant till the fusion zone boundary then decreases through the fusion zone and is at a minimum at the Al-5754 alloy region. The simulated result is in good agreement with the experimental results which manifests the validity of the model to predict solute distribution during laser welding.
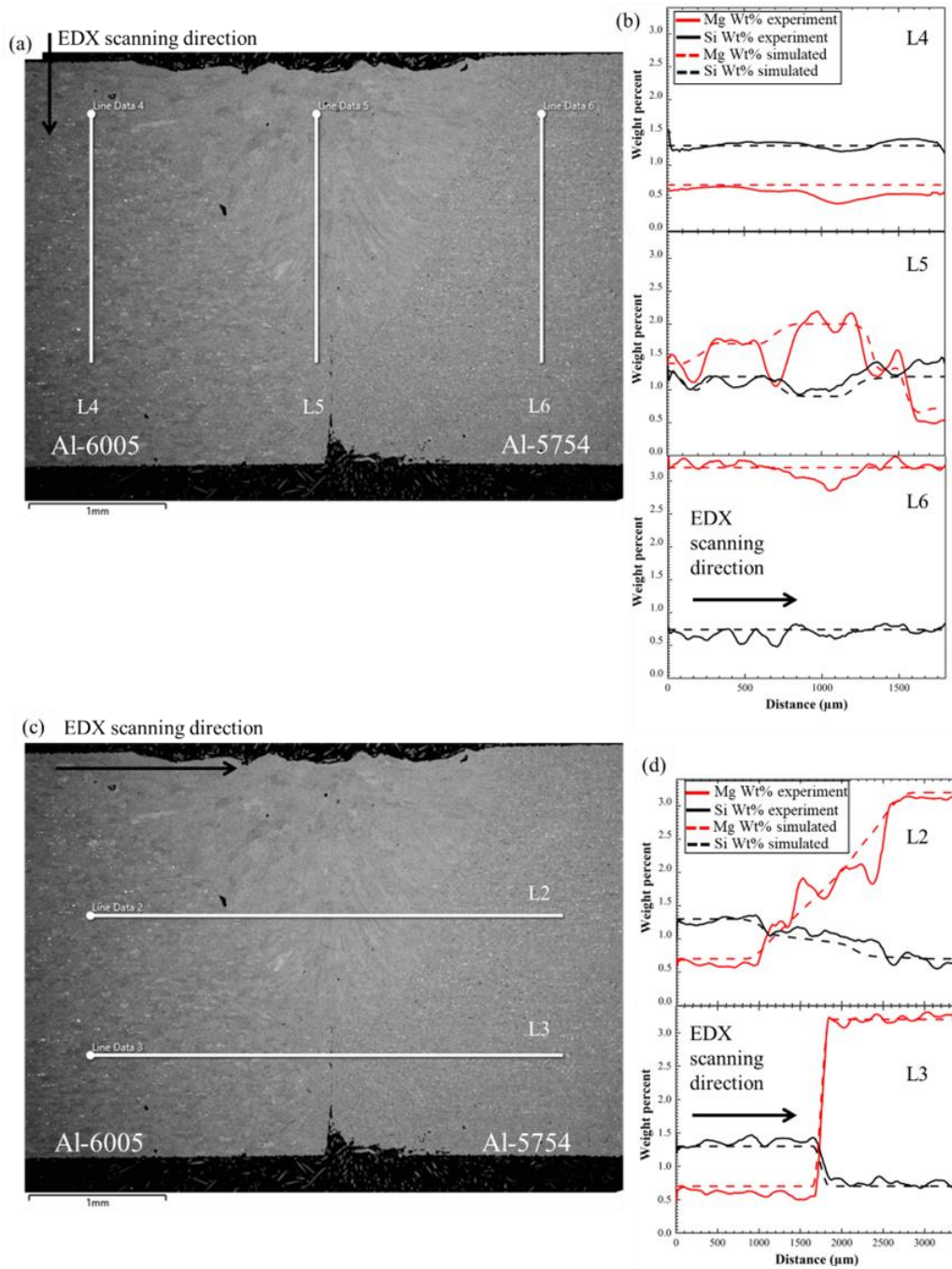
Figure 5.2(a) SEM micrograph with the position of the line scan for element distribution, (b) element distribution experimental using EDS line scan and simulated (c) SEM micrograph with the position of the line scan for element distribution, (d) element distribution experimental using EDS line scan and simulated having Laser power of 4.5kW, welding speed of 4 m/min, oscillation Amplitude = 0.6 mm and oscillation frequency = 100 Hz.

188

5.4.2 Effect of process parameters on the solute intermixing layer
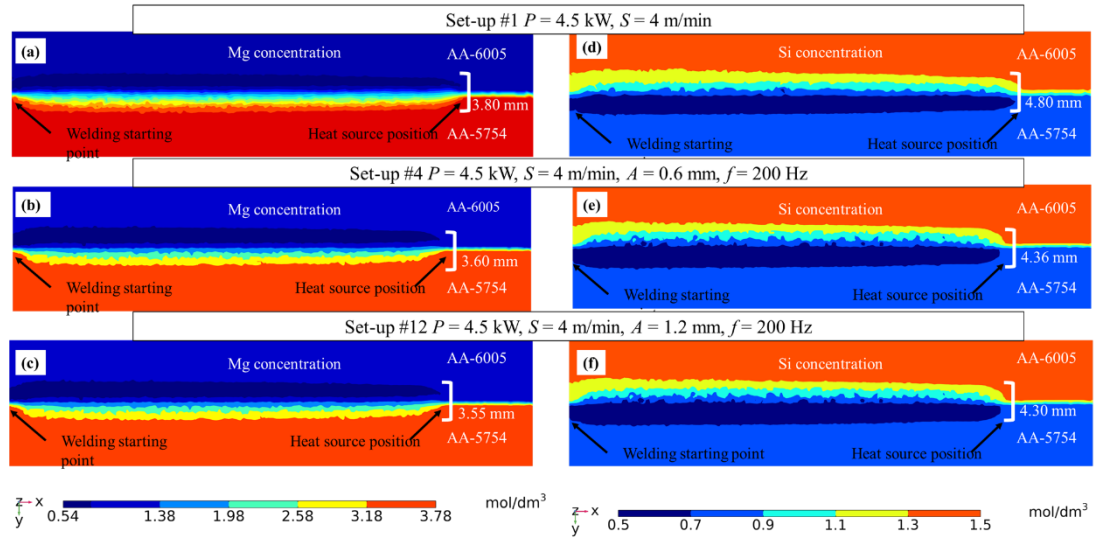
Figure 5.3 shows the Mg concentration (a-c) and Si concentration (d-f) at different setups. The experimental setup is given in Table 3.3

Figure 5.3 shows the concentration of Mg and Si for no oscillation and beam oscillation conditions. AA-5754 is Mg-rich and AA-6005 is a Si-rich alloy. During welding, there is a mixing of Mg and Si from the alloy having a higher concentration to a lower concentration around the fusion zone. This intermixing is due to convection and diffusion. The thickness of the solute intermixing layer depends upon the process parameters. The thickness of the Si-layer for setups #1, #4 and #12 are 4.80 mm, 4.36 mm and 4.30 mm respectively. Similarly, for Mg-layer for setups #1, #4 and #12 are 3.80 mm, 3.60 mm and 3.55 mm. At the same welding speed and laser power, the thickness of this layer decreases when beam oscillation is applied due to a decrease in thermal gradient and an increase in cooling rate. Solute movement is dominant at the fusion zone boundary due to the diffusion mechanism. It should be noted that the weld width is ≤ 3.1 mm for all the cases and the width of the intermixing layer is more than the weld width. This suggests that the solute distribution occurs due to both diffusion

189

and convection during welding. The thickness of this layer further decreases with the increase in oscillation amplitude due to a decrease in thermal gradient and increase in cooling rate which diminishes the effect of diffusion at the boundary. Figure 5.3 also depicts the start and the position of the heat source. The start point is 1 mm from the end of the coupons. Therefore, the mixing starts when the welding starts till the position of the heat source which logically follows the results depicted.

5.4.3 Process capability space based on the sequential modelling approach based on combined heat transfer, fluid flow and mass transport model
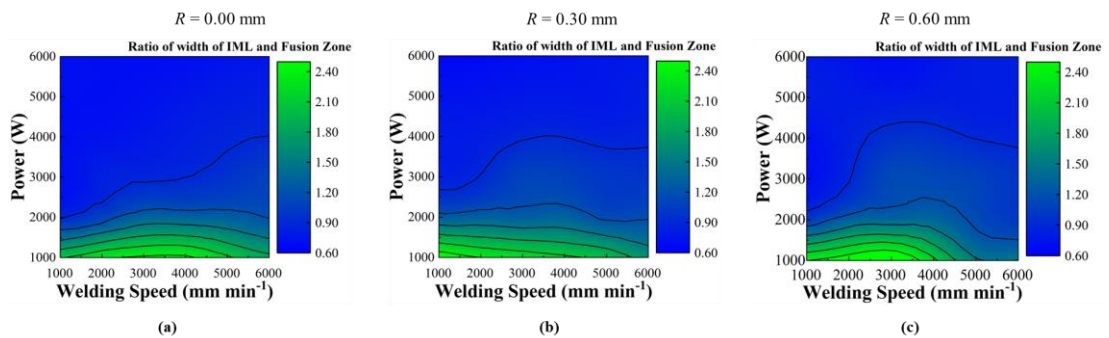
Figure 5.4 Parametric contour maps for laser power vs welding speed with and without oscillation conditions at a constant frequency of oscillation of 200 Hz. (a-c) shows a contour map for the ratio of the width of intermixing layer and the width of the fusion zone.

Figure 5.4 show the simulated ratio of the width of intermixing layer (IML) and the width of the fusion zone at the top surface of the workpiece for different combinations of welding speed and laser power for both with and without beam oscillation conditions. The width of the IML is calculated as the average width for the thickness of the Si-layer and Mg-layer in and around the fusion zone. The movement of alloying elements is governed by both diffusion (due to thermal and concentration gradients) and convection (due to fluid flow in the molten weld pool) which is dependent on the

190

process parameters. At a constant laser power, this ratio increases with an increase in welding speed up to critical welding speed and then again decreases with a further increase in welding speed. At a constant welding speed, the ratio of the width of intermixing layer (IML) and the width of the fusion zone decreases which suggests that the intermixing is more dominant towards the conduction mode of welding and this type of movement is more dominant due to diffusion phenomena. Also, from Figure 5.4, it can be visualised that the width of intermixing layer is more as compared to the no oscillation condition. This is due to the churning action by the oscillating beam leading to more convection in the molten pool. Figure 5.5 shows the process capability space for no oscillation welding based on the ratio of the width of IML and fusion zone. The ω_5 is the process capability space from the combined heat transfer and fluid flow model which acts as a parameters space for the mass transport model combined with previous models. The lower limit of the ratio of the width of intermixing later and fusion zone is taken as 1 as in principle the modification of chemical composition should be at least cover the whole fusion zone. From Figure 5.5, it is clear there is no solution due to the two opposing boundary constraints. As in this section, the intermixing is more prevalent close to the conduction mode of welding while the requirement from the section is to have higher penetration which leads to no solution. This shows that the material will be prone to cracking and is independent of the process parameters. To overcome the problem there should be a balance between the depth of penetration and material mixing. Less mixing at a high depth of penetration makes the joint susceptible to cracking which leads to failure and at a low depth of penetration joint will have lower mechanical strength due to lower coalescence between the plates. It also suggests that there is a need to modify the linear

191

welding in the RLW process in such a way that it increases the mixing at a higher depth of penetration such as beam oscillation and beam shaping.
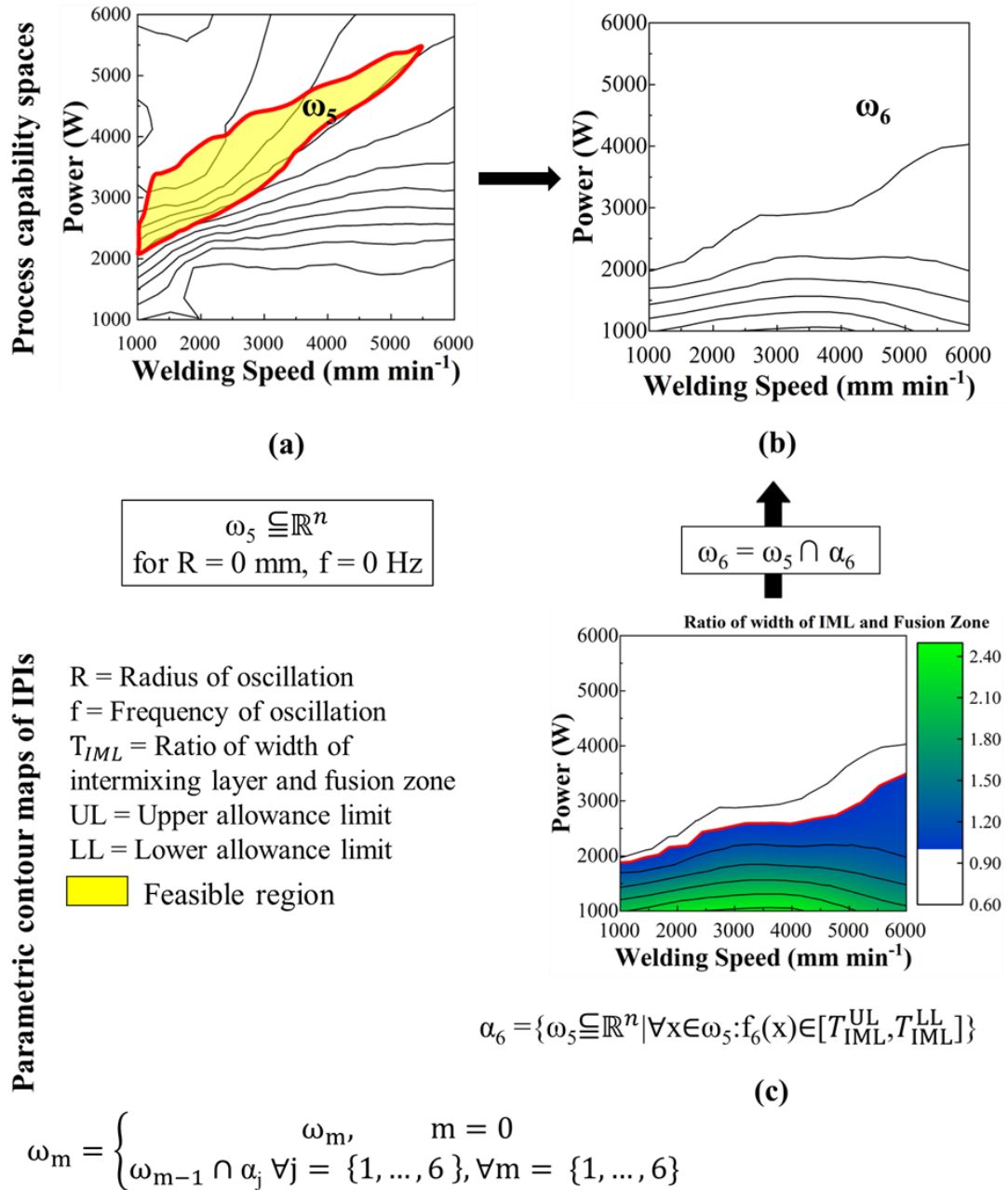
Figure 5.5 Process capability space (C_p-Space) for no oscillation condition (where R = 0 mm and f = 0 Hz). The top row shows the process capability spaces (at each step with an intersection with IPIs) and the bottom row shows the parametric contour maps of each IPIs with the allowance limit.

Other way is to modify the chemical composition of the weld either by adding the alloying element in the base metal which increase the grain refinement such as Titanium or using filler wire.

Figure 5.6 shows the effect of beam oscillation on the final process capability space. The results show that with the application of beam oscillation small intersecting region is there which increases with an increase in oscillation radius. The increase in the feasible region is due to the increase in convection due to the churning action of the beam oscillation.
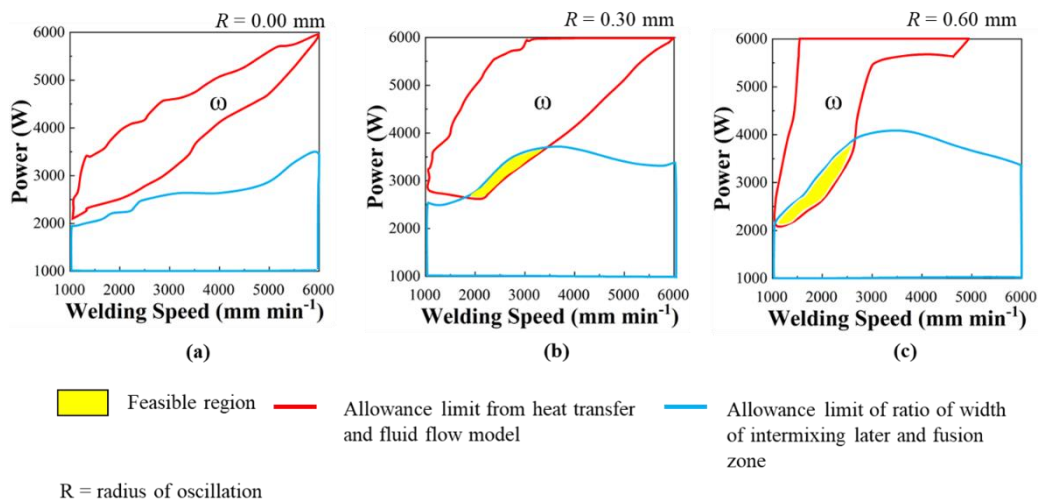
Figure 5.6 shows the final process capability space for three process parameters to show the 3D response surface as a stacked-up 2D contour map. The z-axis for the 3D response surface is radius of oscillation which is varied at (a) $R = 0$ mm, (b) $R = 0.30$ mm and (c) $R = 0.60$ mm.

5.5 Conclusions

The transport phenomena during laser welding with and without beam oscillation have been developed with various combinations of volumetric hybrid heat sources. The simulated model was verified by comparing the solute distribution measured

experimentally using EDX line scans and from the simulated graph. The sudden dip in the values of solute concentration during the line scan is due to the presence of pores on the path. The mechanism of solute movement is both diffusion and convection which can be attributed by comparing the weld width and thickness of intermixing layer. As the thickness of intermixing layer is larger than the weld width this shows that solute transport is due to diffusion as there is no convection outside the fusion zone. So, convection is dominant in the molten pool region which is the fusion zone and diffusion is dominant at the fusion boundary. Both mechanisms are comparable in the mushy zone. At the same welding speed and laser power, the solute intermixing layer thickness decreases when beam oscillation is applied as diffusion of solute at the boundary decreases due to a decrease in thermal gradient and an increase in cooling rate.

The parametric contour maps show that the ratio of the width of intermixing layer and the width of the fusion zone increases with the application of beam oscillation. This is a more reliable parameter to investigate the effect of beam oscillation on material mixing in place of comparing the actual width for the same combination of welding speed and laser power as the penetration depth decreases with the application of beam oscillation. The final process capability space shows that without oscillation condition has no solution while for beam oscillation condition generates the solution. The final process capability space increases with an increase in the radius of oscillation.

Chapter 6. Use of thermal and fluid flow modelling to investigate the capability of beam shaping technology using Adjustable-Ring-Mode (ARM) laser beam on the solidification parameters and grain morphology in remote laser welding of high strength aluminium alloys[4]

6.1 Introduction

This chapter aims to explore the capability of new emerging laser technology of beam shaping for E-mobility manufacturing by investigating the impact of the Adjustable Ring Mode laser beam on the weld microstructure and mechanical performance of 6xxx series aluminium alloy lap joints. Aluminium 6xxx alloys are well known for their susceptibility to hot cracking. Optimising the chemical composition in the fusion zone is a well-studied metallurgical approach to improving the performance of laser welds, for example, the selection of proper filler material during the conventional laser welding process [281]. Concerning the nature of the RLW process where no filler wire is used, the addition of alloying elements to the base material [105] and utilisation of multi-layer base material [282] have been reported alternatively. Researchers proposed the beam oscillation technique as a thermal approach to improving the weld performance, which is enabled by the scanning welding head and can be fully integrated into the RLW process, providing flexibility in defining spatial energy distribution within the weld zone. The wavelength and shape of the laser are the key parameters during the laser materials processing which affects the absorption rate of the laser on the surface of the material [284]. Therefore, it is of

---

great significance to investigate the beam shaping technique, which enables the tuning of beam shape and size directly from the feeding fibre, was proposed as an additional thermal approach to improve welding performance [285].

Subsequently, Coherent Inc introduced the adjustable-ring-mode (ARM) laser beam [189], consisting of an inner spot beam and an outer ring beam. The idea of using the Adjustable Ring Mode (ARM) laser is to improve the laser absorptivity of Aluminium and provide freedom related to the orientation of two concentric beams as compared to twin-spot laser. In this technique, the front part of the ring is used to preheat the workpiece followed by core laser which improves the laser absorptivity [286]. The combination of centre and ring laser leads to superior temperature distribution during ARM laser. This superior temperature distribution influences the grain evolution during welding of Aluminium alloys. This chapter implements the developed research methodology to investigate the effect of ARM laser welding of Aluminium alloys. The influence of laser power combinations on the weld geometry, weld mechanical performance, weld zone grain structure and temperature field are analysed. The effect of temperature distribution on the solidification parameters is analysed to provide insight into the solidification behaviour during ARM laser welding. Along with ARM laser beam oscillation is also employed based on the previous study. The total power i.e., the total power of core and ring lasers is kept constant such that the net heat input to the workpiece remains constant. A coupled three-dimensional heat transfer and fluid flow model was developed to investigate the effect of core/ring power ratio on the thermal history and provide insight into the resultant solidified grain morphology.

The chapter is organised as follows: Section 6.2 discusses the modelling strategy for the ARM laser welding with beam oscillation in lap joint configuration;

Section 6.3 presents the experimental strategy, the steps involved for the characterisation of weld geometry, weld mechanical performance and grain structure; Section 6.4 presents the effect of varying power ratio the weld attributes and relation between the solidification parameters calculated from the numerical model with the grain structure. Finally, conclusions are summarised in Section 6.5.

6.2 Modelling strategy

6.2.1 Assumptions and governing Equations

To understand the evolution of thermal history as a function of the power ratio of ARM laser, a transient three-dimensional numerical model is developed based on the finite element method (FEM). A volumetric hybrid heat source is employed to model the heat distribution from the laser to the workpiece. A three-dimensional cartesian system is utilised with the laser head moving in the positive x-axis, the y-axis is defined as the weld cross-section direction along the width of the workpiece, and the z-axis is defined as the direction of weld penetration. The oscillating laser beam is composed of two types of motions in the x-y plane: a sinusoidal motion and a linear forward motion in the welding direction. Following assumptions are made to improve the efficiency of the calculation without affecting the accuracy: (a) the liquid metal formed is considered Newtonian and incompressible, and fluid flow is considered laminar; (b) Boussinesq's approximation is used to account for the change of density due to temperature variations [264]; (c) the surface of weld pool formed is considered flat and keyhole dynamics are not considered to simplify the model and decrease the computational time, whereas a volumetric heat source model is used to replicate keyhole which is a common practice as evidenced by [222,239,264,266,287,288]; (d) temperature-dependent material properties are considered; (e) no vapour and plasma

flow is considered in the simulation; (f) the absorption of laser energy by the workpiece is kept constant which is assumed to be independent of temperature changes; (g) the laser absorption coefficient is kept the same for the ring and the core. Just to note that the absorption have been increased by 10% when the model was calibrated for the beam shaping as compared to without beam shaping. This observation matches with idea to improve the laser absorptivity of Aluminium using the front part of the ring beam to preheat the materials thus increasing the laser absorptivity [286]. Please note that the other assumptions related to heat transfer and fluid flow are mentioned in Sections 3.2.1, and 4.2.1.1. The governing equations of conservation of energy (Eq. 4.4), mass (Eq. 4.1) and momentum (Eq. 4.2) and corresponding force terms are adopted as expressed in section 4.2.1.2 and 4.2.1.3. The initial temperature of the workpiece is assumed to be maintained at ambient temperature (T_0). Heat loss at the top surface due to convection, radiation and evaporation is given as follows in Eq. 2.15-2.16 in section 2.6.1. Flow condition for the free liquid surface due to the surface tension gradient due to variations in temperature is given in Eq. 2.21 in section 2.6.2.

6.2.2 Heat source design

The general trajectory of the moving laser beam is defined in Eq. 3.3 where (x_0, y_0, z_0) is the origin, S is the welding speed, A is the oscillation amplitude, and f is the oscillation frequency. To include beam inclination as illustrated in Figure 6.2, the trajectory of laser beam can be further determined as:

$$x' = x_{(t)} \qquad\qquad 6.1$$
$$y' = \cos(a)\big(y - y_{(t)}\big) - \sin(a)(z - z_{(t)})$$
$$z' = \cos(a)\big(z - z_{(t)}\big) - \sin(a)(y - z_{(t)})$$

Where a is the angle of inclination, x', y' and z' are the coordinates of laser beam after the inclination. The total heat input to the workpiece is the summation of

198

energy absorbed by the core and the ring part of the laser as given in Eq. 6.2 where Q_{core} is the heat input by the core beam and Q_{ring} is the heat input by the ring beam.

$$Q_{laser}(x, y, z, t) = Q_{core}(x, y, z, t) + Q_{ring}(x, y, z, t) \qquad 6.2$$

The core beam is simulated as a hybrid volumetric heat source consisting of a double ellipsoid heat source [258] and a rotating Gauss body heat source [218,247] as described in Section 3.2.4 and defined in Eqs. 3.11 - 3.12. The ring beam is simulated as surface heat flux in the top-hat mode and expressed in Eq. 6.3

$$Q_{ring}(x, y, z, t) = \frac{\alpha P_r}{\pi(r_o^2 - r_i^2)} \qquad 6.3$$

Where P_r is the power of the ring beam, r_o and r_i is the outer and inner radius of the ring, respectively.

6.2.3 Calculation domain and numerical implementation

The simulations were performed using COMSOL Multiphysics 6.0 software. The algebraic multigrid (AMG) solver was adopted as it provides robust solutions for large CFD simulations. For problems solved for space and time, discretisation in space is done using the finite element method and time is discretised using the backwards differential formula (BDF). The damped Newton method is used to solve a fully coupled system of non-linear equations and the generalised minimal residual (GMRES) method is used to solve fluid flow. The simulation domain for a single plate has a geometry of 100 mm × 50 mm × 3 mm. Each plate has been divided into five domains to improve mesh distribution having very fine mesh at the weld centerline, fine mesh at the fusion zone and coarser mesh at the base metal as shown in Figure 6.2. The mesh was finer for the upper plate where the laser beam is deposited as compared to the bottom plate to reduce the computation time. Mesh sensitivity

analysis was conducted based on both temperature and fluid flow velocity before finalizing the mesh size and distribution. Tetragonal mesh with linear interpolation is used with a total of 1550639 mesh elements having degrees of freedom at 1679454. At the weld centerline, the minimum mesh size is $r/2$ which is 35 μm, maximum mesh size is $2r$ having a maximum element growth rate of 1.05 with a curvature factor of 0.2 is used (r is the laser spot radius of the core beam). At the fusion zone, the minimum mesh is r, the maximum mesh size is $5r$ having a maximum element growth rate of 1.02 with a curvature factor of 0.2 and at the base metal, the minimum mesh size is 830 μm having a maximum element growth rate of 1.13 with a curvature factor of 0.5. No gaps between plates are considered. The main material properties of the studied material are listed in Table 6.1 calculated from JMatPro [289].
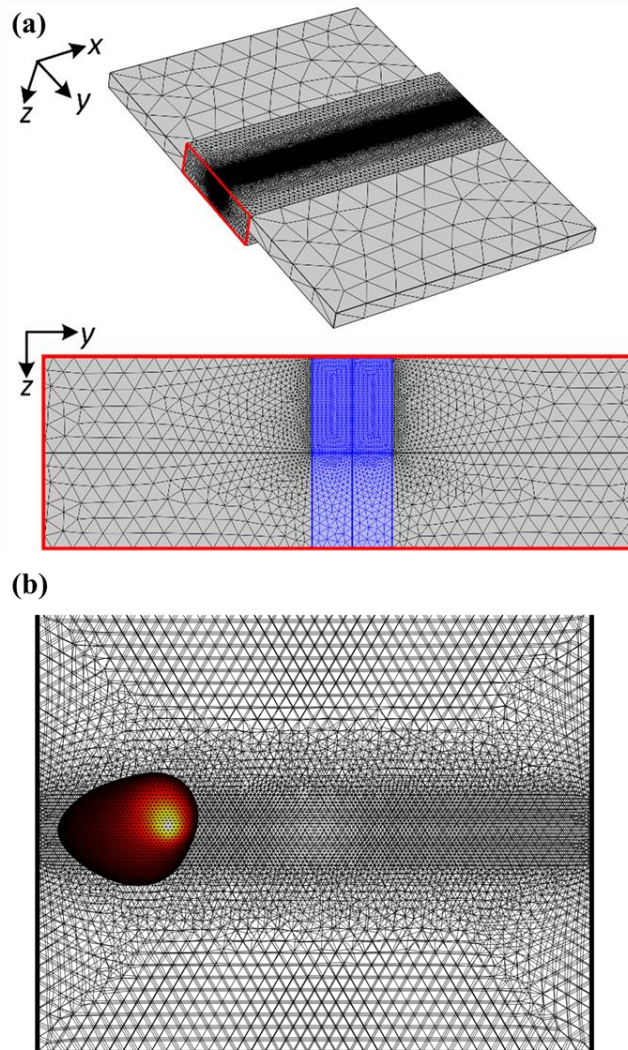
Figure 6.1 (a) Schematic illustration of modelling domain and mesh distribution used for the simulation and (b) weld pools with mesh distribution. Just to note weld dimensions have no significant variation for all the power ratios.

Table 6.1 Material properties of the 6xxx aluminium alloys calculated by JMatPro [289]

Density of solid (kg·m^{-3})	2695 (293K)	Density of liquid (kg·m^{-3})	2389
Specific heat of solid (J·kg^{-1}·K^{-1})	903 (293K)	Specific heat of liquid(J·kg^{-1}·K^{-1})	0.00117 (923K)
Viscosity (Pa·s)	0.0013 (923K)	Solidus (K)	823
Surface tension (kg·s^{-2})	0.82 (923K)	Liquidus (K)	923
Thermal conductivity (W·mm^{-2}·K^{-1})	207 (293K)	Latent heat of fusion (J·kg^{-1})	3.96E+5

6.3 Experimental details

The material studied in this paper belongs to 6xxx series aluminium alloy in T6 temper and the nominal chemical composition is shown in Table 6.2, measured by Foundry-Master Pro2 optical emission spectrometer. Plates were machined into the size of 100 mm (length) $\times$ 45 mm (width) $\times$ 3 mm (thickness) and cleaned with acetone to remove surface contaminations prior to welding. A lap joint configuration with an overlap length of 20 mm was employed, as schematically illustrated in Figure 6.2 (a). To avoid heat sinking, a slot with a width of 15 mm was machined in the backplate and located well beneath the weld seam. No shielding gas or filler wire was used throughout.

Table 6.2 Nominal compositions of the studied material, measured by Foundry-Master Pro2 optical emission spectrometer.

Chemical composition limits	Element (wt. %)						
	Mg	Si	Cu	Mn	Fe	Ti	Al
Minimum	0.54	0.52	-	0.12	0.15	0.08	Balance
Maximum	0.62	0.58	0.05	0.17	0.25	0.10	Balance

A 10 kW ARM fibre laser source (HighLight FL10000-ARM, Coherent), evenly assigned to ring beam and core beam, delivered by Precitec YW52 remote welding head with a collimating length of 150 mm and focal length of 300 mm. A glass material with a low refraction index is designed to isolate the core and ring beam [290]. Fibres with a diameter of 70 µm for the core beam and 180 µm for the ring beam diameter were utilised, which leads to the diameter at the focus of 140 µm for the core beam (d_c) and 360 µm for the ring beam (d_r), respectively, as shown in Figure 6.2 (a).
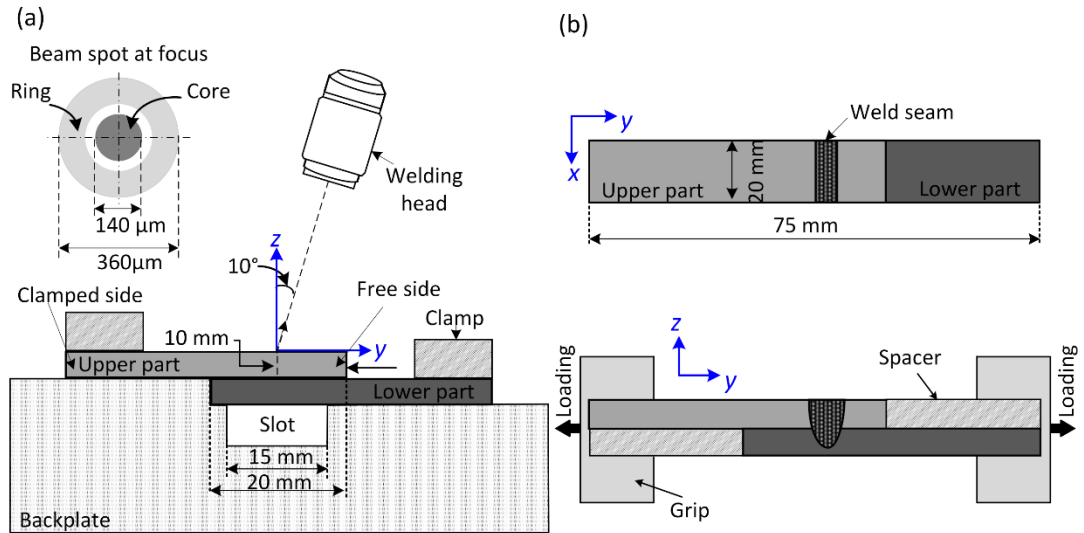
Figure 6.2 Fig. 1. Schematic diagram showing the experimental setup for (a) welding test with the ARM laser beam and (b) specimen geometry and tensile lap shear tests.

During welding, the welding head was tilted at 10° from the vertical direction (*z*-axis) and the laser beam was focused on the top surface of the upper part at 10 mm (along the *y*-axis) from the free edge, as illustrated in Figure 6.2. Constant welding speed (*S*) of 50 mm/s and the transverse oscillation frequency of 50 Hz was adopted throughout all welding trials. The matrix of studied welding parameters, including transverse oscillation width (*A*) and core/ring power ratio (P_c / P_r) is summarised in Table 6.3. The optimised *A* was subsequently employed to investigate the impact of power ratios on the grain morphology of the weld and mechanical strength. It should be noted that the total power in the study of power ratio was increased by 0.75 kW compared to weld trials for the pre-selection of *A* to allow sufficient bonding between the two plates over a wide range of power ratios. Theoretical Intensity profiles of the ARM laser at the focus plane with different power ratios with a constant total power of 6 kW are visualised in Figure 6.3. It is worth to note that due to the limitation of the equipment to have core and ring have maximum power of 5 kW. So, no experiments

can be done with only core and only ring but these conditions are simulated by the model to develop the complete trend on the effect of ARM laser beam welding.

Table 6.3 Matrix of welding parameters studied in this paper.

Pre-selection of Beam Oscillation Width			
Oscillation width A (mm)	0; 0.5; 1.5; 2.5; 3.5	Power of core beam P_c (kW)	3.25
Power of ring beam P_r (kW)	2.00	Power ratio P_c/P_r	1.63
Study of Power Ratio			
Oscillation width A (mm)	2.5;	Power of core beam P_c (kW)	1.00; 1.50;2.00; 2.50; 3.50;
Power of ring beam P_r (kW)	5.00; 4.50; 4.00; 3.50; 2.50;	Power ratio P_c/P_r	0.20; 0.33; 0.50; 0.71; 1.40

P_c/P_r=0.20 P_c/P_r=0.33 P_c/P_r=0.50 P_c/P_r=0.71 P_c/P_r=1.40
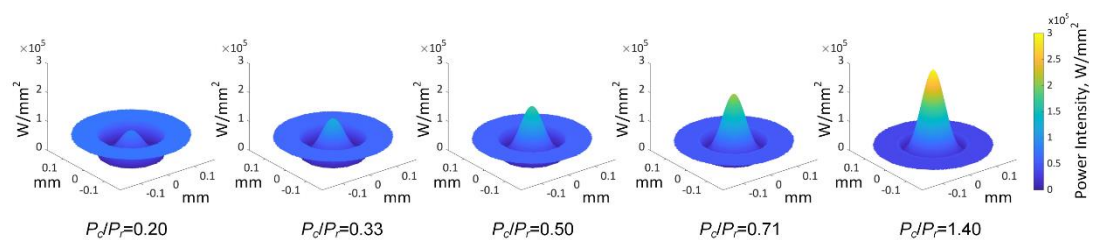
Figure 6.3 Theoretical Intensity profiles of ARM laser at focus plane with different power ratios with a constant total power of 6 kW.

The welded samples were sectioned normal to the welding direction and polished to a 0.06 µm surface finish, followed by etching in caustic sodium fluoride reagent (2% NaOH + 5% NaF + 93% water). The weld geometry was determined using Keyence VHX7000 optical microscope along the transverse (y-z) cross-section. Weld zone grain structure was characterised by EBSD mapping on unetched samples with additional vibratory polishing in colloidal silica suspension for three hours. EBSD was conducted on a JEOL 7800F scanning electron microscope, equipped with an Oxford

Instruments' Symmetry II EBSD detector and AZtec acquisition software with an accelerating voltage of 20 kV and a step size of 3 µm. Tensile lap shear tests were conducted along the transverse direction at a constant extension rate of 1 mm/min, following ISO standards 6892 [291] on Instron® 3360 tensile machine equipped with the 30 kN load cell, Figure 6.2 (b). Specimens for the tensile test had an effective weld seam length of 20 mm and tests were repeated four times at each welding condition. The mechanical strength of the welded structure was evaluated by the maximum load (kN) from the load-strain curve. It should be noted that both micro-hardness measurement and tensile test were conducted after post-weld natural ageing for one month.

6.4 Results and discussion

6.4.1 Pre-selection of Beam Oscillation Width

Weld cross-sections at different oscillation widths were shown in Figure 6.4 (a), and the evolution of fusion zone geometry, e.g., weld interface width (W_I) and weld penetration (P), was summarised in Figure 6.4 (b) - (c). Results show that a higher oscillation width can effectively increase weld interface width but reduce weld penetration. In addition, an excessive oscillation width, i.e., A_y= 3.5 mm, leads to an unbonded area in the weld centre as highlighted and consequently reduces the effective weld interface width. The evolution of weld geometry is closely related to the change in laser energy distribution. With the transverse oscillation, peak laser energy density is redistributed at two turning points of the oscillating path instead of the weld centre (as seen in the case of non-oscillation (A_y= 0)). Furthermore, as the oscillation width increases, the energy deposited field is more spread but with a mitigated intensity due to the fixed total input power.
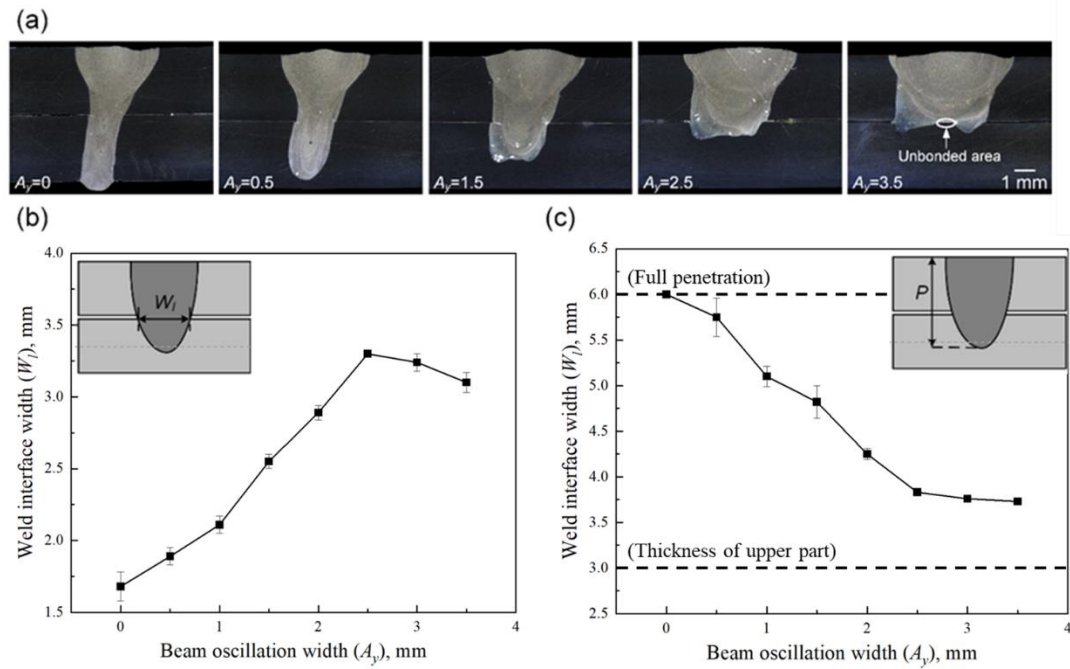
Figure 6.4 (a) Cross-section morphology of welds produced with different oscillation widths at the power of $P_c = 3.25$ kW, and $P_r = 2$ kW, and evolution of weld geometry: (b) weld interface width (W_I) and (c) weld penetration (P). Welding trials were conducted at the constant total power of 5.25 kW, a power ratio of 1.63, an oscillation frequency of 50 Hz and a welding speed of 50 mm/s.

The evolution of joint strength in response to the beam oscillation width was investigated by tensile lap shear tests along the transverse direction and demonstrated in Figure 6.5 (a). An improvement of the maximum linear load from 170 N/mm to 275 N/mm can be gained by increasing the beam oscillation width, which is essentially related to the enhanced weld interface width. Failure position was determined within the fusion zone for all tests as shown in Figure 6.5 (b) and two failure modes were identified i.e., interface failure and fusion boundary failure. For the overlap joint configuration, stress concentration under tensile shear loading initiates at the fusion boundary near faying surface between two plates and predominantly develops along the shortest path [292]. Therefore, the transition of failure mode at $W_I \geq 3.1$ mm results from the fact that the shortest path for the accommodation of stress concentration diverts into the through-thickness direction instead of the width interface direction.

Similar observations were also reported in [292,293]. In addition, the fractography in Figure 6.5 (c) confirms the presence of an un-bonded region at an excessive oscillation width, which reduces the effective weld interface width and, resultantly, the joint strength. Therefore, an optimised A_y of 2.5 mm was determined for studying the effect of the power ratio of the ARM laser in the following sections.
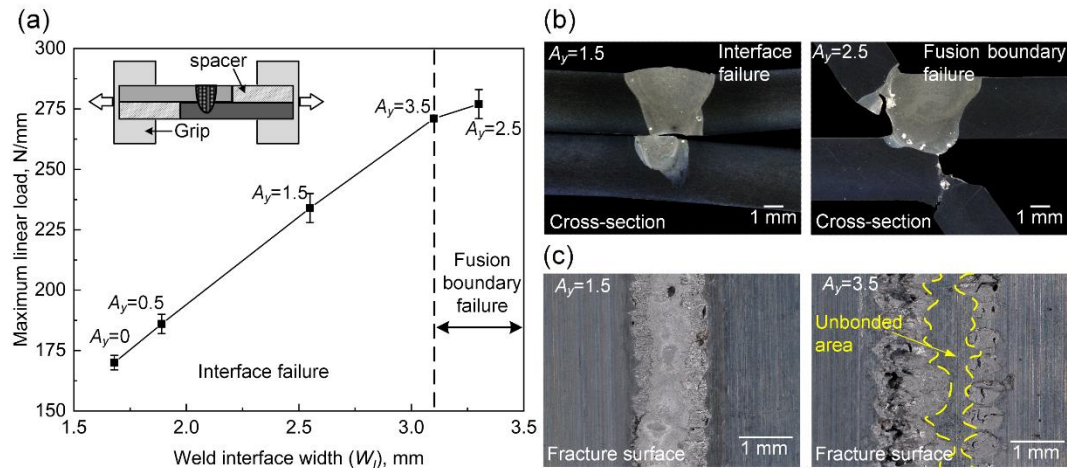
Figure 6.5 (a) Plot of the maximum linear load during tensile lap shear test as a function of weld interface width, (b) cross-section view of interface failure and fusion boundary failure, and (c) comparison of fractography in welds at A_y= 1.5 mm and A_y = 3.5 mm, showing the reduction of weld strength as a result of the unbonded region at excessive oscillation width.

6.4.2 Effect of ARM laser power ratio on weld geometry

Figure 6.6 shows optical cross-sections of welds produced at different core/ring power ratios. Overall, a slight reduction of weld interface width and a minor increase in weld penetration was determined when a higher portion of power was assigned to the core beam. In addition, it is clear that the variation of weld geometry resulting from different power ratios is significantly reduced compared to the case with various beam oscillation widths, as indicated by the grey area.
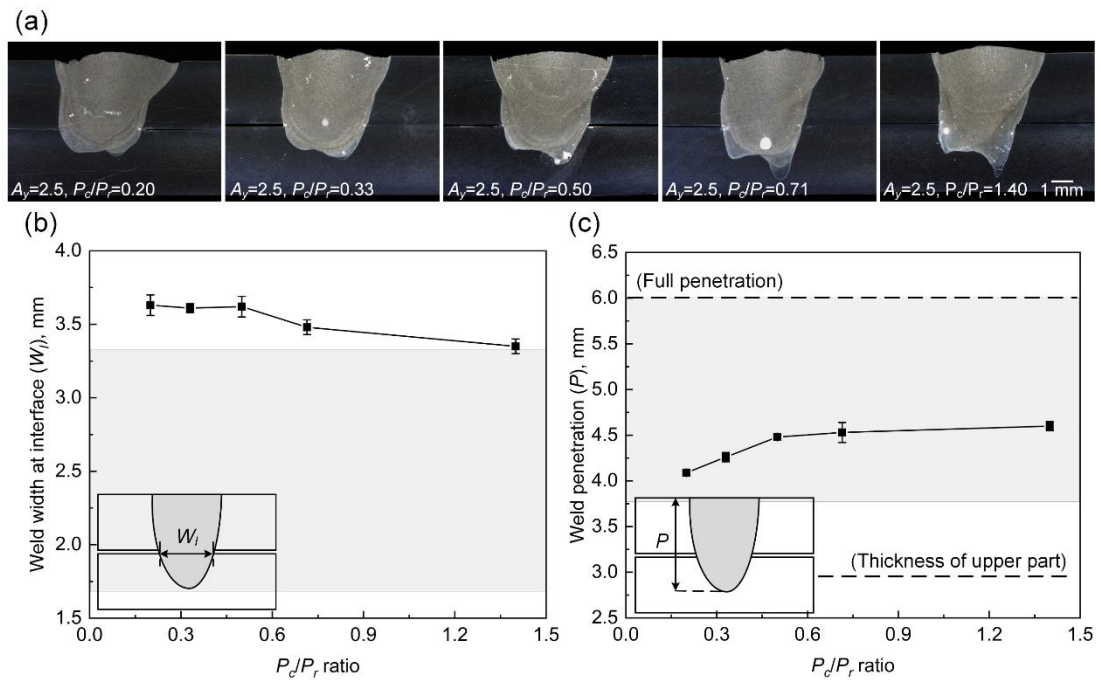
Figure 6.6 (a) Cross-section morphology of welds produced at different core/ring power ratios and evolution of weld geometry: (b) weld interface width (W_I) and (c) weld penetration (P). Note that the space highlighted in grey in (b) and (c) indicates the values obtained in the study of pre-selection of beam oscillation width (Figure 6.4).

6.4.3 Effect of ARM laser power ratio on the temperature field

A steep thermal gradient and rapid solidification behaviour of the molten material are generally expected in the laser welding process, it is challenging to obtain accurate evolution of the position-sensitive and time-sensitive temperature fields by direct experimental measurement. Therefore, numerical simulation was developed to reconstruct the temperature field and provide insight into the impact of power ratio on the mechanism of microstructural formation. The model was first evaluated using the welding trials with different oscillation widths listed in Table 6.3 due to a more significant variation in weld geometry, followed by the welding trials with different power ratios. Figure 6.7 shows the evolution of weld geometry in terms of weld top width and weld penetration. It is evident that the simulated weld profiles are in good

agreement with experimental observation, with the correlation coefficient of 0.94 and 0.95 for weld width and weld penetration, respectively, demonstrating the validity of the employed model.
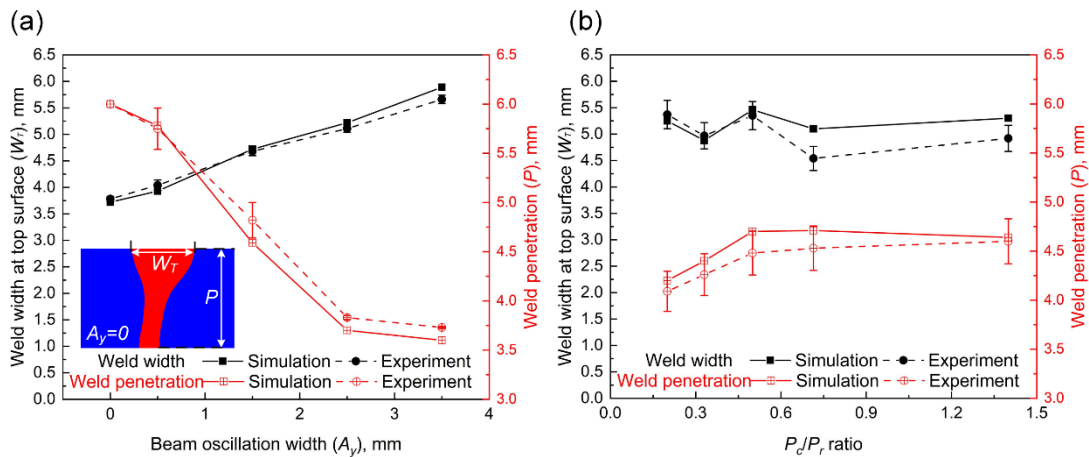
Figure 6.7 Comparison of weld profiles from simulation and experiment for welds produced with (a) various beam oscillation widths and (b) various core/ring power ratios. Note that the image embedded in (a) shows the fusion zone (in red) of weld with A_y= 0 mm from the simulation.

Figure 6.8 shows the evolution of temperature fields at steady-state as a function of power ratio, simulated by the validated model. The yellow dashed line indicates the position of the laser beam along the welding direction, and the molten pool boundary was expressed by the solid white line using the isotherm $T=(T_L+T_S)/2=$ 873 K, where T_L and T_S are the liquidus temperature and solidus temperature, respectively. Overall, a higher peak temperature and broader molten pool were determined in the weld with an increasing power ratio, attributed to the greater intensity of the core beam as visualised in Figure 6.3. Furthermore, a more rapid change in the shape and magnitude of the temperature profile was observed through the depth direction when the power ratio increased, indicating that the ring beam is beneficial for stabilising the keyhole and maintaining a more uniform thermal field.
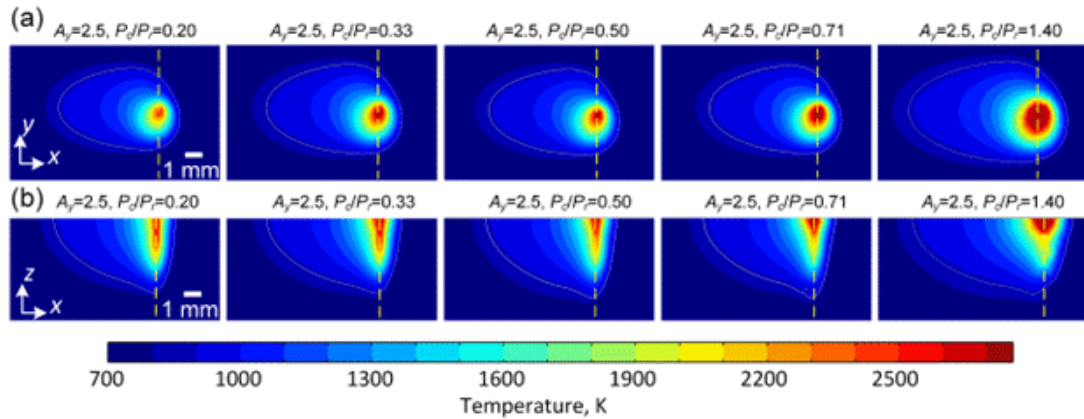
Figure 6.8 Comparison of simulated steady-state temperature field in welds produced with different power ratios: (a) from the top surface (x-y plane) and (b) from a longitudinal cross-section along weld centre (x-z plane). Note that the dashed yellow lines indicate the position of the laser beam along the welding direction and solid white lines represent the molten pool boundary, expressed by the isothermal $(T_L + T_S)/2$ in the mushy zone.

6.4.4 Effect of ARM laser power ratio on weld grain structure

Due to the significant impact on weld mechanical performance, the grain structures of welds with different power ratios were investigated by combining the simulated thermal field results and the solidification principle. To demonstrate the evolution of solidification behaviour in transverse and depth directions, solidification parameters were studied along the molten pool boundary on the top surface and the longitudinal cross-section at the weld centre, respectively (see Figure 6.9). It has been proposed that the temperature gradient (G) and solidification rate (R) at the solidification front play a significant role in the grain formation during the solidification process, where G/R influences the grain morphology and $G{\times}R$ is associated with the scale of solidified grains [18]. It should be noted that welding trials in the pure ring beam (power ratio = 0) and pure core beam (power ratio = ∞) modes

at an identical total power were also simulated to reveal the evolution from the pure ring beam mode to the dual beam mode, which is not feasible by the experiment work yielded by the maximum power of the individual beam.

In the transverse direction, the G exhibits a relatively uniform distribution in the weld centre and increases rapidly towards the fusion boundary, Figure 6.9 (a). The G is determined to increase first from the power ratio of 0 (ring only) until the power ratio approaches 0.33 and then continuously drops as the power ratio increases. In comparison, the R decreases from the weld centre towards the fusion boundary and only a slight difference was identified among welds with different power ratios except from the pure core beam mode Figure 6.9 (b). Consequently, the G/R follows a 'U' shape distribution with the minimum value located in the weld centre, Figure 6.9 (c). For aluminium alloy, a threshold value of G/R at approximately 7×10^3 Ks/mm^2 was estimated over which the planar solidification occurs stably [294]. As the G/R values determined in all welds here are apparently lower than this critical value, cellular or dendritic solidified grains are expected in the fusion zone. The cooling rate $G \times R$ (Figure 6.9 (d)) followed an inverted 'U' shape distribution with the peak value determined in the weld centre, indicating the refined grain structure in the weld centre and promoted grain growth towards the fusion boundary. As the power ratio increases from zero (ring-only mode), a parabolic distribution of the peak $G \times R$ is observed, with the highest value at the power ratio of 0.33. This could be explained by the combined impact of the ring beam and core beam as follows: At the extremely low power ratio, for example, the ring only mode at the power ratio of zero, the ring provides excessive pre-heating and post-heating, promoting a mitigating thermal gradient and slowing down the cooling process. At the excessively high power ratio, for instance, the core only mode (infinite power ratio), the excessive intensity of the core beam results in a

high peak temperature and a long time for heat dissipation prior to the occurrence of solidification, which consequently reduces the thermal gradient at the isothermal of $(T_L + T_S)/2$, and also lowers the cooling rate, as the temperature range for solidification moves towards the tail of the cooling curve. It is believed that the evolution of the cooling rate is dominated by the ring beam at a low power ratio, for example, from 0 (ring only) to 0.33, where the ring beam has comparable intensity to the core beam but a significantly larger affected area (see Figure 6.3). In contrast, the core beam dominates the change of cooling rate at a high power ratio because of the higher beam intensity. Therefore, a balance associated with the highest cooling rate was determined at the power ratio of ~0.33 for the welding parameters employed in this study, which principally attributes to the most promising grain refinement.

In the depth direction, a uniform distribution of G is seen with a slight increase near the interface of two plates (depth= 3mm), Figure 6.10 (a), and the R decreases as the depth increases, Figure 6.10 (b). Consequently, a sustained decline in cooling rate $G \times R$ is observed, Figure 6.10 (d), suggesting the increasing grain size from the top surface. Furthermore, the evolution of magnitudes of G, R, G/R and $G \times R$ as a function of the power ratio follows the same trend as seen in the transverse direction, Figure 6.9.
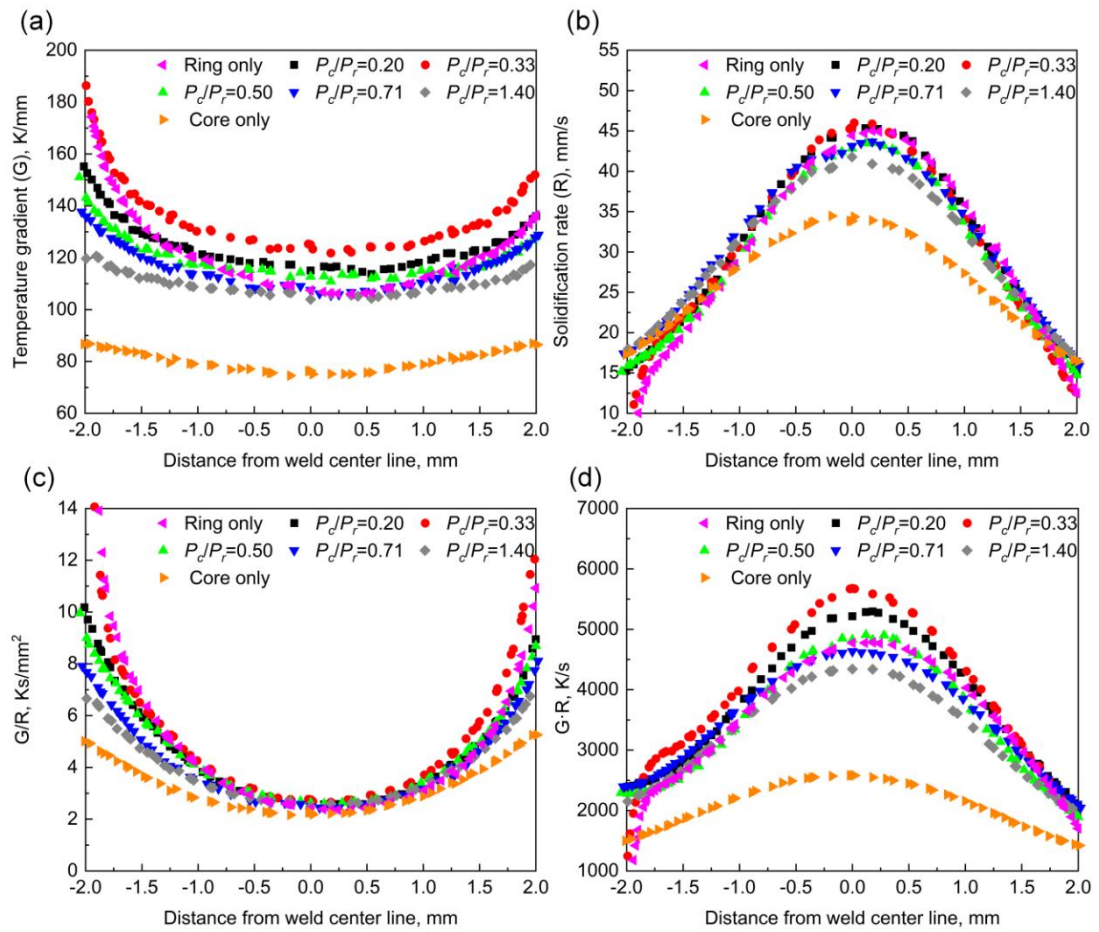
Figure 6.9 Comparison of the solidification parameters for welds produced with different power ratios, extracted from the simulated top surface isothermal $(T_L + T_S)/2$ in the mushy zone on the top surface (Figure 6.8 (a) and (b)): (a) temperature gradient (G), (b) solidification rate (R), (c) G/R and (d) $G{\times}R$.
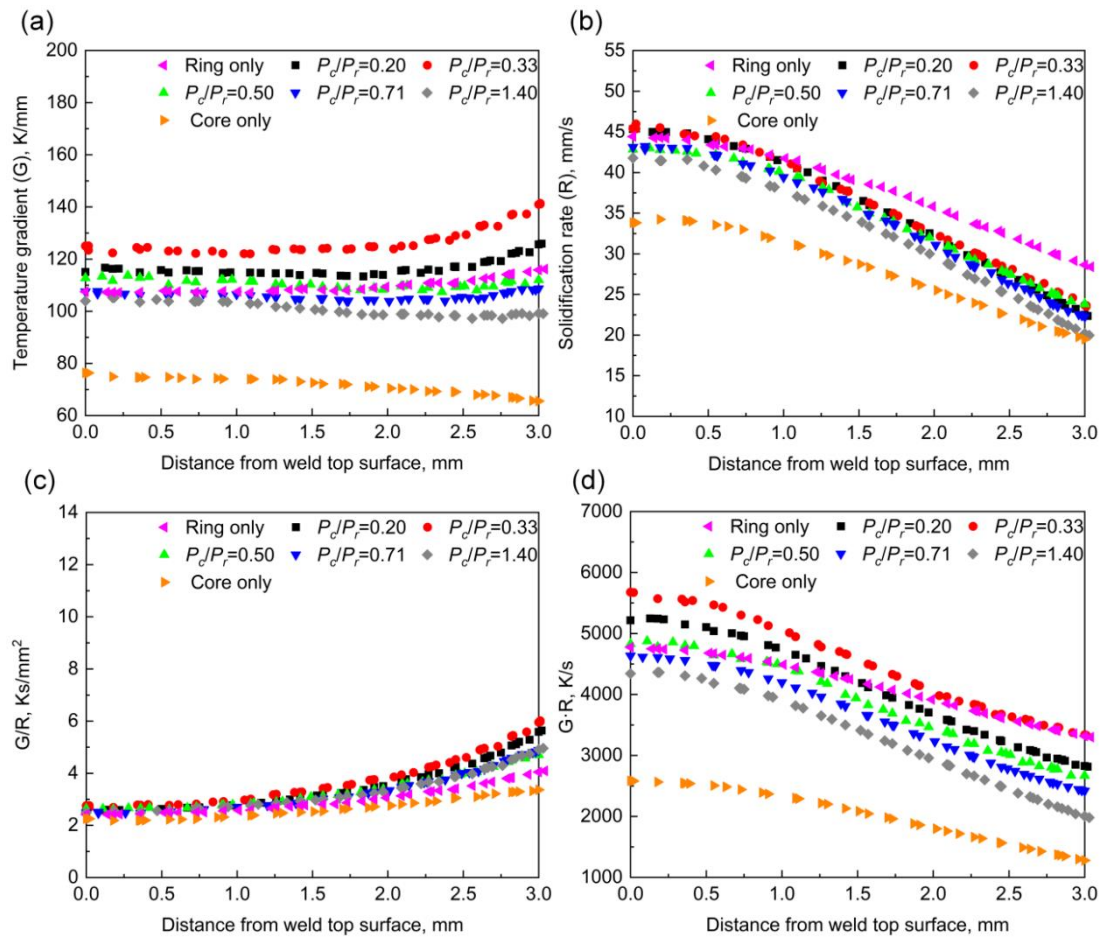
Figure 6.10 Comparison of the solidification parameters for welds produced with the power ratios, extracted from the simulated isothermal $(T_L + T_S)/2$ in the mushy zone on the longitudinal cross-section (Figure 6.8 (c) and (d)): (a) temperature gradient (G), (b) solidification rate (R), (c) G/R and (d) $G{\times}R$.

EBSD analysis was performed across the weld zone on the transverse cross-section to quantitively investigate the impact of power ratio on the grain structure and validate findings obtained from the numerical simulation. Grain structure maps presented in Figure 6.11 and the statistical grain size distribution in the fusion zone of the upper sheet, where the failure occurs during the tensile lap shear test, are shown in Figure 6.12. Overall, the columnar grains grow from the fusion line towards the weld centre both transversely and vertically, indicating the thermal gradient during the solidification process. In addition, a significant amount of fine equiaxed grains were

observed in the weld centre because the beam oscillation results in a more uniform temperature distribution in the weld centre and resultantly wider constitutive undercooling region [130,295]. It is also evident from Figure 6.11 that an increasing power ratio promotes the nucleation and growth of columnar grains near the interface between two plates. This can be statistically demonstrated by the more spread distribution of grain size in welds at a higher power ratio. For example, frequencies of grains finer than 50 µm are much reduced while frequencies of grains coarser than 100 µm gradually develop when comparing Figure 6.12 (e) with Figure 6.12 (b). It is believed that in the case of a high power ratio, the evolution of grain structure in the depth direction is related to the sufficiently low cooling rate at the interface, which is observed to be comparable to the cooling rate at the fusion boundary (see Figure 6.9 (d) and Figure 6.10 (d)). Furthermore, the minimum area-weighted mean grain size and restricted formation of columnar grains near the interface in the weld with a power ratio of 0.33 are well correlated to the highest cooling rate, $G \times R$, in both transverse and depth directions, which confirms the reliability of the numerical simulation.
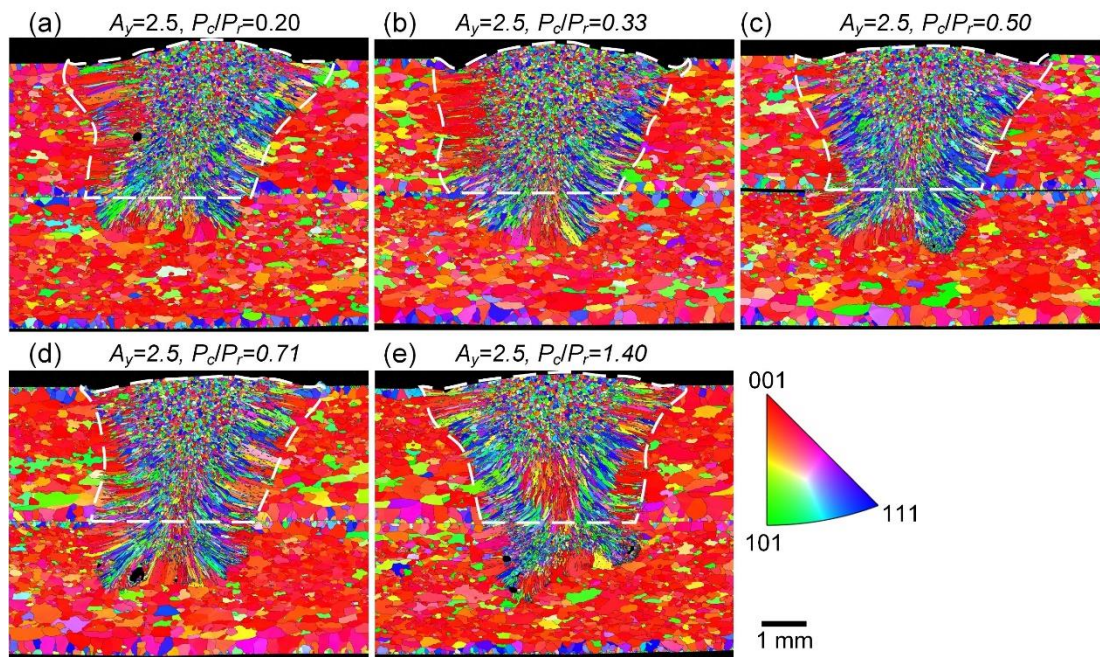
Figure 6.11 EBSD IPF maps showing the grain structures in welds produced with the power ratio of core to ring beam at (a) 0.20, (b) 0.33, (c) 0.5, (d) 0.71 and (e) 1.40. The dashed line indicates the region for the statistical analysis of grain size distribution in Figure 6.12. Welding trials were conducted at the constant total power of 6.0 kW, oscillation width of 2.5 mm, oscillation frequency of 50 Hz and welding speed of 50 mm/s.
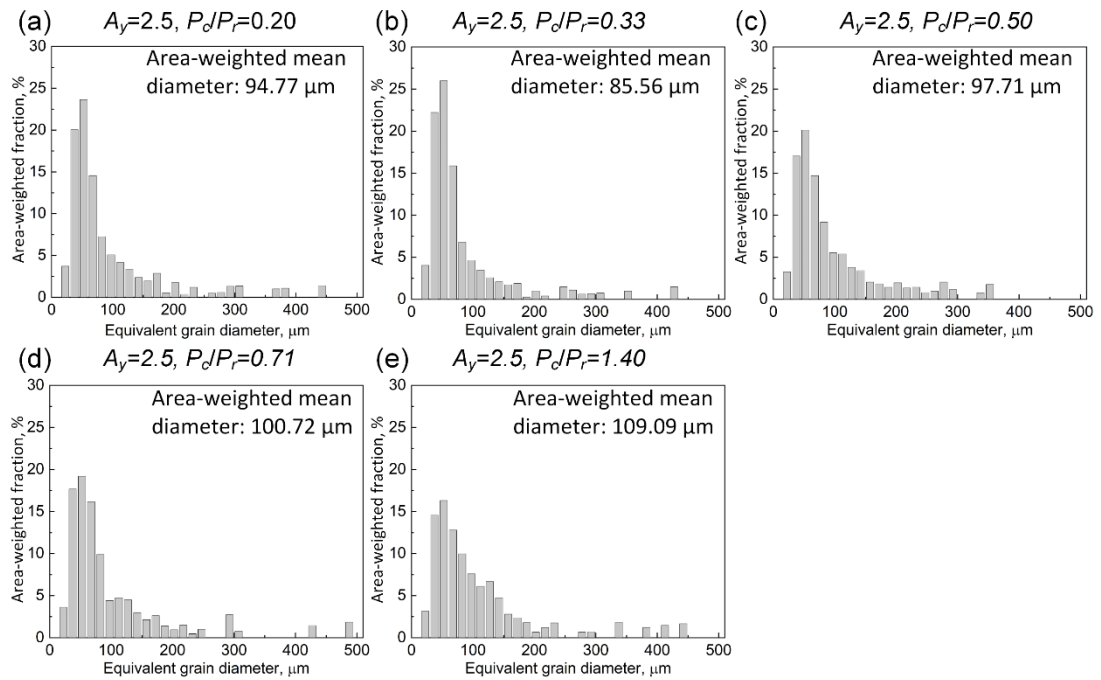
Figure 6.12 Weld zone grain size distribution in welds produced with the power ratio of core to ring beam at (a) 0.20, (b) 0.33, (c) 0.5, (d) 0.71 and (e) 1.40, summarised from the fusion zone of upper part as indicated in EBSD maps. Note that grain size is expressed by the equivalent diameter of the circle with an area equal to the grain.

6.4.5 Effect of ARM laser power ratio on weld mechanical performance

Figure 6.13(a) plots the evolution of the mechanical strength of welds with different power ratios. Overall, the joint strength increases from ~275 N/mm to ~400 N/mm as the power ratio decreases, with the peak value captured at the power ratio of 0.33. It is interesting to see that the variation of joint strength resulting from different power ratios is more significant than in the cases with different oscillation widths, although the weld interface width remains comparable. In addition, fusion boundary failure was observed among all welds, confirming the findings in Figure 6.5 that the weld interface width determines the failure mode. The linear correlation between the joint strength and area-weighted mean grain diameter, with R-square = 0.901 in Figure 6.13 (b), indicates that grain refinement is one of the primary mechanisms that lead to

the improvement of joint strength when optimising the power ratio of the ARM laser beam.
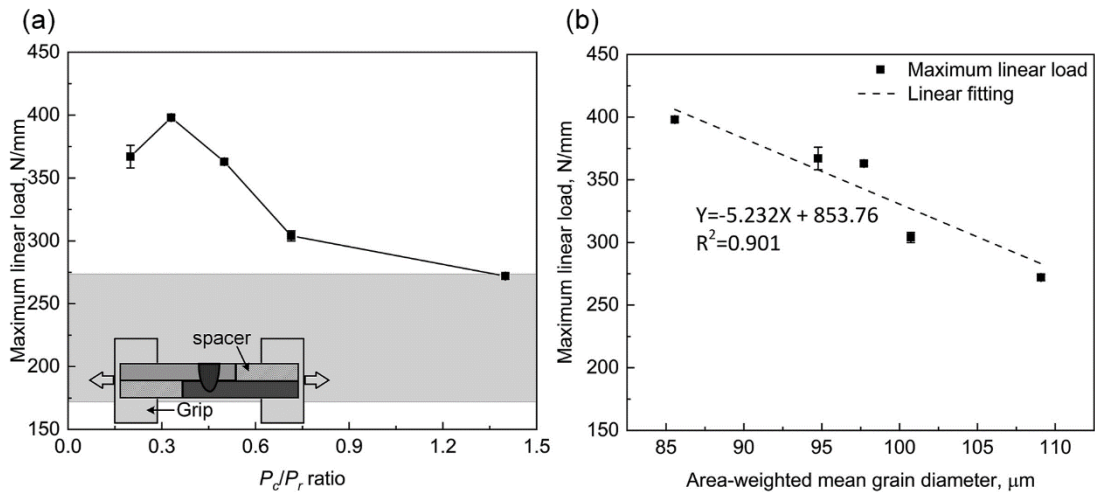
Figure 6.13 Plots of (a) cross-weld hardness profile and (b) weld load-bearing capacity as a function of core/ring power ratio. Tests were conducted after post-weld natural ageing for one month. Note that the space highlighted in grey in (b) indicates the variation of load-bearing capacity in the study of oscillation width. Welding trials were conducted at the constant total power of 6.0 kW, oscillation width of 2.5 mm, oscillation frequency of 50 Hz and welding speed of 50 mm/s.

Figure 6.14 shows the fractography of welds produced at the power ratio of 0.33 and 1.40 after the tensile lap shear test, corresponding to the maximum and minimum joint strength. Uniform distribution of dimples was observed in the case with a power ratio of 0.33, with few pores and micro-cracks. In comparison, a much more frequent presence of pores and micro-cracks was captured in the weld produced at the power ratio of 1.40, which significantly reduces the resistant area and facilitates the rapid failure subjected to external tensile loading. Results indicate a more stable keyhole is expected during the welding processing with a lower power ratio. The direct observation of keyhole behaviour as a function of power ratio will be carried out in the future.
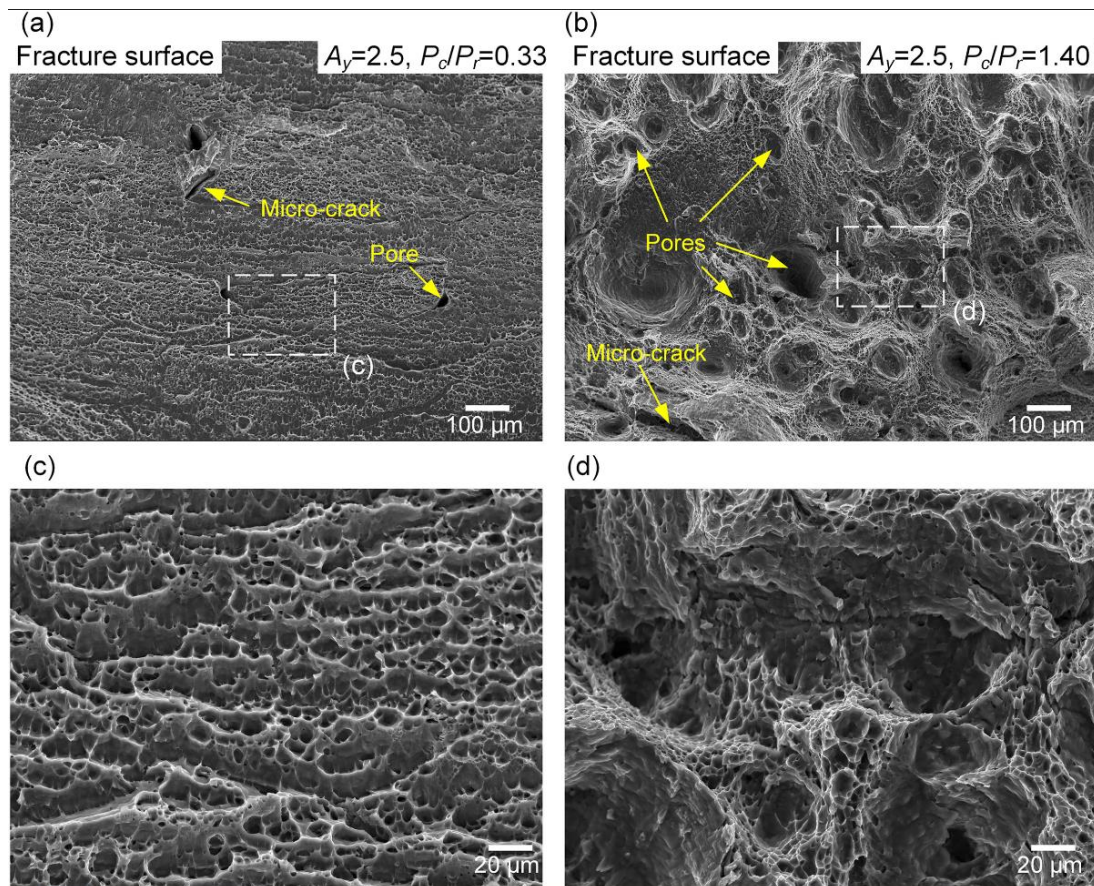
Figure 6.14 SEM fractography of welds produced at the power ratio of (a) 0.33 and (b) 1.40, after the tensile lap shear test. (c) and (d) are high-magnification views of the area highlighted in (a) and (b), respectively. Representative microcracks and pores are highlighted by arrows.

6.5 Conclusions

This chapter studied the impact of Adjustable-Ring-Mode (ARM) laser beam on the grain morphology of the weld and mechanical performance of laser welded 6xxx aluminium alloy. A remote laser welding system equipped with transverse beam oscillation was employed and welding parameters, including the beam oscillation width and core/ring power ratio of the ARM laser beam, were investigated sequentially. A combination of experiments and FEM modelling have been presented to study weld geometry, fusion zone grain structure and weld mechanical strength, as well thermal evolutions within and around the weld. The FEM model provided

information about temperature gradient and solidification behaviour, which are difficult to measure directly via experiments. The two main findings were summarised as follows:

The core/ring power ratio of the ARM laser beam at a constant total power has limited control over the weld geometry when integrated with beam oscillation.

A proper core/ring power ratio can restrict the formation of columnar grains near the interface between the two plates, resulting in grain refinement within the weld zone. Extremely high power ratio, for example, the core beam alone mode (infinite power ratio), results in high peak temperature and allows a long time for heat dissipation prior to solidification, leading to low thermal gradient and the cooling rate at the solidification front; Extremely low power ratio, for example, the ring beam along mode (zero power ratio), provides excessive pre-heating and post-heating, mitigating the thermal gradient and slowing down the cooling process. Results showed that a compromised solution which balances the wider formation of equiaxed dendrites and better grain refinement was determined at the power ratio of 0.33. This translated to the improvement in joint strength up to 400 N/mm.

The chapter proved the feasibility of controlling the grain morphology of laser welded 6xxx aluminium alloy by using ARM laser technology. This opens interesting future opportunities in the area of laser beam shaping as a tool to create bespoke grain morphology, as well as control of phase formations and intermetallic during the joining of dissimilar materials.

Chapter 7. Conclusions and Future Work

RLW is increasingly adopted for lightweight manufacturing in the automotive industry as it offers the inherent flexibility of imposing heat in a localised manner by modulating the power and location of the heat source. This provides an opportunity to modify or tailor the temperature field, fluid flow field and concentration field during the welding process using RLW capability for laser beam oscillation, beam shaping and power modulation. These capabilities provide an opportunity to modify the weld thermal cycle, solidification behaviour, grain morphology and mass transport which is critical for the weld quality to achieve near-zero defect manufacturing. However, the relationship between the welding process parameters and the weld quality indicators (IPIs/KPIs) is not fully understood. Also, with the increase in the number of input parameters, it is challenging to select robust process parameters using experimental investigation. Therefore, previous chapters comprehensively discuss the sequential modelling approach for the development of the proposed numerical models for the estimation of the weld thermal cycle, fluid flow profile and material mixing during laser welding of high-strength aluminium alloys. The effect of process parameters on the weld profile, fusion zone dimensions, solidification behaviour, grain morphology and solute transport is established with consideration to beam oscillation and beam shaping. The process capability framework is built on these underlined numerical models of heat transfer, fluid flow and mass transport by defining the constraints on the IPIs and KPIs to ensure the required weld quality. The process capability space framework is established for the selection of robust process parameters. The developed framework provides the range of WPPs which satisfies all the IPIs/KPIs to ensure the required weld quality. It would help in reducing the number

of necessary experiments to be conducted to determine robust process parameters by providing the initial range of process parameters which satisfies the required weld quality during the early design phase. It can be used for the analysis of different laser welding process key technological innovations such as beam oscillation and beam shaping as it modifies the weld thermal cycle, solidification behaviour and grain morphology and thus, affect the weld quality. This chapter draws conclusions, presents gaps addressed, contributions, the impact of the research, limitations and future work. The rest of the chapter is organized as follows: Section 7.1 discusses the conclusion and the contributions; Section 7.2 discusses the limitation of this work and suggestions for future work.

7.1 Conclusions and contributions

This research work aimed to develop a framework for the quick selection of robust welding process parameters during the early design phase to achieve the weld quality requirements and to comprehensively understand the effect of different laser welding process parameters on the weld thermal cycle, fluid flow, solidification behaviour, grain morphology and mass transport during the laser butt-welding of high-strength aluminium alloys with consideration to beam oscillation and beam shaping. This was accomplished by developing the Multiphysics numerical model to simulate heat transfer, fluid flow and mass transport for laser welding and including key laser welding technological advancements such as beam oscillation and beam shaping as input parameters in the numerical model. The key conclusions are:

- Welding speed and laser power have a significant effect on the weld thermal cycle as established from the contour maps in case of no oscillation condition. In the case of beam oscillation, the significance of the radius and frequency of oscillation

has been developed on top of welding speed and laser power. From the parametric contour maps, it was found that the frequency of oscillation has no significant effect on the weld thermal cycle for the range it is investigated, and a significant effect was observed for the radius of oscillation. Thus, the main parameter affecting the weld thermal cycle during beam oscillation is the radius of oscillation in addition to laser power and welding speed which provides beam oscillation just one extra degree of freedom reducing the four parameters space to three parameters space.

- The process capability space refining strategy presented, decreases the number of paths within the process capability space from the initial parameter settings to optimize process parameters. For example, the same peak temperature can be attained by various combinations of welding process parameters which, however, may lead to different values of HAZ volume and cooling rate. This non-linear relation of HAZ volume and cooling rate with the change in the radius of oscillation can be visualised by the process capability space.

- The area of process capability space increases with the application of beam oscillation. This increase in area exhibits the increase in flexibilities due to the application of beam oscillation as the process will be more robust due to larger acceptable regions and smaller fall-out areas.

- The ratio of the Marangoni number to the Grashof number is of the order of 10^3 in all the cases which suggested that the surface tension force is dominant rather than the buoyancy force. Given a constant circumferential velocity in oscillating welding conditions, it was found that peak temperature, weld dimensions and the thermal gradient decrease with an increase in oscillation radius. At the same time,

the peak flow rates in the melt pool, however, decrease with an increase in the oscillation radius. It can therefore be concluded that beam oscillation offers two additional parameters to control fluid flow and heat transport to optimise welding performance.

- For the sinusoidal beam oscillation, three vortices are formed as compared to no oscillation condition where only two vortices are formed. The formation of the third vortex is attributed to the churning action of the beam oscillation. This shows that beam oscillation leads to more convection in a molten pool of metal which leads to more mixing and affects solidification behaviour. This leads to a decrease in thermal gradient and hinders the growth of columnar grains in the mushy zone.

- The $G{\times}R$ follows a peak-shape distribution with a peak value at the weld centre suggesting that the refined grains are formed at the weld centre and grain growth occurs towards the fusion boundary. During full penetration welding, tensile strength increases by 21.4% with the application of beam oscillation as compared to no oscillation conditions. This is due to an increase in the percentage of equiaxed grains formed along the tensile direction which hinders crack propagation.

- The solidification rate and the peak of $G{\times}R$ increase with an increase in oscillation frequency suggesting that the smallest grain will be formed at the highest oscillation frequency. The broadening of the peak with increasing oscillation frequency suggests that grain growth is hindered and more regions of finer grains will be formed.

- The process capability space from the heat transfer model is further refined based on the depth of penetration and ratio of the width of the equiaxed zone to the fusion zone. There is an intersection of the process capability spaces based on independently analysed heat transfer and fluid flow models which reduces the feasible region demonstrating the decrease in the number of experiments required to select the robust parameters. The process capability space increases with the application of beam oscillation which suggests that the beam oscillation provides an extra degree of freedom to modify the weld thermal cycle, fluid flow and solidification behaviour of the weld.

- The mechanism of solute movement is found to be governed by both diffusion and convection which can be attributed by comparing the weld width and thickness of intermixing layer. This can be inferred as the thickness of intermixing layer is larger than the weld width which shows that solute transport is due to diffusion as there is no convection outside the fusion boundary. So, convection is dominant in the molten pool region which is the fusion zone and diffusion is dominant at the fusion boundary. Both mechanisms are comparable in the mushy zone.

- The solute intermixing layer thickness decreases when beam oscillation is applied. This is due to a decrease in diffusion at the fusion boundary which is attributed to the decrease in a thermal gradient. It was also found that introducing solute distribution in the mass transfer model improves the prediction of fusion zone boundary as compared to the fluid flow model.

- The parametric contour maps show that the ratio of the width of intermixing layer and the width of the fusion zone increases with the application of beam oscillation.

This is a more reliable parameter to investigate the effect of beam oscillation on material mixing in place of comparing the actual width for the same combination of welding speed and laser power as the penetration depth decreases with the application of beam oscillation. The final process capability space shows that without oscillation condition has no solution while for beam oscillation condition generates the solution. This shows that the chemical composition of the fusion zone is far away from the peak of crack susceptibility and can be attained during the beam oscillation condition. The final process capability space increases with an increase in the radius of oscillation.

- Utilizing an adjustable-ring mode laser beam (beam shaping) during laser welding allows for the control of columnar grain formation near the plate interface. By selecting an appropriate core/ring power ratio, grain refinement within the weld zone can be achieved. An excessively high power ratio, such as using the core beam alone mode (infinite power ratio), leads to elevated peak temperatures and extended heat dissipation before solidification. Consequently, this results in low thermal gradient and reduced cooling rate at the solidification front. Conversely, an extremely low power ratio, such as the ring beam along mode (zero power ratio), leads to excessive pre-heating and post-heating, thereby mitigating the thermal gradient and slowing down the cooling process. The experimental results demonstrated that a compromised solution, achieved at a power ratio of 0.33, balances the formation of equiaxed dendrites and enhances grain refinement. This compromise ultimately leads to an improvement in joint strength of up to 400 N/mm.

Overall, the main contributions of this study to the scientific community are:

- This study demonstrates that the sequential modelling approach decreases the total computation time to survey the whole parameters space by 55%.

- This study provides a comprehensive understanding of the effect of process parameters on the weld thermal cycle, fluid flow, solidification behaviour, grain morphology and solute transport to understand the root cause of defects which provides critical insights to improve the performance of the welded structure.

- Development of a multi-physics model capable of simulating technological advancements such as beam oscillation, beam shaping and power modulation. This provides extensive details of the influence of these advancements and critical boundaries for the user depending on the requirements of the downstream processes. This provides an opportunity to modify or tailor the performance of the welds.

- The developed numerical model provides qualitative information about the grain morphology and grain size by simulating the solidification parameters. The grain morphology and grain size have a critical relationship with the strength of the welded structure. During welding, qualitative measurement is very important when comparing different possible process parameter combinations.

- The development of the process capability space framework provides a boundary region for the selection of the initial process parameters window and also provides qualitative measurements such as HAZ volume, grain size and grain morphology. It demonstrated that the beam oscillation provides more flexibility as the final process capability space for no oscillation condition has no solution whereas the

beam oscillation condition generates a solution and the feasible region increases with an increase in the radius of oscillation. These qualitative measurements provide details about the weld quality and performance of the welded structure. The process capability framework provides the influence of process parameters on the IPIs and KPIs and reduces the number of experiments and design time for NPI.

7.2 Limitations and Future work

The framework developed in this thesis has many advantages compared to the state-of-the-art which is discussed in the previous sections. Below are the limitations of the research work in terms of scope, advantages and applications.

- Scope: This work is done within the scope of coupons and has not been tested on the surrogate parts, prototypes and actual components. The effect of heat input on welding seams longer than 125 mm is not included in this study. The process parameters are kept constant while welding one weld seam and the effect of the change of process parameters on the single weld seam is not understood.

- The effect of clamping and the gap between the plates is not studied. No particular weld defect is simulated. The weld profile is quantified and the rest of the weld quality is analysed qualitatively.

- The effect of vapour plume and plasma formation is not modelled while a volumetric heat source is considered. The instability of the keyhole is not considered whereas volumetric heat sources always have a stable keyhole. Further, it will be advantageous to consider the effect of material removal and recoil pressure while maintaining a reasonable computation time.

- The process capability space framework may have no solution if lots of process parameters and performance indicators are considered. Process capability space framework works for the MIMO scenario but will be very complicated for a higher number of inputs and outputs.

- The present methodology cannot be used for closed-loop in-process (CLIP) quality control as the models take hours to solve.

The developed methodology can be extended to lay a foundation for a much needed and industrially relevant field of study which will combine physics-based modelling and data-driven approach such as Artificial intelligence. This methodology provides a forward loop from process parameters to weld quality indicators and there is a need for the backward synthesis to provide process parameters when weld quality is known. The process capability space framework will not be able to provide the root cause of the defects. The topics of the future work are as follows:

- As an extension of the considered physics, a ray-tracing can be included in the model to model the laser intensity distribution inside the keyhole for a more realistic model of the keyhole and keyhole features.

- Implementation of the material mixing to more complex alloy systems such as welding of Aluminium to steel and predicting the conditions for the formation of intermetallic phases and suggesting measures to control them.

- Implementing volume of fluid method or phase-field modelling to model undercut and convexity at the weld surface.

- Using CLIP quality control using the AI for the root cause analysis and providing the countermeasure in real-time. As AI-based models require a large size of data to train a model which is one of the prime challenges of the use of AI in manufacturing. A real-time physics-based simulation can be explored based on a reduced-order model or non-intrusive methods.

References

[1] E. Ghassemieh, Materials in Automotive Application, State of the Art and Prospects, New Trends Dev. Automot. Ind. (2011). https://doi.org/10.5772/13286.

[2] D. Ceglarek, M. Colledani, J. Váncza, D.Y. Kim, C. Marine, M. Kogel-Hollacher, A. Mistry, L. Bolognese, Rapid deployment of remote laser welding processes in automotive assembly systems, CIRP Ann. - Manuf. Technol. 64 (2015) 389–394. https://doi.org/10.1016/j.cirp.2015.04.119.

[3] M. Javaid, A. Haleem, R.P. Singh, S. Rab, R. Suman, Significant applications of Cobots in the field of manufacturing, Cogn. Robot. 2 (2022) 222–233. https://doi.org/10.1016/j.cogr.2022.10.001.

[4] A. Papacharalampopoulos, P. Stavropoulos, D. Petrides, Towards a digital twin for manufacturing processes: Applicability on laser welding, Procedia CIRP. 88 (2020) 110–115. https://doi.org/10.1016/j.procir.2020.05.020.

[5] P. Stavropoulos, A. Papacharalampopoulos, V. Siatras, D. Mourtzis, An AR based Digital Twin for Laser based manufacturing process monitoring, Procedia CIRP. 102 (2021) 258–263. https://doi.org/10.1016/J.PROCIR.2021.09.044.

[6] International Organization for Standardization, ISO 13919-1: Welding - Electron and laser beam welded joints - Guidance on quality levels for imperfections, 1996 (1996) 1–9.

[7] P. Franciosa, D. Ceglarek, Hierarchical synthesis of multi-level design parameters in assembly system, CIRP Ann. 64 (2015) 149–152. https://doi.org/10.1016/J.CIRP.2015.04.028.

[8] P. Franciosa, M. Sokolov, S. Sinha, T. Sun, D. Ceglarek, Deep learning enhanced digital twin for Closed-Loop In-Process quality improvement, CIRP Ann. 69 (2020) 369–372. https://doi.org/10.1016/j.cirp.2020.04.110.

[9]   T. Sun, P. Franciosa, M. Sokolov, D. Ceglarek, Challenges and opportunities in laser welding of 6xxx high strength aluminium extrusions in automotive battery tray construction, Procedia CIRP. 94 (2020) 565–570. https://doi.org/10.1016/J.PROCIR.2020.09.076.

[10]   E.C. Ozkat, P. Franciosa, D. Ceglarek, Laser dimpling process parameters selection and optimization using surrogate-driven process capability space, Opt. Laser Technol. 93 (2017) 149–164.

[11]   E.C. Ozkat, P. Franciosa, D. Ceglarek, Development of decoupled multi-physics simulation for laser lap welding considering part-to-part gap, J. Laser Appl. 29 (2017) 022423.

[12]   G. Davies, Materials for Automobile Bodies, Mater. Automob. Bodies. (2003) 1–277. https://doi.org/10.1016/B978-0-7506-5692-4.X5014-6.

[13]   H. Ramiarison, N. Barka, F. Mirakhorli, F. Nadeau, C. Pilcher, Parameter optimization for laser welding of dissimilar aluminum alloy: 5052-H32 and 6061-T6 considering wobbling technique, Int. J. Adv. Manuf. Technol. 118 (2022) 4195–4211. https://doi.org/10.1007/s00170-021-08122-y.

[14]   R.M. Mahamood, E.T. Akinlabi, Non-contact Welding Technologies: Fusion Welding, in: Adv. Noncontact Cut. Join. Technol., Springer Cham, 2018: pp. 139–165.

[15]   R.M. Mahamood, E.T. Akinlabi, Advanced Noncontact Cutting and Joining Technologies: Micro- and Nano-manufacturing, 1st ed., Springer Cham, 2018.

[16]   A. Salminen, H. Piili, T. Purtonen, The characteristics of high power fibre laser welding:, J. Mech. Eng. Sci. 224 (2010) 1019–1029.

[17]   L. Quintino, A. Costa, R. Miranda, D. Yapp, V. Kumar, C.J. Kong, Welding with high power fiber lasers – A preliminary study, Mater. Des. 28 (2007) 1231–1237.

[18]   S. Kou, Welding metallurgy, New Jersey, USA. 431 (2003) 223–225.

[19] M.P. Ochoa, A. Deshpande, S. García-Muñoz, S. Stamatis, I.E. Grossmann, Flexibility Analysis For Design Space Definition, Comput. Aided Chem. Eng. 47 (2019) 323–328. https://doi.org/10.1016/B978-0-12-818597-1.50051-5.

[20] M. Goede, M. Stehlin, L. Rafflenbeul, G. Kopp, E. Beeh, Super Light Car-lightweight construction thanks to a multi-material design and function integration, Eur. Transp. Res. Rev. 1 (2009) 5–10.

[21] J.M. Sánchez Amaya, M.R. Amaya-Vázquez, F.J. Botana, Laser welding of light metal alloys: Aluminium and titanium alloys, in: Handb. Laser Weld. Technol., Elsevier Inc., 2013: pp. 215–254. https://doi.org/10.1533/9780857098771.2.215.

[22] N. Coniglio, C.E. Cross, T. Michael, M. Lammers, Defining a Critical Weld Dilution to Avoid Solidification Cracking in Aluminum, Weld. J. 87 (2008) 237–247.

[23] D. Weller, C. Hagenlocher, T. Steeb, R. Weber, T. Graf, Self-restraint hot cracking test for aluminum alloys using digital image correlation, Procedia CIRP. 74 (2018) 430–433. https://doi.org/10.1016/J.PROCIR.2018.08.165.

[24] M.A. Easton, H. Wang, J. Grandfield, C.J. Davidson, D.H. Stjohn, L.D. Sweet, M.J. Couper, Observation and Prediction of the Hot Tear Susceptibility of Ternary Al-Si-Mg Alloys, (n.d.). https://doi.org/10.1007/s11661-012-1132-6.

[25] B.J. C, Generalized theory of supersolidus cracking in welds and castings, Br Weld J. 7 (1960) 508–512. https://jglobal.jst.go.jp/en/detail?JGLOBAL_ID=201602017708010470 (accessed October 13, 2022).

[26] M. Norouzian, M. Amne Elahi, P. Plapper, A review: Suppression of the solidification cracks in the laser welding process by controlling the grain structure and chemical compositions, J. Adv. Join. Process. 7 (2023). https://doi.org/10.1016/j.jajp.2023.100139.

[27] L. Chen, C. Wang, L. Xiong, X. Zhang, G. Mi, Microstructural, porosity and mechanical properties of lap joint laser welding for 5182 and 6061 dissimilar aluminum alloys under different place configurations, Mater. Des. 191 (2020) 108625. https://doi.org/10.1016/J.MATDES.2020.108625.

[28] A. Mohan, D. Ceglarek, M. Auinger, Numerical modelling of thermal quantities for improving remote laser welding process capability space with consideration to beam oscillation, Int. J. Adv. Manuf. Technol. 123 (2022) 761–782. https://doi.org/10.1007/s00170-022-10182-7.

[29] A. Mohan, D. Ceglarek, M. Auinger, Effect of Beam Oscillation on the Fluid Flow During Laser Welding, Mater. Today Proc. 2022 (2022) 1–6. https://doi.org/10.1016/j.matpr.2022.04.435.

[30] A. Mohan, D. Ceglarek, P. Franciosa, M. Auinger, Numerical study of beam oscillation and its effect on the solidification parameters and grain morphology in remote laser welding of high strength aluminium alloys, Sci. Technol. Weld. Join. (2022).

[31] A. Mohan, P. Franciosa, D. Ceglarek, M. Auinger, Numerical simulation of transport phenomena and its effect on the weld profile and solute distribution during laser welding of dissimilar aluminium alloys with and without beam oscillation, Int. J. Adv. Manuf. Technol. (2022).

[32] T. Sun, A. Mohan, C. Liu, P. Franciosa, D. Ceglarek, The impact of Adjustable-Ring-Mode (ARM) laser beam on the microstructure and mechanical performance in remote laser welding of high strength aluminium alloys, J. Mater. Res. Technol. 21 (2022) 2247–2261. https://doi.org/10.1016/J.JMRT.2022.10.055.

[33] D. Leroy, T.A. Siewert, S. Liu, G.R. Edwards, ASM Handbook Volume 6: Welding, Brazing, and Soldering, 1993.

[34] M.M. Němeček S, Mužík T, Differences between Laser and Arc Welding of HSS Steels, (2012) 67–74. https://doi.org/10.1016/j.phpro.2012.10.015.

[35]   S. Kou, Welding Metallurgy. Second Edition, John Wiley & Sons, New Jersey, 2003.

[36]   E. Assuncao, S. Williams, Comparison of continuous wave and pulsed wave laser welding effects, Opt. Lasers Eng. 51 (2013) 674–680. https://doi.org/10.1016/J.OPTLASENG.2013.01.007.

[37]   W.M. Steens, J. Mazumder, K.G. Watkins, Laser Material Processing, Springer, 2003.

[38]   B. Brickstad, B.L. Josefson, A parametric study of residual stresses in multi-pass butt-welded stainless steel pipes, 75 (1998).

[39]   S. Zhao, G. Yu, X. He, Y. Zhang, W. Ning, Numerical simulation and experimental investigation of laser overlap welding of Ti6Al4V and 42CrMo, J. Mater. Process. Tech. 211 (2011) 530–537. https://doi.org/10.1016/j.jmatprotec.2010.11.007.

[40]   W. Guo, Laser Welding of High Strength Steels, University of Manchester, 2015.

[41]   E.G. ASSUNÇÃO, Investigation of conduction to keyhole mode transition, Cranfield University, 2012.

[42]   M. Courtois, M. Carin, S. Gaeid, P.L.E. Masson, Heat and fluid flow modeling of keyhole formation in laser welding, COMSOL Multiphysics User's Conf. (2012).

[43]   J.C. Sun Z, Ion, Laser welding of dissimilar metal combinations, J. Mater. Sci. 30 (1995) 4205–4214.

[44]   J.M. Sánchez-Amaya, T. Delgado, J.J. De Damborenea, V. Lopez, F.J. Botana, Laser welding of AA 5083 samples by high power diode laser, Sci. Technol. Weld. Join. 14 (2009) 78–86. https://doi.org/10.1179/136217108X347629.

[45]   S. Nakamura, M. Sakurai, K. Kamimuki, T. Inoue, Y. Ito, Detection technique

for transition between deep penetration mode andshallow penetration mode in CO2 laser welding of metals, J. Phys. D. Appl. Phys. 33 (2000) 2941. https://doi.org/10.1088/0022-3727/33/22/311.

[46]   R. Wang, Y. Lei, Y. Shi, Numerical simulation of transient temperature field during laser keyhole welding of 304 stainless steel sheet, Opt. Laser Technol. 43 (2011) 870–873. https://doi.org/10.1016/j.optlastec.2010.10.007.

[47]   T. Delgado, J.J. De Damborenea, V. Lopez, F.J. Botana, T. Delgado, J.J. De Damborenea, V. Lopez, T. Delgado, J.J. De Damborenea, V. Lopez, F.J. Botana, Laser welding of AA 5083 samples by high power diode laser, 14 (2009) 78–86. https://doi.org/10.1179/136217108X347629.

[48]   T. Sibillano, A. Ancona, V. Berardi, E. Schingaro, G. Basile, P.M. Lugar, Optical detection of conduction/keyhole mode transition in laser welding, 191 (2007) 364–367. https://doi.org/10.1016/j.jmatprotec.2007.03.075.

[49]   A. Kaplan, A model of deep penetration laser welding based on calculation of the keyhole profile, J. Phys. D. Appl. Phys. 27 (1994) 1805. https://doi.org/10.1088/0022-3727/27/9/002.

[50]   R. Rai, G.G. Roy, T. Debroy, A computationally efficient model of convective heat transfer and solidification characteristics during keyhole mode laser welding, J. Appl. Phys. 101 (2007) 054909. https://doi.org/10.1063/1.2537587.

[51]   E.C. Ozkat, P. Franciosa, D. Ceglarek, Development of decoupled multi-physics simulation for laser lap welding considering part-to-part gap, J. Laser Appl. 29 (2017) 022423. https://doi.org/10.2351/1.4983234.

[52]   H. Bley, L. Weyand, A. Luft, An Alternative Approach for the Cost-efficient Laser Welding of Zinc-coated Sheet Metal, 56 (2007) 17–20. https://doi.org/10.1016/j.cirp.2007.05.006.

[53]   Z. Li, G. Fontana, Autogenous laser welding of stainless steel to free-cutting steel for the manufacture of hydraulic valves, 74 (1998) 174–182.

[54] M. Sokolov, A. Salminen, M. Kuznetsov, I. Tsibulskiy, Laser welding and weld hardness analysis of thick section S355 structural steel, Mater. Des. 32 (2011) 5127–5131. https://doi.org/10.1016/j.matdes.2011.05.053.

[55] C. Bagger, F.O. Olsen, Review of laser hybrid welding, 17 (2005) 2–14.

[56] M. Schweier, J.F. Heins, M.W. Haubold, M.F. Zaeh, Spatter formation in laser welding with beam oscillation, Phys. Procedia. 41 (2013) 20–30. https://doi.org/10.1016/j.phpro.2013.03.047.

[57] P.Z. Zhao, Y.F. Pan, J. Tao, X.J. Shi, Q. Zhang, Effect of Intermetallic Compounds Content on Laser Welding Performance of Al-Fe Alloy Sheets, Mater. Sci. Forum. 794–796 (2014) 401–406. https://doi.org/10.4028/www.scientific.net/msf.794-796.401.

[58] J. Fan, C. Thomy, F. Vollertsen, Effect of thermal cycle on the formation of intermetallic compounds in laser welding of aluminum-steel overlap joints, Phys. Procedia. 12 (2011) 134–141. https://doi.org/10.1016/j.phpro.2011.03.017.

[59] H. Park, S. Rhee, Analysis of mechanism of plasma and spatter in CO2 laser welding of galvanized steel, Opt. Laser Technol. 31 (1999) 119–126. https://doi.org/10.1016/S0030-3992(99)00013-4.

[60] A. Kouadri, L. Barrallier, Texture characterisation of hexagonal metals: Magnesium AZ91 alloy, welded by laser processing, Mater. Sci. Eng. A. 429 (2006) 11–17. https://doi.org/10.1016/J.MSEA.2006.03.100.

[61] B.J. Aalderink, B. Pathiraj, R.G.K.M. Aarts, Seam gap bridging of laser based processes for the welding of aluminium sheets for industrial applications, Int. J. Adv. Manuf. Technol. 48 (2010) 143–154.

[62] K. Rubben, H. Mohrbacher, E. Leirman, Advantages of using an oscillating laser beam for the production of tailored blanks, Lasers Mater. Process. 3097 (1997) 228–241.

[63] R.W. Messler, Principles of Welding: processes, physics, chemistry and

metallurgy, Princ. Weld. (1999). https://doi.org/10.1002/9783527617487.

[64] Y. Miyashita, Y. Mutoh, M. Akahori, H. Okumura, I. Nakagawa, X. Jin-Quan, Welding International Laser welding of dissimilar metals aided by unsteady thermal conduction boundary element method analysis, Q. J. Japan Weld. Soc. 19 (2005) 16–24. https://doi.org/10.1533/wint.2005.3487.

[65] K.R. Balasubramanian, S. Shanmugam, ; Buvanashekaran, K. Sankaranarayanasamy, NUMERICAL AND EXPERIMENTAL INVESTIGATION OF LASER BEAM WELDING OF AISI 304 STAINLESS STEEL SHEET, Adv. Prod. Eng. Manag. 3 (2008) 93–105.

[66] Y.B. Chen, Z.L. Lei, L.Q. Li, & L. Wu, L. Wu, Experimental study on welding characteristics of CO 2 laser TIG hybrid welding process, Sci. Technol. Weld. Join. 11 (2013) 403–411. https://doi.org/10.1179/174329306X129535.

[67] M.M.A. Khan, L. Romoli, G. Dini, M. Fiaschi, A simplified energy-based model for laser welding of ferritic stainless steels in overlap configurations, CIRP Ann. - Manuf. Technol. 60 (2011) 215–218. https://doi.org/10.1016/J.CIRP.2011.03.112.

[68] Y. Li, S. Hu, J. Shen, L. Liu, Microstructures and mechanical properties of H62 brass-316L stainless steel in overlap welded joints by continuous-wave laser, Int. J. Adv. Manuf. Technol. 2015 791. 79 (2015) 627–634. https://doi.org/10.1007/S00170-015-6843-6.

[69] C. Hagenlocher, M. Sommer, F. Fetzer, R. Weber, T. Graf, Optimization of the solidification conditions by means of beam oscillation during laser beam welding of aluminum, Mater. Des. 160 (2018) 1178–1185. https://doi.org/10.1016/j.matdes.2018.11.009.

[70] T.A. Mai, A.C. Spowage, Characterisation of dissimilar joints in laser welding of steel–kovar, copper–steel and copper–aluminium, Mater. Sci. Eng. A. 374 (2004) 224–233. https://doi.org/10.1016/J.MSEA.2004.02.025.

[71]   N.L. Richards, X. Huang, M.C. Chaturvedi, Heat affected zone cracking in cast inconel 718, Mater. Charact. 28 (1992) 179–187. https://doi.org/10.1016/1044-5803(92)90080-2.

[72]   E. Schubert, M. Klassen, I. Zerner, C. Walz, G. Sepold, Light-weight structures produced by laser beam joining for future applications in automobile and aerospace industry, J. Mater. Process. Technol. 115 (2001) 2–8. https://doi.org/10.1016/S0924-0136(01)00756-7.

[73]   J.N. DuPont, Fundamentals of Weld Solidification, Weld. Fundam. Process. 6A (2011) 0. https://doi.org/10.31399/asm.hb.v06a.a0005609.

[74]   N. Matsumoto, Y. Kawahito, K. Nishimoto, S. Katayama, Effects of laser focusing properties on weldability in high-power fiber laser welding of thick high-strength steel plate, J. Laser Appl. 29 (2016) 012003. https://doi.org/10.2351/1.4966258.

[75]   T. Sun, P. Franciosa, D. Ceglarek, Effect of focal position offset on joint integrity of AA1050 battery busbar assembly during remote laser welding, J. Mater. Res. Technol. 14 (2021) 2715–2726. https://doi.org/10.1016/J.JMRT.2021.08.002.

[76]   M. Pastor, H. Zhao, R.P. Martukanitz, T. Debroy, Porosity, underfill and magnesium loss during continuous wave Nd:YAG laser welding of thin plates of aluminum alloys 5182 and 5754, Weld. J. (Miami, Fla). 78 (1999).

[77]   Y.C. Liao, M.H. Yu, Effects of laser beam energy and incident angle on the pulse laser welding of stainless steel thin sheet, J. Mater. Process. Technol. 190 (2007) 102–108. https://doi.org/10.1016/J.JMATPROTEC.2007.03.102.

[78]   Z. Sun, J.C. Ion, Laser welding of dissimilar metal combinations, J. Mater. Sci. 1995 3017. 30 (1995) 4205–4214. https://doi.org/10.1007/BF00361499.

[79]   S. Chatterjee, T.A. Abinandanan, K. Chattopadhyay, Microstructure development during dissimilar welding: Case of laser welding of Ti with Ni involving intermetallic phase formation, J. Mater. Sci. 41 (2006) 643–652.

[80] G. Göbel, B. Brenner, E. Beyer, New application possibilities for fiber laser welding, in: Int. Congr. Appl. Lasers Electro-Optics, Laser Institute of America, 2007: p. 209. https://doi.org/10.2351/1.5061058.

[81] J. Weberpals, F. Dausinger, G. Göbel, B. Brenner, Role of strong focusability on the welding process, J. Laser Appl. 19 (2007) 252–258. https://doi.org/10.2351/1.2795748.

[82] K.N. Lankalapalli, J.F. Tu, M. Gartner, A model for estimating penetration depth of laser welding processes, J. Phys. D. Appl. Phys. 29 (1996) 1831. https://doi.org/10.1088/0022-3727/29/7/018.

[83] J.C. Ion, H.R. Shercliff, M.F. Ashby, Diagrams for laser materials processing, Acta Metall. Mater. 40 (1992) 1539–1551. https://doi.org/10.1016/0956-7151(92)90097-X.

[84] A. Unt, A. Salminen, Effect of welding parameters and the heat input on weld bead profile of laser welded T-joint in structural steel, J. Laser Appl. 27 (2015) S29002. https://doi.org/10.2351/1.4906378.

[85] L. Mannik, S.K. Brown, A Relationship between Laser Power, Penetration Depth and Welding Speed in the Laser Welding of Steels, J. Laser Appl. 2 (1990) 22–25. https://doi.org/10.2351/1.4745264.

[86] D.T. Swift-, A.E.F. Gick, Penetration Welding with Lasers Analytical study indicates that present laser beam weld-ing capabilities may be extended tenfold, (n.d.).

[87] K.H. Leong, H.K. Geyer, K.R. Sabo, P.G. Sanders, Threshold laser beam irradiances for melting and welding, J. Laser Appl. 9 (1997) 227–231. https://doi.org/10.2351/1.4745464.

[88] M.J. Torkamany, J. Sabbaghzadeh, M.J. Hamedi, Effect of laser welding mode on the microstructure and mechanical performance of dissimilar laser spot welds between low carbon and austenitic stainless steels, Mater. Des. 34 (2012) 666–672. https://doi.org/10.1016/J.MATDES.2011.05.024.

[89] M.N. Esfahani, J. Coupland, S. Marimuthu, Microstructure and mechanical properties of a laser welded low carbon–stainless steel joint, J. Mater. Process. Technol. 214 (2014) 2941–2948. https://doi.org/10.1016/J.JMATPROTEC.2014.07.001.

[90] T.V. Eagar, N.-S. Tsai, Temperature Fields Produced by Traveling Distributed Heat Sources, (n.d.).

[91] J. Goldak, A. Chakravarti, M. Bibby, A new finite element model for welding heat sources, Metall. Trans. B. 15 (1984) 299–305.

[92] J. Mazumder, W.M. Steen, Heat transfer model for cw laser material processing, J. Appl. Phys. 51 (1980) 941–947.

[93] Y. Kawahito, M. Mizutani, S. Katayama, Elucidation of high-power fibre laser welding phenomena of stainless steel and effect of factors on weld geometry, J. Phys. D. Appl. Phys. 40 (2007) 5854. https://doi.org/10.1088/0022-3727/40/19/009.

[94] Y.F. Tzeng, Parametric analysis of the pulsed Nd:YAG laser seam-welding process, J. Mater. Process. Technol. 102 (2000) 40–47. https://doi.org/10.1016/S0924-0136(00)00447-7.

[95] W.H. Cheng, W.H. Wang, J.G. Chen, Defect formation mechanisms in laser welding techniques for semiconductor laser packaging, IEEE Trans. Components Packag. Manuf. Technol. Part B. 19 (1996) 764–769. https://doi.org/10.1109/96.544368.

[96] W.J. Suder, S.W. Williams, Investigation of the effects of basic laser material interaction parameters in laser welding, J. Laser Appl. 24 (2012) 032009. https://doi.org/10.2351/1.4728136.

[97] M. Haider, P. Hubert, L. Lessard, An experimental investigation of class A surface finish of composites made by the resin transfer molding process, Compos. Sci. Technol. 67 (2007) 3176–3186. https://doi.org/10.1016/J.COMPSCITECH.2007.04.010.

[98] D. Wu, X. Hua, F. Li, L. Huang, Understanding of spatter formation in fiber laser welding of 5083 aluminum alloy, Int. J. Heat Mass Transf. 113 (2017) 730–740. https://doi.org/10.1016/J.IJHEATMASSTRANSFER.2017.05.125.

[99] M. Schweier, J.F. Heins, M.W. Haubold, M.F. Zaeh, Spatter formation in laser welding with beam oscillation, Phys. Procedia. 41 (2013) 20–30. www.sciencedirect.com (accessed October 5, 2020).

[100] P. Stritt, M. Boley, A. Heider, F. Fetzer, M. Jarwitz, A.P. Stritt, D. Weller, R. Weber, P. Berger, T. Graf, Comprehensive process monitoring for laser welding process optimization, in: High-Power Laser Mater. Process. Lasers, Beam Deliv. Diagnostics, Appl., SPIE, 2016: pp. 193–202. https://doi.org/10.1117/12.2212814.

[101] G. Brüggemann, A. Mahrle, T. Benziger, Comparison of experimental determined and numerical simulated temperature fields for quality assurance at laser beam welding of steels and aluminium alloyings, NDT E Int. 33 (2000) 453–463. https://doi.org/10.1016/S0963-8695(00)00017-7.

[102] S.A. David, T. DebRoy, Current Issues and Problems in Welding Science, Science (80-.). 257 (1992) 497–502. https://doi.org/10.1126/SCIENCE.257.5069.497.

[103] C.T. Kwok, S.L. Fong, F.T. Cheng, H.C. Man, Pitting and galvanic corrosion behavior of laser-welded stainless steels, J. Mater. Process. Technol. 176 (2006) 168–178. https://doi.org/10.1016/J.JMATPROTEC.2006.03.128.

[104] R.R. Ambriz, D. Jaramillo, Mechanical Behavior of Precipitation Hardened Aluminum Alloys Welds, Light Met. Alloy. Appl. (2014). https://doi.org/10.5772/58418.

[105] C. Hagenlocher, D. Weller, R. Weber, T. Graf, Reduction of the hot cracking susceptibility of laser beam welds in AlMgSi alloys by increasing the number of grain boundaries, Sci. Technol. Weld. Join. 24 (2019) 313–319.

[106] E. Raouache, Z. Boumerzoug, F. Delaunois, F. Khalfallah, Investigation by

Thermal Cycle Simulation of Heat Affected Zone in Welded AA2014 Aluminum Alloy, Res. Dev. Mater. Sci. 13 (2020). https://doi.org/10.31031/RDMS.2020.13.000812.

[107] G. V. Inamke, L. Pellone, J. Ning, Y.C. Shin, Enhancement of weld strength of laser-welded joints of AA6061-T6 and TZM alloys via novel dual-laser warm laser shock peening, Int. J. Adv. Manuf. Technol. 104 (2019) 907–919. https://doi.org/10.1007/S00170-019-03868-Y/FIGURES/17.

[108] D.M. Douglass, J. Mazumder, Mechanical properties of laser welded aluminum alloys, Int. Congr. Appl. Lasers Electro-Optics. 1996 (2018) 31. https://doi.org/10.2351/1.5059103.

[109] F. Chen, C. Liu, Improving the low-cycle fatigue properties of laser- welded Al – Zn – Mg – Cu alloy joints using double- sided ultrasonic impact treatment Improving the low-cycle fatigue properties of laser-welded Al – Zn – Mg – Cu alloy joints using double-sided ultraso, Mater. Res. Express. 8 (2021).

[110] R. Sepe, J. Wiebesiek, C.M. Sonsino, Numerical and experimental validation of residual stresses of laser-welded joints and their influence on the fatigue behaviour, Fatigue Fract. Eng. Mater. Struct. 43 (2020) 1126–1141. https://doi.org/10.1111/ffe.13180.

[111] G.H. Little, A.G. Kamtekar, The effect of thermal properties and weld efficiency on transient temperatures during welding, Comput. Struct. 68 (1998) 157–165.

[112] D. Bardel, M. Perez, D. Nelias, A. Deschamps, C.R. Hutchinson, D. Maisonnette, T. Chaise, J. Garnier, F. Bourlier, Coupled precipitation and yield strength modelling for non-isothermal treatments of a 6061 aluminium alloy, Acta Mater. 62 (2014) 129–140. https://doi.org/10.1016/J.ACTAMAT.2013.09.041.

[113] A. Simar, Y. Bréchet, B. De Meester, A. Denquin, C. Gallais, T. Pardoen, Integrated modeling of friction stir welding of 6xxx series Al alloys: Process,

microstructure and properties, Prog. Mater. Sci. 57 (2012) 95–183. https://doi.org/10.1016/J.PMATSCI.2011.05.003.

[114] S. Gao, S. Geng, P. Jiang, C. Han, L. Ren, Numerical study on the effect of residual stress on mechanical properties of laser welds of aluminum alloy 2024, Opt. Laser Technol. 146 (2022) 107580. https://doi.org/10.1016/J.OPTLASTEC.2021.107580.

[115] H. Liu, D.G. Shang, J.Z. Liu, Z.K. Guo, Fatigue life prediction based on crack closure for 6156 Al-alloy laser welded joints under variable amplitude loading, Int. J. Fatigue. 72 (2015) 11–18. https://doi.org/10.1016/J.IJFATIGUE.2014.10.012.

[116] M. Zain-ul-abdein, D. Nélias, J.F. Jullien, F. Boitout, L. Dischert, X. Noe, Finite element analysis of metallurgical phase transformations in AA 6056-T4 and their effects upon the residual stress and distortion states of a laser welded T-joint, Int. J. Press. Vessel. Pip. 88 (2011) 45–56. https://doi.org/10.1016/J.IJPVP.2010.10.008.

[117] A.A. Luo, A.K. Sachdev, D. Apelian, Alloy development and process innovations for light metals casting, J. Mater. Process. Technol. 306 (2022) 117606. https://doi.org/10.1016/j.jmatprotec.2022.117606.

[118] Hybrid Electric Vehicles Market Size, Share, Growth 2031, (n.d.). https://www.factmr.com/report/270/hybrid-electric-vehicles-market (accessed July 5, 2023).

[119] C. Berlanga-Labari, M. V. Biezma-Moraleda, P.J. Rivero, Corrosion of cast aluminum alloys: A review, Metals (Basel). 10 (2020) 1–30. https://doi.org/10.3390/met10101384.

[120] M.R.S. Ganesh, N. Reghunath, M. J.Levin, A. Prasad, S. Doondi, K. V. Shankar, Strontium in Al–Si–Mg Alloy: A Review, The Korean Institute of Metals and Materials, 2022. https://doi.org/10.1007/s12540-021-01054-y.

[121] V. Vijeesh, K.N. Prabhu, Review of microstructure evolution in hypereutectic

Al-Si alloys and its effect on wear properties, Trans. Indian Inst. Met. 67 (2014) 1–18. https://doi.org/10.1007/s12666-013-0327-x.

[122] Electric Vehicles: Making Them Lighter, Safer and More Efficient with Aluminum Alloys, (n.d.). https://www.armi.com/blog/electric-vehicles-making-them-lighter-safer-and-more-efficient-with-aluminum-alloys (accessed July 5, 2023).

[123] M. Sahul, M. Sahul, M. Haršáni, M. Dománková, On the microstructure and mechanical properties of AW2099 aluminium lithium alloy joints produced with electron beam welding, Mater. Lett. 276 (2020) 128276. https://doi.org/10.1016/j.matlet.2020.128276.

[124] S.K. Dinda, D. Das, A. Mohan, P. Srirangam, G.G. Roy, Effect of Beam Oscillation on Electron Beam Butt Welded Dual-Phase (DP600) Steel to 5754 Aluminum Alloy Joints, Metall. Mater. Trans. A Phys. Metall. Mater. Sci. 52 (2021) 1723–1731. https://doi.org/10.1007/s11661-021-06181-0.

[125] L. Huang, D. Wu, X. Hua, S. Liu, Z. Jiang, F. Li, H. Wang, S. Shi, Effect of the welding direction on the microstructural characterization in fiber laser-GMAW hybrid welding of 5083 aluminum alloy, J. Manuf. Process. 31 (2018) 514–522. https://doi.org/10.1016/j.jmapro.2017.12.010.

[126] V. Msomi, N. Mbana, S. Mabuwa, Microstructural analysis of the friction stir welded 1050-H14 and 5083-H111 aluminium alloys, Mater. Today Proc. 26 (2019) 189–192. https://doi.org/10.1016/j.matpr.2019.10.038.

[127] H.R. Kotadia, P. Franciosa, D. Ceglarek, Challenges and Opportunities in Remote Laser Welding of Steel to Aluminium, MATEC Web Conf. 269 (2019) 1–4. https://doi.org/10.1051/matecconf/201926902012 (accessed June 22, 2020).

[128] M. Garavaglia, A. Gökhan Demir, S. Zarini, B.M. Victor, B. Previtali, Fiber laser welding of AA 5754 in the double lap-joint configuration: process development, mechanical characterization, and monitoring, Int. J. Adv. Manuf. Technol. 111 (2020) 1643–1657.

[129] S. Ferraris, L.M. Volpone, Aluminum alloys in third millennium shipbuilding: materials, technologies, persepectives., 5th Int. Forum Alum. Ships. (2005) 1–10.

[130] Z. Jiang, X. Chen, H. Li, Z. Lei, Y. Chen, S. Wu, Y. Wang, Grain refinement and laser energy distribution during laser oscillating welding of Invar alloy, Mater. Des. 186 (2020). https://doi.org/10.1016/j.matdes.2019.108195.

[131] L. Huang, X. Hua, D. Wu, L. Fang, Y. Cai, Y. Ye, Effect of magnesium content on keyhole-induced porosity formation and distribution in aluminum alloys laser welding, J. Manuf. Process. 33 (2018) 43–53. https://doi.org/10.1016/j.jmapro.2018.04.023.

[132] I. Bunaziv, O.M. Akselsen, A. Salminen, A. Unt, Fiber laser-MIG hybrid welding of 5 mm 5083 aluminum alloy, J. Mater. Process. Technol. 233 (2016) 107–114. https://doi.org/10.1016/j.jmatprotec.2016.02.018.

[133] Y. Huang, C. Shen, X. Ji, F. Li, Y. Zhang, X. Hua, Correlation between gas-dynamic behaviour of a vapour plume and oscillation of keyhole size during laser welding of 5083 Al-alloy, J. Mater. Process. Technol. 283 (2020) 116721. https://doi.org/10.1016/j.jmatprotec.2020.116721.

[134] T. Yako, K. Fukui, M. Naito, M. Takeda, Precipitation Behavior in an Al-Mg Alloy with High Mg Composition, Mater. Sci. Metall. Eng. 5 (2018) 1–4. https://doi.org/10.12691/msme-5-1-1.

[135] R. Zhang, M.A. Steiner, S.R. Agnew, S.K. Kairy, C.H.J. Davies, N. Birbilis, Experiment-based modelling of grain boundary β-phase (Mg2Al3) evolution during sensitisation of aluminium alloy AA5083, Sci. Rep. 7 (2017) 1–14. https://doi.org/10.1038/s41598-017-03090-4.

[136] S. Li, G. Mi, C. Wang, A study on laser beam oscillating welding characteristics for the 5083 aluminum alloy: Morphology, microstructure and mechanical properties, J. Manuf. Process. 53 (2020) 12–20. https://doi.org/10.1016/j.jmapro.2020.01.018.

[137] H.J. McQueen, Dynamic Recovery and Recrystallization, Encycl. Mater. Sci. Technol. (2001) 2375–2381. https://doi.org/10.1016/B0-08-043152-6/00419-8.

[138] Y. Funamizu, K. Watanabe, Interdiffusion in the Al-Mg system, Mater. Lett. 1 (1982) 58–60. https://doi.org/10.1016/0167-577X(82)90006-4.

[139] E.M. Tanguep Njiokep, M. Salamon, H. Mehrer, Growth of Intermetallic Phases in the Al-Mg System, Defect Diffus. Forum. 194–199 (2001) 1581–1586. https://doi.org/10.4028/WWW.SCIENTIFIC.NET/DDF.194-199.1581.

[140] J.L. Murray, The Al−Mg (Aluminum−Magnesium) system, J. Phase Equilibria. 3 (1982) 160–163. https://doi.org/10.1007/10655491_40.

[141] M.˙Poková, M. Cieslar, J. Lacaze, TEM Investigation of Precipitation in Al-Mn Alloys with Addition of Zr, Http://Journalmt.Com/Doi/10.21062/Ujep/x.2012/a/1213-2489/MT/12/2/212.Html. 12 (2012) 212–217. https://doi.org/10.21062/UJEP/X.2012/A/1213-2489/MT/12/2/212.

[142] S. Geng, P. Jiang, L. Guo, X. Gao, G. Mi, Multi-scale simulation of grain/sub-grain structure evolution during solidification in laser welding of aluminum alloys, Int. J. Heat Mass Transf. 149 (2020). https://doi.org/10.1016/j.ijheatmasstransfer.2019.119252.

[143] M. Vyskoc, M. Sahul, M. Dománková, J. Peter, M. Sahul, M. Vyskocová, M. Martinkovic, The Effect of Process Parameters on the Microstructure and Mechanical Properties of AW5083 Aluminum Laser Weld Joints, Metals (Basel). 10 (2020) 1–22.

[144] AlMgSi Alloys :: Total Materia Article, (n.d.). https://www.totalmateria.com/page.aspx?ID=CheckArticle&site=ktn&NM=348 (accessed July 5, 2023).

[145] G.A. Edwards, K. Stiller, G.L. Dunlop, M.J. Couper, The precipitation sequence in Al-Mg-Si alloys, Acta Mater. 46 (1998) 3893–3904.

https://doi.org/10.1016/S1359-6454(98)00059-7.

[146] N. Wanderka, R. Schiffmann, J. Banhart, Characterization of precipitates in aluminium-basedalloy AW 6016, Surf. Interface Anal. 39 (2007) 221–226. https://doi.org/10.1002/sia.2518.

[147] S.S. Dash, D. Chen, A Review on Processing–Microstructure–Property Relationships of Al-Si Alloys: Recent Advances in Deformation Behavior, Metals (Basel). 13 (2023). https://doi.org/10.3390/met13030609.

[148] C.D. Marioara, S.J. Andersen, H.W. Zandbergen, R. Holmestad, The influence of alloy composition on precipitates of the Al-Mg-Si system, Metall. Mater. Trans. A Phys. Metall. Mater. Sci. 36 (2005) 691–702. https://doi.org/10.1007/s11661-005-1001-7.

[149] IMEA - Proceedings of the 9th International Conference on Aluminium Alloys (ICAA9), (n.d.). http://www.icaa-conference.net/ICAA9/data/welcome.htm (accessed July 5, 2023).

[150] S. Esmaeili, X. Wang, D.J. Lloyd, W.J. Poole, On the precipitation-hardening behavior of the Al-Mg-Si-Cu alloy AA6111, Metall. Mater. Trans. A Phys. Metall. Mater. Sci. 34 (2003) 751–763. https://doi.org/10.1007/s11661-003-1003-2.

[151] C.S. Tsao, C.Y. Chen, U.S. Jeng, T.Y. Kuo, Precipitation kinetics and transformation of metastable phases in Al-Mg-Si alloys, Acta Mater. 54 (2006) 4621–4631. https://doi.org/10.1016/j.actamat.2006.06.005.

[152] A. Graf, Aluminum alloys for lightweight automotive structures, Mater. Des. Manuf. Light. Veh. (2021) 97–123. https://doi.org/10.1016/B978-0-12-818712-8.00003-3.

[153] R. Modaresi, S. Pauliuk, A.N. Løvik, D.B. Mü Ller, Global Carbon Benefits of Material Substitution in Passenger Cars until 2050 and the Impact on the Steel and Aluminum Industries, Environ. Sci. Technol. 48 (2014) 10776–10784.

[154] Ducker, Aluminum Consumption in Light Vehicles in North America from 1975 to 2030 (in Net Pounds per Vehicle)., Stat. Stat. Inc. (2020). https://www.statista.com/statistics/496185/pounds-of-aluminum-per-car-in-north-america/#statisticContainer.

[155] A. Mayyas, M. Omar, M. Hayajneh, A.R. Mayyas, Vehicle's lightweight design vs. electrification from life cycle assessment perspective, J. Clean. Prod. 167 (2017) 687–701. https://doi.org/10.1016/j.jclepro.2017.08.145.

[156] L. Chen, C. Wang, G. Mi, X. Zhang, Effects of laser oscillating frequency on energy distribution, molten pool morphology and grain structure of AA6061/AA5182 aluminum alloys lap welding, J. Mater. Res. Technol. 15 (2021) 3133–3148. https://doi.org/10.1016/J.JMRT.2021.09.141.

[157] E. Schubert, Challenges in Thermal Welding of Aluminium Alloys, World J. Eng. Technol. 6 (2018) 296–303.

[158] T.S. Kabasakaloglu, M. Erdogan, Characterisation of figure-eight shaped oscillation laser welding behaviour of 5083 aluminium alloy, Sci. Technol. Weld. Join. 25 (2020) 609–616.

[159] D.W. Moon, E.A. Metzbower, Laser Beam Welding of Aluminum Alloy 5456 More than 90% of precipitates are vaporized during laser irradiation to enhance the toughness of the laser weld, (n.d.).

[160] S. Ramasamy, C.E. Albright, CO2 and Nd–YAG laser beam welding of 5754–O aluminium alloy for automotive applications, Sci. Technol. Weld. Join. 6 (2013) 182–190. https://doi.org/10.1179/136217101101538730.

[161] S. Venkat, C.E. Albright, S. Ramasamy, J.P. Hurley, S. Ra-, CO2 Laser Beam Welding of Aluminum 5 754-O and 6111-T4 AI Ioys Rapid joining techniques for the production of aluminum tailor welded blanks will be necessary to build lighter-weight, more fuel-efficient vehicles, (n.d.).

[162] K.M. A. El-Batahgy, Laser Beam Welding of AA5052, AA5083, and AA6061 Aluminum Alloys, 2009 (2009).

https://doi.org/10.1155/2009/974182.

[163] M.J. Cieslak, P.W. Fuerschbach, On the weldability, composition, and hardness of pulsed and continuous Nd:YAG laser welds in aluminum alloys 6061,5456, and 5086, Metall. Trans. B 1988 192. 19 (1988) 319–329. https://doi.org/10.1007/BF02654217.

[164] H. Zhao, D.R. White, T. Debroy, H. Zhao, D.R. White, T. Debroy, Current issues and problems in laser welding of automotive aluminium alloys Current issues and problems in laser welding of automotive aluminium alloys, 6608 (2013). https://doi.org/10.1179/095066099101528298.

[165] R.R. Ambriz, G. Barrera, R. García, V.H. López, Effect of the weld thermal cycles of the modified indirect electric arc on the mechanical properties of the AA6061-T6 alloy, Weld. Int. 24 (2010) 321–328. https://doi.org/10.1080/09507110903568778.

[166] T. Sun, P. Franciosa, M. Sokolov, D. Ceglarek, Challenges and opportunities in laser welding of 6xxx high strength aluminium extrusions in automotive battery tray construction, Procedia CIRP. 94 (2020) 565–570. https://doi.org/10.1016/j.procir.2020.09.076.

[167] G. Madhusudhana Reddy, C. V. Srinivasa Murthy, K. Srinivasa Rao, K. Prasad Rao, Improvement of mechanical properties of Inconel 718 electron beam welds-influence of welding techniques and postweld heat treatment, Int. J. Adv. Manuf. Technol. 43 (2009) 671–680. https://doi.org/10.1007/s00170-008-1751-7.

[168] L. Chen, G. Mi, X. Zhang, C. Wang, Effects of sinusoidal oscillating laser beam on weld formation, melt flow and grain structure during aluminum alloys lap welding, J. Mater. Process. Technol. 298 (2021) 117314. https://doi.org/10.1016/j.jmatprotec.2021.117314.

[169] K. Hao, G. Li, M. Gao, X. Zeng, Weld formation mechanism of fiber laser oscillating welding of austenitic stainless steel, J. Mater. Process. Technol. 225 (2015) 77–83. https://doi.org/10.1016/j.jmatprotec.2015.05.021.

[170] S. V Kuryntsev, A.K. Gilmutdinov, The effect of laser beam wobbling mode in welding process for structural steels, Int. J. Adv. Manuf. Technol. 81 (2015) 1683–1691.

[171] D50 Wobble and Seam Tracking Head, (n.d.). https://www.ipgphotonics.com/en/products/beam-delivery/process-heads/welding/d50-wobble-and-seam-tracking-head (accessed June 19, 2022).

[172] L. Wang, M. Gao, C. Zhang, X. Zeng, Effect of beam oscillating pattern on weld characterization of laser welding of AA6061-T6 aluminum alloy, Mater. Des. 108 (2016) 707–717. https://doi.org/10.1016/j.matdes.2016.07.053.

[173] H. Hiraga, K. Fukatsu, K. Ogawa, M. Nakayama, Y. Muto, Nd:YAG laser welding of pure titanium to stainless steel, Weld. Int. 16 (2002) 623–631. https://doi.org/10.1080/09507110209549587.

[174] J. Kar, S.K. Roy, G.G. Roy, Effect of beam oscillation on electron beam welding of copper with AISI-304 stainless steel, J. Mater. Process. Tech. 233 (2016) 174–185.

[175] S.K. Dinda, J. Kar, S. Jana, G. Gopal Roy, P. Srirangam, Effect of beam oscillation on porosity and intermetallics of electron beam welded DP600-steel to Al 5754-alloy, J. Mater. Process. Technol. 265 (2019) 191–200. https://doi.org/10.1016/j.jmatprotec.2018.10.026.

[176] C.V.. Murthy, Electron beam welding of Inconel 718- a study on the effects of different beam oscillation techniques, 2003.

[177] K. Sivaprasad, S.G.S. Raman, C.V.S. Murthy, G.M. Reddy, Coupled effect of heat input and beam oscillation on mechanical properties of alloy 718 electron beam weldments, Sci. Technol. Weld. Join. 11 (2006) 127–134.

[178] F. Fetzer, M. Sommer, R. Weber, J.P. Weberpals, T. Graf, Reduction of pores by means of laser beam oscillation during remote welding of AlMgSi, Opt. Lasers Eng. 108 (2018) 68–77. https://doi.org/10.1016/j.optlaseng.2018.04.012.

[179] C. Hagenlocher, M. Sommer, F. Fetzer, R. Weber, T. Graf, Optimization of the solidification conditions by means of beam oscillation during laser beam welding of aluminum, Mater. Des. 160 (2018) 1178–1185. https://doi.org/10.1016/j.matdes.2018.11.009.

[180] Z. Wang, J.P. Oliveira, Z. Zeng, X. Bu, B. Peng, X. Shao, Laser beam oscillating welding of 5A06 aluminum alloys: Microstructure, porosity and mechanical properties, Opt. Laser Technol. 111 (2019) 58–65. https://doi.org/10.1016/j.optlastec.2018.09.036.

[181] L. Wang, M. Gao, C. Zhang, X. Zeng, Effect of beam oscillating pattern on weld characterization of laser welding of AA6061-T6 aluminum alloy, Mater. Des. 108 (2016) 707–717. http://dx.doi.org/10.1016/j.matdes.2016.07.053.

[182] C. Zhang, X. Li, M. Gao, Effects of circular oscillating beam on heat transfer and melt flow of laser melting pool, J. Mater. Res. Technol. 9 (2020) 9271–9282.

[183] G. Barbieri, F. Cognini, M. Moncada, A. Rinaldi, G. Lapi, Welding of Automotive Aluminum Alloys by Laser Wobbling Processing, Mater. Sci. Forum. 879 (2017) 1057–1062.

[184] H. Ramiarison, N. Barka, C. Pilcher, E. Stiles, G. Larrimore, S. Amira, Weldability improvement by wobbling technique in high power density laser welding of two aluminum alloys: Al-5052 and Al-6061, J. Laser Appl. 33 (2021) 032015.

[185] W.U. Mirihanage, M. Di Michiel, A. Reiten, L. Arnberg, H.B. Dong, R.H. Mathiesen, Time-resolved X-ray diffraction studies of solidification microstructure evolution in welding, Acta Mater. 68 (2014) 159–168.

[186] P. Jiang, S. Gao, S. Geng, C. Han, G. Mi, Multi-physics multi-scale simulation of the solidification process in the molten pool during laser welding of aluminum alloys, Int. J. Heat Mass Transf. 161 (2020) 120316. https://doi.org/10.1016/J.IJHEATMASSTRANSFER.2020.120316.

[187] M. Rasch, C. Roider, S. Kohl, J. Strauß, N. Maurer, K.Y. Nagulin, M. Schmidt, Shaped laser beam profiles for heat conduction welding of aluminium-copper alloys, Opt. Lasers Eng. 115 (2019) 179–189. https://doi.org/10.1016/j.optlaseng.2018.11.025.

[188] M. Duocastella, C.B. Arnold, Bessel and annular beams for materials processing, Laser Photonics Rev. 6 (2012) 607–621. https://doi.org/10.1002/lpor.201100031.

[189] M.R. Maina, Y. Okamoto, A. Okada, M. Närhi, J. Kangastupa, J. Vihinen, High surface quality welding of aluminum using adjustable ring-mode fiber laser, J. Mater. Process. Technol. 258 (2018) 180–188. https://doi.org/10.1016/j.jmatprotec.2018.03.030.

[190] M. Mohammadpour, L. Wang, F. Kong, R. Kovacevic, Adjustable ring mode and single beam fiber lasers: A performance comparison, Manuf. Lett. 25 (2020) 50–55. https://doi.org/10.1016/j.mfglet.2020.07.003.

[191] M. Sokolov, P. Franciosa, T. Sun, D. Ceglarek, V. Dimatteo, A. Ascari, A. Fortunato, F. Nagel, Applying optical coherence tomography for weld depth monitoring in remote laser welding of automotive battery tab connectors, J. Laser Appl. 33 (2021) 012028. https://doi.org/10.2351/7.0000336.

[192] Q. Guan, J. Long, P. Yu, S. Jiang, W. Huang, J. Zhou, Effect of steel to aluminum laser welding parameters on mechanical properties of weld beads, Opt. Laser Technol. 111 (2019) 387–394. https://doi.org/10.1016/j.optlastec.2018.09.060.

[193] S. Chatterjee, T.A. Abinandanan, K. Chattopadhyay, Microstructure development during dissimilar welding: Case of laser welding of Ti with Ni involving intermetallic phase formation, J. Mater. Sci. 2006 413. 41 (2006) 643–652. https://doi.org/10.1007/S10853-006-6480-4.

[194] Z. Chen, X. Gao, Detection of weld pool width using infrared imaging during high-power fiber laser welding of type 304 austenitic stainless steel, (n.d.). https://doi.org/10.1007/s00170-014-6081-3.

[195] M. Speka, S. Matteï, M. Pilloz, M. Ilie, The infrared thermography control of the laser welding of amorphous polymers, NDT E Int. 41 (2008) 178–183. https://doi.org/10.1016/J.NDTEINT.2007.10.005.

[196] M. Moradi, M. Ghoreishi, Influences of laser welding parameters on the geometric profile of NI-base superalloy Rene 80 weld-bead, Int. J. Adv. Manuf. Technol. 55 (2011) 205–215. https://doi.org/10.1007/S00170-010-3036-1.

[197] Z. Gao, X. Shao, P. Jiang, L. Cao, Q. Zhou, C. Yue, Y. Liu, C. Wang, Parameters optimization of hybrid fiber laser-arc butt welding on 316L stainless steel using Kriging model and GA, Opt. Laser Technol. 83 (2016) 153–162. https://doi.org/10.1016/J.OPTLASTEC.2016.04.001.

[198] L.-J. Zhang, G.-F. Zhang, X.-Y. Bai, J. Ning, X.-J. Zhang, Effect of the process parameters on the three-dimensional shape of molten pool during full-penetration laser welding process, (n.d.). https://doi.org/10.1007/s00170-015-8249-x.

[199] M. Courtois, M. Carin, P. Le Masson, S. Gaied, M. Balabane, Guidelines in the experimental validation of a 3D heat and fluid flow model of keyhole laser welding, J. Phys. D. Appl. Phys. 49 (2016). https://doi.org/10.1088/0022-3727/49/15/155503.

[200] S. Pang, L. Chen, J. Zhou, Y. Yin, T. Chen, A three-dimensional sharp interface model for self-consistent keyhole and weld pool dynamics in deep penetration laser welding, J. Phys. D. Appl. Phys. 44 (2011). https://doi.org/10.1088/0022-3727/44/2/025301.

[201] R. Rai, J.W. Elmer, T.A. Palmer, T. Debroy, Heat transfer and fluid flow during keyhole mode laser welding of tantalum, Ti-6Al-4V, 304L stainless steel and vanadium, J. Phys. D Appl. Phys. 40 (2007) 5753–5766. https://doi.org/10.1088/0022-3727/40/18/037.

[202] A. Otto, H. Koch, K. Leitz, M. Schmidt, Numerical Simulations - A Versatile Approach for Better Understanding Dynamics in Laser Material Processing,

12 (2011) 11–20. https://doi.org/10.1016/j.phpro.2011.03.003.

[203] K. Kazemi, J.A. Goldak, Numerical simulation of laser full penetration welding, Comput. Mater. Sci. 44 (2009) 841–849.

[204] T. Mukherjee, V. Manvatkar, A. De, T. DebRoy, Dimensionless numbers in additive manufacturing, J. Appl. Phys. 121 (2017). https://doi.org/10.1063/1.4976006.

[205] M.A. Geiger K-H Leitz AE H Koch AE A Otto, PRODUCTION PROCESS A 3D transient model of keyhole and melt pool dynamics in laser beam welding applied to the joining of zinc coated sheets, (n.d.). https://doi.org/10.1007/s11740-008-0148-7.

[206] A. Otto, H. Koch, K.H. Leitz, M. Schmidt, Numerical Simulations - A Versatile Approach for Better Understanding Dynamics in Laser Material Processing, Phys. Procedia. 12 (2011) 11–20. https://doi.org/10.1016/J.PHPRO.2011.03.003.

[207] Z.S. Saldi, A. Kidess, S. Kenjereš, C. Zhao, I.M. Richardson, C.R. Kleijn, Effect of enhanced heat and mass transport and flow reversal during cool down on weld pool shapes in laser spot welding of steel, Int. J. Heat Mass Transf. 66 (2013) 879–888. https://doi.org/10.1016/J.IJHEATMASSTRANSFER.2013.07.085.

[208] S.A. Tsirkas, P. Papanikos, T. Kermanidis, Numerical simulation of the laser welding process in butt-joint specimens, J. Mater. Process. Technol. 134 (2003) 59–69.

[209] K. Salonitis, D. Drougas, G. Chryssolouris, Finite element modeling of penetration laser welding of sandwich materials, Phys. Procedia. 5 (2010) 327–335. https://doi.org/10.1016/J.PHPRO.2010.08.059.

[210] S. Pang, X. Chen, W. Li, X. Shao, S. Gong, Efficient multiple time scale method for modeling compressible vapor plume dynamics inside transient keyhole during fiber laser welding, Opt. Laser Technol. 77 (2016) 203–214.

https://doi.org/10.1016/J.OPTLASTEC.2015.09.024.

[211] M.M. Atabaki, M. Nikodinovski, P. Chenier, J. Ma, W. Liu, R. Kovacevic, Experimental and numerical investigations of hybrid laser arc welding of aluminum alloys in the thick T-joint configuration, Opt. Laser Technol. 59 (2014) 68–92.

[212] M. Bachmann, V. Avilov, A. Gumenyuk, M. Rethmeier, CFD simulation of the liquid metal flow in high power laser welding of aluminum with electromagnetic weld pool support, Recent Res. Mech. - Proc. 2nd Int. Conf. FLUIDSHEAT'11, TAM'11,Proc. 4th WSEAS Int. Conf. UPT'11, CUHT'11. (2011) 179–184.

[213] D. Rosenthal, Mathematical theory of heat distribution during welding and cutting, Weld. J. 20 (1941) 220–234.

[214] Z. Li, G. Yu, X. He, S. Li, Y. Zhao, Numerical and Experimental Investigations of Solidification Parameters and Mechanical Property during Laser Dissimilar Welding, Metals (Basel). 8 (2018) 799–814. https://doi.org/10.3390/met8100799.

[215] W.-I. Cho, S.-J. Na, M.-H. Cho, J.-S. Lee, Numerical study of alloying element distribution in CO_2 laser-GMA hybrid welding, (n.d.). https://doi.org/10.1016/j.commatsci.2010.06.025.

[216] X. Han, X. Tang, T. Wang, C. Shao, F. Lu, H. Cui, Role of ambient pressure in keyhole dynamics based on beam transmission path method for laser welding on Al alloy, Int. J. Adv. Manuf. Technol. 2018 995. 99 (2018) 1639–1651. https://doi.org/10.1007/S00170-018-2592-7.

[217] C.S. Wu, H.G. Wang, Y.M. Zhang, A New Heat Source Model for Keyhole Plasma Arc Welding in FEM Analysis of the Temperature Profile The model takes into consideration keyhole configuration and decay of heat distribution along the workpiece thickness, (n.d.).

[218] L. Shi, X. Li, L. Jiang, M. Gao, Numerical study of keyhole-induced porosity

suppression mechanism in laser welding with beam oscillation, Sci. Technol. Weld. Join. 26 (2021) 349–355.

[219] A.K. Unni, M. Vasudevan, Computational fluid dynamics simulation of hybrid laser-MIG welding of 316 LN stainless steel using hybrid heat source, Int. J. Therm. Sci. 185 (2023) 108042. https://doi.org/10.1016/j.ijthermalsci.2022.108042.

[220] A.H. Faraji, A. Bahmani, M. Goodarzi, S.H. Seyedein, M.O. Shabani, Numerical and experimental investigations of weld pool geometry in GTA welding of pure aluminum, J. Cent. South Univ. 21 (2014) 20–26.

[221] F. Farrokhi, B. Endelt, M. Kristiansen, A numerical model for full and partial penetration hybrid laser welding of thick-section steels, Opt. Laser Technol. 111 (2019) 671–686. https://doi.org/10.1016/J.OPTLASTEC.2018.08.059.

[222] Y. Ai, P. Jiang, X. Shao, P. Li, C. Wang, A three-dimensional numerical simulation model for weld characteristics analysis in fiber laser keyhole welding, Int. J. Heat Mass Transf. 108 (2017) 614–626.

[223] Q. Shi, D. Gu, M. Xia, S. Cao, T. Rong, Effects of laser processing parameters on thermal behavior and melting/solidification mechanism during selective laser melting of TiC/Inconel 718 composites, Opt. Laser Technol. 84 (2016) 9–22.

[224] D. Rosenthal, The Theory of Moving Source of Heat and it's Application to Metal Treatment, Trans. ASME. (1946) 849–866.

[225] J. Goldak, A. Chakravarti, M. Bibby, A New Finite Element Model for Welding Heat Sources, Metall. Trans. B. 15B (1983) 299–305.

[226] P.S.M. V.Pavelec, R. Tanbakuchi, O.A. Uyehara, No Title, Weld. J. Res. Suppl. 48 (1969) 295–305.

[227] D.T. Swift-Hook, A.E.F. Gick, Penetration Welding with Lasers, Weld. Res. Suppl. (1973) 492–499.

[228] M. Lax, Temperature rise induced by a laser beam, J. Appl. Phys. 48 (1977) 3919–3924.

[229] J. Dowden, Some aspects of the fluid dynamics of laser welding, J. Fluid Mech. 126 (1983) 123–146.

[230] H. Modest, M.F. and Abakians, Heat Conduction in a moving Semi-Infinite Solid Subjected to Pulsed Laser Beam, Heat Transf. (1986) 597–601.

[231] N.. Nguyen, A. Ohta, K. Matsuoka, N. Suzuki, Y. Maeda, Analytical Solutions for Transient Temperature of Semi-Infinite Body Subjected to 3-D Moving Heat Sources, Weld. Res. Suppl. (1999) 265–274.

[232] Z.B. Hou, R. Komanduri, General solutions for stationary/moving plane heat source problems in manufacturing and tribology, Int. J. Heat Mass Transf. 43 (2000) 1679–1698.

[233] G. Gutierrez, J.G. Araya, Temperature Distribution in a Finite Solid Due to a Moving Laser Beam, Int. Mech. Eng. Congr. R&D Expo. 3 (2003) 259–271.

[234] N. Bianco, O. Manca, S. Nardini, S. Tamburino, Transient Heat Conduction in Solids Irradiated by a Moving Heat Source, in: Defect Diffus. Forum, 2008: pp. 358–363.

[235] N. Bianco, O. Manca, S. Nardini, S. Tamburrino, A Numerical Model for Transient Heat Conduction in Semi-Infinite Solids Irradiated by a Moving Heat Source, in: 2008.

[236] N.S. Shanmugam, G. Buvanashekaran, K. Sankaranarayanasamy, S. Ramesh Kumar, A transient finite element simulation of the temperature and bead profiles of T-joint laser welds, Mater. Des. 31 (2010) 4528–4542.

[237] N.S. Shanmugam, G. Buvanashekaran, K. Sankaranarayanasamy, Some studies on temperature distribution modeling of laser butt welding of AISI 304 stainless steel sheets, World Acad. Sci. Eng. Technol. 7 (2013) 1532–1541.

[238] K. Hu, W. Muneer, J. Zhang, X. Zhan, Effect of beam oscillating frequency

258

on the microstructure and mechanical properties of dissimilar laser welding of AA2060 and AA6061 alloy, Mater. Sci. Eng. A. 832 (2022). https://doi.org/10.1016/j.msea.2021.142431.

[239] K. Abderrazak, S. Bannour, H. Mhiri, G. Lepalec, M. Autric, Numerical and experimental study of molten pool formation during continuous laser welding of AZ91 magnesium alloy, Comput. Mater. Sci. 44 (2009) 858–866.

[240] H.G. Fan, H.L. Tsai, S.J. Na, Heat transfer and Fluid Flow in a partially or fully penetrated weld pool in gas tungsten arc welding, 44 (2001) 417–428.

[241] A. Karimipour, E. Abedini, H. Ajam, S.M.H. Sarvari, Modeling of Fluid Flow and Heat Transfer in Laser Welding with a Moving Heat Source, Adv. Mater. Res. 622–623 (2012) 618–622.

[242] G. Phanikumar, P. Dutta, K. Chattopadhyay, Computational Modeling of Laser Welding of Cu-Ni Dissimilar Couple, (n.d.).

[243] Y. Hu, X. He, G. Yu, Z. Ge, C. Zheng, W. Ning, Heat and mass transfer in laser dissimilar welding of stainless steel and nickel, Appl. Surf. Sci. 258 (2012) 5914–5922. https://doi.org/10.1016/j.apsusc.2012.02.143.

[244] T. Kik, Heat source models in numerical simulations of laser welding, Materials (Basel). 13 (2020) 1–24. https://doi.org/10.3390/ma13112653.

[245] A.H. Faraji, C. Maletta, G. Barbieri, F. Cognini, L. Bruno, Numerical modeling of fluid flow, heat, and mass transfer for similar and dissimilar laser welding of Ti-6Al-4V and Inconel 718, Int. J. Adv. Manuf. Technol. 114 (2021) 899–914. https://doi.org/10.1007/s00170-021-06868-z.

[246] W. Cho, S. Na, C. Thomy, F. Vollertsen, Numerical simulation of molten pool dynamics in high power disk laser welding, J. Mater. Process. Tech. 212 (2012) 262–275. https://doi.org/10.1016/j.jmatprotec.2011.09.011.

[247] C. Zhang, X. Li, M. Gao, Effects of circular oscillating beam on heat transfer and melt flow of laser melting pool, J. Mater. Res. Technol. 9 (2020) 9271–9282. https://doi.org/10.1016/j.jmrt.2020.06.030.

[248] C. Panwisawas, Y. Sovani, R.P. Turner, J.W. Brooks, H.C. Basoalto, I. Choquet, Modelling of thermal fluid dynamics for fusion welding, J. Mater. Process. Technol. 252 (2018) 176–182. https://doi.org/10.1016/J.JMATPROTEC.2017.09.019.

[249] N. Rietmann, T. Lieven, How policy measures succeeded to promote electric mobility – Worldwide review and outlook, J. Clean. Prod. 206 (2019) 66–75.

[250] P.J.C. González, T. Furubayashi, T. Nakata, Energy use and CO2 emissions reduction potential in passenger car fleet using zero emission vehicles and lightweight materials, Energy. 48 (2012) 548–565.

[251] O. Seffer, R. Pfeifer, A. Springer, S. Kaierle, Investigations on laser beam welding of different dissimilar joints of steel and aluminum alloys for automotive lightweight construction, Phys. Procedia. 83 (2016) 383–395.

[252] G. Pardal, S. Meco, A. Dunn, S. Williams, S. Ganguly, D.P. Hand, K.L. Wlodarczyk, Laser spot welding of laser textured steel to aluminium, J. Mater. Process. Technol. 241 (2017) 24–35.

[253] F.S. Bayraktar, P. Staron, M. Koçak, A. Schreyer, Analysis of Residual Stress in Laser Welded Aerospace Aluminium T-joints by Neutron Diffraction and Finite Element Modelling, Mater. Sci. Forum. 571–572 (2008) 355–360. www.scientific.net.

[254] COMSOL, Using the Material Libraries in COMSOL Multiphysics® | COMSOL Blog, (2020). https://www.comsol.com/blogs/using-the-material-libraries-in-comsol-multiphysics/ (accessed August 16, 2022).

[255] S. D'Ostuni, P. Leo, G. Casalino, FEM Simulation of Dissimilar Aluminum Titanium Fiber Laser Welding Using 2D and 3D Gaussian Heat Sources, Metals (Basel). 7 (2017) 1–15.

[256] H. Seli, M. Awang, A.I.M. Ismail, E. Rachman, Z.A. Ahmad, Evaluation of properties and FEM model of the friction welded mild steel-Al6061-alumina, Mater. Res. 16 (2013) 453–467.

[257] M.A. Bramson, Infrared Radiation: A Handbook for Applications, Plenum Press, New York, 1968.

[258] M. Slováček, V. Diviš, L. Junek, V. Ochodek, Numerical Simulation of the Welding Process — Distortion and Residual Stress Prediction, Heat Source Model Determination, Weld. World. 49 (2005) 15–29.

[259] L. Wang, M. Gao, X. Zeng, Experiment and prediction of weld morphology for laser oscillating welding of AA6061 aluminium alloy, Sci. Technol. Weld. Join. 24 (2019) 334–341.

[260] S.B. Green, How many subjects does it take to do a regression analysis., Multivariate Behav. Res. 26 (1991) 499–510.

[261] Y. Li, Y. Zhao, J. Wang, X. Zhan, Effect of laser power on the grain morphology and microhardness of dual laser-beam bilateral synchronous welded 2219 aluminium alloy T-joint, Sci. Technol. Weld. Join. 26 (2021) 540–550.

[262] W. Tao, Z. Yang, C. Shi, D. Dong, Simulating effects of welding speed on melt flow and porosity formation during double-sided laser beam welding of AA6056-T4/AA6156-T6 aluminum alloy T-joint, J. Alloys Compd. 699 (2017) 638–647.

[263] A. De, T. Debroy, Improving reliability of heat and fluid flow calculation during conduction mode laser spot welding by multivariable optimisation, Sci. Technol. Weld. Join. 11 (2006) 143–153. https://www.tandfonline.com/action/journalInformation?journalCode=ystw20 (accessed February 5, 2022).

[264] A.H. Faraji, C. Maletta, G. Barbieri, F. Cognini, L. Bruno, Numerical modeling of fluid flow, heat, and mass transfer for similar and dissimilar laser welding of Ti-6Al-4V and Inconel 718, Int. J. Adv. Manuf. Technol. 114 (2021) 899–914.

[265] W. Piekarska, M. Kubiak, M. Vaško, Numerical Estimation of the Shape of

Weld and Heat Affected Zone in Laser-arc Hybrid Welded Joints, Procedia Eng. 177 (2017) 114–120.

[266] S. Bag, A. Trivedi, A. De, Development of a finite element based heat transfer model for conduction mode laser spot welding process using an adaptive volumetric heat source, Int. J. Therm. Sci. 48 (2009) 1923–1931.

[267] S. Geng, P. Jiang, X. Shao, L. Guo, X. Gao, Heat transfer and fluid flow and their effects on the solidification microstructure in full-penetration laser welding of aluminum sheet, J. Mater. Sci. Technol. 46 (2020) 50–63. https://doi.org/10.1016/j.jmst.2019.10.027.

[268] C.S. Wu, T. Zhang, Y.H. Feng, Numerical analysis of the heat and fluid flow in a weld pool with a dynamic keyhole, Int. J. Heat Fluid Flow. 40 (2013) 186–197.

[269] X. He, J.W. Elmer, T. Debroy, Heat transfer and fluid flow in laser microwelding, J. Appl. Phys. 97 (2005) 084909. https://doi.org/10.1063/1.1873032.

[270] M. Behúlová, E. Babalová, M. Sahul, Design of Laser Welding Parameters for Joining Ti Grade 2 and AW 5754 Aluminium Alloys Using Numerical Simulation, Adv. Mater. Sci. Eng. 2017 (2017) 1–15.

[271] H. Guo, J. Hu, H.L. Tsai, Three-Dimensional Modeling of Gas Metal Arc Welding of Aluminum Alloys, J. Manuf. Sci. Eng. 132 (2010) 1–10.

[272] S. Fouladi, A.H. Ghasemi, M. Abbasi, M. Abedini, A.M. Khorasani, I. Gibson, The effect of vibration during friction stir welding on corrosion behavior, mechanical properties, and machining characteristics of stir zone, Metals (Basel). 7 (2017). https://doi.org/10.3390/met7100421.

[273] T. Sun, P. Franciosa, D. Ceglarek, Effect of focal position offset on joint integrity of AA1050 battery busbar assembly during remote laser welding, J. Mater. Res. Technol. 14 (2021) 2715–2726. https://doi.org/10.1016/j.jmrt.2021.08.002.

[274] D.W. Cho, W.I. Cho, S.J. Na, Modeling and simulation of arc: Laser and hybrid welding process, J. Manuf. Process. 16 (2014) 26–55.

[275] C. Zhang, X. Li, M. Gao, Effects of circular oscillating beam on heat transfer and melt flow of laser melting pool, J. Mater. Res. Technol. 9 (2020) 9271–9282. https://doi.org/10.1016/j.jmrt.2020.06.030.

[276] J.D. Hunt, Steady state columnar and equiaxed growth of dendrites and eutectic, Mater. Sci. Eng. 65 (1984) 75–83. https://doi.org/10.1016/0025-5416(84)90201-5.

[277] M. Gäumann, C. Bezençon, P. Canalis, W. Kurz, Single-crystal laser deposition of superalloys: processing–microstructure maps, Acta Mater. 49 (2001) 1051–1062. https://doi.org/10.1016/S1359-6454(00)00367-0.

[278] S.C. Flood, J.D. Hunt, Columnar and equiaxed growth: II. Equiaxed growth ahead of a columnar front, J. Cryst. Growth. 82 (1987) 552–560. https://doi.org/10.1016/0022-0248(87)90347-2.

[279] M. Vandyoussefi, A.L. Greer, Application of cellular automaton–finite element model to the grain refinement of directionally solidified Al–4.15 wt% Mg alloys, Acta Mater. 50 (2002) 1693–1705. https://doi.org/10.1016/S1359-6454(02)00015-0.

[280] J. Cheng, G. Song, X. Zhang, C. Liu, L. Liu, Review of techniques for improvement of softening behavior of age-hardening aluminum alloy welded joints, 2021. https://doi.org/10.3390/ma14195804.

[281] A.W. Alshaer, L. Li, A. Mistry, Effect of filler wire properties on porosity formation in laser welding of AC-170PX aluminium alloy for lightweight automotive component manufacture, Proc. Inst. Mech. Eng. Part B J. Eng. Manuf. 231 (2017) 994–1006. https://doi.org/10.1177/0954405415578584.

[282] D. Weller, C. Bezençon, P. Stritt, R. Weber, T. Graf, Remote laser welding of multi-alloy aluminum at close-edge position, Phys. Procedia. 41 (2013) 164–168. https://doi.org/10.1016/j.phpro.2013.03.065.

[283] J. Wu, H. Zhang, Y. Feng, B.B. Luo, 3D multiphysical modelling of fluid dynamics and mass transfer in laser welding of dissimilar materials, Metals (Basel). 8 (2018). https://doi.org/10.3390/met8060443.

[284] L. Wang, M. Mohammadpour, X. Gao, J.P. Lavoie, K. Kleine, F. Kong, R. Kovacevic, Adjustable Ring Mode (ARM) laser welding of stainless steels, Opt. Lasers Eng. 137 (2021). https://doi.org/10.1016/j.optlaseng.2020.106360.

[285] B. Victor, D. Kliner, M. Hepp, Is beam shaping the future of laser welding?, Ind. Laser Solut. (2019).

[286] F. Kong, J.P. Lavoie, K. Kleine, R. Kovacevic, Computational modeling and experimental validations of the heat transfer and residual stresses in the aluminum 6061-T6 plate welded by an Adjustable Ring Mode (ARM) Laser, J. Light Met. Weld. 58 (2020) 293–299. https://doi.org/10.11283/jlwa.58.19.

[287] A. Artinov, M. Bachmann, M. Rethmeier, Equivalent heat source approach in a 3D transient heat transfer simulation of full-penetration high power laser beam welding of thick metal plates, Int. J. Heat Mass Transf. 122 (2018) 1003–1013.

[288] L. Shi, X. Li, L. Jiang, M. Gao, Numerical study of keyhole-induced porosity suppression mechanism in laser welding with beam oscillation, Sci. Technol. Weld. Join. 26 (2021) 349–355. https://doi.org/10.1080/13621718.2021.1913562.

[289] S.S. Ltd., JMatPro, (2014).

[290] M.R. Maina, Y. Okamoto, A. Okada, M. Närhi, J. Kangastupa, J. Vihinen, High surface quality welding of aluminum using adjustable ring-mode fiber laser, J. Mater. Process. Technol. 258 (2018) 180–188. https://doi.org/10.1016/j.jmatprotec.2018.03.030.

[291] E.N. ISO, 6892-1. Metallic materials-Tensile testing-Part 1: Method of test at room temperature, Int. Organ. Stand. (2009).

[292] J. Ma, F. Kong, W. Liu, B. Carlson, R. Kovacevic, Study on the strength and

failure modes of laser welded galvanized DP980 steel lap joints, J. Mater. Process. Technol. 214 (2014) 1696–1709. https://doi.org/10.1016/j.jmatprotec.2014.03.018.

[293] Y. Miyazaki, S. Furusako, Tensile shear strength of laser welded lap joints, Nippon Steel Tech. Rep. (2007) 28–34.

[294] S. Geng, P. Jiang, X. Shao, G. Mi, H. Wu, Y. Ai, C. Wang, C. Han, R. Chen, W. Liu, Effects of back-diffusion on solidification cracking susceptibility of Al-Mg alloys during welding: A phase-field study, Acta Mater. 160 (2018) 85–96.

[295] L. Li, J. Gong, H. Xia, G. Peng, Y. Hao, S. Meng, J. Wang, Influence of scan paths on flow dynamics and weld formations during oscillating laser welding of 5A06 aluminum alloy, J. Mater. Res. Technol. 11 (2021) 19–32. https://doi.org/10.1016/j.jmrt.2020.12.102.

Appendix: Selection of time step and mesh size

To capture and visualize the behaviour of an oscillating beam, a time step is chosen to ensure that at least four solutions are obtained within a single oscillation. The mesh size is determined through a two-step process: (*i*) In the first step, the minimum mesh size is set smaller than the laser spot size to adequately represent the laser beam with sufficient mesh elements. (*ii*) In the second step, the mesh size is adjusted until the model output remains consistent regardless of changes in mesh size. For the first step, the minimum mesh size at the fusion zone is defined as $r/4$, where r represents the radius of the laser spot. In the second step, a mesh sensitivity analysis, depicted in Figure 3.2. is conducted to ensure the final mesh size satisfies both steps. An illustrative example is provided to demonstrate the selection of the time step and mesh size.

The laser spot size is 0.2 mm. The frequency of oscillation, f is 500 Hz and the maximum welding speed, s studied in this study is 6000 mm/min.

The radius of laser spot, $r = 0.1$ mm.

The mesh size, m in fusion zone $= r/4$

$m = 0.025$ mm.

The time step, $t = 1/(4f)$

$t = 0.0005$ sec

For each time step the laser beam moves the distance, d by $(t \times s)$

$d = 0.05$ mm

Number of mesh element for each time step $= d/m$

Number of mesh element for each time step $= 2$.

This calculation shows that there is sufficient number of elements for the laser beam movement in between each time step.